Response of the High-Latitude Ionospheric Convection to Changes in the Interplanetary Medium

Thesis submitted for the degree of
Doctor of Philosophy
at the University of Leicester

Hina Khan
Department of Physics and Astronomy
University of Leicester

November 1999

ProQuest LLC
789 East Eisenhower Parkway
P.O. Box 1346
Ann Arbor, MI 48106-1346

Response of the High-Latitude Ionospheric Convection to Changes in the Interplanetary Medium

Hina Khan

Abstract

Studies have been conducted on the flow in the high-latitude ionosphere and how this depends on the properties of the interplanetary medium. Specifically, the response of the convection pattern to changes in the interplanetary magnetic field (IMF) have been studied in detail, using the European Incoherent Scatter (EISCAT) radar to measure ~300 h of tristatic field-perpendicular F region ionospheric velocities at 66.3° magnetic latitude, in combination with simultaneous solar wind/IMF measurements from the IMP-8 spacecraft located upstream of the bow shock.

Firstly, a statistical cross-correlation analysis is performed using each ionospheric flow component and a function of IMF B_z for all local times. Upon combining the response delays from each of the velocity components to determine the 'first response' of the flow to IMF changes, the minimum response delay was found to occur at 1400 MLT. The average response delay over the 12 h interval centred on 1400 MLT is 1.3±0.8 min, while that for the 12 h sector centred on 0200 MLT is 8.8±1.7 min. A second complementary 'event study' was conducted on the same data set, where polarity changes in IMF B_z were located and the time for the ionosphere to respond examined. The combined data set also indicated a minimum response delay centred on 1400 MLT, with the 'dayside' average as 4.8±0.5 min, and the 'nightside' increasing to 9.2±0.8 min.

Finally, the perturbation flow effect on auroral zone field lines associated with IMF B_y was examined through a cross-correlation analysis of the velocity components with IMF B_y. A principally zonal eastward flow perturbation ~several tens of $m\,s^{-1}\,nT^{-1}$ was observed for positive IMF B_y. A model describing the distortion of the magnetospheric field lines with a perturbation IMF B_y was used, producing the correct orientation and magnitude of the flow effect observed, when an appropriate magnetospheric model was used.

I would like to dedicate this thesis to

my Mother and Father

Acknowledgements

I would like to thank the following people for their help and encouragement over the course of the last few years:

The University of Leicester for funding my PhD.

Professor Stan Cowley for giving me the opportunity to study in the Radio and Space Plasma Physics Group, and offering unprecedented insight into the world of space plasma physics. Our constant and often lengthy discussions have provided me with a greater understanding of the subject, and of life in general.

Dr. Mark Lester for making me realise that things are never as bad as they seem, and that it will all be worth it is the end. I'm still waiting...

Dr. Jackie Davies for showing me the wonders of the EISCAT radar and teaching me the beautifully simplistic nature of the analysis packages. Also Dr. Darren Wright for taking me to the EISCAT facility and making me dig out an antenna mast from 10 feet of snow!

All the members of the group, past and present, including Tim Yeoman (who has placed a roof over my head), Steve Milan, Gabby Provan (plus bump!), Paul Eglitis, Giles Bond, Brian Shand (even though all of his software was wrong!), Jim Wild, Jonny Rae, Jon Storey, Kathryn McWilliams and Emma Bunce - the 'Psycho Reebok team', Eric and Debbie Bradshaw and baby Sarah, Dave Neudegg, Mick Parsons, Stuart Crooks, Pete Chapman, Alison Wesley, for their friendship and for making Leicester a place I could call home.

To my parents and family who have supported me throughout my education and realised that this was something I had always wanted to do. I thank them for understanding how much this Ph.D. means to me and for always encouraging me to excel in whatever I chose to do in my life.

Finally I would like to thank all the people who have helped me achieve the success I have today. There isn't enough space to thank you all personally, but you know who you are.

Contents

CHAPTER 1

Introduction and background

1.1 Introduction

This thesis investigates some aspects of solar-terrestrial coupling, emphasising particularly the effect that solar wind-magnetosphere interactions have on the nature of plasma convection observed within the ionospheric region. The primary coupling occurs between the solar wind and embedded interplanetary magnetic field (IMF), extending radially towards the Earth from the Sun, and the principally dipolar geomagnetic field at the magnetopause interface between these two regimes, and predominately involves magnetic reconnection at the interface. The resulting interaction dominates the plasma flow observed in the high-latitude ionosphere such that substantial information can be derived concerning the nature of the coupling taking place. Differing IMF conditions produce distinctly different patterns of ionospheric convection, with the north-south (Z) component of the field producing the most important effect. The present chapter will review basic knowledge of the solar terrestrial environment, while in Chapter 2 attention is directed to the nature of the solar wind-magnetosphere-ionosphere coupling which leads to ionospheric plasma flows, and the present conceptions about the time scales on which the flow changes in response to variations in interplanetary conditions. Variations in the ionospheric flow can be observed by incoherent scatter radar systems such as EISCAT, and in Chapter 3 the basic theory of incoherent scatter radars is outlined, and the measuring techniques explained with reference to the ionospheric parameters that are used in the subsequent studies. Our results are then presented and discussed in Chapters 4, 5 and 6.

1.2 The solar-terrestrial environment

1.2.1 The sun and the solar wind

The Sun is a hot gaseous body consisting of ~90% hydrogen and ~10% helium [see e.g. *Priest*, 1985], held together and compressed under its own gravitational attraction, with a mass of $\sim 10^{30}$ kg and a core temperature of $\sim 10^{7}$ K. A diagram illustrating the overall structure of the solar interior is shown in Figure 1.1 [*Priest*, 1995]. The solar surface is the 'visible' *photosphere* at a radius of $\sim 6.96 \times 10^{6}$ km and a surface temperature of ~5700 K. This forms the lowest layer of the solar atmosphere and although it is only

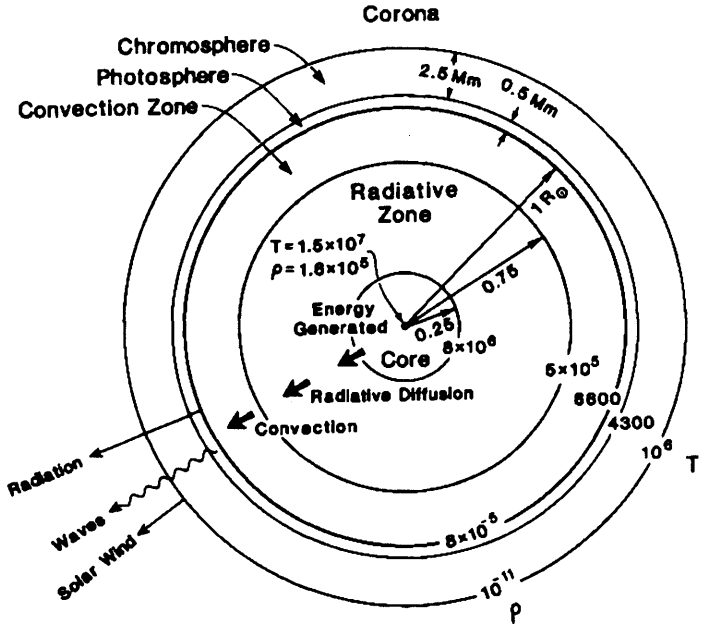

FIGURE 1.1 Overall structure of the solar interior and the solar atmosphere. [From *Priest*, 1995]

~500 km thick, it emits most of the solar lumination. Above this 'skin' layer lies the more transparent but thicker (~2500 km) *chromosphere*, followed by the extensive solar *corona* above altitudes of ~3000 km. The temperature increases slowly through the chromosphere from an initial value of ~4300 K, increasing sharply to ~2×10^6 K [e.g. *Priest*, 1995] as one enters the hot rarefied plasma of the corona. These high coronal temperatures naturally require there to be a high pressure at the base of the solar corona, which decreases to a limiting value of ~10^{-6} Nm^{-2} far from the Sun. If this pressure were less than the pressure of the local interstellar medium (*LISM*), then the expanding solar corona would eventually be bound by the *LISM*, allowing the formation of an interface across which the pressures would balance. However, the typical pressure in interstellar space is ~10^{-13} Nm^{-2}, which is many orders of magnitude less than the solar wind plasma pressure at such distances. Thus an equilibrium between the corona and the distant medium can not exist, resulting in a continuous plasma outflow emitted radially from the Sun which was mathematically described by *Parker* [1958] and became known as the *solar wind.* At the mean position of the Earth, defined as 1 Astronomical Unit (AU) from the Sun, the typical parameters of the solar wind velocity (v_{sw}), particle number density (ρ_{sw}) and temperature (T_{sw}) are 300-600 km s^{-1}, 5-15 $\times$ 10^6 m^{-3} and ~10^5 K respectively [see *e.g. Gosling et al.*, 1976; *Hundhausen*, 1995].

1.2.2 Solar magnetic structure and the interplanetary magnetic field

The Sun has an active magnetic field which reverses polarity every 11 years. This reversal can be monitored by observing cool *sunspots* (~4000 K) on the solar photosphere, appearing in pairs of opposite polarity and moving in latitude across the solar surface. It is observed that at the start of the 11-year *solar cycle*, sunspots appear at high latitudes near ±30° from the equator. During the course of the cycle solar activity increases, as does the number of sunspots, moving to more equatorial latitudes. However towards the end of the cycle, solar activity reaches a minimum corresponding to a minimum in sunspot number, all of which are now located close to the equator. The solar magnetic field distorts from a near dipolar field when solar activity is low, to a much more structured field when activity is a maximum. The residue of this solar magnetic field in the solar wind is the weak interplanetary magnetic field (IMF), amounting to a few nanoteslas in strength which propagates outward with the radially expanding solar wind. The magnetic Reynolds number (R_m) gives an indication of the nature of the plasma and magnetic field coupling. It is defined by taking the ratio of convective and magnetic diffusive terms in a time varying

magnetic field from the *diffusion equation* and is given by the order of magnitude expression, $\mu_0 \sigma v L$, where μ_0 is the permeability of free space, σ is the conductivity of the medium, v is the characteristic speed of the plasma, and L is the scale length for magnetic variations, known as the characteristic scale length of the system. The behaviour of the plasma and magnetic field depend critically on the magnitude of this ratio, and principally on the value of L. If R_m is very much larger than unity, i.e. L is large, then the convective term dominates and the magnetic field is said to be 'frozen' to the plasma. For the solar wind/IMF system with a scale size of ~5 solar radii, R_m is of the order 10^{11}, thus convection dominates and the IMF is carried with the expanding solar wind plasma. However the addition of solar rotation causes the magnetic field to form an Archimedean spiral often referred to as the *Parker Spiral* [*Parker*, 1958], as shown in Figure 1.2 [*Holzer*, 1979], since the field is frozen into the radially propagating plasma while the solar wind sources rotate with the Sun underneath. At the orbit of the Earth, the field lines on average are directed at an angle of 45° to the radial (X) direction, with the radial and the dawn-dusk (Y) components of the IMF roughly equal in magnitude. However, the field can point in either direction, towards or away from the Sun. A current sheet separating regions of differing magnetic polarity extends outward into space. If the solar magnetic structure were a simple dipole aligned with the solar rotation axis, this current sheet would lie in the solar equatorial plane, separating northern and southern hemispheres of opposite magnetic polarity. By tilting the dipole axis away from the rotation axis, as illustrated in Figure 1.3 [*Hundhausen*, 1977], the distortion in the current sheet results in a *sector structure* of 'towards' and 'away' fields observed near the Earth, as the Earth passes above and below the current sheet over the course of the solar rotation. Long periods of the magnetic field directed 'towards' or 'away from' the Earth are interrupted by sudden sector crossings on a time scale dependent on the intensity of the magnetic disturbance, switching the field to point in the opposite direction to that prior to the crossing. At solar minimum, the solar magnetic field is similar to an inclined dipole field causing little disturbance in the current sheet allowing the formation of a typical two-sector structure of the IMF. During solar maximum, the source field becomes far more structured, resulting in the appearance of four or more sectors [*e.g. Yeoman et al.*, 1990]. The sector structure determines the principal direction of the radial (X) and the dawn-dusk (Y) components of the field, which may remain in a consistent sense for several days. However, the polarity of the north-south (Z) component can vary much more rapidly due to disturbances within the solar

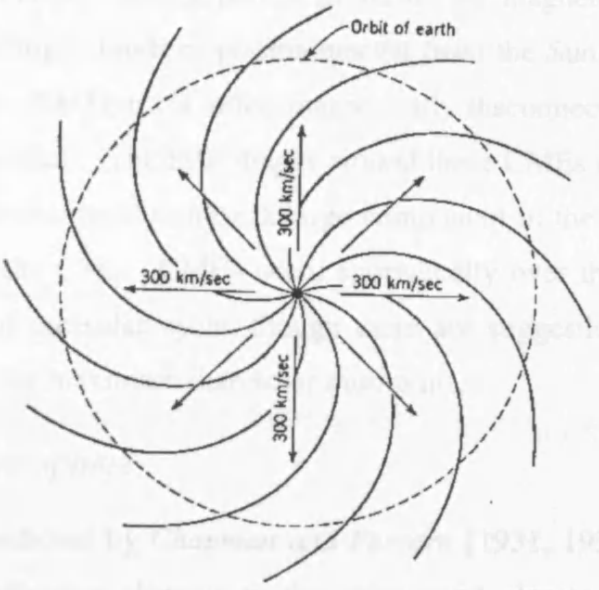

FIGURE 1.2 Parker spiral formation of the interplanetary magnetic field lines (solid lines) in the solar equatorial plane, due to an anticlockwise rotation of the Sun and a radial solar wind plasma speed of 300 km s^{-1}. [From *Holzer*, 1979]

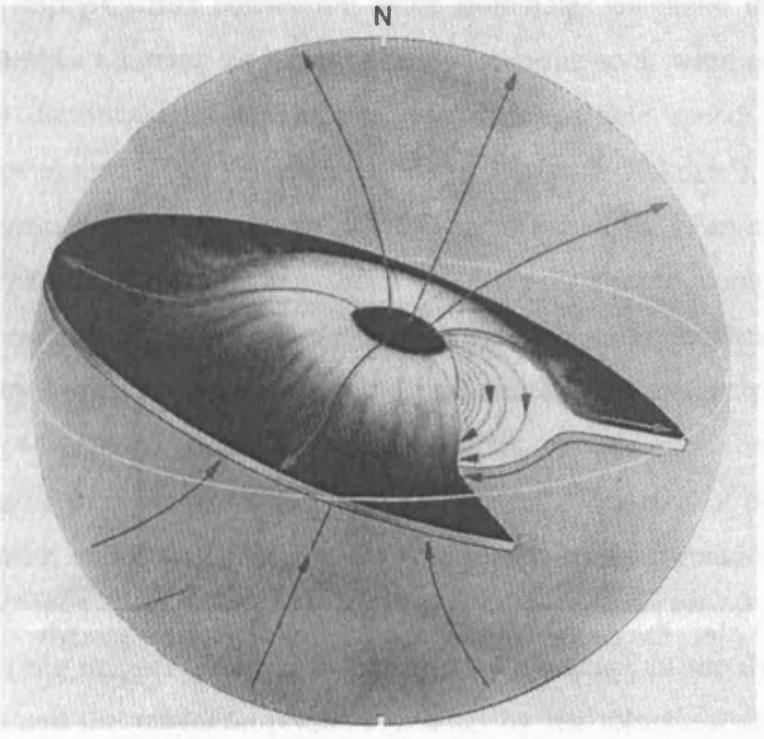

FIGURE 1.3 Distortion of the current sheet when the dipole axis is tilted away from the rotation axis, producing the sector structure in the magnetic field. [From *Hundhausen,* 1977]

wind, such as *coronal mass ejections* (CMEs), MHD waves, shocks and other discontinuities, ultimately causing perturbations in the magnetospheric and ionospheric regions. CMEs are huge clouds of plasma ejected from the Sun at extremely high speeds (several hundred to ~2000 km s^{-1}), often magnetically disconnected from the Sun to form closed loops, or 'bubbles'. The IMF drapes around these CMEs such that the Parker spiral magnetic field is re-orientated to have a large component in the Z direction in a localised region surrounding the CME. CMEs occur sporadically over the surface of the Sun and during the course of the solar cycle, though there are suggestions that they occur more frequently during solar maximum than solar minimum.

1.2.3 The magnetosphere

As correctly predicted by *Chapman and Ferraro* [1931, 1932], a planetary magnetic field provides an effective obstacle to the solar wind plasma, the latter confining the geomagnetic field into a *magnetospheric cavity*, which extends out into a long tail antisunward, known as the *magnetotail*. Figure 1.4 [*Vasyliunas*, 1983] shows a schematic of the Earth's magnetospheric cavity, as proposed by Chapman and Ferraro [1931, 1932]. Consideration of the magnetic Reynolds number yields a value of $R_M \sim 10^{16}$ for scale lengths ~1 R_E, implying that convection again dominates magnetic diffusion inside the magnetosphere, thus allowing no penetration between the solar wind and magnetospheric systems. The dominance of the highly supersonic particle speed of the solar wind (>400 km s^{-1}) over the *Alfvén wave* speed of the plasma (~50 km s^{-1}), results in a shock front forming upstream from the Earth at a distance of ~13-15R_E [*Peredo et al.*, 1995]. As the solar wind passes through the *bow shock* the plasma is slowed, compressed and heated, entering the region known as the *magnetosheath*. The magnetosheath plasma is also characterised by a high level of waves and turbulence. The magnetosheath on average tends to be a few R_E in thickness, Earthward of which a boundary is formed separating the solar wind plasma from the terrestrial field and plasma. The lack of penetration between the magnetosheath and magnetospheric plasmas results in the formation of a thin current sheet, known as the *magnetopause*, located ~9-11 R_E upstream [*Roelof and Sibeck*, 1993]. The position of the magnetopause is determined by a balance of the dynamic pressure of the solar wind and the magnetic pressure exerted by the terrestrial field [e.g. *Fairfield*, 1971]. The incident solar wind compresses the Earth's dipolar magnetic field on the dayside and stretches it out into the magnetotail on the nightside. The downstream extent of the magnetotail is not known, though spacecraft have detected the magnetotail out as far

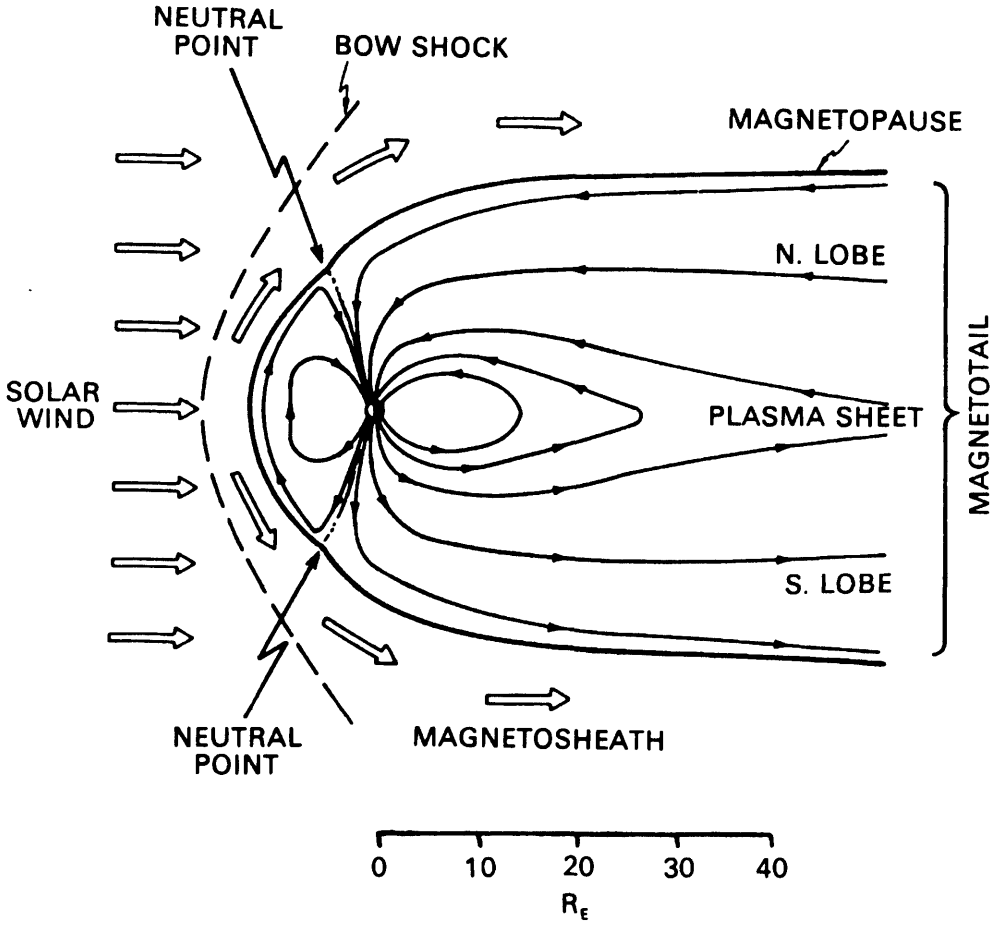

FIGURE 1.4 Schematic illustrating the magnetosphere in the noon-midnight meridian, as formed by a supersonic approaching solar wind, with the creation of an upstream shock (bow shock) and the magnetopause. [Adapted from *Vasyliunas*, 1983]

as 1000 R_E from the Earth [*Villante*, 1975]. This simple model of the magnetosphere also predicts two *neutral points* on the dayside magnetopause where the total field is zero. These points connect along field lines to magnetic latitudes near ±77° in the polar ionosphere providing the only direct means of entry for magnetosheath plasma (and hence plasma of solar wind origin) into the magnetosphere in this model. However, such particles have in fact been detected in a region extending over some 5° in latitude around ±77° and over ~8h of local time around noon. These regions are called the *polar cusps* (or *clefts*), and result from magnetic reconnection between the IMF and terrestrial field that results in the open magnetic structure, to be described in see §2.2.2. The regions of open flux produced by this coupling are defined as the *polar caps*, a definition that is adopted throughout this thesis. The polar cusps are then indicative of the dayside boundary between open and closed flux in the northern and southern polar caps, where the solar wind plasma can penetrate into the magnetosphere and flow down into the ionosphere. We shall return to the significance of these regions in the following chapter when the discussion will turn to magnetospheric convection and the effect on the high-latitude ionosphere.

1.2.4 The ionosphere

The Earth's neutral upper atmosphere is primarily ionised by solar radiation inducing photoionisation and by energetic particle precipitation form the magnetosphere. Photoionisation processes dominate at high latitudes during the hours of daylight, however at night and during winter, particle precipitation produces the majority of the ionisation in the upper atmosphere. These processes produce sufficient numbers of free electrons and positive ions to create a conducting medium in the atmosphere at altitudes of ~60-1000 km, though the medium as a whole remains electrically neutral. The existence of such a region was confirmed by the transmission of radio waves into the atmosphere in the 1930's, with the reflection height indicating the altitude and extent of an ionised medium with the atmosphere [see e.g. *Davies*, 1966]. The medium became known as the Earth's *ionosphere*. Below 60 km, the loss rate from recombination of ions and electrons dominates due to higher atmospheric gas densities, so the ion densities are low. The *ionosphere* is subdivided into four regions, labelled the D, E, F_1 and F_2 layers, which are characterised by the electron density profile and by the reflection height of electromagnetic waves. Figure 1.5 shows the typical day and night vertical structure of the electron density present in the ionosphere, where the inflections in the electron density profile indicate the different layers mentioned.

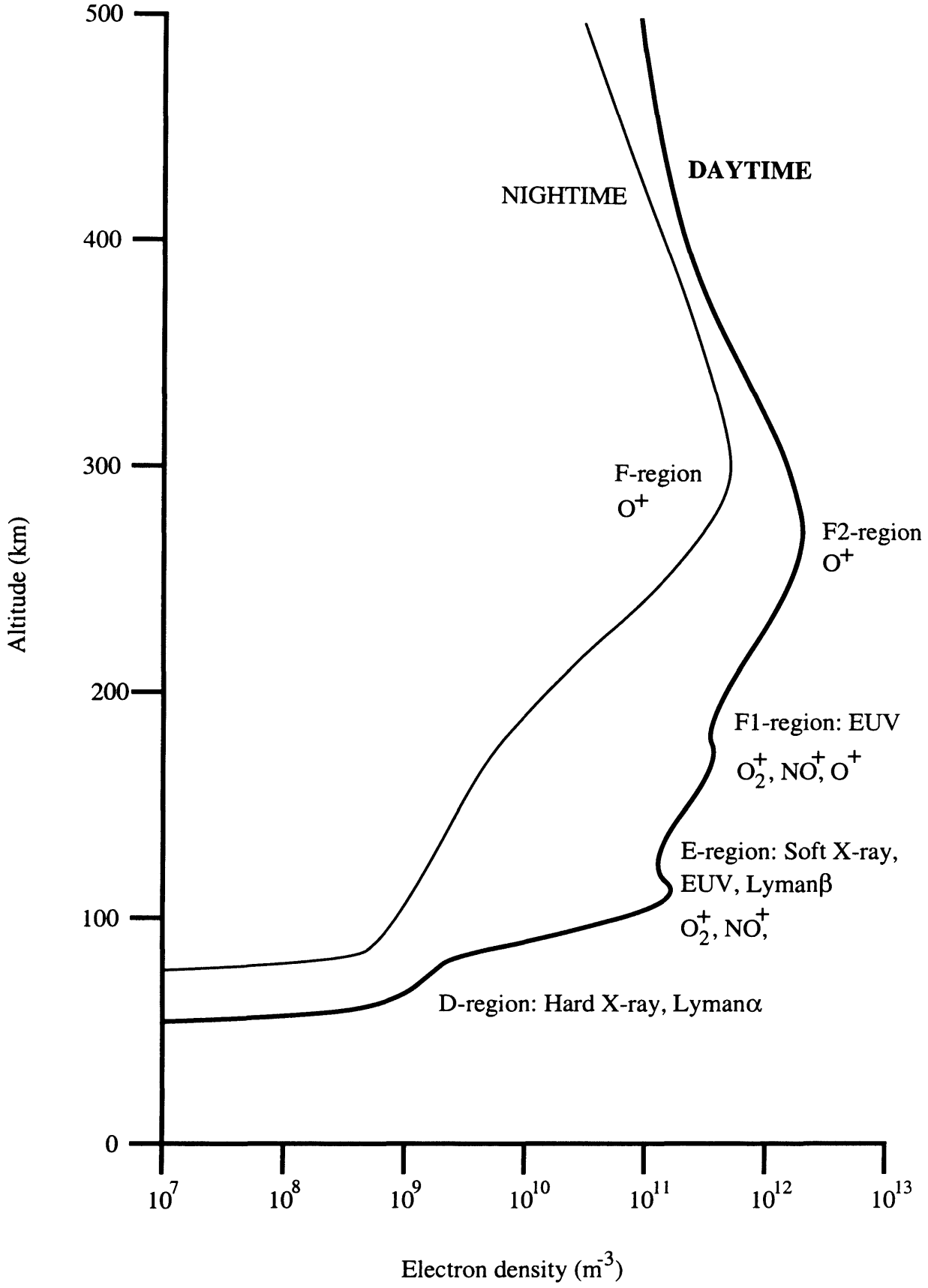

FIGURE 1.5 Typical mid-latitude electron density profiles for moderate solar activity

The D-region spans the altitude range from ~60 km to ~90 km and is produced by energetic electromagnetic radiation such as hard X-ray photons and cosmic rays. The layer is principally characterised by complex photochemical reactions, NO^+, water clusters ions and the presence of negative ions rather than electrons, with ion densities ~10^9 m^{-3}. The layer is dominated by solar X-ray production of the ionisation and rapid recombination processes, such that it almost disappears during the hours of darkness. Above this, the E-region extends from ~90 km to ~160 km and a noticeable change is present in the daytime slope of the electron density profile near 110 km, shown in Figure 1.5. The ion composition in this layer consists of molecular ions of oxygen and nitrogen, which are produced mainly by EUV radiation although near solar maximum soft X-rays become significant. Dissociative recombination of these ions occurs more rapidly in this layer resulting in the formation of atomic molecules. Increasing in altitude to the F-region (>160 km), ionised oxygen is the principal ion species, with the peak in the electron density occurring at ~250-300 km. Bifurcation of the F-region takes place during the day forming two peaks in the density profile, dividing the region into the F_1 and F_2 layers. Chemical reactions in the F_1 layer lead to an ion composition similar to that in the E-region.

The mobility of the plasma particles varies considerably through the ionospheric region, due to the increasing collision frequency of both the ions and electrons with decreasing altitude. The magnitude and direction of the ion (electron) flow depends on the ratio of the ion- (electron-) neutral collision frequency to the ion (electron) gyrofrequency. For the ionospheric electrons, this ratio remains small throughout the ionosphere where appreciable plasma densities are present (>90 km), allowing the electrons to $\boldsymbol{E}\times\boldsymbol{B}$ drift at all heights. However, the ion-neutral collision frequency (ν_{in}) increases rapidly with decreasing altitude due to the increasing neutral density, and becomes comparable to the ion gyrofrequency (Ω_i) at ~125 km. Below this height the ions become increasing immobile since $\nu_{in}/\Omega_i >> 1$, while the electrons $\boldsymbol{E}\times\boldsymbol{B}$ drift, resulting in the formation of the *Hall current* in the $-\boldsymbol{E}\times\boldsymbol{B}$ direction. In the region above ~125 km, both the ions and electrons $\boldsymbol{E}\times\boldsymbol{B}$ drift, although the ions also have some mobility in the direction of $\boldsymbol{E}$, due to the ion-neutral interaction. The *Pedersen current* in the direction of the electric field is thus formed, and is dominant above ~125 km. The Pedersen current peaks where $\nu_{in}/\Omega_i = 1$ (i.e. at ~125 km), since the ions then have the peak mobility in the direction of **E**, i.e. a speed of ½E/B; they also move with the same speed in the $\boldsymbol{E}\times\boldsymbol{B}$ direction. Both the Hall

and the Pedersen current densities are therefore equal there, with the Pedersen current decreasing with altitude as the ions become collision-free, such that both ions and electrons move with $\boldsymbol{E}\times\boldsymbol{B}$ drift only (>150 km).

1.3 Summary

A brief overview of the solar-terrestrial environment has been presented in this chapter. The form of the propagating solar wind with embedded magnetic field has been discussed, together with the formation of the magnetosphere in the near-Earth region. The interaction between these two regimes will be investigated further in the following chapter, and the nature of the plasma convection patterns in the high-latitude ionosphere.

CHAPTER 2

Solar wind-magnetosphere coupling and ionospheric convection

2.1 Introduction

Convection in the ionosphere is produced as a direct result of the magnetospheric coupling with the solar wind. Over the course of the last thirty years many differing theories have been proposed to describe the nature of this interaction. Two of the most important theories, introduced by *Axford and Hines* [1961] and by *Dungey* [1961] will be briefly discussed here, describing the nature of the interaction and the resulting large-scale ionospheric convection. The most successful of these, by *Dungey* [1961], is based on reconnection at the magnetopause but describes the ionospheric convection in a steady state manner. Later studies [e.g. *Reiff et al.*, 1981; *Willis et al.*, 1986] have indicated how the shape and size of the convection pattern is modulated in response to different orientations of the IMF. However, observations indicate the need for a time-dependent convection pattern, due to variability in the interaction mechanism and variations in the IMF. Both the steady-state and time-dependent convection models will be discussed, with the latter providing a fuller description of the observed ionospheric flow.

2.2 Solar wind-magnetosphere coupling

2.2.1 Viscous interaction and the closed magnetosphere model

Axford and Hines [1961] assumed that the magnetosphere is formed in the manner described by *Chapman and Ferraro* [1931, 1932], but proposed that some kind of 'viscous' interaction transfers energy and momentum from the solar wind to the magnetosphere at the magnetopause boundary The exact mechanism for this transfer was and is not known, and the particle densities of both the solar wind and magnetosphere are too low for particle-particle collisions to be significant. Also since the frozen-in approximation eliminates any direct transfer, scattering by plasma waves or large-scale instabilities could be responsible. The most likely instability is the Kelvin-Helmholtz instability, which is analogous to the momentum transfer for 'wind over water', where a circulatory flow is produced over the surface and interior. Whatever the process, however, it will transfer momentum from the solar wind into the magnetosphere causing the

magnetospheric plasma to flow antisunward around the flanks of the magnetosphere. A pressure gradient between the day and night sides resulting from this transfer of plasma results in plasma convecting from the nightside back towards the dayside within the inner magnetosphere region, closing the loop of plasma flow (Figure 2.1). These magnetospheric motions are mapped into the high-latitude ionosphere forming a twin-cell convection pattern (see Figure 2.2a) [*Axford and Hines*, 1961], with antisunward flow at high-latitudes and return sunward flows on the dawn and dusk flanks. The effects of corotation of the near Earth plasma can also be incorporated, producing a more asymmetric flow pattern in the inertial frame, as shown in Figure 2.2b.

2.2.2 *Magnetic reconnection and the open magnetosphere model*

An alternative mechanism describing the interaction was proposed by *Dungey* [1961], where the radical new concept of *magnetic reconnection* was first applied to the magnetosphere. Instead of dealing with the solar wind and magnetosphere as separate regions allowing no direct transfer of material between them as explained above, the new model embraced the suggestion that over certain key regions field lines can 'reconnect' with different partners producing a more violent and effective coupling and transfer mechanism. The frozen-in approximation requires the magnetic Reynolds number (R_M) and thus the scale length (L), to be very large so that convection dominates over magnetic diffusion. However at the surface of the magnetosphere, the Chapman-Ferraro magnetopause current sheet has a relatively small scale width (~few 100 km). With magnetic variations (e.g. oppositely directed fields) occurring over distances of this order, the particles will 'diffuse' in the boundary between the two plasma regimes. A neutral line can then form, allowing the field lines of one regime to 'reconnect' with those from the other. The newly reconnected field lines then contract away from the reconnection site due to the $\mathbf{j}\times\mathbf{B}$ magnetic tension force, allowing more field lines to enter the reconnection region. Figure 2.3 illustrates the reconnection process as described here.

The open magnetospheric model envisaged by *Dungey* [1961] assumed a southward IMF ($B_z < 0$) interacting with the northward terrestrial magnetic field at the dayside boundary. Figure 2.4 [*Kivelson and Russell*, 1995] illustrates the motion of the magnetic field lines and plasma when reconnection is occurring. A neutral line forms at the subsolar magnetopause producing newly reconnected field lines (IMF field line 1' reconnecting with geomagnetic field line 1 in Figure 2.4), which contract over the dayside magnetopause under the influence of the $\mathbf{j}\times\mathbf{B}$ force. The tension force acts to straighten the

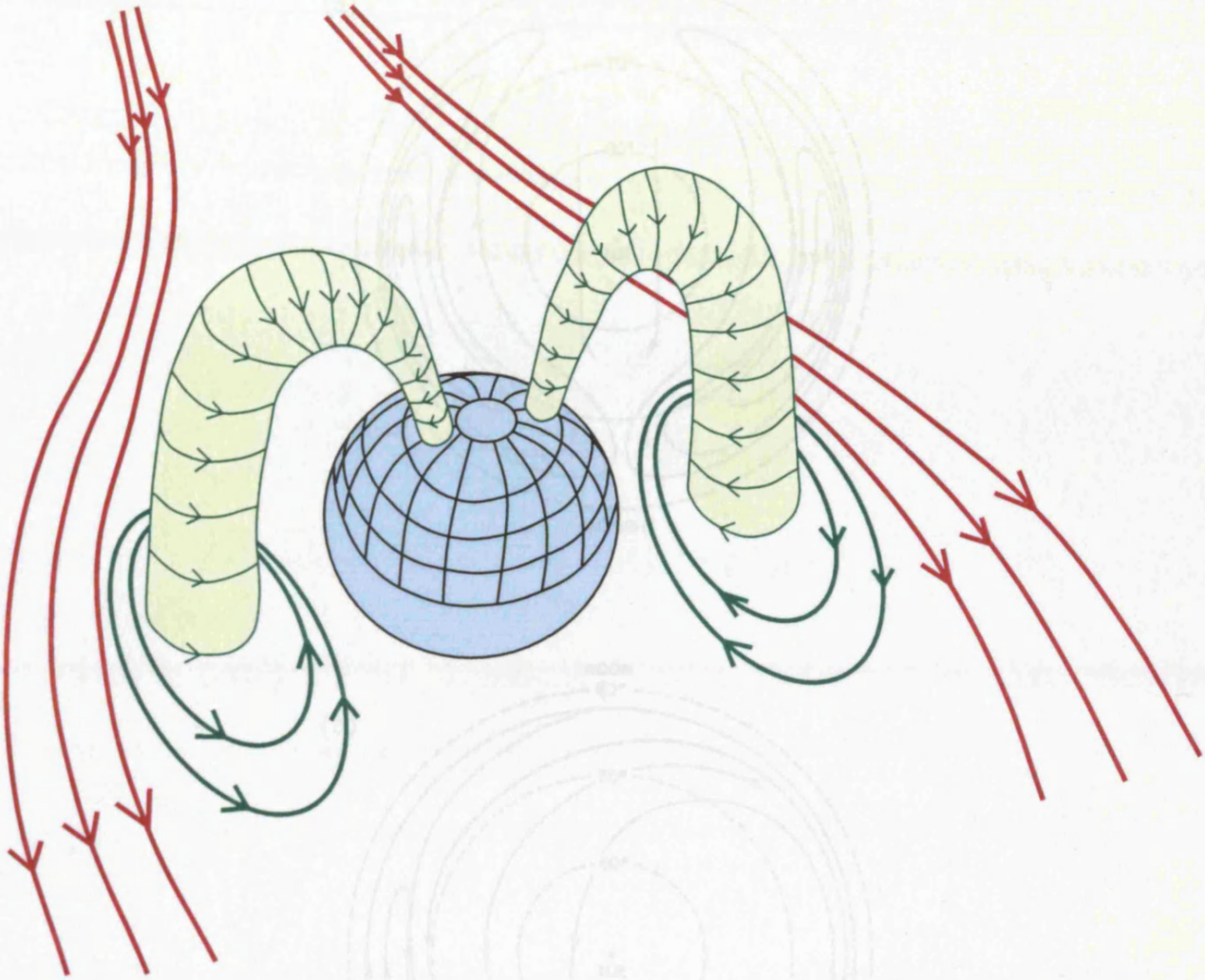

FIGURE 2.1 Schematic illustrating the magnetospheric flow configuration as described during the *viscous* interaction between the solar wind and the magnetosphere, proposed by *Axford and Hines*, [1961].

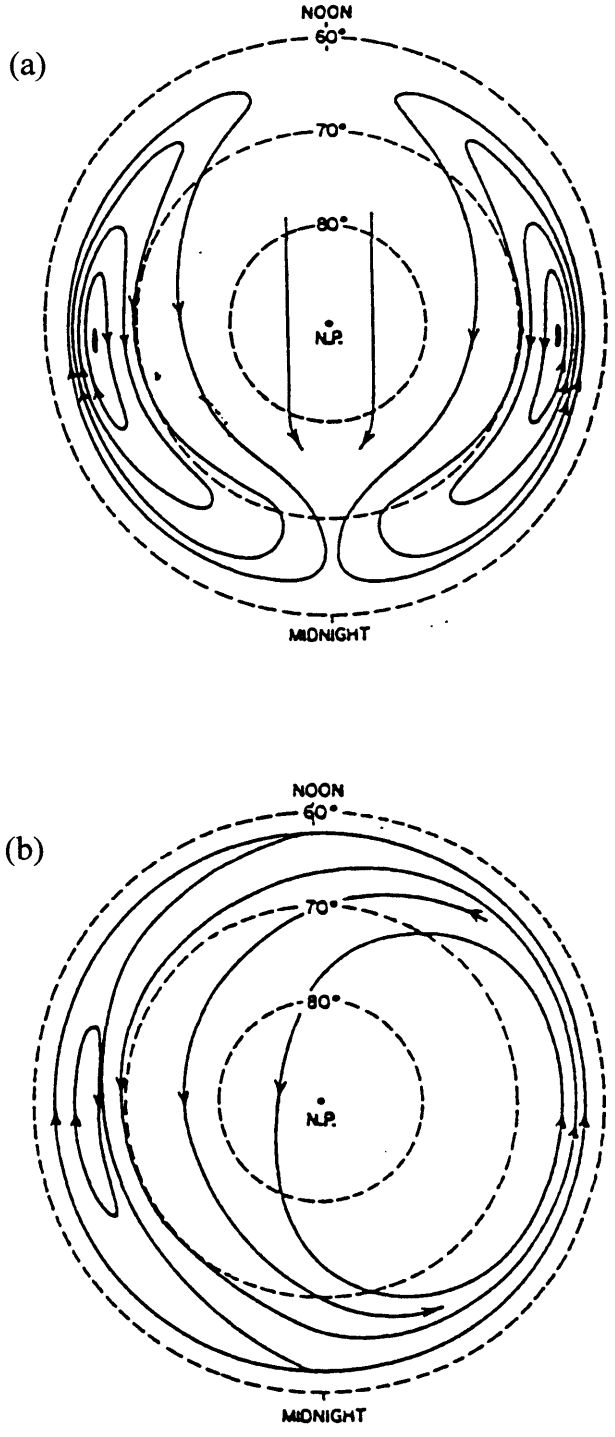

FIGURE 2.2a. Ionospheric convection in the high-latitude ionosphere resulting from the mapping of the magnetospheric flows generated by the viscous interaction, **b.** now, with the additional effects of corotation included. [From *Axford and Hines*, 1961]

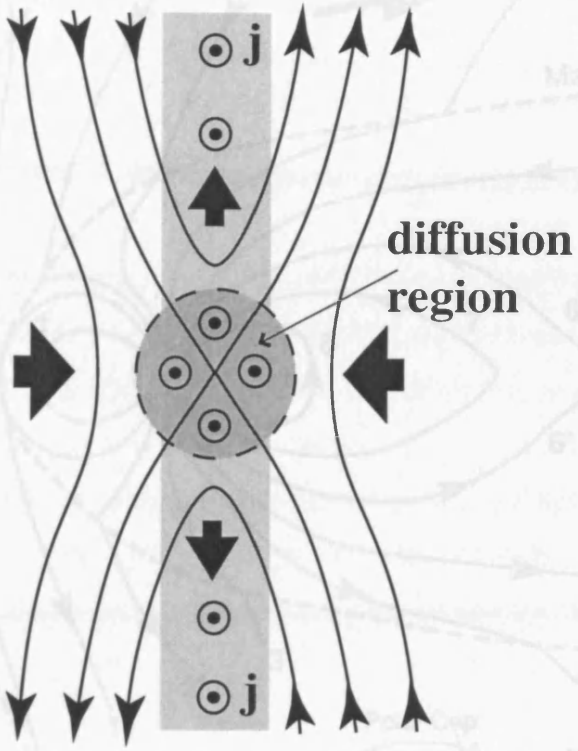

FIGURE 2.3 Magnetic reconnection between two oppositely directed magnetic field orientations. A current sheet (light grey region), with current density **j**, initially separates the differing magnetic fields, however diffusion occurs in a localised disruption at the centre of the current sheet (dashed circle). Field lines 'reconnect' with different partners at the neutral point at the the centre of the diffusion region, and are accelerated away from the reconnection site (large arrows) by the magnetic tension force at the Alfvén velocity.

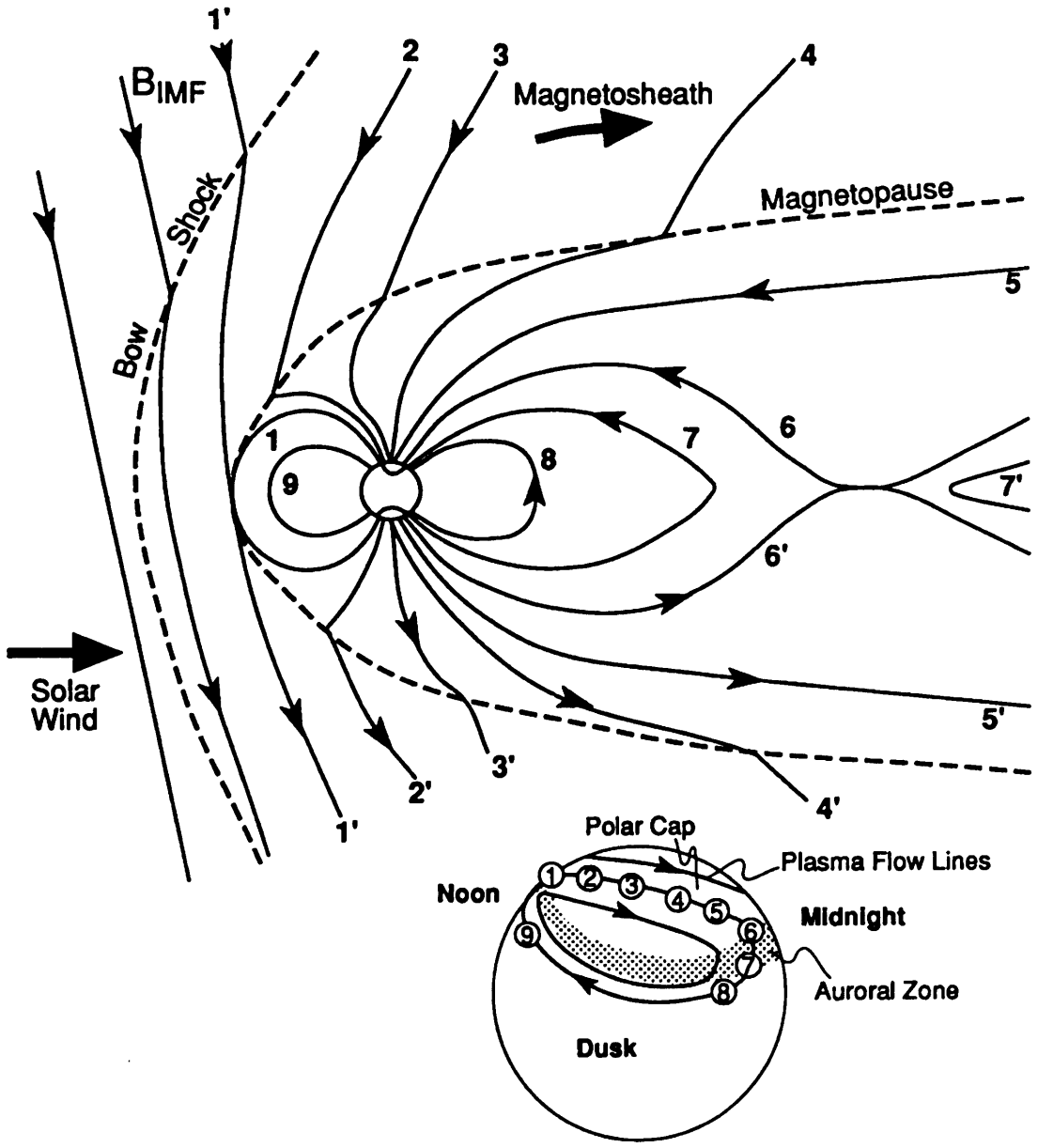

FIGURE 2.4 Schematic of the open magnetospheric model in the noon-midnight meridian produced during southward IMF conditions, with the formation of reconnection neutral lines at the front of the magnetopause and in the central tail on the nightside. The field lines are carried around the outside of the magnetosphere with the magnetosheath plasma flow (numbered 1-4), whilst the footprints of these field lines map into the high-latitude ionosphere (similarly numbered in the inset). [From *Kivelson and Russell,* 1995]

newly reconnected field lines, and the plasma is accelerated away from the reconnection site and simultaneously heated. Subsequently the magnetosheath flow carries the 'open' magnetic field lines downstream towards the magnetotail (motion of field lines 1 through 4 in Figure 2.4), dragging the feet of these field lines antisunward over the polar cap in the ionosphere (see Figure 2.4 inset). This motion is associated with a dawn/dusk electric field given by $\mathbf{E}= -v_{SW}\times\mathbf{B}$. The electric field maps down magnetic field lines, which to a first approximation are equipotentials, into the auroral ionosphere establishing a potential across the polar cap region known as the *cross polar cap potential* [e.g. *Cowley*, 1984].

A consequence of dayside reconnection and the antisunward convection of newly reconnected field lines is the erosion of the dayside magnetopause boundary and the input of magnetic flux and plasma into the nightside [*Freeman and Southward*, 1988]. Tail reconnection eventually occurs after the open field lines have sunk into the centre of the magnetotail (~2-4 hours after initial reconnection), establishing another neutral line in the tail. Earthward of the tail reconnection site the magnetic tension pulls the newly 'closed' field lines into a more dipolar configuration (field lines 6 through 8 in Figure 2.4) with plasma and magnetic flux convecting back towards the dayside at lower latitudes. The mapping of these field lines into the ionosphere gives the return flow at auroral and sub-auroral latitudes, completing the basic twin-cell convection pattern (see Figure 2.4 inset). Asymmetries in the convection pattern also appear due to the effects of the dawn/dusk (Y) component of the IMF [*Cowley et al.*, 1991 and references therein] as will be discussed in §2.2.4.

2.2.3 Reconnection or viscous interaction?

Both the reconnection-driven model for southward IMF conditions, and the viscous interaction model predict similar circulatory flow patterns in the ionosphere, however the interaction mechanism is very different. Ionospheric flows have been observed directly from polar orbiting spacecraft [*Reiff et al.*, 1981; *Heppner and Maynard*, 1987], ground-based radars [*Willis et al.*, 1986; *de la Beaujardière et al.*, 1987; *Clauer and Friis-Christensen*, 1988], and from ground magnetometer data [*Reiff et al.*, 1985]. The results from these studies illustrated the strong dependence of the high-latitude convection pattern on the direction and strength of the IMF which impinges on the dayside magnetopause. In particular, the asymmetric patterns observed during periods of strong IMF B_y conditions can only be explained in terms of the open magnetospheric model allowing the interconnection of interplanetary and geomagnetic field lines. Nevertheless, when the IMF

is predominately northward and reconnection in the dayside subsolar region becomes negligible, geomagnetic activity at very high latitudes suggests that ionospheric convection is still present within the polar cap. This is thought to be due to lobe reconnection as will be mentioned further below. In order to gauge the relative importance of the flows generated due to 'viscous' mechanisms and those generated by reconnection processes, their contributions to the cross polar cap potential have to be investigated [*Reiff et al.*, 1981, 1985; *Cowley*, 1984]. Magnetospheric and ionospheric observations have indicated that the voltage associated with the 'viscous' process is typically ~10 kV [*Cowley*, 1984], whilst that associated with reconnection is typically ~50-100 kV, though it can vary between essentially zero and 200 kV as the IMF turns from north to south. Thus, during northward IMF conditions and quiet magnetospheric periods when reconnection is relatively weak, 'viscous' interaction can play a significant role in generating flow, although in general reconnection plays the dominant role.

Figure 2.5 [*Cowley*, 1996] illustrates the typical flow configurations in the northern hemisphere during different orientations of the IMF. As one would expect, reconnection-driven flows are dominant when the IMF is southward (top three diagrams) with a very weak contribution from 'viscous' coupling processes at latitudes slightly lower than the open-closed field line boundary (solid circle). The bottom three diagrams illustrate the ionospheric flows for northward IMF, consisting of the sum of 'viscous' and 'lobe' reconnection contributions. The latter occurs when the northward-directed IMF reconnects with oppositely directed open flux in the tail lobe poleward of the cusp, it being assumed in the figure that reconnection occurs in one lobe only. This results in the 'stirring' of the polar cap flow with no net change in the amount of open flux, thus confining the ionospheric reconnection-driven convection to the region of open field lines. Weaker flows resulting from viscous interaction will again be present at lower latitudes on closed field lines, and may contribute a comparable amount to the cross polar cap potential as flows from lobe reconnection. When the IMF is strongly northward, lobe reconnection can occur in both hemispheres (though not necessarily simultaneously), forming closed loops of previously open field lines draped over the dayside magnetopause, which decreases the amount of open flux in the system. The 'reversed' twin-cell flow pattern would then not simply be confined to the region of open flux, but would produce a transfer of flux across the open-closed field line boundary, as originally proposed by *Dungey* [1963]. The asymmetric effects of the IMF B_y component are also included in the ionospheric flow configurations in Figure 2.5, with negative (dawnward) and positive

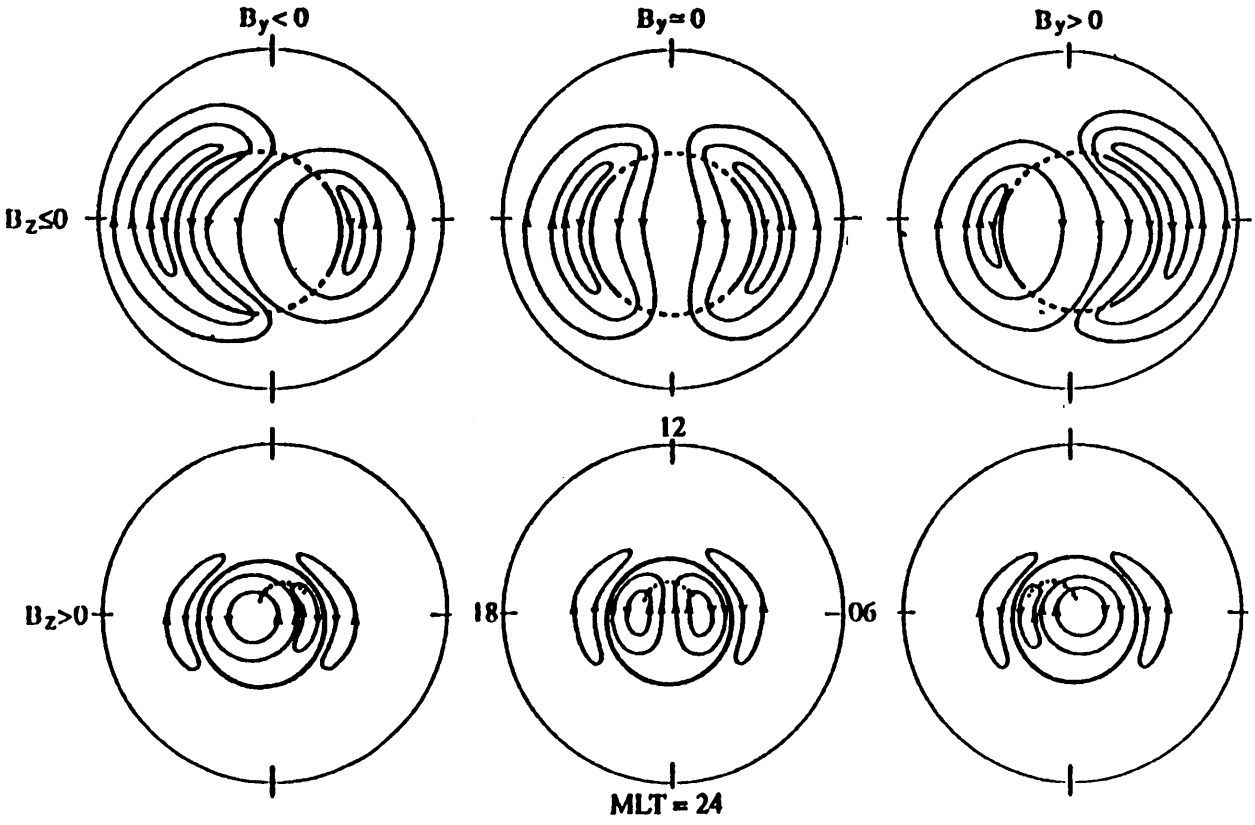

FIGURE 2.5 Northern hemisphere convection patterns established for variation orientations of the interplanetary magnetic field. Top three sketches show high-latitude ionospheric flow for southward IMF B_Z, whereas the bottom three show positive IMF B_Z flow configuration. [From *Cowley*, 1996]

(duskward) B_y generating the flows on the left and right of Figure 2.5, respectively. A detailed discussion of the effects of the IMF B_y component in both the magnetosphere and ionosphere is presented in the following section.

Thus it is clear that the main contributor to the convection flows in the ionospheric and indeed in the magnetospheric region is reconnection at the subsolar magnetopause, dictated by the orientation of the interplanetary magnetic field. However another mechanism able to transfer energy and momentum into the magnetosphere is a sudden change in the dynamic pressure of the solar wind plasma. Details of this transfer mechanism are not fully understood, although the process is akin to the 'viscous' interaction previously discussed. In the simplest case, if the solar wind pressure were to uniformly compress or rarefy the magnetosphere, no flow changes in the ionosphere would be observed since the field strength at ionospheric heights is very strong and incompressible. However, if 'pressure fronts' present in the solar wind propagate over the magnetosphere, the front of the magnetopause becomes compressed and field-aligned currents (FAC) may be generated at the 'edges' of this compression, allowing the transfer of information into the ionospheric region via Alfvén waves. This current system would then close in the ionosphere by a Pedersen current flowing in the direction of the electric field. Two oppositely-directed vortical flow cells are then excited orthogonal to the FACs in the ionosphere, around which a Hall current flows in the opposite direction to the $\boldsymbol{E}\times\boldsymbol{B}$ direction. As the compression feature moves around the magnetopause boundary, the vortical flows in the ionosphere also move in an azimuthal direction. These ionospheric features have been termed 'travelling convection vortices' (TCVs) and have been observed for many years [e.g. *Friis-Christensen et al.*, 1988], propagating east or west away from noon at high latitudes. Each vortex has a spatial scale of ~1000 km such that at any instant the twin vortices encompass several hours of local time, propagating over a few tens of minutes at phase speeds of ~5 km s^{-1}. The physical origin of these features is still under great debate, although it is reasonable to assume that the overall effect of TCVs on the large scale convection pattern is minimal since the energy and momentum transfer due to reconnection is by far the dominating process. Only when reconnection becomes weak do the TCV-driven and 'viscous'-driven flows significantly contribute to the overall convection, as is illustrated in the bottom three panels of Figure 2.5.

2.2.4 IMF B_y effects on magnetospheric and ionospheric convection

Although the strongest reconnection will occur when the magnetic shear is a maximum, as in the case of oppositely directed field lines, theoretically reconnection can occur with any magnitude of magnetic shear. However, as the IMF 'clock angle' (i.e. the angle of the IMF relative to north in the Y-Z plane) varies, the effect of reconnection on the production of open flux changes. For clock angles less than ~45° (strongly northward IMF conditions), high-latitude lobe reconnection occurs in one or both hemispheres, causing lobe stirring in the first case and closure of open flux in the second. As the clock angle increases to ~45°-90°, reconnection at the subsolar magnetopause begins, producing twin-vortical ionospheric flows as previously closed field lines are opened and flux transfer occurs, together with flows generated due to continuing lobe reconnection. When the clock angle is >90° (southward IMF), lobe reconnection ceases, leaving only subsolar dayside reconnection to establish the convection pattern, which takes the forms of the typical twin-cell pattern. Therefore, when the IMF has a component directed in the dawn/dusk (B_y) direction reconnection will still occur at the dayside magnetopause albeit weaker than with a directly southward IMF. It is usual to consider the reconnection effect of the IMF B_y component in conjunction with the north-south (B_z) component. Evidence that B_y does influence the magnetospheric and ionospheric convection was first noticed by *Svalgaard* [1968] and *Mansurov* [1969], who observed deflections in the ground magnetometer signatures in the dayside cusp region which were dependent on the dawn/dusk IMF component. This disturbance was interpreted as the magnetic signature of an azimuthal flow driving a Hall current in the opposite direction to the flow along the poleward edge of the open/closed field line boundary, occurring in the presence of B_y on the open magnetic flux tubes [e.g. *Friis-Christensen and Wilhjelm*, 1975; *Cowley*, 1981 and references therein]. This azimuthal flow in the dayside cusp region implies that open flux tubes are added asymmetrically into the tail lobes [*Jørgensen et al.*, 1972; *Stern*, 1973; *Cowley*, 1981]. Figure 2.6 [*Gosling et al.*, 1990] shows the corresponding magnetospheric configuration, where the addition of a positive duskward B_y (Figure 2.6a) leads to the addition of flux tubes to the dawn side of the northern tail lobe but to the dusk side of the southern tail lobe. The converse is true for negative B_y (Figure 2.6b). *Reiff and Burch* [1985] investigated ionospheric convection patterns for different orientations of B_y and B_z, using a global convection model described in the companion paper *Burch et al.* [1985]. In this they modelled Birkeland current and ion convection observations from the

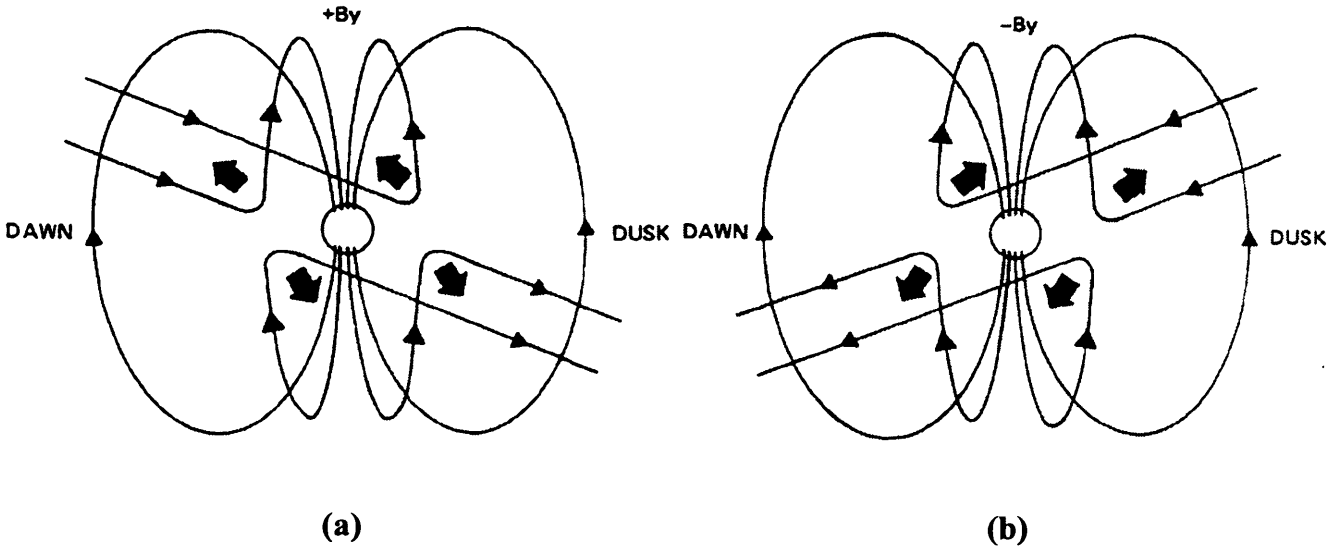

FIGURE 2.6 Illustration of the shape of newly reconnected field lines in the dawn-dusk meridian of the magnetosphere with southward and **a.** positive (duskward) B_y and **b.** negative B_y. The short broad arrows in each diagram represent the direction of the magnetic tension force acting on the field lines. [Adapted from *Gosling et al.*, 1990]

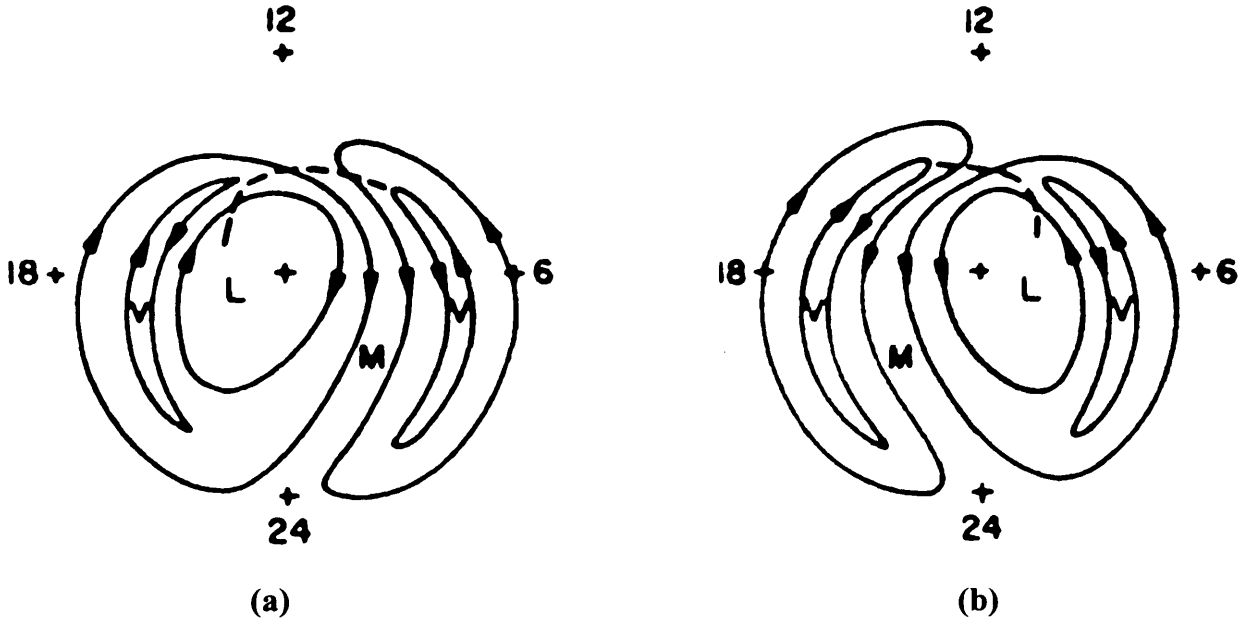

FIGURE 2.7 Simplified sketches of the ionospheric convection pattern with the effects of IMF B_y as derived from an empirical model [*Burch et al.*, 1985] for **a.** positive B_y (duskward) and **b.** negative B_y (dawnward).

Dynamics Explorer satellites (DE-1 and -2) to describe the B_y-dependent ionospheric convection pattern. The northern hemisphere convection patterns derived for a southward IMF with duskward ($+B_y$) and dawnward ($-B_y$) asymmetries are given in Figure 2.7a and b [*Burch et al.*, 1985] respectively. Notice how the twin cell convection pattern is strongly skewed in the opposite sense to the added B_y field; in the northern hemisphere positive B_y pulls flow streamlines preferentially towards dawn (Figure 2.7a) whereas negative B_y enhances flow on the duskward side (Figure 2.7b). The effect of B_y is oppositely directed in the southern hemisphere.

Additional IMF-associated asymmetries have been reported to involve the closed auroral flux tubes in the magnetosphere as well, such as the displacement of the auroral oval as a function of IMF B_y observed by *Holzworth and Meng* [1984], using DMSP images. The centre of the northern (southern) oval was displaced dawnward (duskward) for positive B_y, with the overall displacement of the oval between periods of positive and negative B_y (~±4nT) typically around 2.5° in each hemisphere. Although not all of the data subsets demonstrated a clear displacement, many previous and subsequent studies concentrating on ionospheric flows have shown a strong dawn/dusk asymmetry over the central polar region [*Heppner*, 1972; *Mozer et al.*, 1974; *Heppner and Maynard*, 1987]. A second asymmetric feature was pointed out by *Newell et al.* [1989], highlighting the local time shift of the dayside cusp which is in the opposite sense to the motion of the auroral oval. For B_y positive, the authors reported a duskward shift of the cusp in the northern hemisphere, and dawnward in the southern hemisphere, and vice versa for B_y negative.

The apparent discrepancy between the two displacements observed on closed field lines in the presence of IMF B_y by *Holzworth and Meng* [1984] and *Newell et al.* [1989], was addressed and explained by *Cowley et al.* [1991], through application of the basic 'dipole plus uniform field' model framework [*Cowley*, 1973; *Lyons*, 1985, *Cowley*, 1981]. This is sketched in Figure 2.8 [*Cowley et al.*, 1991]. This figure represents a view of the Earth from the Sun, and shows dipole terrestrial field lines (dashed lines) being distorted by the presence of a perturbation field having the same sense as the IMF, shown positive in Figure 2.8 (solid lines). It is clear that the field lines lying in the noon-midnight meridian will be distorted such that the footprints on the Earth will be shifted in local time in the same direction as the added field in the northern hemisphere, and in the opposite sense in the southern hemisphere. These longitudinal displacements are then consistent with the local time shift of the dayside cusp as observed by *Newell et al.* [1989]. However, in the dawn-dusk meridian, the field lines are simultaneously shifted in latitude in the opposite

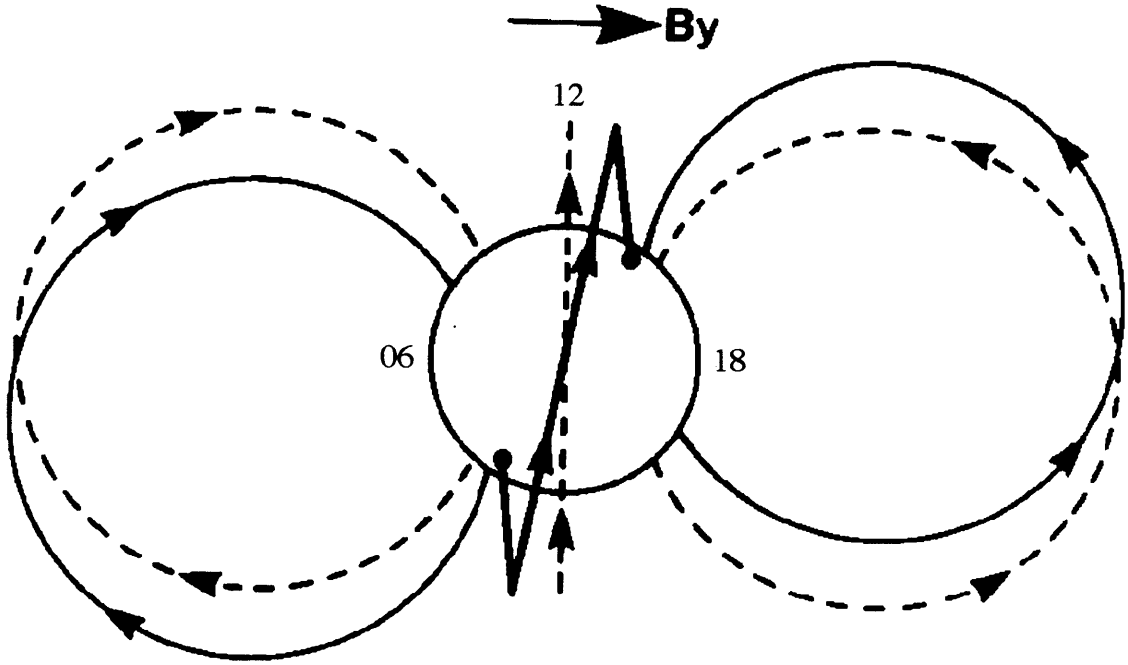

FIGURE 2.8 Sketch showing the distortion of the Earth's dipolar field lines (dashed lines), as viewed from the Sun, with the addition of uniform positive B_y field. Field lines lying initially in the plane perpendicular to the added perturbation field (i.e. in the noon-midnight plane), as shown at the centre of the diagram, move such that the footprints of these field lines shift in longitude in the same direction as the added field in the northern hemisphere and in the opposite direction in the southern hemisphere. However, field lines contained in the same plane as the added field (i.e. dawn-dusk meridian), observe a footprint shift in the opposite direction to the added field in the northern hemisphere and in the same sense in the southern hemisphere. The solid lines indicate the position of the field lines after the addition of the perturbation field. [From *Cowley et al.*, 1991]

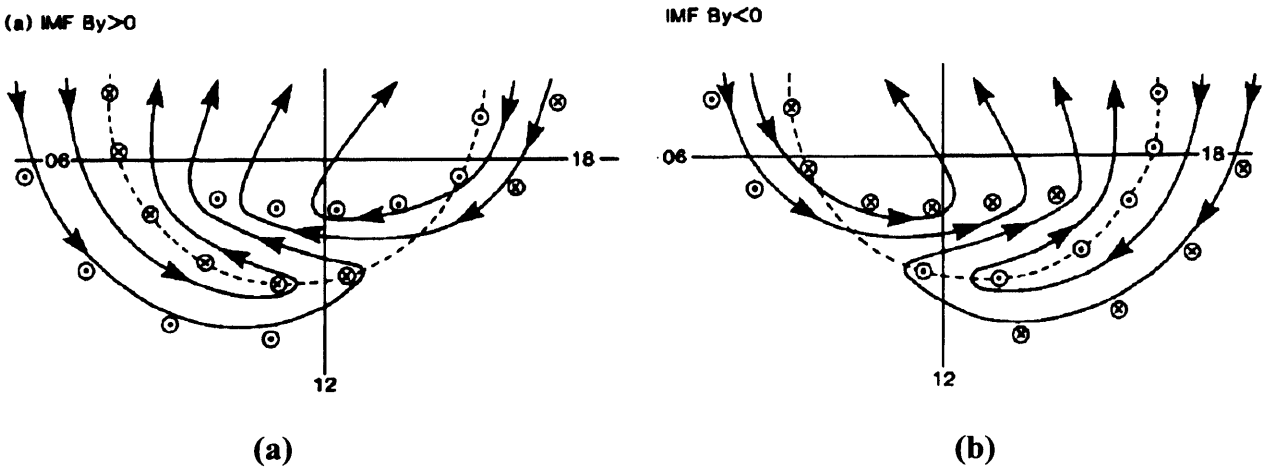

(a) **(b)**

FIGURE 2.9 Northern hemisphere ionospheric flow streamlines (solid lines) and open/closed field line boundary (dashed curve) illustrating the three main asymmetry effect of **a.** positive IMF B_y **b.** negative IMF B_y. The circular and cross symbols represent the upward and downward field-aligned currents. [From *Cowley et al.*, 1991]

direction to the added field in the northern hemisphere and in the same direction in the southern. These displacements are then consistent with the auroral oval motions described by *Holzworth and Meng* [1984]. Figure 2.9 [*Cowley et al.*, 1991] illustrates the three main B_y-induced asymmetries in the high latitude convection as just explained, with regard to open and closed flux tubes. The westward flows in the cusp region immediately poleward of the open-closed field line boundary (dashed circle) for positive B_y (Figure 2.9a) and the corresponding eastward flows for negative B_y (Figure 2.9b) conform with the localised magnetic signatures originally observed by *Svalgaard* [1968] and *Mansurov* [1969]. The movement of the open-closed field line boundary in latitude and the local time shift of the centre of the flow across the open-closed field line boundary about noon are in accordance with the corresponding displacements involving closed auroral flux tubes in the magnetosphere. The overall flow effects illustrated here can be described in a simple manner by adding a net clockwise azimuthal flow in the open field line region for positive B_y and an anticlockwise azimuthal flow on closed field lines, and vice versa for negative B_y.

2.2.5 *Magnetospheric substorms and nightside reconnection*

Whilst reconnection is occurring at the subsolar magnetopause, a significant amount of open flux is being transferred into the tail lobes. This energy is stored in the lobes until tail reconnection is established giving the system a means of releasing the flux back towards the dayside. Although reconnection may occur in a bursty manner in the tail nearly all of the time, the dominant release of open flux and its stored magnetic energy occurs during a *magnetospheric substorm.* This involves an instability of the near-Earth tail which accelerates tail plasma and produces auroral enhancements and particle precipitation in the nightside ionosphere [e.g. *Rostoker et al.*, 1980]. The evolution of a substorm can be described in three distinct steps, namely the 'growth phase' during which the energy storage takes place in the tail, the 'expansion phase' characteristic of the energy release, and the 'recovery phase' where the system relaxes to a quieter state. Despite the fact that substorms are basically a nightside process, the energy required to produce them is accumulated after a southward turn of the IMF establishing reconnection at the dayside magnetopause. Magnetic flux is eroded from the dayside boundary as a result of reconnection and transferred into the tail, which flares slightly to accommodate the new flux. The plasma sheet thins in response to the pressures exerted by the loading of magnetic flux into the tail, enhancing the cross-tail current and elongating the tail.

Typically the growth phase will last between 30-60 minutes, storing enough energy in the tail to cause a major disruption [e.g. *McPherron*, 1970].

The onset of the expansion phase was originally identified by the brightening of the most equatorward auroral arc and the subsequent motion of the disturbed region poleward and east-west [*Akasofu*, 1964]. The sudden release of energy characteristic of the substorm expansion phase onset is associated with a rapid reconfiguration of the nightside field lines to a more dipolar form. The implication of the dipolarisation in a localised region of the tail is the formation of a substorm-associated current system, in which the cross–tail current is diverted along field lines into the E-region of the ionosphere within the *auroral break-up region*. The field-aligned currents (FACs) flow between the ionosphere and the tail along the eastward and westward edges of the localised dipolarisation region, forming the *substorm current wedge* shown in Figure 2.10 [*Clauer and McPherron*, 1974]. The auroral enhancements observed by *Akasofu* [1964] are associated with this current wedge, with the upward FAC flowing at the western edge which maps into the *westward travelling surge* in the aurora.

The reconfiguration of field lines also initiates transient magnetohydrodynamic waves observed in the ground magnetic field as wavepackets of period 20-200 s, known as Pi2 pulsations. These waves are a highly distinct feature of substorm onset covering a wide range of local time at latitudes lower than the substorm activity. Other signatures of the expansion phase onset are the energisation and injection of magnetospheric particles observed by spacecraft at geostationary orbit, and the ejection of a hot plasma 'bubble' (plasmoid) downtail away from a near-earth reconnection site. Figure 2.11 [*Hones*, 1984] illustrates one possible sequence of events in the magnetotail during a substorm, with the expansion phase triggered by the formation of a near-Earth neutral line and the ejection of a plasmoid. The exact configuration of the magnetotail during the expansion phase is not yet established and although several models have been suggested [e.g. *Lui*, 1991 and references therein], the results are not conclusive. Finally the 'recovery phase' indicates the period when the energy release is complete and the magnetosphere returns to some quiet state, similar to that previous to the growth phase.

From a basic viewpoint, substorms can be considered to contribute to, even to dominate the return flow portion of the magnetospheric convection described earlier, with tail reconnection closing previously open field lines and transferring closed flux back towards the dayside as the field lines become more dipolar in shape. However, the ionospheric flow changes reported to be associated with substorm onset have mainly been

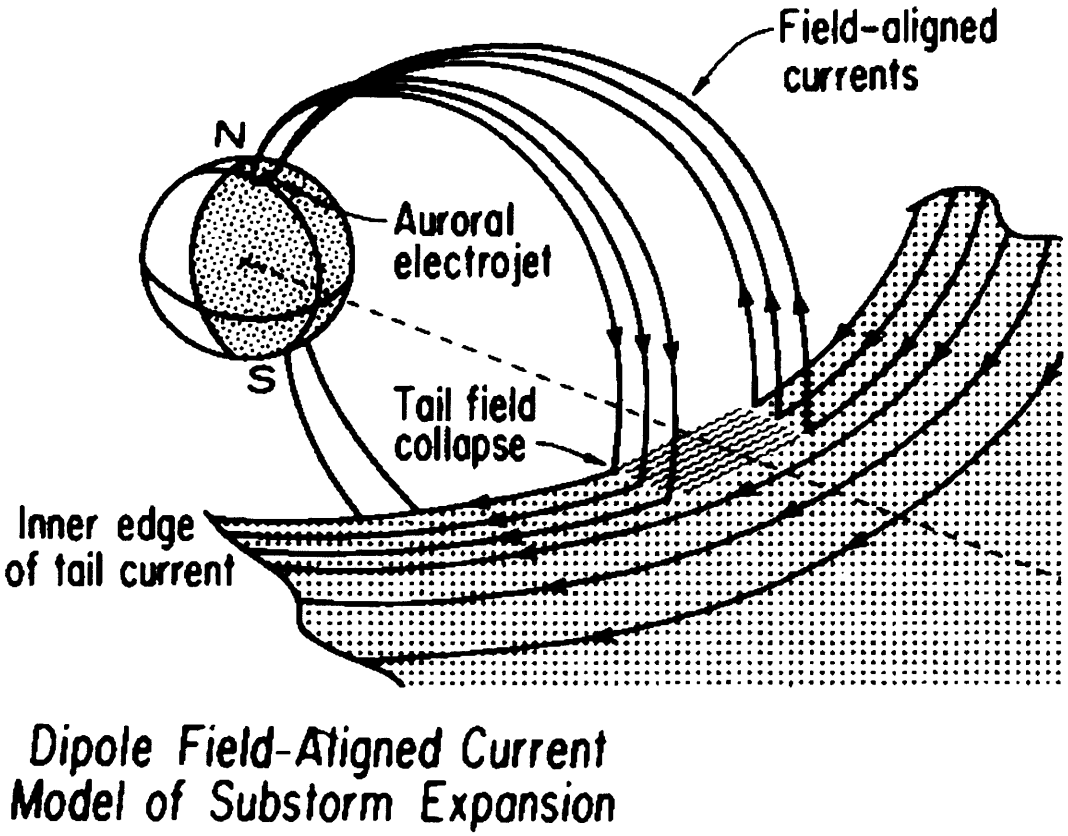

FIGURE 2.10 Schematic of the three-dimensional current wedge produced during the expansion phase of a substorm. The cross-tail current is diverted into the ionosphere via field-aligned currents, forming the substorm current wedge. [From *Clauer and McPherron*, 1974]

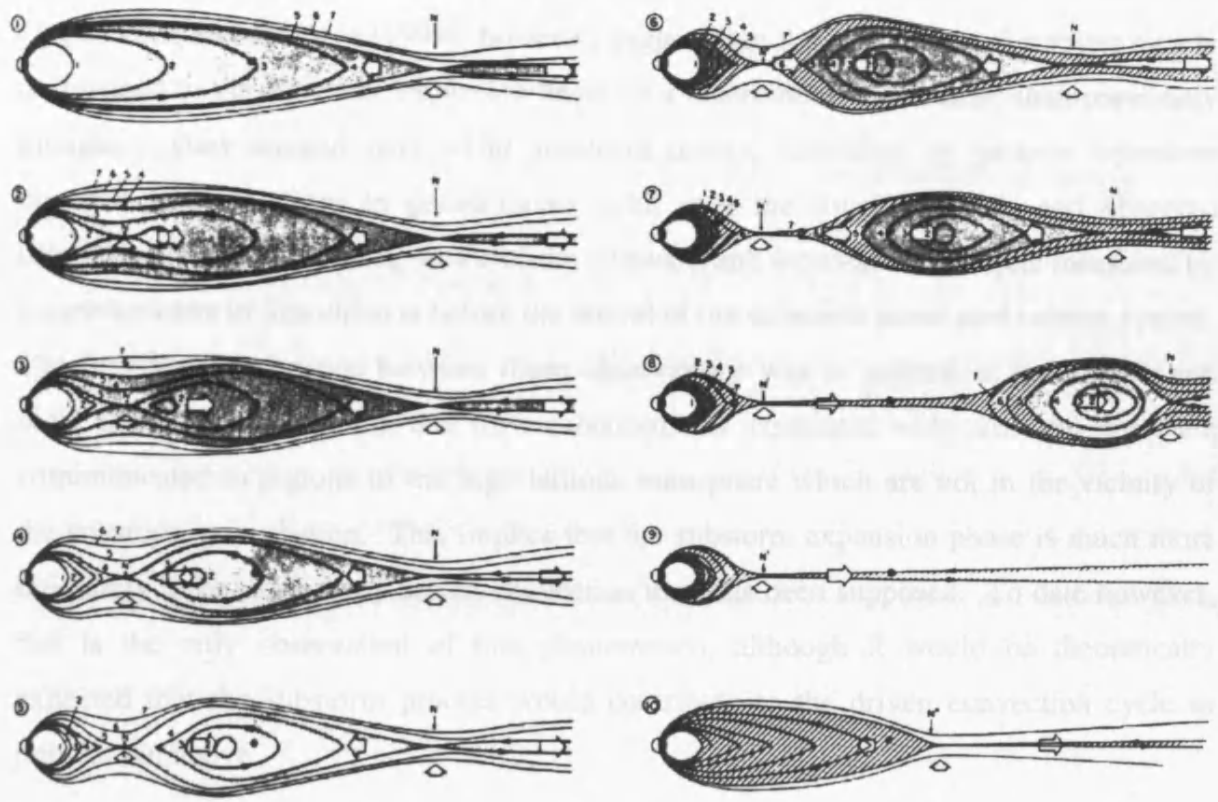

FIGURE 2.11 Possible sequence of events in the magnetotail during a magnetospheric substorm. Large white arrows indicate the direction of the plasma flows from the various neutral lines formed in the tail. N' indicates the formation of the near-Earth neutral line (picture 3), with the expulsion of the plasmoid downtail occurring slightly later (picture 7-8). See text for detailed explanation. [From *Hones*, 1984]

observed within the substorm electrojet/auroral bulge region rather than being related to the global convection pattern [e.g. *Baumjoham*, 1983; *Kennel*, 1995]. The directly-driven convection electrojets (i.e. eastward and westward current systems associated with the dusk and dawn flow cells, respectively), and the westward current flowing within the ionospheric portion of the substorm current wedge have generally been discussed separately when models of the substorm process are described. Recent observations by *Opgenoorth and Pellinen* [1999], however, suggest that the convection electrojets clearly do respond to the substorm expansion onset on a much more global scale than previously thought. They studied over ~100 substorm onsets, identified by particle injections obtained from satellites in geostationary orbit over the Russian sector, and observed enhancements in the evening sector of the eastward and westward electrojets measured by magnetometers in Scandinavia before the arrival of the substorm associated current system. The longitudinal distance between these observations was in general at least ~50°, and more often ~90°, indicating that flow enhancements associated with substorm onset are communicated to regions of the high-latitude ionosphere which are not in the vicinity of the substorm perturbation. This implies that the substorm expansion phase is much more intimately linked to directly driven convection than has been supposed. To date however, this is the only observation of this phenomenon, although it would be theoretically expected that the substorm process would contribute to the driven convection cycle as pointed out above.

2.3 Theoretical models of ionospheric convection

2.3.1 Steady state vs. time-dependent model

All of the studies and observations cited above define how the high-latitude convection relates to the coupling of the solar wind-magnetosphere-ionosphere system. Apart from substorms processes, they all in essence present a steady-state description of the flow pattern and are therefore inherently incapable of accommodating the fundamental time variability in the environment. The very nature of a steady-state reconnection-driven system assumes the rapid response of tail reconnection to the dayside rate, such that the amount of open flux in the system is constant [*Dungey*, 1961]. However, since there is a large separation in distance between the nightside and dayside reconnection sites (see Figure 2.4) typically ~100 R_E during quiet times and ~30-40 R_E during substorm activity, an information propagation delay of 15-30 minutes will exist between the two regions.

Therefore a time-dependent ionospheric convection pattern is inescapable. The direction of the IMF can also vary on rapid time scales, such as those which occur across tangential discontinuities in the convecting solar wind. The response and reconfiguration of the convection pattern to these changes, and also an explanation of substorm effects, can only be described in a time-dependent model. Finally, observations of pulsed reconnection-associated coupling at the magnetopause on time scales of 5-10 minutes called *flux transfer events* (FTEs) [*Russell and Elphic*, 1979] produce characteristic pulsed flows and precipitation patterns in the dayside cusp [*Elphic et al.*, 1990]. Clearly a time-dependent model describing the ionospheric flow pattern is necessary to encompass these observations.

2.3.2 *Steady unbalanced reconnection*

An increase in the amount of open flux during dayside reconnection causes the expansion of the polar cap. The ionospheric flow produced under these circumstances, in the complete absence of tail reconnection, was modelled theoretically by *Siscoe and Huang* [1985]. They assumed that flux was transferred from the closed field line region of the dayside auroral zone into the open field line region of the polar cap through a finite breach in the polar cap boundary near noon, known as the *merging gap*, which maps to the reconnection neutral line at the dayside magnetopause. The remainder of the boundary was considered 'adiaroic', meaning that the magnetic flux does not cross this boundary i.e. it moves with the plasma. Consequently, as unbalanced dayside reconnection takes place, the area of the polar cap increases with time, such that the rate of change of open magnetic flux is equal to the voltage along the dayside reconnection neutral line, in accordance with Faraday's Law. A sketch of the ionospheric flow pattern is this situation is shown in Figure 2.12a [*Lockwood et al.*, 1990]. The model illustrates that under the influence of unbalanced dayside reconnection, recently opened flux that was previously outside but adjacent to the polar cap boundary, now flows into the polar cap through the merging gap. Streamlines associated with this flow appear to emanate from the outside wall of the polar cap boundary as the expansion causes the adiaroic boundary (solid circle) to move with the plasma flow, as denoted by the large solid arrows. The streamlines then curve around the boundary towards and through the opening (dashed line) finally terminating on the inside wall. The convection pattern driven in the ionosphere is a large-scale twin vortical pattern with high-speed flows generally confined to the dayside.

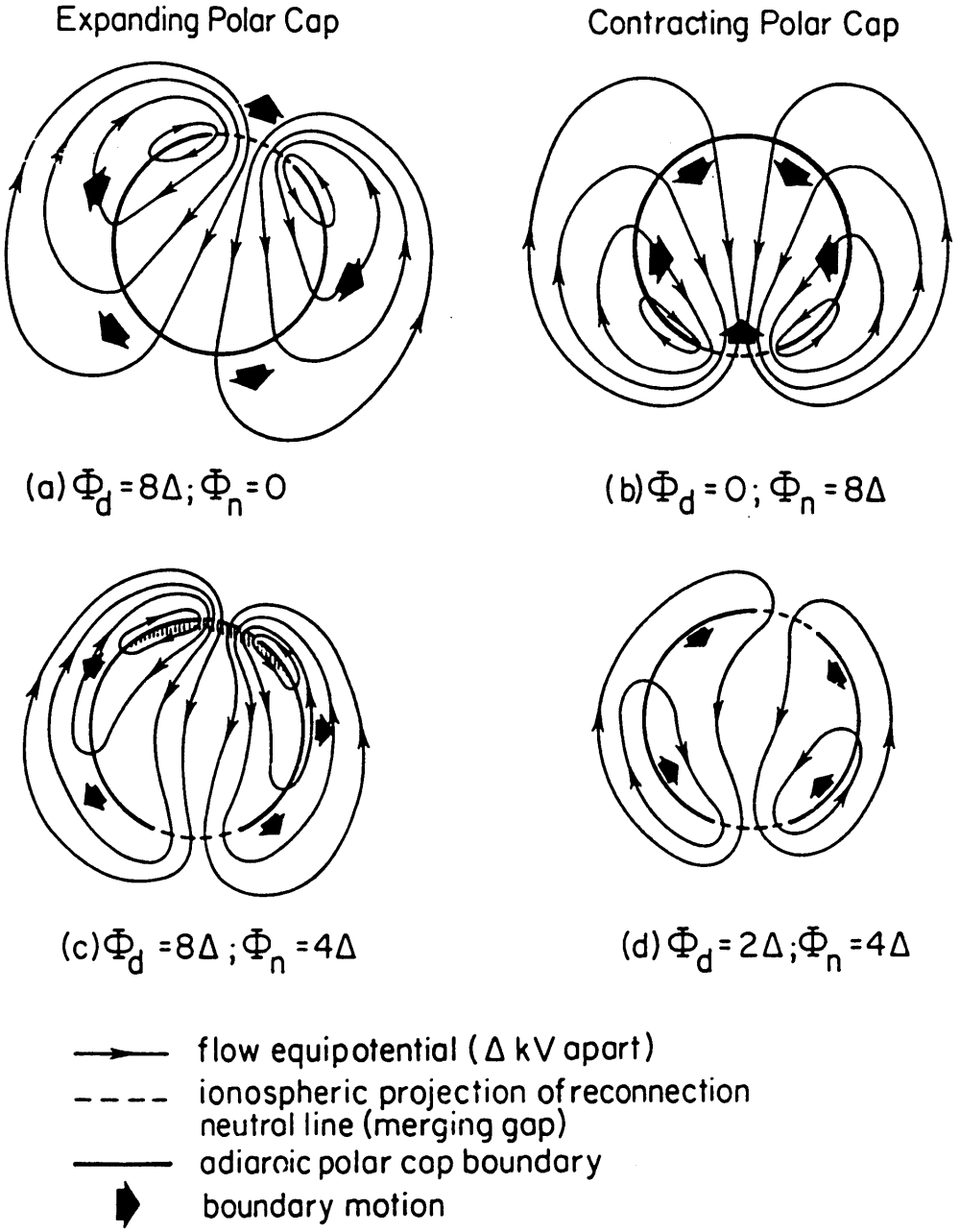

FIGURE 2.12 Illustrations of ionospheric convection patterns due to dayside and nightside reconnection processes. The 'adiaroic' boundary (solid circle) expands and contracts depending on the net gain or loss of flux through the dayside merging gap (dashed line) and nightside merging gap respectively for; **a.** unbalanced dayside reconnection where the polar cap expands (represented by the short broad arrows), as modelled by *Siscoe and Huang* [1985]; **b.** unbalanced nightside reconnection resulting in a contraction of the polar cap; **c.** a net increase in open flux, causing the boundary to expand and flow to be driven by the dayside reconnection rate, and finally; **d.** a net decrease in open flux resulting in a contraction of the boundary. The final convection pattern is established through a superposition of the basic dayside and nightside extremes. [From *Lockwood et al.*, 1990]

The work of *Siscoe and Huang* [1985] was extended by *Lockwood et al.* [1990] suggesting that the observed convection pattern can be described by considering the summation of two intrinsically time-dependent patterns, namely those due to dayside and nightside reconnection. The rate at which the reconnection is occurring in both the tail and in the dayside governs the nature of the convection produced. Dayside coupling will principally drive the strongest flows on the dayside, associated with the expansion of the polar cap boundary, whereas nightside processes drive flows originating near the nightside merging gap together with a contraction of the polar cap. Figure 2.12 [*Lockwood et al.*, 1990] demonstrates the effect of both these dayside and nightside processes on the overall convection pattern in the ionosphere. Figure 2.12a describes the case of only dayside reconnection driving the plasma flows [*Siscoe and Huang,* 1985], as described above. On the other hand, Figure 2.12b illustrates the convection pattern generated with only nightside reconnection present. Here the closure of open flux causes the polar cap to contract as the flow streamlines cross the nightside merging gap, producing the largest flows in the vicinity of the merging gap. Figures 2.12c and d are two examples showing convection patterns from the superposition of the basic unbalanced dayside and nightside extremes [*Lockwood and Freeman*, 1989]. When the dayside voltage ϕ_D, is twice the nightside ϕ_N, (Figure 2.12c), the net gain in open flux causes the boundary to expand overall with stronger flows on the dayside. Correspondingly when ϕ_N is twice ϕ_D (Figure 2.12d) nightside processes dominate, and there is a net loss of open flux through the nightside merging gap together with a contraction of the polar cap area.

2.3.3 Excitation and decay model for ionospheric convection

The two-component flow picture of ionospheric convection presented by *Lockwood et al.* [1990] indicates that it is not simply the existence of open flux in the system which produces ionospheric flow. Instead it is the creation by reconnection of new open flux on the dayside and new closed flux on the nightside, or both together in general, which generates the convection patterns. These ideas were extended by *Cowley and Lockwood* [1992, 1997] to propose a model of ionospheric convection in the light of recent observational evidence. The most important advances resulting from this model were firstly the realisation that if all magnetopause coupling were to cease, the near-Earth flow regime would reach an equilibrium position with *zero flow*, even though an amount of open flux is still present in the system. Such a scenario was already implicit in the *Siscoe*

and Huang [1985] model since it was the increase in open flux due to dayside reconnection that generated the flow. Naturally this *zero flow* scenario is physically almost impossible since reconnection (or other coupling processes) will always occur in some region on the magnetopause, or inside the magnetosphere, thus exciting flow in the ionosphere. However, if it were possible to 'switch off' all magnetopause and tail reconnection and other coupling processes as well, the flow in the near-Earth system would decay to very low values, even if there remains open flux present within the system. This *zero flow* state is then the starting point in the discussion of flow excitation. Any subsequent perturbation to this system caused by reconnection at the subsolar magnetopause would increase the total amount of open flux, perturbing the system from equilibrium. This causes the excitation of flow taking the system to a new equilibrium position with greater open flux than before. This scenario is illustrated in Figure 2.13 [*Cowley and Lockwood*, 1992], looking down onto the northern polar ionosphere. In these diagrams the solid line indicates the open-closed field line boundary. The initial sketch (Figure 2.13a) assumes a *zero flow* equilibrium situation with no flow in the near-Earth region, though open flux F exists. In Figure 2.13b, the system is perturbed by an impulse of dayside reconnection (e.g. a flux transfer event) which produces an additional amount of open flux dF, causing the open-closed field line boundary to impulsively expand equatorward near noon. Flow is excited over the polar cap (Figure 2.13c) as the boundary expands towards the dot-dashed circle representing the new equilibrium position with total amount of open flux $F+dF$. Once this has been achieved, the flow stops (Figure 2.13d), returning the system to a state of *zero flow* until the next perturbation arrives. The dotted line indicates the boundary of the newly-opened flux created during the impulsive dayside reconnection event.

The corresponding expansion flows in the magnetosphere are sketched in Figure 2.14 [*Cowley and Lockwood*, 1992]. Figure 2.14a shows the magnetospheric configuration in the equatorial plane just after the occurrence of the impulse of dayside reconnection. Erosion of the dayside magnetopause boundary occurs as newly opened flux tubes are stripped away towards the tail, causing the magnetosheath plasma pressure to establish a new equilibrium boundary [*Freeman and Southwood*, 1988]. The field lines thus move outward in the vicinity of the perturbation and inward elsewhere in the near-Earth system, as flux is transferred in the region of closed field lines to try to restore equilibrium. This motion corresponds to the ionospheric flow on closed flux tubes in Figure 2.13c. As the disturbance propagates into the tail (Figure 2.14b), the increase in the normal stresses exerted by the solar wind push the new open flux into the lobe near the perturbed region

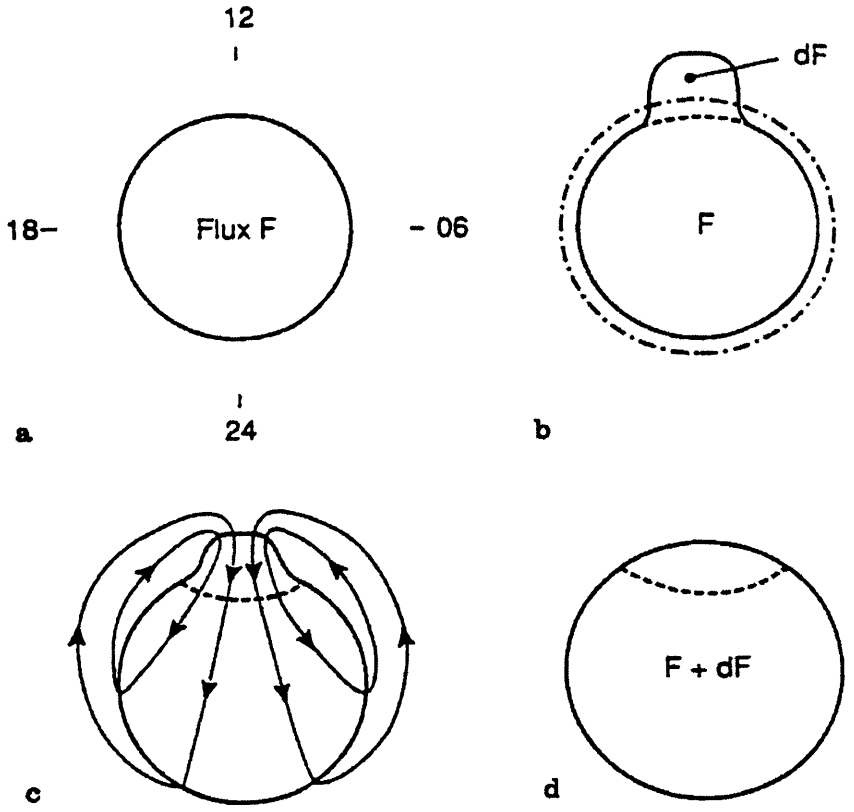

FIGURE 2.13 Theoretical ionospheric flow response to an impulsive dayside reconnection event, as viewed looking down onto the polar ionosphere with the solid line representing the open-closed field line boundary. **a.** Equilibrium state with open flux F present; **b.** impulse of dayside reconnection produces open flux dF, causing the open-closed field line boundary to expand in the region of the perturbation. The dot-dashed circle indicates the position of the equilibrium boundary containing open flux F+dF; **c.** flow is generated as the boundary expands to the new equilibrium position; **d.** flow stops once the new equilibrium position is achieved with open flux F+dF, the dotted line indicates the boundary of the open flux created during the impulsive event. [From, *Cowley and Lockwood*, 1992]

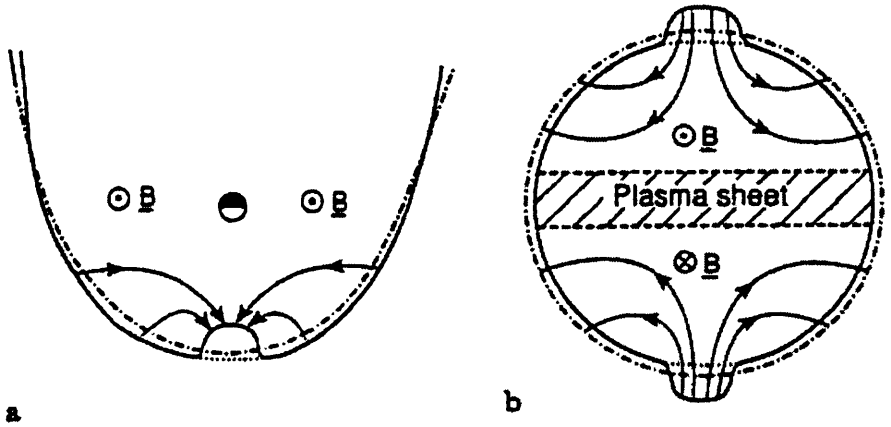

FIGURE 2.14 Magnetospheric response to the onset of dayside reconnection from an original unperturbed state, as viewed down onto the pole in **a.**, and along the sunward direction from the tail in **b.**. The arrowed lines indicate the direction of the plasma flow as erosion of the dayside boundary occurs and a new pressure balance is established. The boundary moves in response to these pressures, from its original position (solid line) to the new equilibrium position (dashed line). [From *Cowley and Lockwood*, 1992]

and outward elsewhere (as shown in tailward portion of Figure 2.14a). This then corresponds to the ionospheric flows on open flux tubes in Figure 2.13c.

A similar flow pattern in the high-latitude ionosphere can be considered to occur during an impulsive nightside reconnection event, as shown in Figure 2.15 [*Cowley and Lockwood*, 1992], in the same format as Figure 2.13 [*Cowley and Lockwood*, 1992]. Here, the impulsive tail reconnection event reduces the total amount of open flux in the system by *dF*, causing the open-closed field line boundary to impulsively contract poleward in the vicinity of the perturbation, and excite flow to establish a new equilibrium state with total open flux *F-dF*.

2.3.4 *Time scales for excitation and decay of ionospheric convection*

The impulsive reconnection-driven ionospheric flows described above demonstrate how and why flow is generated in the ionospheric region. The time scale on which these flows are excited and decay in the basic model was suggested to be ~10-15 min, indicating the time it would take the system to establish a new equilibrium after a perturbation occurred. It was not explicitly stated how the information was transmitted over the polar cap area. In later paper, *Cowley and Lockwood* [1997] considered this issue and argued that the flow would first be excited in the vicinity of the feet of newly-reconnected field lines, with the flow then expanding over the polar regions with phase speeds of several km s^{-1}. A particular example is shown in Figure 2.16, where the flow effects associated with the onset and cessation of an extended interval of open flux production, which can be associated with a corresponding interval of southward IMF, are illustrated [*Cowley and Lockwood*, 1997]. For simplicity lobe and tail reconnection have not been included in this discussion. Assuming the IMF has been predominantly northward for a significant period of time, the ionospheric flow will have died away to leave the system in equilibrium with open flux F_1 present (Figure 2.16a). Following a southward turn and the onset of dayside reconnection, the dayside boundary expands equatorward as open flux is produced (Figure 2.16b), followed by the excitation of flow which first appears in the noon sector after a few minutes (Figure 2.16c). The twin vortex flow pattern expands away from noon to the dawn and dusk sectors at phase speeds of several km s^{-1}, covering the entire polar cap on time scales of ~10-15 min (Figure 2.16d). The open-closed field line boundary also expands as the flow cells evolve, indicated by the thick arrows and the dashed line in (d), which corresponds to the work of *Siscoe and Huang* [1985] and *Lockwood et al* [1990]. If a northward turn of the IMF were to stop the production of open flux, the flow cells would

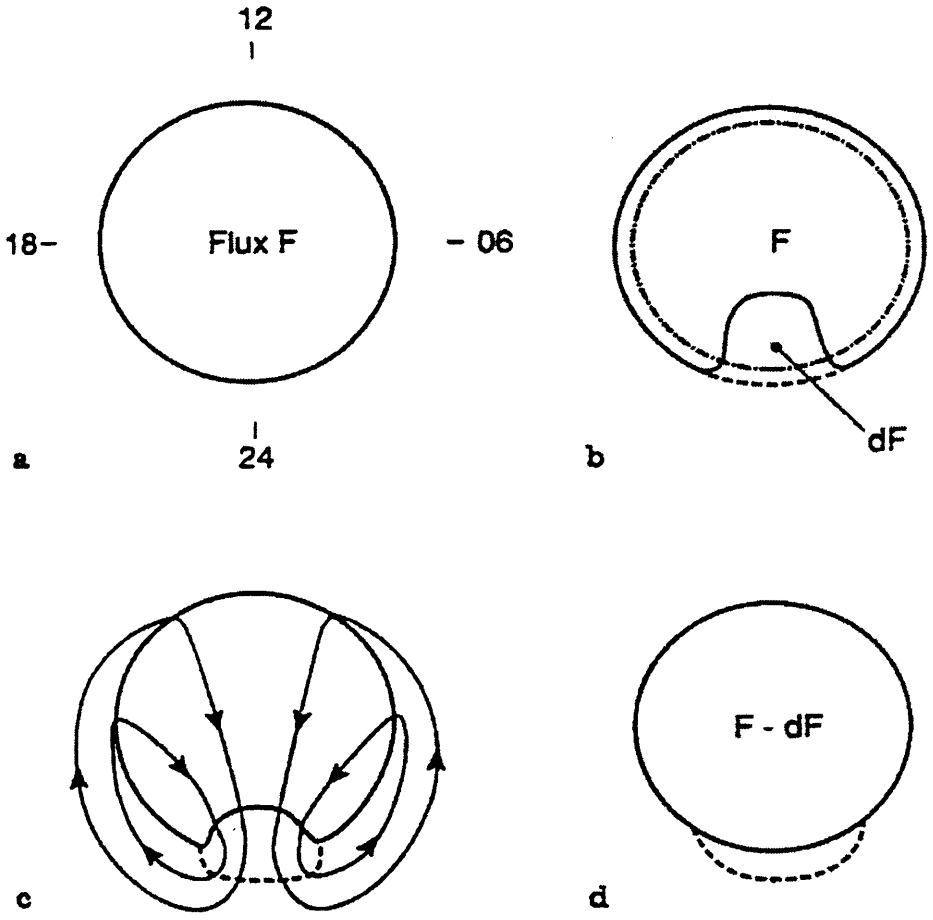

FIGURE 2.15 Theoretical ionospheric flow response to an impulsive nightside reconnection event in the same format as Figure 2.13.

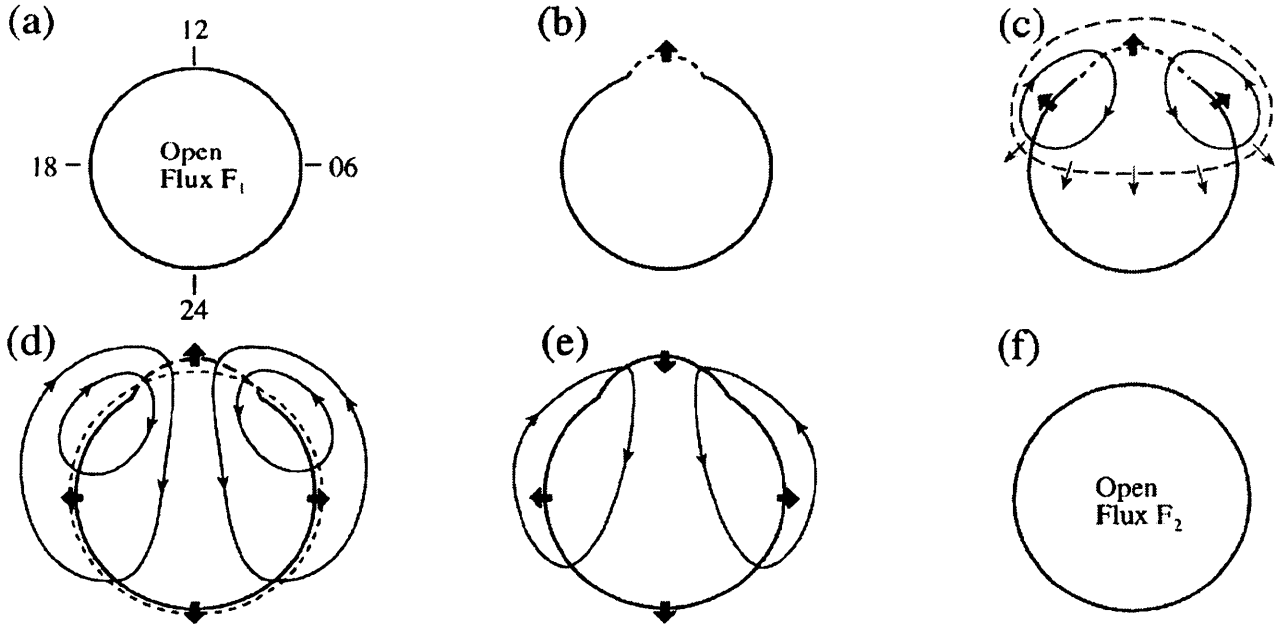

FIGURE 2.16 Excitation and decay of ionospheric convection produced by extended period of open flux production during a southward condition of the IMF B_z impinging at the dayside magnetopause. The heavy solid/dashed lines represent the open/closed field line boundary, while the arrows indicate the motion of the boundary. The lighter arrowed lines show the plasma streamlines. [From *Cowley and Lockwood*, 1997]

gradually die away on a similar time scale (Figure 2.16e), until a *zero flow* state is resumed, but with increased open flux F_2 present (Figure 2.16f).

Although in Figure 2.16 the onset of an interval of steady unbalanced dayside reconnection has been described, the above description of excitation of flow initially occurring near noon before expanding over the entire polar cap at a finite speed, can apply to both transient and steady reconnection.

2.3.5 *Observations of the ionospheric response delay to changes in the IMF orientation*

The temporal response of the ionospheric convection pattern to changes in the IMF conditions was first observed through the response of ground magnetic disturbances to the IMF [e.g. *Burton et al.*, 1975; *Clauer et al.*, 1981; *Holzer and Slavin*, 1982]. *Nishida* [1968] used globally distributed magnetic records to find that the *DP 2* magnetic disturbance was excited 7±1 min at the pole and 9±5 min at the equator after a southward turn in the IMF was incident at the bow shock. The equivalent *DP 2* current system is of twin vortical form and is believed to be the geomagnetic counterpart of the twin vortex convection flow in the ionosphere. Since the propagation time for information to travel from the bow shock to the dayside ionosphere is comparable to the delays measured by *Nishida* [1968], the implication is that the ionospheric flow response is very prompt. Similar observations have been reported in several case studies of high-latitude geomagnetic disturbances responding to north-south polarity changes in the IMF [*Pellinen et al.*, 1982; *Nishida and Kamide*, 1983; *McPherron and Manka*, 1985; *Clauer and Kamide*, 1985]

On the other hand, the correlation of different interplanetary parameters with magnetic indices derived from ground-based magnetometer records, such as the auroral electrojet indices which are primarily influenced by nightside currents, indicated longer delays [*Baker et al.*, 1981, 1983; *Clauer et al.*, 1981; *Bargatze et al.*, 1985]. These studies revealed two distinct time scales present in the data; a short delay of ~20 min and a longer delay of nearer 60 min. In making these measurements no account was taken of the slowing of plasma through the magnetosheath or the Alfvénic propagation into the ionosphere, which give a combined effect of shortening these times by ~10 min. The shorter response delay was then suggested to be associated with the directly-driven

convection by dayside reconnection, whereas the longer delay was more likely to indicate the onset of substorm activity on the nightside, i.e. tail reconnection.

Ground-based radars have also been used to study the ionospheric flow, and provide a means of monitoring the temporal variations in a given region. By combining ionospheric plasma data measured by the radar with IMF measurements made by spacecraft, response delay of the flow reconfiguration after IMF changes are incident at the subsolar magnetopause can be accurately determined [e.g. *Rishbeth et al.* 1985; *Willis et al.* 1986; *Lockwood et al.*, 1986]. *Etemadi et al.* [1988] and *Todd et al.* [1988] used plasma data obtained from the high-time resolution EISCAT UHF radar (see Chapter 3) 'Polar' experiment and IMF data from the AMPTE-IRM and -UKS spacecraft to determine response delays of the flow at 71°-73° magnetic latitude after IMF variations were mapped to the subsolar magnetopause. The former of these two studies [*Etemadi et al.*, 1988] analysed all of the EISCAT-AMPTE data available in a statistical manner performing a cross correlation on overlapping 2h local time intervals of the data. In contrast, *Todd et al.* [1988] used the same data set to construct a database of north-south turnings of IMF B_Z and calculated the time after which a clear response in the ionospheric plasma was observed. A summary of these response delays is given in Figure 2.17 [*Todd et al.*, 1988], with the individual points corresponding to the 'event' analysis of *Todd et al.* [1988], and the dotted line representing the cross correlation results of *Etemadi et al.* [1988]. Observations were confined mainly to the dayside ionosphere (08-19MLT), however a diurnal variability is apparent in the response delays. Minimum response delays of 5.5±3.2 min and 5.2±2.7 min were observed in the early to mid-afternoon sector by *Todd et al.* [1988] and *Etemadi et al.* [1988] respectively, increasing to ~10-15 min near the dawn and dusk sectors. These estimates should be reduced by ~2 min if the Alfvénic propagation time from the subsolar magnetopause to the ionosphere is taken into account. Similar very short response delays on the dayside (~2 min) were recorded by *Ruohoniemi et al.* [1993] using the Goose Bay HF radar observing at a higher magnetic latitude (~75°) after a northward turning of the IMF.

To date, very few response delays determined from nightside flow data have been derived. Figure 2.18 [*Taylor et al.* 1994] illustrates the results from two case studies conducted by *Lester et al.* [1993] and *Taylor et al.* [1994]. *Lester et al.* [1993] considered the nightside response to a southward turning of the IMF, establishing local time delays from data collected by several radars, namely Millstone Hill (MHR), Sondrestrom

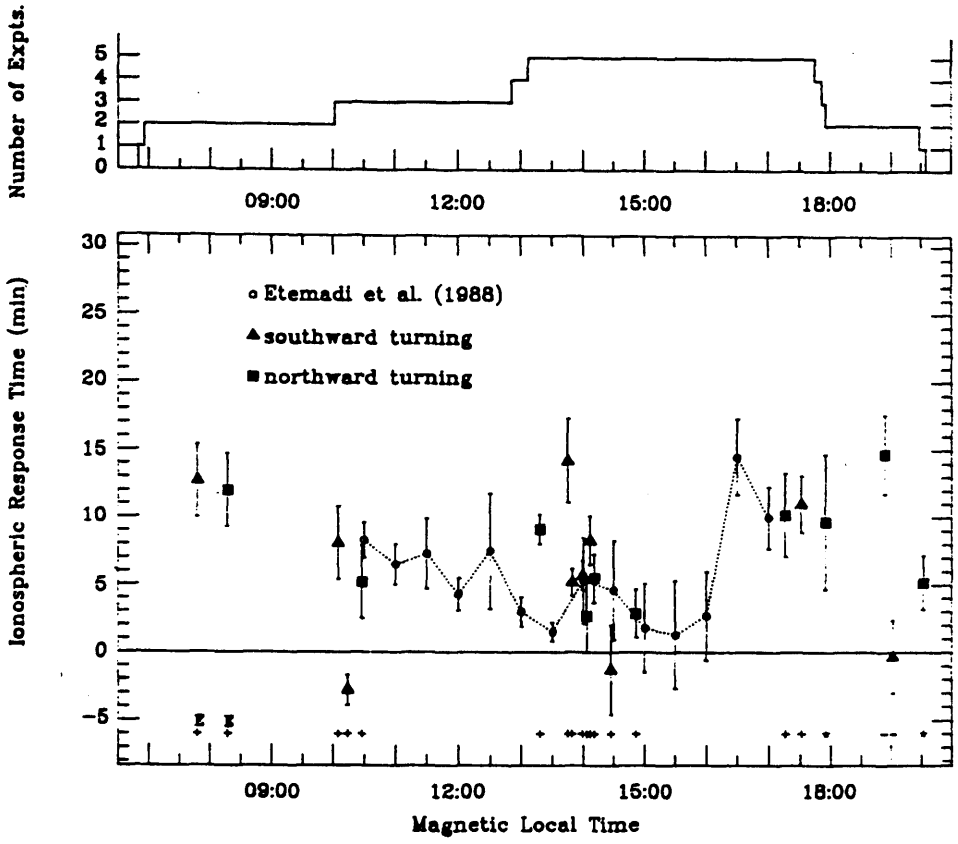

FIGURE 2.17 Summary plots showing the ionospheric response delays to changes in the polarity of IMF B_z as a function of local time, determined from the 'case-study type' analysis of *Todd et al.* [1988] (solid symbols), and the cross correlation analysis of *Etemadi et al.* [1988] (open symbols joined by the dotted line). The upper panel presents a histogram of the local time coverage of the simultaneous data sets used in these studies. [From *Todd et al.*, 1988]

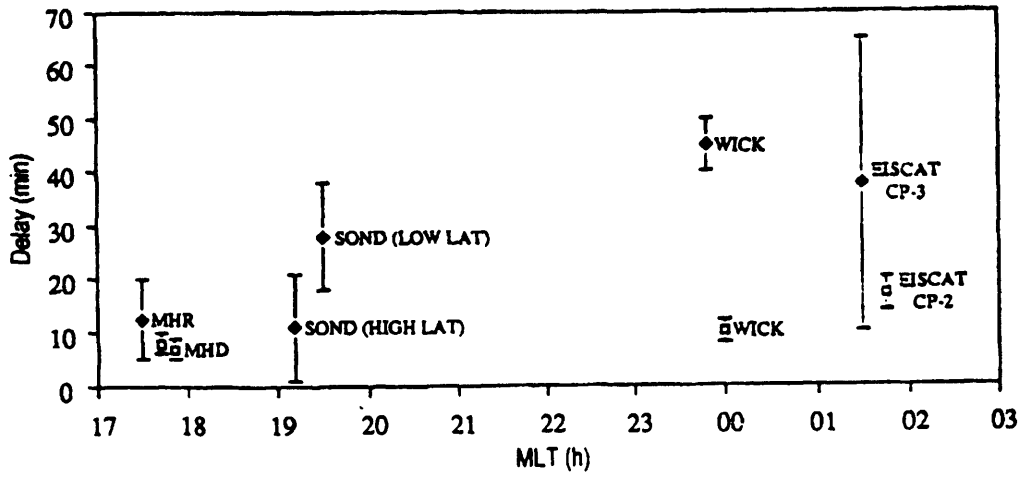

FIGURE 2.18 Nightside ionospheric response delays determined by *Lester et al.* [1993] (solid diamond symbols) and *Taylor et al.* [1994] (open square symbols). Delays tend to increase from ~10-15 min in the dusk sector to ~40 min near midnight [From *Taylor et al.*, 1994].

(SOND), Wick and EISCAT, which are plotted as solid symbols in Figure 2.18. Delays of ~10-15 min were measured near dusk, increasing to ~40 min at midnight measured at the Wick radar. The latter longer delay could be accounted for by the relatively low latitude of the Wick station (~60°), requiring the flow system to expand before the onset of backscatter was observed. The shorter delays are in agreement with those previously cited in the dusk sector. The open symbols in Figure 2.18 represent the delays obtained by *Taylor et al.* [1994], where although the results show slightly lower response times, the southward IMF turn in this study was accompanied by an interplanetary shock. This causes additional flow effects not related to the direct response of the IMF turning. In contrast to these findings, *Ruohoniemi and Greenwald* [1998] recently presented an example of data obtained from the SuperDARN HF radar where flow changes were observed to occur almost simultaneously on both the day and the night sides (within ~2 mins) in response to a southward switch in the IMF. These radars are located at magnetic latitudes of ~75°-80°, thus indicating that the entire high-latitude area reconfigures on a time scale of 1-2 min once the IMF effects appear on the dayside, though it is claimed that the effects can be substantially delayed overall In addition, *Ridley et al.* [1998, 1999] investigated the flow patterns generated using the AMIE (Assimilative Mapping of Ionospheric Electrodynamics) modelling technique as the IMF field orientation changed. The 'residual' patterns, established from the subtraction of the 'base' (reference) pattern from the changing pattern, were interpreted as indicating the coherent evolution of the flow over the whole polar ionosphere with no significant delays greater than ~1 min between the day and the night sides. The onset of the convection was calculated to start 8.4±8.2 min after the IMF change was incident at the subsolar magnetopause. *Lockwood and Cowley* [1999] have disputed the interpretation of the results presented by *Ridley et al.* [1998, 1999], and claim that the data does show delays on the nightside relative to the dayside.

The results from the majority of the studies discussed above suggest a diurnal variation in the ionospheric flow response polarity changes in the IMF B_Z component, with short ~5 min delays near noon, increasing to ~10-15 min at dawn and dusk towards the nightside. However, these results are far from resolved and a closer investigation of the time delays determined on the nightside in particular is required, as will be discussed further in this thesis in chapters 4 and 5.

2.4 Summary

In this chapter the interaction of the solar wind with the magnetosphere has been reviewed and discussed with specific reference to the resulting pattern of convection observed in the high-latitude ionosphere. The complexity of the interaction gives rise to many features that can be recognised in ionospheric convection data, thus aiding in the understanding of the physical processes occurring in the solar wind-magnetosphere system. Magnetic reconnection is by far the most important coupling mechanism, driving the magnetospheric system on both the dayside and the nightside, resulting in a twin-cell convection flow pattern in the ionosphere. Satellite and ground-based observations over many local time sectors suggest an evolving convection pattern in response to IMF variations, with flow rapidly excited on the dayside (~few minutes) and expanding away towards the nightside on time scales of ~10-15 min. However, recent observations, in particular those by *Ridley et al.*, [1998, 1999] and *Ruohoniemi and Greenwald*, [1998], indicate that the nightside flow reconfigures almost simultaneously with the dayside, within ~1-2 min or less, suggesting that there is essentially no evolution of flow. These observations are in direct conflict with the suggestions of how flow evolves in the 'Cowley and Lockwood model' [*Cowley and Lockwood*, 1992, 1997].

In subsequent chapters, we investigate the uncertainty concerning the flow evolution in the ionosphere after changes in the IMF instigate dayside reconnection at the subsolar magnetopause, and try to quantify the ionospheric response delay as a function of local time.

CHAPTER 3

Theory of incoherent scatter and the EISCAT radar system

3.1 Introduction

Remote sensing of the ionosphere and upper atmosphere with ground-based instrumentation such as radar systems has proven to be a very powerful technique, utilising different physical processes to measure different ionospheric parameters. The main distinction between the various methods employed by these systems is the usage of different radio frequencies to measure specific ionospheric properties. The radar techniques used include total reflection, Faraday rotation, coherent backscatter and incoherent scatter, of which the latter is probably the most important, transmitting high-powered radio waves scattering off ion- and electron-acoustic waves present naturally in the ionosphere. The most extensive incoherent scatter radar facility is the European Incoherent SCATter (EISCAT) system located in Northern Scandinavia, consisting of one monostatic VHF radar and a tristatic UHF radar. In this chapter the principles of incoherent scatter theory will be discussed, together with a detailed description of the EISCAT system, with particular reference to the UHF radar.

3.2 Incoherent scatter theory

3.2.1 History of incoherent scatter

Scattering electromagnetic radiation off free electrons was first proposed by *J. J. Thomson* [1906], with the scattering cross-section dependent on the classical radius of the electron and the polarisation angle (i.e. the angle between the incident radiation and the direction of the observer). Later, *Fabry* [1928] applied the concept of Thomson scattering to probe the ionosphere and suggested that by illuminating the ionospheric electrons with a monochromatic beam the returned spectrum would be a single-peaked distribution centred at the transmitted frequency. Also the peak would be Doppler broadened corresponding to the thermal velocity of the thermal electrons. However, the lack of sensitive radar equipment at the time rendered practical investigation impossible. In 1958, *Gordon* demonstrated that radar were sufficiently sensitive to detect Thomson scattering from the

ionosphere and that the spectrum would have a Doppler shift arising from the bulk motion of the ionospheric electrons and a width determined by their thermal velocity given by

$$\Delta f_e = \left(\frac{8 k_B T_e}{m_e \lambda^2} \right)^{1/2} \tag{3.1}$$

where Δf_e is the Doppler shift of an electron approaching the radar at the electron thermal speed and λ is the wavelength of the radar.

The predictions of both *Fabry* [1928] and *Gordon* [1958] were experimentally tested by *Bowles* [1958] using a high-power transmitter at Long Branch, Illinois, where a spectrum with the same power as that predicted by these authors was observed, but with a significantly narrower bandwidth. Bowles suggested that the narrower distribution could be associated with the thermal motions of the ions rather than the electrons, as proposed by *Fabry* [1928].

In a plasma, electrostatic forces between the electrons and positive ions result in the formation of a 'shielding' layer of ions around each electron. The extent of this layer is determined by the balance between the electrostatic potential and the random thermal energy, and is termed the Debye length, D, expressed as

$$D = \left(\frac{\varepsilon_0 k T_e}{N_e e^2} \right)^{1/2} \approx 69 \left(\frac{T_e}{N_e} \right)^{1/2}, \tag{3.2}$$

in which ε_0 is the permittivity of free space. Since both the temperature (T_e) and the electron number density (N_e) vary with altitude in the ionosphere, the Debye length of the ionospheric plasma tends to be larger at upper F-region and topside altitudes than at E-region altitudes. Furthermore, the Debye length varies with season, time of day, solar activity and geographic location, with typical values ranging from ~0.3 cm at the peak of the F region (~250 km) to ~6 cm or more in the lower E region (~90 km). If the radar wavelength is less than the Debye length, 'true' incoherent scatter or electron-dominated scatter occurs from 'free' electrons with the total scattered power and bandwidth as predicted by *Fabry* [1928] and *Gordon* [1958]. However, as the transmitted wavelength increases to comparable and larger values than this characteristic scale length, random thermal motions of the electrons generate longitudinal oscillations in the plasma resulting from electrostatic coupling, known as *ion-acoustic* and *electron-acoustic waves*. These waves produce fluctuations in the electron density, which in turn give rise to the observed

scattered signal. The theoretical nature of these waves and their importance in the ionosphere was studied extensively by several authors independently, including *Fejer* [1960]; *Dougherty and Farley* [1960]; *Hagfors* [1961] amongst others.

The acoustic modes propagate isotropically over a wide and continuous spectrum of wavelengths, including wavelengths satisfying the Bragg condition for the transmitted radar wavelength, $\Lambda=\frac{1}{2}\lambda$. The scattered signal from these acoustic waves is then quasi-coherent, with the resulting spectrum consists of four components corresponding to scatter from the upward and downward travelling ion and electron waves. The frequencies of these scattered signals experience a Doppler shift equal to the frequency of the scattering wave; $F_i(\lambda)$ and $F_e(\lambda)$ for the ion- and electron-acoustic waves respectively, predicted by theory as follows

$$F_i(\lambda)=\pm\frac{2}{\lambda}\left[\left(\frac{k_B T_i}{m_i}\right)\left(1+\frac{T_e}{T_i}\right)\right]^{\frac{1}{2}} \tag{3.3a}$$

$$F_e(\lambda)=\pm f_p\left(1+\frac{48\pi^2 D^2}{\lambda^2}\right)^{\frac{1}{2}}, \tag{3.3b}$$

in which T_i is the ion temperature, m_i is the ion mass and f_p is the plasma frequency of the medium, given by

$$f_p=\left(\frac{N_e e^2}{4\pi^2\varepsilon_0 m_e}\right)^{\frac{1}{2}}. \tag{3.4}$$

The transmitted radar signal is scattered off those waves whose phase fronts lie in the normal plane to the 'mirror direction' defined as the bisector of the angle between the transmitted and scattered signals. For a monostatic system, the transmitter and receiver are co-located, so the scattered signal is received from phase fronts perpendicular to the incident beam, since the mirror direction is along the line-of-sight of this beam.

Particles travelling in the same direction as the wave but at a slightly slower velocity gain energy from the wave, whilst the slightly faster particles transfer energy to the wave. However, in a usual spectrum more particles travel at slower speeds than faster speeds, resulting in the net acceleration of the particles and attenuation of the wave. This is termed 'Landau damping' and results in a broadening of the spectral features of the returned spectrum. In particular, since the ion-acoustic wave velocity is well within the velocity

distribution of the thermal ion population at temperature T_i, the higher concentration of slower moving ions cause significant attenuation of the wave. The two ion-acoustic spectral lines thus broaden and merge to form the characteristic 'double-humped' spectrum of the returned signal. In contrast, the plasma wave or electron-acoustic waves travel at a much greater phase speed than the thermal electrons, and so little or no attenuation is observed on the corresponding spectral lines. Both these features are illustrated in Figure 3.1 [*Beynon and Williams*, 1978] showing a representation of the typical returned frequency spectrum when the radar wavelength greatly exceeds the Debye length and the ion and electron temperatures are equal. The double-humped ion spectrum is distributed on either side of the transmitted frequency with the two sharp plasma lines Doppler shifted by the amount described in Equation 3.3b.

The spectral shape of the ion line varies as a function of the sounding wavelength, λ, particularly for wavelengths less than the Debye length. This effect is illustrated in Figure 3.2 [*Evans*, 1969], plotting the ionic component of the spectrum through variations in the α parameter defined as

$$\alpha = \frac{4\pi D}{\lambda}. \tag{3.5}$$

Other factors that influence the shape of the ion spectral line include the ratio of the ion and electron temperatures, the ion composition, magnetic fields and collisional effects, as will be discussed further below.

If the transmission wavelength is longer than the Debye length, then the scattered signal from the ion-acoustic waves contains information about the ions as well as the electrons, making this scattering mechanism a very powerful diagnostic tool in the ionosphere.

3.2.2 Parameters measured and calculated by incoherent scatter

The shape and definition of the returned signal spectrum allows several ionospheric plasma parameters to be directly measured and others derived from those measurements. The ionospheric electron density (N_e) may be determined from the total scattered power received from a signal transmitted with a wavelength greater than the Debye length. In a monostatic radar arrangement, the scattered power can be measured as a function of altitude, giving a means of calculating the electron density profile of the ionosphere along the line of sight. Since returned power is proportional to electron density, the radar system

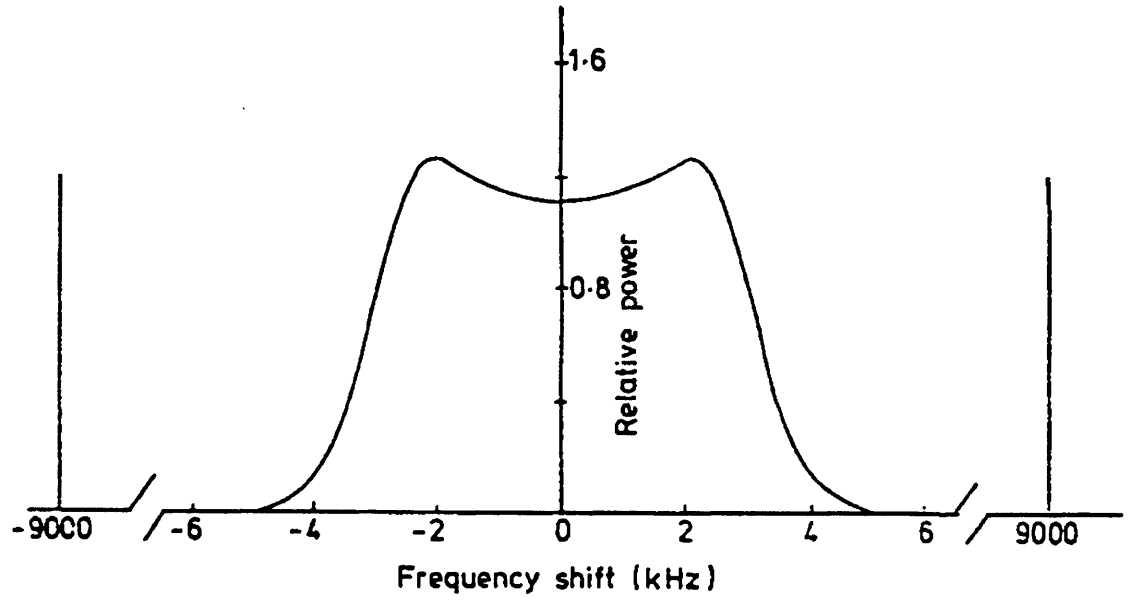

FIGURE 3.1 Typical incoherent scatter spectrum of returned frequency. $N_e=10^{12}$ m^{-3}, $T_e=T_i=1000$ K, $\lambda=1$ m, $m_i=16$. [From *Beynon and Williams*, 1978]

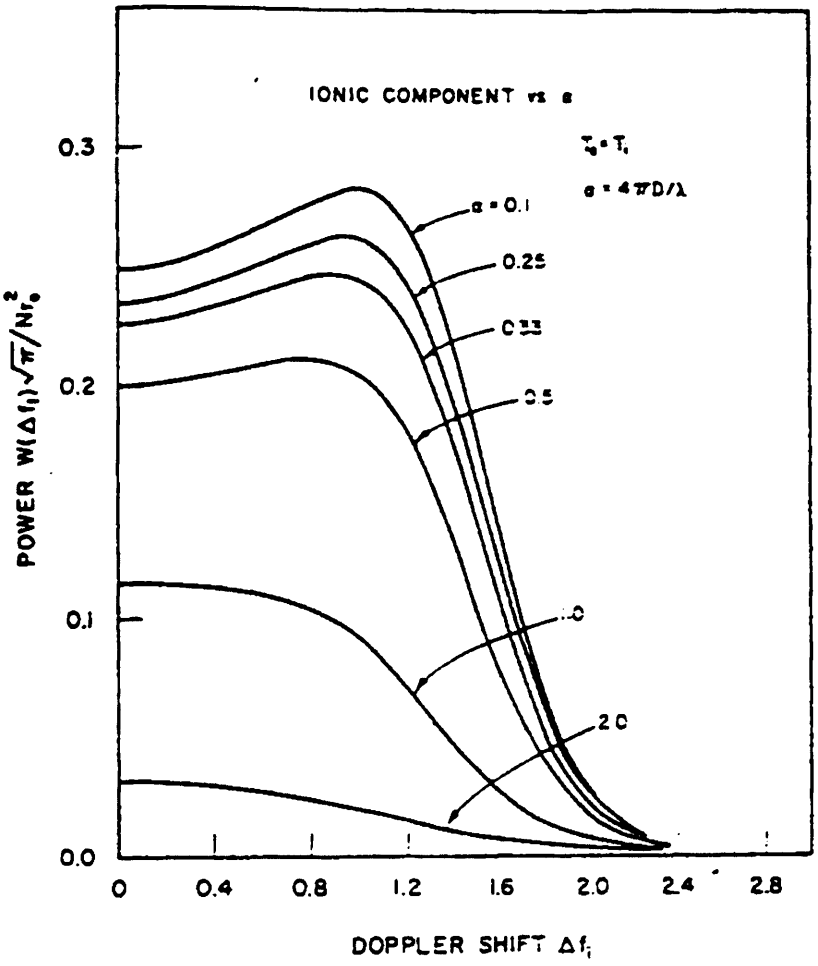

FIGURE 3.2 Variation of the ionic component of the scattered signal for equal electron and ion temperatures with the a parameter. [From *Evans*, 1969]

constant is required to provide an absolute value, which can be easily determined by calibration of the measured electron density with an independent source, such as an ionosonde.

The shape of the ion-line spectrum broadens with Landau damping, the degree of which is determined by the ratio of the electron to ion temperature. As this ratio increases, the degree of attenuation of the wave decreases causing the two peaks to become shaper and more defined, as shown in Figure 3.3 [*Beynon and Williams*, 1978]. Thus, a measure of the plasma temperature ratio can be determined from the ratio of the peak to trough power of the ion-line spectrum. Furthermore, since the peak to peak separation of the ion spectrum is approximately equal to twice the ion-acoustic frequency given by equation 3.3(a), the ion temperature to ion mass ratio can easily be calculated. The ion mass can usually be estimated in regions of the ionosphere, e.g. in the F region, where the ion composition can be assumed or easily determined, leading to the absolute values of the ion and electron temperatures.

Bulk motion of the ion population produces a Doppler shift of the ion-line spectrum corresponding to the component of the ion velocity (v_i) in the mirror direction of the radar beam. Figure 3.4 [*Rishbeth and Williams*, 1985] illustrates this for a bistatic system, where this component is along the bisector of the transmitting and receiving beams. For a monostatic system this component is along the line-of-sight of the radar. The Doppler shift due to an ion mirror velocity, v_m is,

$$\Delta F_i = \frac{2v_m}{\lambda}\cos\left(\frac{\gamma}{2}\right). \tag{3.6}$$

Figure 3.5 [*Beynon and Williams*, 1978] shows that the extent of the frequency-shift of the spectrum resulting from the Doppler effect is usually small compared to the spectral width. Nevertheless, measurements of this shift with sufficient accuracy allow the determination of the ion mirror velocity. If measurements of this kind are taken simultaneously at three receiving stations suitably located, the three components of the plasma drift velocity can be measured and combined to give the true plasma drift velocity of that volume of plasma. The EISCAT UHF radar system is the only incoherent scatter radar capable of establishing a tristatic arrangement from which the ion vector velocity can be measured. Details of this will be discussed later in this chapter.

All of the above parameters can be routinely measured from the returned frequency spectrum, however a number of other parameters can be derived under specific conditions

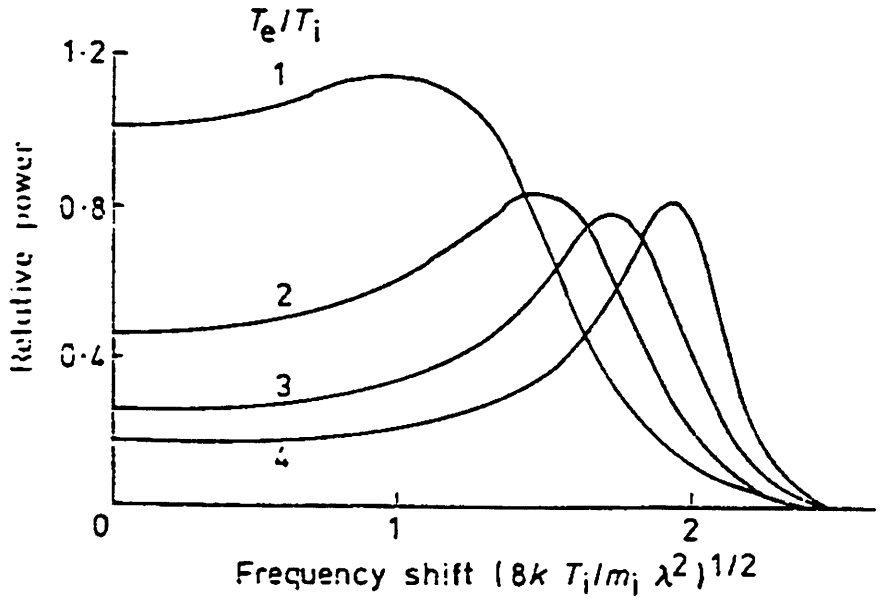

FIGURE 3.3 Dependence of the ion-line spectral shape on the ratio of plasma temperatures (T_e/T_i). [From *Beynon and Williams*, 1978]

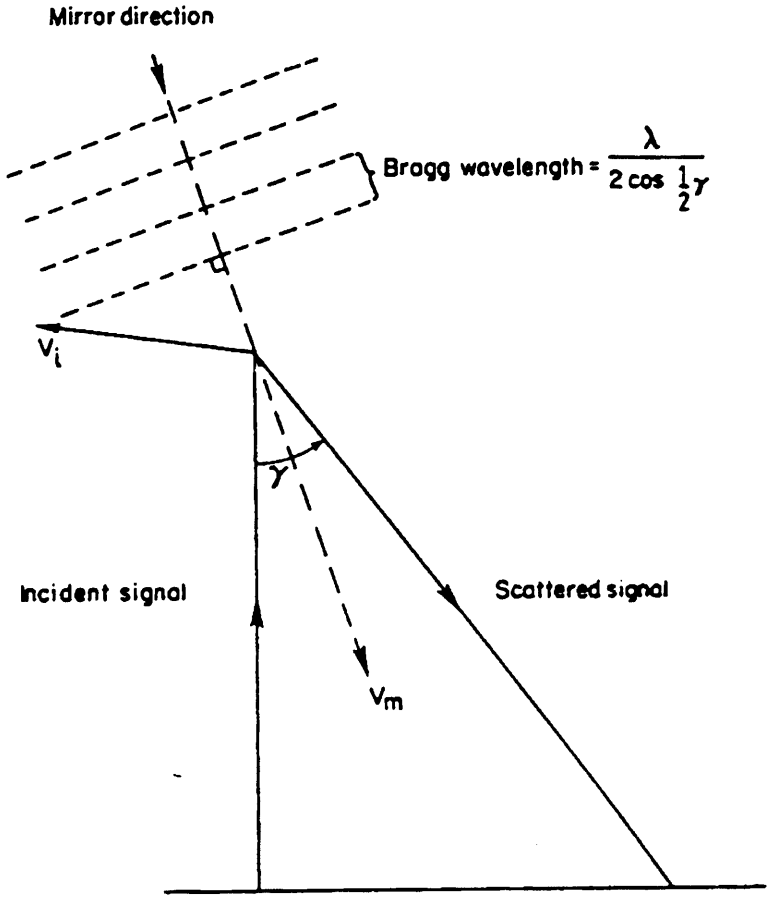

FIGURE 3.4 Direction of the mirror velocity, v_m, as determined from the scattering geometry for a bistatic incoherent scatter radar. [From *Rishbeth and Williams*, 1985]

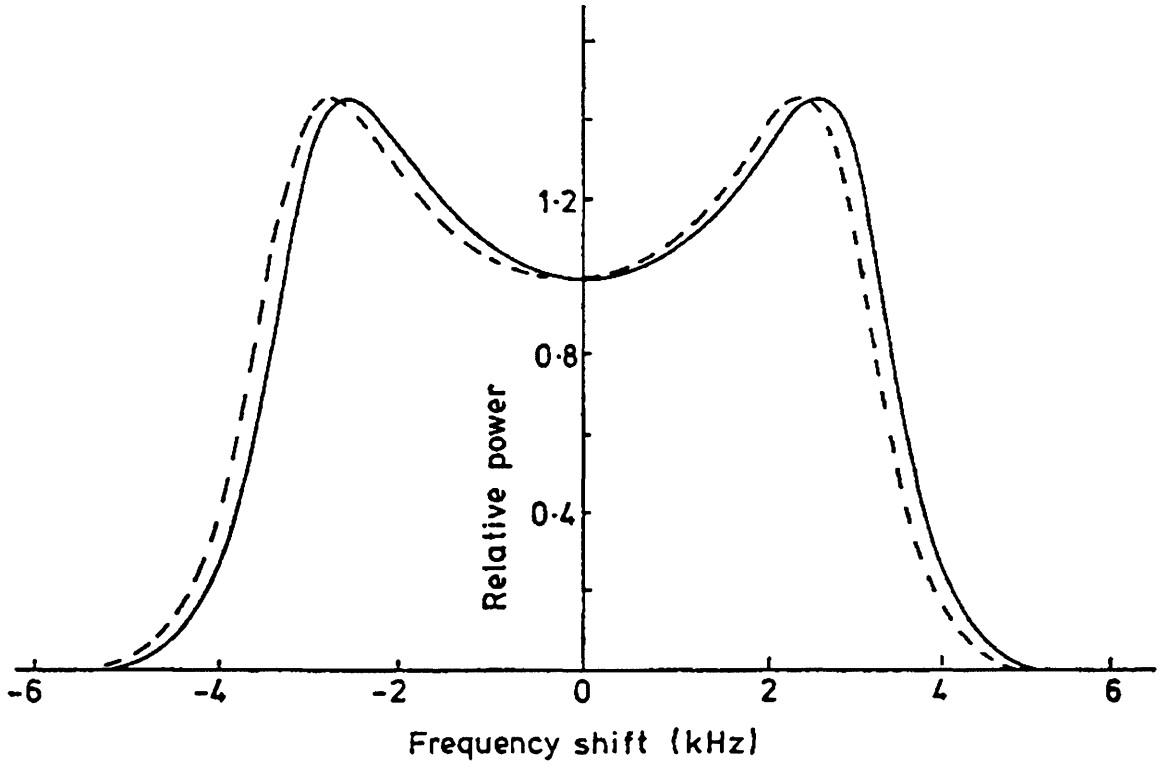

FIGURE 3.5 Doppler shift of the ion-line spectrum associated with a plasma velocity of 100 m s^{-1} away from the radar in the mirror direction (dashed line), compared with the unshifted spectrum (solid line). [From *Beynon and Williams*, 1978]

and height ranges. Table 3.1 presents a list of the parameters both derived directly from the returned spectrum and those inferred from the results. Those parameters denoted with an asterisk cannot be fully described by a monostatic system, rather it is only the component along the line-of-sight of the radar which is resolved. A tristatic arrangement of the radar is required to establish the full vector parameter, such as the ion vector velocity, which is of principal importance to the work in this thesis.

Extensive reviews of incoherent scatter theory and the derivation of ionospheric parameters are discussed in depth throughout the literature [e.g. *Beynon and Williams*, 1978 and *Evans*, 1969].

3.3 Incoherent scatter radar and the EISCAT system

Since the initial experimental measurements of ionospheric backscatter by *Bowles* [1958], illustrating a narrower bandwidth than that predicted by Thomson scattering indicating the influence of the ions in the scattering plasma, several incoherent radar systems have been constructed. These systems are limited in number due to the technical specifications required to observe the very weak backscatter produced by sounding the ionosphere at, say, megawatts of power. Powerful transmitters, large antennas, sensitive receiving equipment and sophisticated signal processing techniques, all increase the cost of constructing an adequate radar facility. Table 3.2 lists the operating characteristics of early incoherent scatter radar facilities, based on the information presented in *Beynon and Williams* [1978].

At the URSI meeting in Canada in 1969, the concept of a high-latitude sophisticated incoherent scatter radar, far superior to those in operation, was discussed. Negotiations for such a facility concluded in 1975 with the signing of an Agreement between the research councils of six European nations, Finland, France, Germany, Norway, Sweden and the United Kingdom, to construct the European Incoherent SCATter radar system (EISCAT).

3.3.1 EISCAT operational characteristics

The European Incoherent Scatter (EISCAT) facility [*Rishbeth and Williams*, 1985] consists of three radars. The first is a tristatic UHF system, which commenced full operation in 1981, currently operating at a central frequency of 931.5 MHz. The transmitter for this radar is located in Tromsø, Northern Norway with receivers sited at Tromsø, Kiruna in Sweden and Sodankylä in Finland. The unique tristatic nature of the UHF system allows the measurement of the three components of plasma velocity in a

Directly measured parameters	**Derived indirectly**
Electron density, N_e	Electric field, $\boldsymbol{E}$
Electron temperature, T_e	Hall conductivity, σ_H
Ion temperature, T_i *	Pederson conductivity, σ_P
Ion composition, m_i	Exopheric heat flux, ϕ
Ion velocity, $\boldsymbol{v}_i$ *	Neutral temperature, T_n
Electron velocity, $\boldsymbol{v}_e$ *	Neutral density, N_n
Ion-neutral collision frequency, ν_{in}	Neutral velocity, $\boldsymbol{v}_n$
Photoelectron flux	
Electric current density, $\mathbf{J}=N_e(\boldsymbol{v}_e-\boldsymbol{v}_i)$ *	

TABLE 3.1 List of measured and derived parameters obtained from incoherent scatter.

Station	Geographic Location	Antenna	Frequency (MHz)	Power	
				Peak (MW)	Mean (MW)
Jicamarca (1962)	11.9° S 76.9° W	290x290 m dipole array	49.9	4.0	0.4
Arecibo (1962)	18.3° N 66.8° W	305 m spherical reflector	430.0	2.0	0.1
Millstone Hill (1963)	42.6° N 71.5° W	68 m parabola	440.0	3.0	0.12
Millstone Hill (1963)	42.6° N 71.5° W	25 m parabola	1295.0	4.0	0.12
Stanford (1965-71)	37.4° N 122.2° W	27 m parabola	1300.0	5.0	0.12
Chatanika (1971-1982)	64.9° N 147.7° W	27 m parabola	1300.0	5.0	0.12
Sondrestrom-fjörd (1982)	67.0° N 51.0° W	27 m parabola	1300.0	5.0	0.12
Kharkov (1972)	48.5° N 36.9° E	100 m parabola	150.0	2.0	
St Santin (1965-87)	44.6° N 2.2° E	20x100 m reflector	935.0		0.15 (cw)
Nancay (1965-87)	47.4° N 2.2° E	40x200 m reflector		Receiver station	
St Cassien (1973-87)	44.7° N 0.8° E	25 m parabola		Receiver station	
Mende (1973-87)	44.5° N 3.5° E	25 m parabola		Receiver station	
Malvern (1968-75)	52.1° N 2.3° W	43 m parabola	400.5	8.0	0.08 (0.04 cw)
Wardle (1971-75)	53.1° N 2.6° W	25x36 m parabola		Receiver station	
Chilbolton (1971-75)	51.1° N 1.4° W	25 m parabola		Receiver station	
Aberystwyth (1972-75)	52.4° N 4.0° W	Two 12x25 m parabolic troughs		Receiver station	
MU (1985)	34.9° N 136.1° W	103 m circular array of 475 crossed Yagis	46.5	1.0	0.05

TABLE 3.2 Operational characteristics of early incoherent scatter radar facilities. [Adapted from *Beynon and Williams,* 1978]

given region of the ionosphere, from which the full vector can be computed. The second radar is a monostatic VHF system with both transmitter and receiver co-located in Tromsø, operating at frequencies around 224.0 MHz, with reliable observations available since 1985. Finally, the monostatic UHF EISCAT Svalbard radar (ESR) completes the set, located at Longyearbyen on the island of Spitsbergen in the Svalbard archipelago, several hundred miles north of mainland Norway. The proposal for a radar located well inside the polar region was presented in 1990 [*Cowley et al.*, 1990], with the full operation of the radar commencing in late 1996. Some general characteristics of these three radars are tabulated in Table 3.3, with the geographic positioning of the mainland radars illustrated in Figure 3.6 [*Rishbeth and Williams*, 1985]. Since the data presented in this thesis were obtained using the tristatic UHF radar, further discussion will be limited to this system. A detailed description of the EISCAT VHF radar may be found in *Hagfors et al.* [1982] and *Folkestad et al.* [1983], for example, and details of the ESR radar in *Wannberg et al.* [1997].

The UHF antennae comprises three fully steerable (both in azimuth and elevation) circular parabolic dishes of diameter 32 m with an effective collecting area of 570 m^2, and have a half-power beam width of ~0.6°. The transmitted signal is circularly polarised from Tromsø and is similarly received at this receiver, with the remote sites receiving an elliptically polarised signal. The single klystron transmitter is capable of providing a peak power of 2 MW and an average power of ~250 kW. The transmitter can operate on any of sixteen frequencies, spaced at 0.5 MHz intervals around the central frequency, and switch between these on the timescale of microseconds, although sampling is limited to eight tuneable receiver channels. The wavelength of UHF transmission (~30 cm) produces incoherent scatter from ionospheric plasma at altitudes between 80 km to 1500 km.

The received signal is modified in frequency by passage through a local oscillator and attenuated in power before being divided into eight receiver channels. The signal from each channel is downconverted in frequency and bandpass filtered, with the resulting signal entering a hybrid detector, to produce two outputs in quadrature. After further baseband filtering and amplification, these signals deliver cosine and sine inputs to an analogue-digital converter (ADC). The width of the baseband filter must be sufficient to allow the maximum amount of information to be retrieved from the signal, taking also into account a possible Doppler shift due to the bulk motion of the plasma along the line-of-sight. The output from each ADC is passed to a correlator, which reads from one half of the buffer memory while simultaneously writing to the other half. The correlator computes

Station	Geographic Location	Antenna	Frequency (MHz)	Power	
				Peak (MW)	Mean(MW)
Tromsø VHF	69.6° N 19.2° E	120x40 m parabolic trough (Tx/Rx)	224.0	5.0	0.62
Tromsø UHF	69.6° N 19.2° E	32 m parabola (Tx/Rx)	933.5	2.0	0.25
Kiruna UHF	67.9° N 20.4° E	32 m parabola	Receiver station		
Sodankylä UHF	67.4° N 26.7° E	32 m parabola	Receiver station		
Longyearbyen ESR	78.2° N 16.1° E	32 m parabola	500.0	0.5	0.125

TABLE 3.3 Operational characteristics of the EISCAT facility.

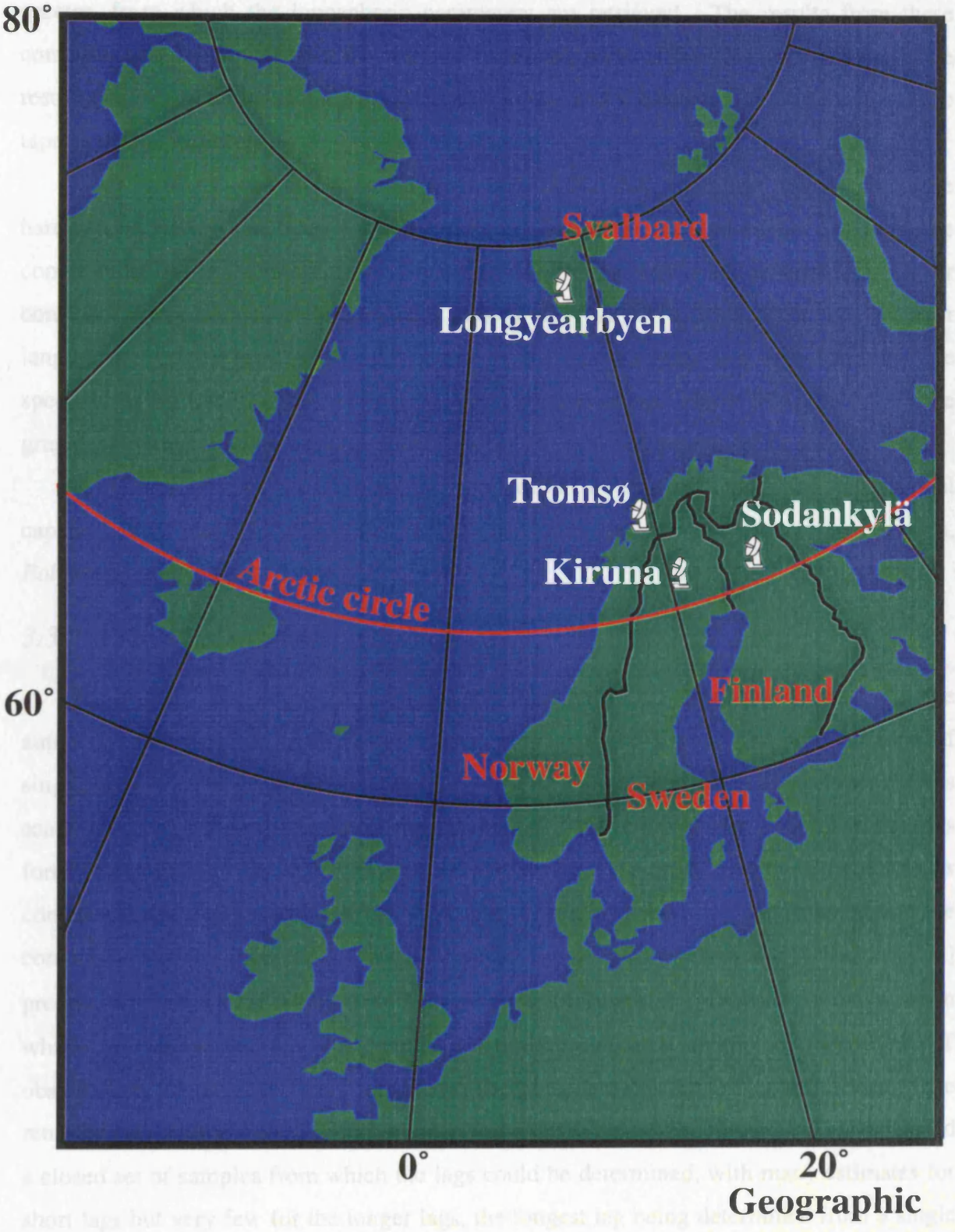

FIGURE 3.6 Map showing the geographic position of the three mainland EISCAT radar and the EISCAT Svalbard radar.

autocorrelation functions (ACFs), Fourier transforms of the incoherent scatter power spectra, from which the ionospheric parameters are retrieved. The results from these computations, containing both the real and imaginary parts of the ACF, are written to the result memory from where they are dumped to disc, and subsequently copied to magnetic tape or digital audiotape.

Each EISCAT site is controlled by a NORD ND-500 computer, interfaced to the hardware devices. The three site computers are linked by telephone lines and inter-site communication via the internet. All high-precision timing signals are generated by a radar controller, programmed in a language known as TARLAN (transmitter and receiver language). Lower level commands, such as antenna pointing and data handling, are specified using EROS (EISCAT real time operating system). The RTGRAPH (real time graphics) system enables real time monitoring of the returned signal, ACFs and spectra.

A comprehensive description of the technical characteristics and operational capabilities of the EISCAT radar facility has been documented by, amongst others, *Folkestad et al.* [1983].

3.3.2 EISCAT measurement techniques

Ionospheric parameters can be retrieved from either the frequency spectrum or the autocorrelation function (ACF) of an incoherently scattered signal. The simplest form of single pulse transmission involves the sampling of the pulse at discrete intervals as it is scattered from different heights in the ionosphere. The cross-products of these samples form an estimate of the ACF. The time delay between the cross-product of two samples constitutes a lag of a given interval. Multiple estimates of each lag are obtained and the combination of the different lags form the ACF. Figure 3.7 [*Rishbeth and Williams*, 1985] presents the range-time diagram for a single pulse of length, τ, illustrating the manner in which the various ACF lags are calculated from the measured sample. In early EISCAT observations, the receiver was 'gated' over the pulse length such that contributions to the returned signal were received from a scattering volume centred on range R. This produced a closed set of samples from which the lags could be determined, with many estimates for short lags but very few for the longer lags, the longest lag being determined from a single estimate. As a result, the effective signal-to-noise ratio for the longer lags was reduced and an uneven spatial distribution for the different lags. These problems were resolved by the implementation of the GEN system correlator programs [*Turunen*, 1986], which introduced gating after the evaluation of the cross-products.

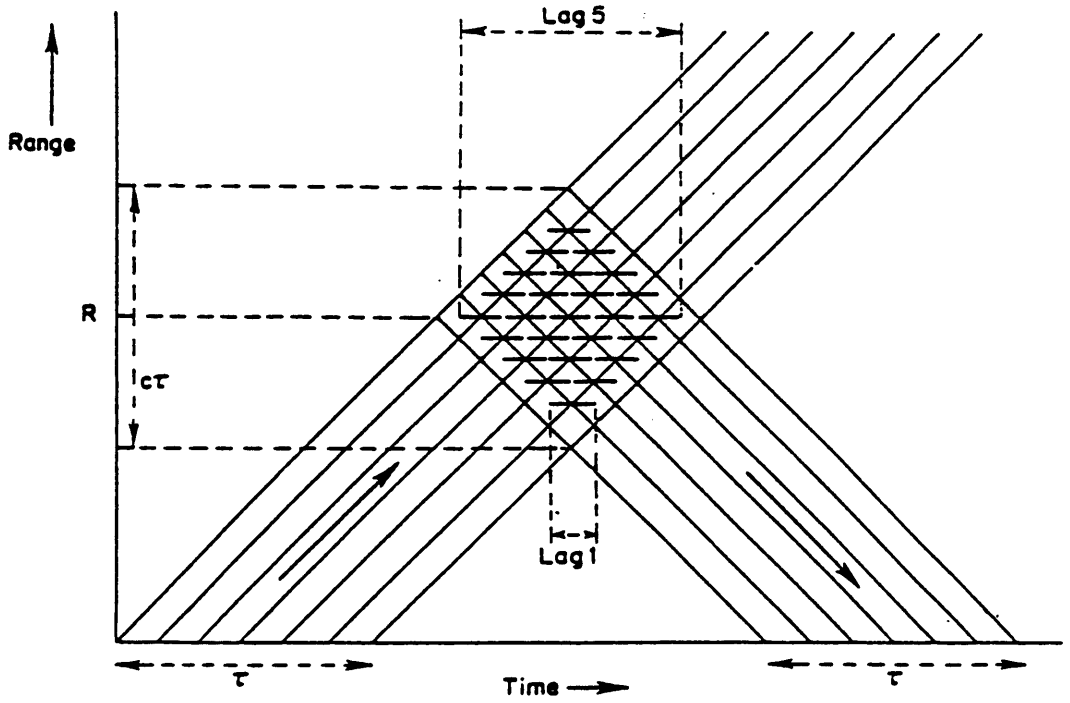

FIGURE 3.7 Range-time diagram for single transmitted pulse of length, τ. The receiver is 'gated' so as to receiver signals from a mean range R, but with contributions from the range R+ct and R-ct, allowing the determination of different lags over the entire range. [From *Rishbeth and Williams*, 1985]

In order to achieve accurate measurements of the ionospheric parameters required, the transmitted signal must be conditioned to provide the best spatial and spectral resolution possible. The accuracy of the returned power spectrum depends critically on the signal-to-noise ratio and the pulse length of the signal [*du Castel and Vasseur*, 1972]. When the pulse length is long, more power is backscattered to the radar and the signal-to-noise ratio is high, indicating that to attain the best spectral resolution the pulse length must be maximised. However, the height resolution of the radar measurements is limited to the scale height, H, of the plasma in the observation region, ranging from several km in the E-region to 50 km in the F-region. The pulse length must then always be shorter than the 2H/c for vertical transmission, although higher spatial resolution may be required for the study of small-scale features. To sustain adequate spatial and spectral resolution of the returned signal, single long pulse transmission cannot be used to provide measurements below ~200 km with the EISCAT UHF system. This problem was resolved by the transmission of multi-pulse [*Farley*, 1969; 1972] or alternating code pulse schemes [*Lehtinen and Häggström*, 1987] which enables measurements to be obtained at altitudes where a single long pulse is unsuitable.

3.3.3 EISCAT common programmes

The EISCAT experimental time is shared between two types of experimental mode, each utilising about half of the observing time. The first are 'common programmes', which operate routinely throughout the year, providing common data available to all members of the associate countries. The second are so-called 'special programmes', which are designed for specific objectives by scientists from individual associate countries and are initially available only for their use. The common programmes (CP) are currently subdivided into seven experiments, three for the VHF (CP-4, 6 and 7) and four for the UHF (CP-1, 2, 3 and 5). These experiments are continually refined and updated to incorporate the wide scientific view of the EISCAT community, although the basic principles are preserved to provide substantial data sets enabling long term studies to be conducted.

For the purpose of the studies conducted in this thesis, the most recent version of common programme 1, CP-1-K running since 1993, was used to obtain the necessary velocity observations. The CP-1 experiment was designed for high time resolution studies of the dynamic processes occurring in the ionosphere (see Chapter 2). In this experiment, the transmitter is aligned along the local magnetic field line direction at Tromsø, which is

approximately southward at an elevation of 77.5°. The remote site beams intersect the transmitter beam at a fixed F-region altitude of 278 km, allowing continuous measurements of the plasma flows at this point with very high time resolution. From the tristatic arrangement, the ion velocity components from the receiver sites can be transformed to give the three orthogonal magnetically-oriented velocity vectors (v_E, v_N and $v_\parallel$), with respect to the magnetic field direction [*Rishbeth*, 1978]. Long pulse, two power profiles, and an alternating code are transmitted, the latter replacing the original multi-pulse scheme.

3.3.4 Incoherent scatter data analysis

The technique adopted for analysing the incoherent scatter data to provide estimates of the ionospheric parameters outlined in §3.2.2, is to assume known values of some of these variables, allowing the remainder to be determined. Figure 3.8 summaries the operation of the analysis package for various forms of radar data.

Post-integration of the data involves the integration of successive ACFs, or ACFs measured on different frequencies, to provide a more accurate ACF, with a reduction in uncorrelated noise at the expense of the temporal resolution of the data. Post-integration in time can only be used if the time between successive dumps in the correlator is shorter than the time resolution required. For studies of the temporal response of the high-latitude ionosphere to magnetospheric changes, high temporal resolution is required and so the 10s data dumps are post-integrated over 2 min intervals. This post-integration time can be reduced, however the signal-to-noise ratio also decreases as a result.

The ACF measured by the radar is the convolution of the transmitted signal and the pulse scattered by the ionosphere. Upon passage of the pulse through the receiver, the signal is modified by the receiver filter, which must be accounted for prior to analysis [*Rishbeth and Williams*, 1985]. The background noise level is estimated by sampling beyond the furthest range gate, and is subtracted from the received signal. Before the ionospheric parameters can be derived from the returned signal, both instrumental and background effects must be removed from the ACFs. A detailed description of the instrumental effects on the measured ACFs is presented in *Rishbeth and Williams* [1985].

The first parameter to be estimated is the 'raw electron density' based upon the total backscattered power, ignoring the system constant and assuming equal ion and electron temperatures. This does not constitute a final value of the electron density, but is simply required for scaling purposes during the subsequent computations.

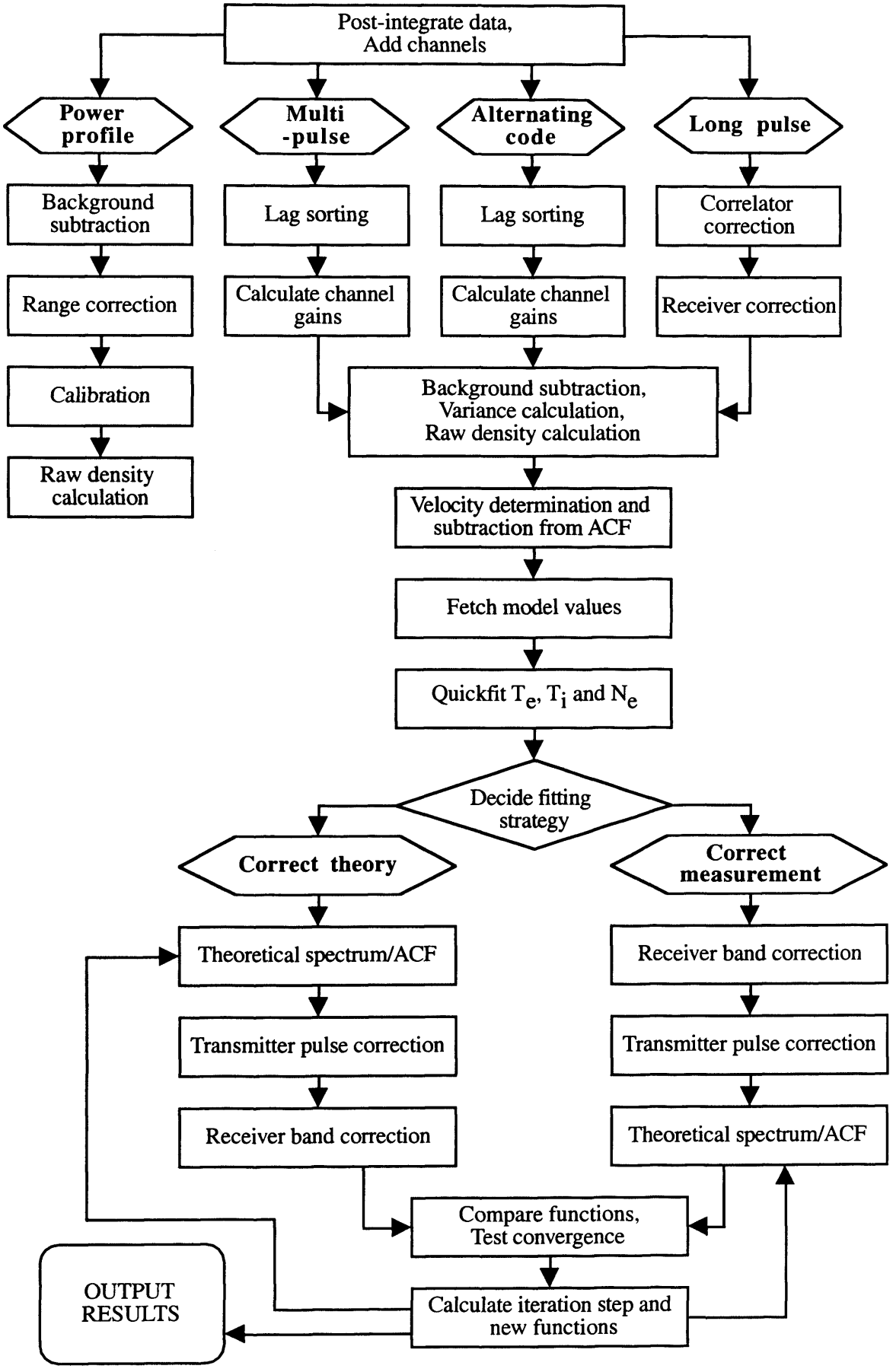

FIGURE 3.8 Block diagram outlining the principle UK incoherent scatter analysis package.

The ion velocity is next determined from the Doppler shift of the frequency spectrum. This shift corresponds to the multiplication of the ACF by a factor $e^{i\phi}$ where

$$\phi = \frac{2v}{c}(2\pi f) \ , \tag{3.7}$$

and f is the transmitted frequency. The quantity ϕ is determined by a 'matched-filter technique' incorporating both real and imaginary components of the ACF, allowing the calculation of the drift velocity. The effect of this can then be removed from the ACF, and the remaining parameters can then be established.

The analysis continues by means of minimising the variance between the measured ACF and a theoretical ACF calculated from known plasma parameters. Initial values of these parameters are set by a 'quick-fit' method applied to the 'unshifted' ACF. Approximate ion and electron temperatures are determined from the first crossover point and first minimum of the ACF (Figure 3.9) and are used to correct the original estimate of the raw electron density. From these estimations, an empirically produced spectral function is derived. Data fitting proceeds as the theoretical spectrum is continually upgraded, and after transformation into the time domain, is compared with the measured ACF through a multi-variant least squares fit technique. Once the variance between the theoretical and observed ACFs is less than a specified threshold, an optimum set of plasma parameters is returned. If, however, convergence is not attained within a pre-set maximum number of iteration, the fit is deemed a failure and a 'bad fit' flag is set.

3.3.5 Error estimates in incoherent scatter measurements

During the derivation of the plasma parameters from the incoherent scatter spectrum, several uncertainties can occur. Random errors generated from the level of noise will reduce the accuracy of the received signal by an amount dependent on the signal-to-noise ratio [*du Castel and Vasseur*, 1972]. Correspondingly, the accuracy of the derived plasma parameters will be similarly affected, with the random error in the line-of-sight ion velocity given by

$$\Delta \mathbf{v}_i = \left(0.5 + snr^{-1}\right)\frac{\lambda}{2}\frac{\Delta f_i}{(b\tau N)^{\frac{1}{2}}} \ , \tag{3.8}$$

where Δf_i is the ion line width, b is the signal bandwidth and N, the number of pulses integrated.

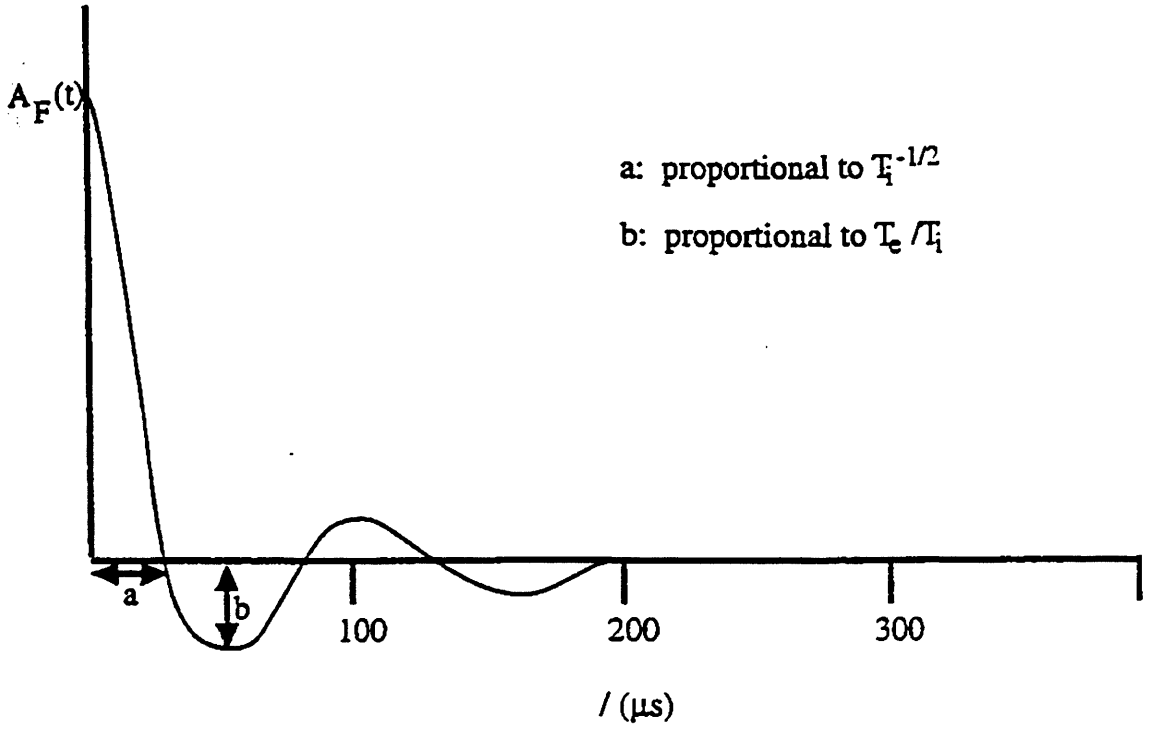

FIGURE 3.9 First approximation of the ACF to provide estimates of ionospheric parameters for the initial 'quick-fit' analysis.

The process of fitting a theoretical function to the measured ACF to determine the plasma parameters will introduce an associated error since the theoretical curve will not exactly match the measured curve. This error is known as the fit error, and can be calculated from the sum of the residuals between the two functions. Further uncertainties arise from the assumption of a maxwellian thermal velocity distribution during the EISCAT analysis. This may not always be a suitable approximation, particularly in regions of high ion-neutral relative flow or in strong field-aligned current flow. These will lead to an overestimation of the ion temperature and an underestimation of the electron density [e.g. *Lockwood et al.*, 1993a; *Moorcroft and Schlegel*, 1988].

3.4 Summary

An overview of incoherent scatter theory has been presented, indicating that since the scattering of radio waves occurs from acoustic waves in the ionosphere for wavelengths greater than the Debye length, this technique can be readily used to determine the plasma properties of the sounding region. The development of incoherent scatter radar, in particular the European Incoherent Scatter facility (EISCAT) has been detailed, together with an in-depth discussion of the analysis technique and the derivation of the plasma parameters. Uncertainties associated with the analysis have also been discussed.

CHAPTER 4

Statistical analysis of ionospheric response delays

4.1 Introduction

In this chapter, solar wind and interplanetary field conditions measured by the IMP-8 spacecraft located upstream of the bow shock are combined with ionospheric velocity vectors measured by the EISCAT radar (see chapter 3), in order to examine the response delay of the ionospheric flow to changes in the north-south component of the IMF (B_z). Approximately 300 h of simultaneous IMF and ionospheric velocity data have been collated and analysed in a statistical cross-correlation study. The east-west and north-south components of the flow are separated into overlapping 2 h intervals of local time and each cross-correlated with a function of the IMF B_z, and the response delay determined from the peak in the cross-correlogram. However, as a necessary prerequisite to this analysis, the delay time between magnetic field observations recorded at the spacecraft and the arrival of these disturbances at the ionosphere must be carefully estimated. This estimation is described fully in the following section in a general manner, before being applied to the specific data sets used in the cross-correlation analysis. The IMF propagation delay is then removed from the data prior to cross-correlating this with the ionospheric velocity components. Details of the cross-correlation results will follow the analysis procedure.

4.2 IMF propagation delay

In order to accurately determine the response time of the ionospheric flow to changes in the direction of the IMF observed by a spacecraft upstream of the bow shock, a careful estimate must be made of the delay between an IMF feature being observed by the spacecraft and the arrival of the first possible effect at the ionosphere. This propagation delay consists of the sum of three components: (1) the time between the appearance of the feature at the spacecraft and its arrival at the subsolar bow shock, (2) the frozen-in transit time across the subsolar magnetosheath, and (3) the Alfvénic propagation time along open field lines from the subsolar magnetopause to the cusp ionosphere. The method used to determine each of these contributions will now be discussed.

4.2.1 Transit time between the spacecraft and subsolar bow shock

For a spacecraft located on the Earth-Sun line, the transit time of field changes between the spacecraft and the subsolar bow shock is simply determined from the distance to the bow shock (determined from empirical models as described below) divided by the observed solar wind speed. However, in general the spacecraft will be located at some distance from the Earth-Sun line, and we then require to know where corresponding field changes are located on the Earth-Sun line at the same time as they are observed by the spacecraft. In other words the orientation of the "phase fronts" in the IMF need to be determined, or assumed, so that the intersection with the Earth-Sun line of the phase front which passes through the satellite can be determined. The IMF data corresponding to each interval of radar data was examined, and the orientation of the plane of the sharp field changes which were observed was determined, assuming that these changes represent tangential discontinuities propagating in the solar wind. Typically the field vectors were averaged over 10-15 min intervals on either side of the discontinuity, and their cross-product taken to determine the discontinuity normal. Usually, several (2 to 6) such determinations could be made for each 2-hour interval, and in these cases the orientations of the discontinuities were generally found to be mutually consistent. These were then used to determine an overall representative delay time for the interval according to the algorithm described below. In a few cases, however, no sharp field changes occurred in the interval in question, and in these cases it was assumed that the phase fronts were aligned perpendicular to the Earth-Sun line.

4.2.2 Estimation of the subsolar magnetosheath transit time from the bow shock to the magnetopause

When the solar wind encounters the subsolar bow shock its speed is suddenly reduced by a factor of ~4 for large upstream magnetosonic Mach numbers. According to gas-dynamic models the speed then continues to fall as the plasma traverses the magnetosheath and reaches the magnetopause. Accurate estimation of the overall propagation time requires that these effects be taken into account. In order to do this the geocentric distances of the magnetopause and bow shock need to be known, and the variation of the plasma speed between them. *Roelof and Sibeck* [1993] have provided a comprehensive empirical model of the position of the magnetopause, in which the boundary is modelled as an ellipsoid of revolution about the aberrated X axis whose form depends on both IMF B_z

and the solar wind dynamic pressure p. For purposes of our study, one representative delay time that can be applied to few-hour segments of interplanetary data needs to be calculated. Since IMF B_z typically varies significantly about a near-zero mean on such time scales, the *Roelof and Sibeck* [1993] model subsolar magnetopause position is employed for IMF $B_z \approx 0$ nT which is valid for a typical dynamic pressure of 2 nPa (a value of ~10.8 R_E), and then scale this value according to the usual one sixth power law of p. The parameterisation of the subsolar magnetopause position R_{MP} thus employed is

$$R_{MP} = \frac{12.1}{p(\mathrm{nPa})^{1/6}} = \frac{111}{[n(\mathrm{cm}^{-3})V^2(\mathrm{km\,s}^{-1})]^{1/6}} \mathrm{R_E}\,. \tag{4.1}$$

This formula is in good overall accord with the *Roelof and Sibeck* [1993] model for $|B_z|$ not too large, and is also in reasonable agreement with the model results of *Petrinec and Russell* [1993].

Using this value, the distance to the subsolar bow shock can then be determined, using the results of the empirical study by *Peredo et al.* [1995]. From a comprehensive analysis of observed shock locations these authors found that the subsolar shock is typically located at a distance which is larger than that of the subsolar magnetopause by a factor of 1.46. Thus the subsolar shock location can be parameterised as

$$R_{BS} = \frac{17.6}{[p(\mathrm{nPa})]^{1/6}} = \frac{162}{[n(\mathrm{cm}^{-3})V^2(\mathrm{km\,s}^{-1})]^{1/6}} \mathrm{R_E}\,. \tag{4.2}$$

Next a model of the flow speed between the subsolar shock and magnetopause is required, and a simple linear variation from a value of V_{BS} just downstream from the shock and V_{MP} at the magnetopause is taken. Integration of (ds/V) between R_{BS} and R_{MP} then yields the frozen-in propagation time across the subsolar magnetosheath as

$$\tau_{sh} = \frac{(R_{BS} - R_{MP})}{V_{BS} - V_{MP}} \ln\left(\frac{V_{BS}}{V_{MP}}\right) = \frac{0.46 R_{MP}}{V_{BS} - V_{MP}} \ln\frac{V_{BS}}{V_{MP}}\,. \tag{4.3}$$

Finally values for V_{BS} and V_{MP} are required. The usual shock jump conditions determine V_{BS} in terms of the upstream speed V_{SW} as

$$\frac{V_{BS}}{V_{SW}} = \frac{(\gamma-1)M^2+2}{(\gamma+1)M^2}\,, \tag{4.4}$$

where M is the magnetosonic Mach number and γ=5/3. Substituting an average value of M = 5.3 [*Peredo et al.*, 1995] into Eq. (4.4) gives $(V_{BS}/V_{SW}) \approx 0.28$, and this is the value for V_{BS} which is adopted here. The reconnection-associated velocity of inflow at the magnetopause, V_{MP}, must be taken to be a finite value to avoid the logarithmic singularity in Eq. (4.3), and so a nominal value of 20 km s^{-1} is assumed. Taken together with reasonable values for the magnetosheath field at the magnetopause of a few tens of nT, and reasonable lengths for the reconnection line of several R_E, this value implies reasonable reconnection-driven convection voltages of several tens of kV. However, the results are not sensitive to the exact choice. Substituting these values into Eq. (4.3) finally yields

$$\tau_{sh} = \frac{1.66 R_{MP}}{(V_{SW} - 72)} \ln\left(\frac{V_{SW}}{72}\right) , \qquad (4.5)$$

where V_{SW} is in km s^{-1}, and R_{MP} is in km, determined from Eq. (4.1) with R_E=6375 km. Thus τ_{sh} is determined directly in terms of the density and velocity of the upstream solar wind plasma.

It is important to note that if Eq. (4.5) is interpreted as the magnetosheath thickness of $0.46R_{MP}$ divided by an "average" magnetosheath speed $\langle V_{sh} \rangle$, then for typical values of V_{SW} ~ 500 km s^{-1} we find $\langle V_{sh} \rangle \approx (V_{SW}/8)$. This formula (Eq. 4.5) therefore produces a final value which is very similar to that obtained by simply dividing the subsolar magnetosheath thickness by an average magnetosheath speed which assumes a jump by a factor of 4 at the shock and a linear decrease to zero at the magnetopause, as employed in previous studies [e.g. *Lester et al.*, 1993].

4.2.3 Alfvénic propagation from the magnetopause to the cusp ionosphere

Once reconnection occurs at the dayside magnetopause, its effects on the flow are transmitted along the newly-opened field lines by an Alfvén wave. The transit time from the subsolar magnetopause to the ionosphere can then be determined as approximately one quarter of the period of fundamental mode eigenoscillations of the outer dayside field lines. Since these periods are typically found to lie in the range 5-10 min [e.g. *Poulter et al.*, 1984], the magnetopause-to-ionosphere transit time is taken to be 2 min.

4.3 Instrumentation and data sets

4.3.1 The EISCAT CP-1-K experiment

The ionospheric flow measurements employed in this study were obtained by the tristatic EISCAT UHF incoherent scatter radar system using the CP-1-K common programme experiment, which has been run typically on several days each year since 1993. Details of the EISCAT radar system have been discussed in the previous chapter, together with details of this experiment (see §3.3.3). The radar configuration during this experiment allows continuous tristatic measurement of the plasma flow at a single point essentially overhead at Tromsø. The data are integrated over 2 min intervals, which sets the limit on the time resolution of this study.

Figure 4.1 shows electric potential patterns for various IMF conditions obtained by fitting electric field measurements from the Dynamics Explorer 2 satellite to a spherical harmonic expansion [*Weimer*, 1995]. The figure shows representative results where the IMF has been divided into eight 45° sectors in the GSM Y-Z plane, in the case where the strength of the field in this plane (B_T) lay between 3.5 and 5.2 nT. The CP-1-K tristatic observing point corresponds to a magnetic latitude of 66.3°, indicated by the dotted circle on the flow maps. This is a somewhat lower latitude than those (~71°-73°) investigated in the previous studies by *Todd et al.* [1988] and *Etemadi et al.* [1988], which used beam-swung EISCAT data from the poleward-pointing 'Polar' experiment. Comparison with these flow maps shows that on the dayside 66.3° typically lies equatorward of the flow cells for northward IMF, but just within their equatorward border for southward IMF. On the nightside the EISCAT latitude lies on average in the equatorward border of the flow cells for northward IMF, and well within the cells on closed field lines for southward IMF. Thus the response of the flow to north-south changes in the IMF should be observable in these data at all local times. The response time of the flow expected on the basis of previous results reviewed in Chapter 2 varies considerably between the prompt, few minute, responses observed on the dayside by *Etemadi et al.* [1988], *Todd et al.* [1988], and *Ruohoniemi et al.* [1993], and the more extended intervals of 20-30 min which are probably more characteristic of reconfigurations of the flow pattern as a whole reported by *Hairston and Heelis* [1995]. Furthermore, *Ridley et al.* [1998] and *Ruohoniemi and Greenwald* [1998] have reported responses of the nightside flow that are essentially simultaneous with the dayside flow, within 1-2 min or less, while other observations cited

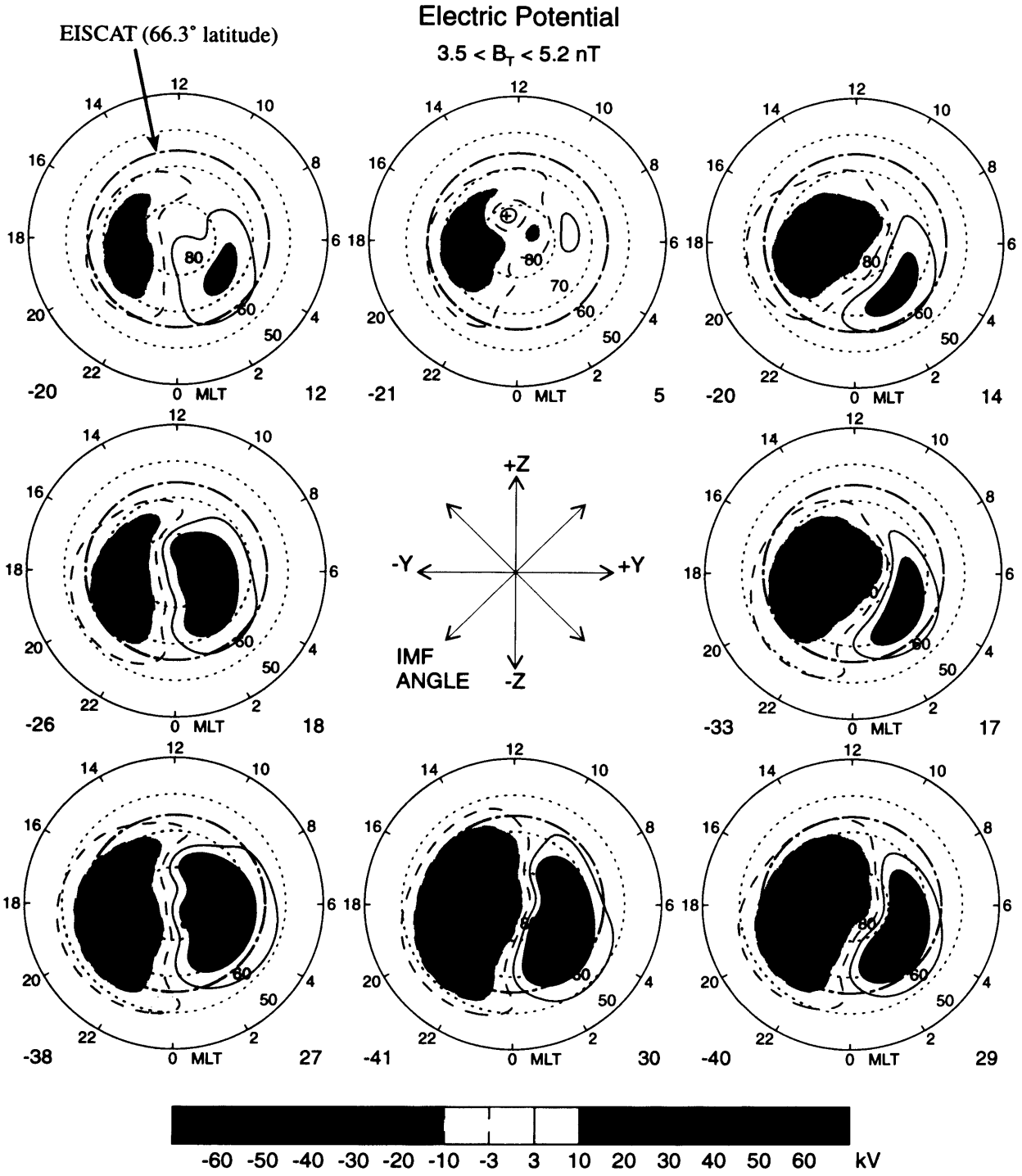

FIGURE 4.1 Ionospheric potential contour plots (plasma streamlines) for eight 45° intervals of the IMF vector in the GSM Y-Z plane, and where the total field strength in this plane (B_T) lies between 3.5 and 5.2 nT. Positive and negative potentials are indicated by solid and dashed lines, respectively. The EISCAT radar location at 66.3° magnetic latitude is marked by the dotted-dashed circle. [After *Weimer*, 1995]

above suggest a slower propagation. If, for example, flow changes propagate away from the open-closed field line boundary at noon at phase speeds e.g. of ~5-10 km s^{-1} [e.g. *Saunders et al.*, 1992; *Lockwood et al.*, 1993b], the resulting delay at EISCAT should vary between ~2-4 min at noon and ~7-14 min at midnight. The 2-min averaged flow data employed here should thus be capable of distinguishing between these possibilities and of resolving day-night differences of this order, though only just so for phase speeds at the top end of the range considered likely.

4.3.2 IMP-8 interplanetary data

For the purposes of this study the EISCAT radar data have been combined with observations of the IMF made upstream of the bow shock by the IMP-8 (Interplanetary Monitoring Platform) spacecraft. This spacecraft, launched by NASA in 1973, moves in a near-circular 35 R_E radius orbit, spending ~8 days out of a 12 day cycle in the solar wind. In recent years, however, the solar wind residence times of the spacecraft have deteriorated by approximately 40%, decreasing the amount of solar wind data returned. The instruments provide IMF vector data at 15 s resolution and solar wind plasma parameters with a resolution between 60 and 300 s.

Since the flow response delays which we wish to measure lie typically in the range ~5-20 min, as just indicated, it is crucial to make a careful estimate of the propagation delay between fields observed at the spacecraft and the arrival of their first effects in the dayside ionosphere, as previously discussed. In preparation for the cross-correlation analysis, the IMF data was separated into 2 h intervals of local time in concert with the radar data, for which a representative propagation delay time was required. The method employed was that outlined in §4.2, but now with specific attention to the individual IMF data set for a particular local time interval. To obtain this delay the corresponding IMF data was scanned for sharp field changes to determine the orientation of the phase fronts in the field, as described in §4.2. Using each orientation so determined, the total delay time as a function of UT over the 2-hour interval was calculated, using the measured solar wind density and velocity values to determine the subsolar shock position according to Eq. (4.2) and the magnetosheath transit time from Eqs. (4.1) and (4.5). The 'delay' time series was then averaged over the whole interval to provide a single averaged delay time determined from that phase front orientation (typically the variation of the delay time over such intervals is ~1 min or less). This procedure was then repeated for each phase front orientation determined during the interval (typically 2-6), yielding a set of averaged delay

times. Normally these proved to be mutually consistent within 1-2 min. A representative delay time value was then chosen for the interval, and 2 min averaged IMF vectors were derived from the 15 s values, corresponding to the 2 min averaged radar values with the representative propagation delay removed. These averaged IMF values were then used for the cross-correlation analysis.

However, these propagation delay times will have an uncertainty associated with them, which can be estimated by investigating the random and systematic errors present in the analysis. The first source of uncertainty arises from the determinations of the IMF "phase front" orientations in the interplanetary medium, together with the variations of this orientation and of the speed of the solar wind over the ~2 h intervals employed in this study. As indicated above, changes in the solar wind speed over such intervals typically produce variations in the estimated propagation delay of ~1 min or less for a fixed "phase front" orientation, and analysis of several "phase fronts" in a particular interval generally provide consistent results within ~1-2 min. These uncertainties thus contribute to a random error in the propagation delay values which are thus estimated to be about ±1 min. The second source of uncertainty lies in the modelled positions of the bow shock and magnetopause, and more particularly the distance between them, and in the magnetosheath flow model employed. As indicated above, the models of the bow shock and magnetopause positions employed here are based on the results of recent statistical studies incorporating large numbers of positional observations, while the model of the subsolar magnetosheath flow is based on shock jump conditions and the results of gas-dynamic models. It therefore seems that large systematic uncertainties are unlikely. Typically, the thickness of the subsolar magnetosheath determined from these models is 4-5 R_E, and judging from the scatter in the positional data in the statistical studies cited above, the uncertainty in this value is probably around 10%, i.e. about ±0.5 R_E. Equation (4.3) then yields a likely random error in the magnetosheath propagation delay of less than ±1 min. The systematic error seems unlikely to be larger than this. The third source of potential error arises from the Alfvénic propagation of information from the magnetopause to the cusp ionosphere, taken to be 2 min on the basis of the measured periods of ULF waves on outer dayside field lines. Based also on the variability of the latter, the random and systematic error of this propagation time is estimated as ±1 min. Taken together, therefore, and recognising the uncorrelated nature of the separate contributions to the uncertainties involved, the random error in the calculated propagation delays is estimated to be about

±2 min (in a total which lies typically in the range 5-15 min), while the systematic error is likely to be comparable with this or smaller.

Using these procedures therefore, an IMF delay time representative of 2-hour intervals of radar data has been determined. Typical values lie in the range 5-15 min, with an estimated random uncertainty of about ±2 min and an estimated systematic uncertainty which is of the same order or less.

4.4 Cross-correlation analysis

4.4.1 Cross-correlation procedure and IMF correlator

The database of EISCAT CP-1-K flow data and IMP-8 solar wind/IMF data employed in this study, obtained during the interval 1993-97, total about 300 simultaneous hours. The data span all local times, though the hemisphere centred on dusk is favoured relative to the hemisphere centred on dawn. Typically ~8 experiment-days contribute data in each local time interval in the dawn hemisphere, compared with ~13 experiment-days in the dusk hemisphere. In order to determine the ionospheric response delays in a statistical cross-correlation analysis, the 2 min-averaged EISCAT velocity data is combined with concurrent and similarly-averaged IMP-8 interplanetary data from which the propagation delay to the cusp ionosphere has been removed, as described in above. The radar data were divided into overlapping 2-hour intervals of MLT (MLT≈UT+2.5 h), and cross-correlations performed on both eastward and northward flow components separately. The interplanetary parameter chosen for this analysis was the 'half-wave rectifier' function V^2B_s, where V is the solar wind speed, and $B_s = B_z$ when the latter is negative, while $B_s = 0$ when B_z is positive. Other IMF B_z parameters, such as B_z, B_s, V^2B_z, were also tested to identify which IMF parameter produced the highest cross-correlation coefficients. Figure 4.2 illustrates the results from this test conducted on the 2 h local time interval 1100 to 1300 MLT, with cross-correlograms for each velocity component shown separately and the four IMF parameters presented as the colour-coded lines on each plot. In common with the results of the previous cross-correlation study by *Etemadi et al.* [1988], the results shown here indicate that the V^2B_s parameter produces correlation coefficients which are generally as high or higher than other simple related interplanetary parameters, although all show reasonable correlations. In particular it produces higher correlations than related functions that use B_z directly, reflecting the fact that at the latitude of Tromsø the flow is

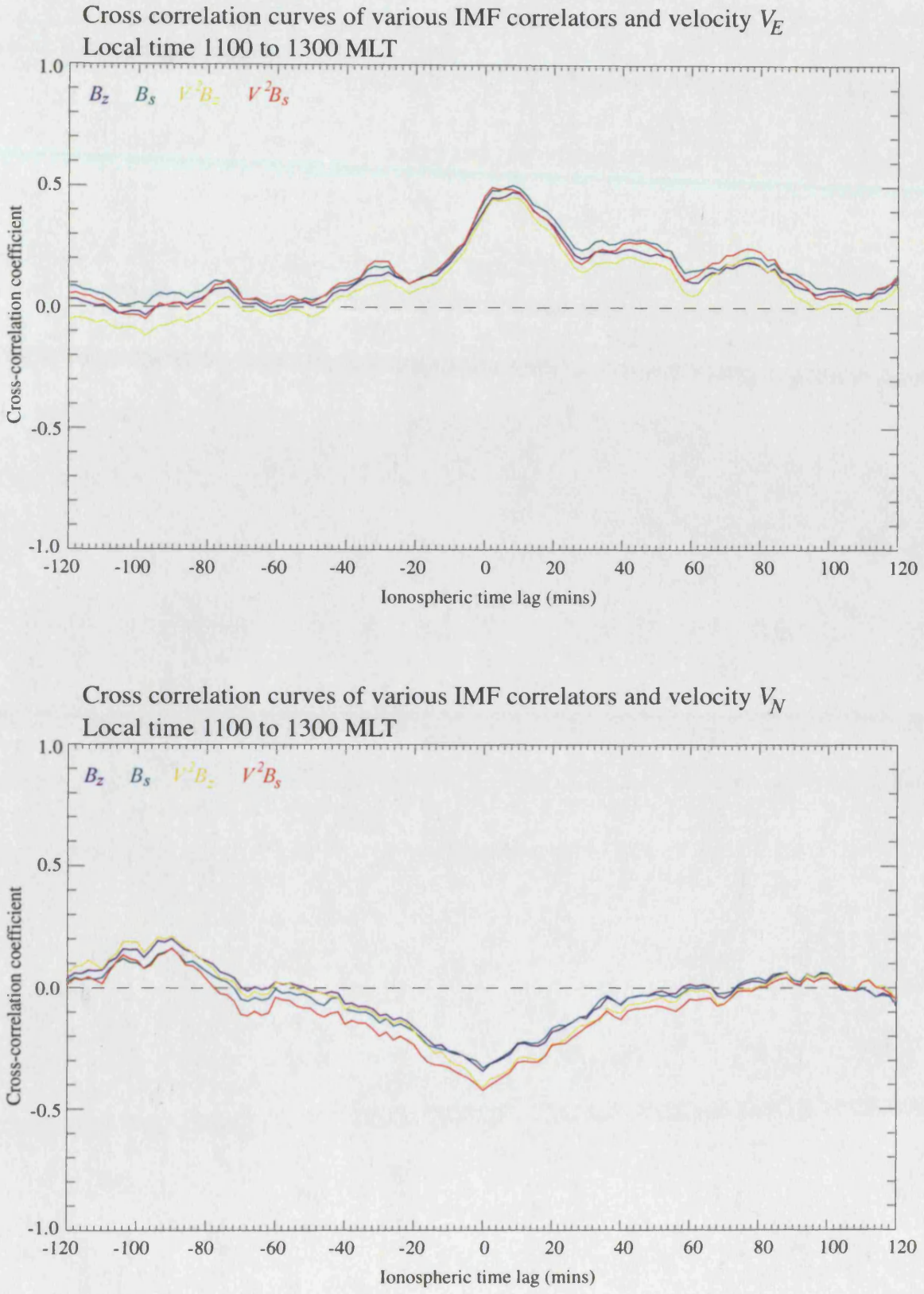

FIGURE 4.2 Cross correlogram illustrating the different IMF correlators tested to identify which function of the IMF produced the greatest cross-correlation coefficients. The IMF parameters tested were B_z , B_s , V^2B_z , and V^2B_s, shown as the colour-coded lines as indicated by the key at the top of the plots. The upper panel presents the results from the eastward velocity, and the lower panel shows the results from the northward velocity. Both plots indicate higher cross correlation values using V^2B_s , together with a sharper peak in the data.

unresponsive to the IMF (and is generally small) when B_z is positive, but grows in magnitude when B_z is negative, as we will demonstrate in the results presented below.

For each 2-h MLT interval of radar data the cross-correlation coefficients of v_E and v_N with V^2B_s were calculated versus time lag over an interval of ±120 min, with a resolution of 2 min (the resolution of the data sets). For positive lags the interplanetary medium leads the ionosphere, while for negative lags the ionosphere (unphysically) leads the interplanetary medium. Before presenting the results, however, it is appropriate to comment on the interpretation of the resulting cross-correlograms, particularly since it seems clear that the high-latitude flow varies in response to the IMF on more than one time scale.

4.4.2 Cross correlograms generated using model flow data

As reviewed in Chapter 2, it is apparent that the high-latitude ionospheric flow responds to the changes in the IMF on two distinct time scales. The first time scale is the delay time of the excitation and decay of the flow in response to north-south changes in the IMF, whose nature is demonstrated in the previous studies presented in Chapter 2 e.g. by *Todd et al.* [1988]. All previous evidence indicates that the delay times involved in this process are of order a few minutes relative to the arrival of first effects, certainly in the dayside ionosphere. The second relates to changes in the local flow which are due to overall expansions or contractions in the flow pattern as the amount of open flux in the system changes. Such changes take place on a significantly longer time scale. For example, unbalanced dayside reconnection at rate of 100 kWb s^{-1} (corresponding to a transpolar voltage of 100 kV) will result in a uniform equatorward expansion of the open-closed field line boundary at a speed of ~200 m s^{-1}. The time scale required for a given point in the ionosphere to move significantly relative to the flow pattern, corresponding to a boundary motion of a few degrees of latitude, for example, is then of order several tens of minutes (about ten minutes per degree). Therefore one can envisage that as the IMF switches between north and south polarities the ionospheric flow will be similarly modulated with the above short delay time scale, whilst also undergoing variations on the longer time scale during each southward-directed IMF interval.

An important question to ask is at what delay time will the peak in the cross-correlation coefficient occur? The answer to this question depends upon the nature of the flow variation which is produced by the variation in the size of the flow cells on the longer

time scales. If the change in the flow component relative to the (usually small) positive IMF B_z background has a consistent sense (e.g. a consistently westward or eastward flow) whose absolute magnitude may be modulated by the size of the flow cells, then it is easy to show that an extremum in the cross-correlation coefficient will occur at the lag corresponding to the flow excitation and decay delay time, irrespective of the nature of the long time scale modulation. This can be seen from the fact that a maximum 'overlap' will invariably occur between the enhanced flow component and the IMF input function at this lag, such that a small shift in lag in either direction will reduce the 'overlap' and hence the cross-correlation coefficient. Figure 4.1 shows that this situation will prevail at EISCAT latitudes in most local time sectors, since the radar will usually be located in the equatorward region of the flow cells where the flows will generally be consistently westward in the dusk cell and consistently eastward in the dawn cell. However, there is one local time sector where this general conclusion does not apply, namely the pre-midnight Harang region. Careful examination of Figure 4.1 shows that in this region the flows will generally be westward for positive and small IMF B_z, while reversing to eastward for significantly negative IMF B_z. Typically then, if the direction of the IMF reverses from north to south, it can be expected that the initial flow excitation will be in the westward direction, reversing later to eastward on a time scale (a few tens of minutes) which may be dependent on the strength of the southward field. In this case consideration of the 'overlap' between the flow component and the interplanetary input shows that a peak in the cross-correlation coefficient need not occur at the lag corresponding to the flow excitation and decay delay time as above, but may occur at a later time characteristic of the reversal in the sense of the flow relative to the positive IMF B_z 'background' value.

These qualitative conclusions are illustrated quantitatively in Figures 4.3 and 4.4. Synthetic data sets consisting of 1000 simultaneous "IMF B_s" and "ionospheric velocity" data points have been constructed, corresponding to 33.3 h of the 2-min averaged data employed here. A random number generator has then been used to select the times of N_{IMF} switches in the value of "IMF B_s", between zero, corresponding to northward IMF, and -1 nT, corresponding to southward IMF, or vice versa. A typical example is shown in the upper panel of Figure 4.3, where N_{IMF}=75, such that the average time between "IMF" switches is ~26 min, corresponding to ~13 data points. Two synthetic "velocity" data sets are shown beneath. In the middle panel the velocity is taken to be a random number between 0 and -300 m s^{-1} whenever "IMF B_s" is negative, and to be zero when "IMF B_s" is

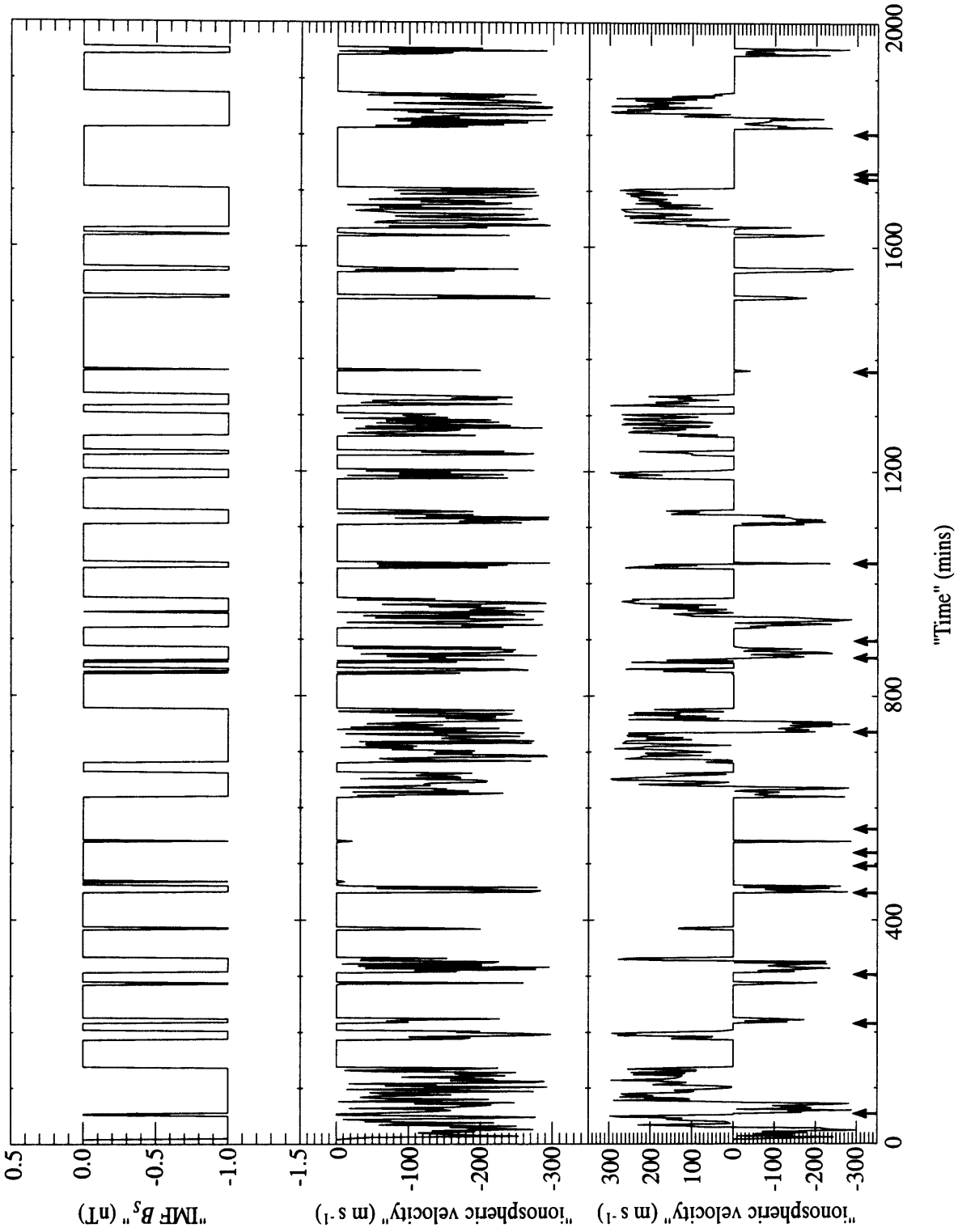

FIGURE 4.3 Synthetic data sets of 1000 2-min "IMF B_s" values (upper panel) and simultaneous "ionospheric velocity" components determined from two different algorithms (lower two panels), as described in the text. In the upper panel, "IMF B_s" varies between zero and –1 nT at 75 randomly-chosen times. In the middle panel the "velocity" is switched "on" and "off" in concert with "IMF B_s", with a randomly-chosen negative value between 0 and –300 m s^{-1} when "IMF B_s" is –1 nT, and zero when "IMF B_s" is zero. In the lower panel the "velocity" is switched "on" and "off" by "IMF B_s" in just the same way, but with the flow initially negative for 10 successive "on" points (i.e. for 20 min), and then switches to positive for all "on" points thereafter until a "substorm" takes place, after which the flow reverts to negative for 10 successive "on" points, etc. Fifteen "substorms" are taken to occur during the interval, at randomly-determined times shown by the arrows in the lower panel.

zero. This corresponds to the excitation of a flow of variable magnitude, but consistent sense, in concert with a southward IMF. The cross-correlation function between these data sets is shown in the upper panel of Figure 4.4, computed every two minutes over a range of lags of ±120 min, with positive lags indicating that the "IMF" leads the "velocity", as indicated above. A single clear peak is obtained at zero lag, as anticipated in the discussion above. The same result is obtained for all the synthetic data sets of this nature which we have generated, having different random variations in the times of the IMF changes and in the velocity, and for various values of N_{IMF} (between 50 and 100), as must be the case. In the synthetic "velocity" data shown in the bottom panel of Figure 4.3, however, the flow is switched "on" and "off" in concert with the "IMF" function just as before, but now the flow may take positive or negative values. Specifically, the flow is taken to be negative (at a random value between 0 and -300 m s^{-1}) for 10 successive "flow on" data points (i.e. 20 min of flow), after which it becomes positive (at a random value between 0 and +300 m s^{-1}) for all subsequent "flow on" data points, until such time as a "substorm" takes place. After this time the flow reverts to negative for 10 successive points, followed by positive again until the next "substorm", etc. The times of N_S "substorms" are again chosen randomly, and are indicated in the lower panel of Figure 4.3 by the arrows, where N_S=15 for the data set displayed (i.e. an average time of ~2 h between "substorms"). This algorithm is intended in the simplest possible way to simulate conditions in the Harang region, where the flow direction may change from west to east after a few tens of minutes of southward IMF due to polar cap expansion (specifically 20 min in our algorithm), followed by the reappearance of westward flow when the polar cap subsequently contracts after a substorm. The cross-correlogram for this data set is shown in the lower panel of Figure 4.4. Here the cross-correlation values are lower than before, and peak at a lag of 20 min, corresponding to the time scale of the switch in the sense of the flow. While such results are typical, it was found that other randomly-chosen data sets having the same basic parameters (i.e. the same N_{IMF} and N_S values) can produce peaks at various lags between ~0 and ~20 min.

Therefore, when examining the cross-correlation results, attention must be paid to the nature of the flow response to IMF B_z. If the flow response is in a consistent sense relative to the IMF B_z positive "background" value (taken to be zero in the above synthetic data sets), then it is reasonable to interpret the time lag of the peak correlation as the flow excitation and decay response delay. However, if the flow is found to reverse in sense with

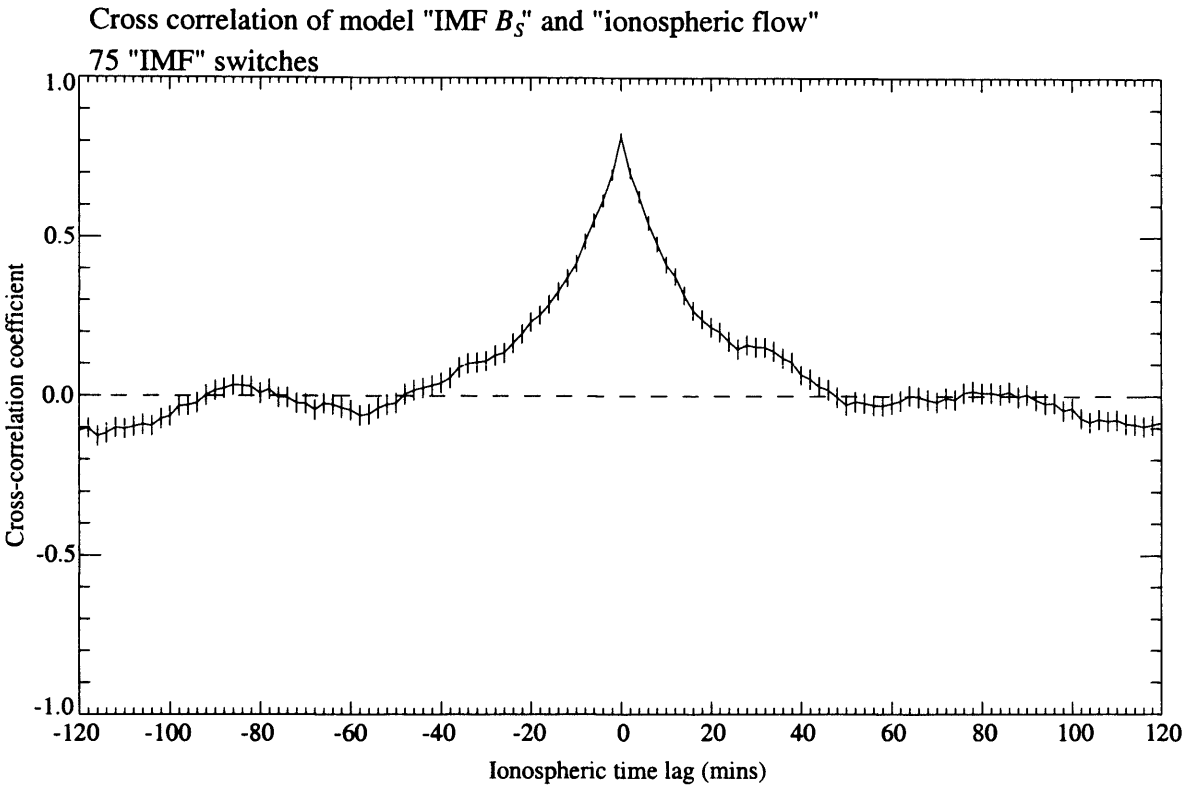

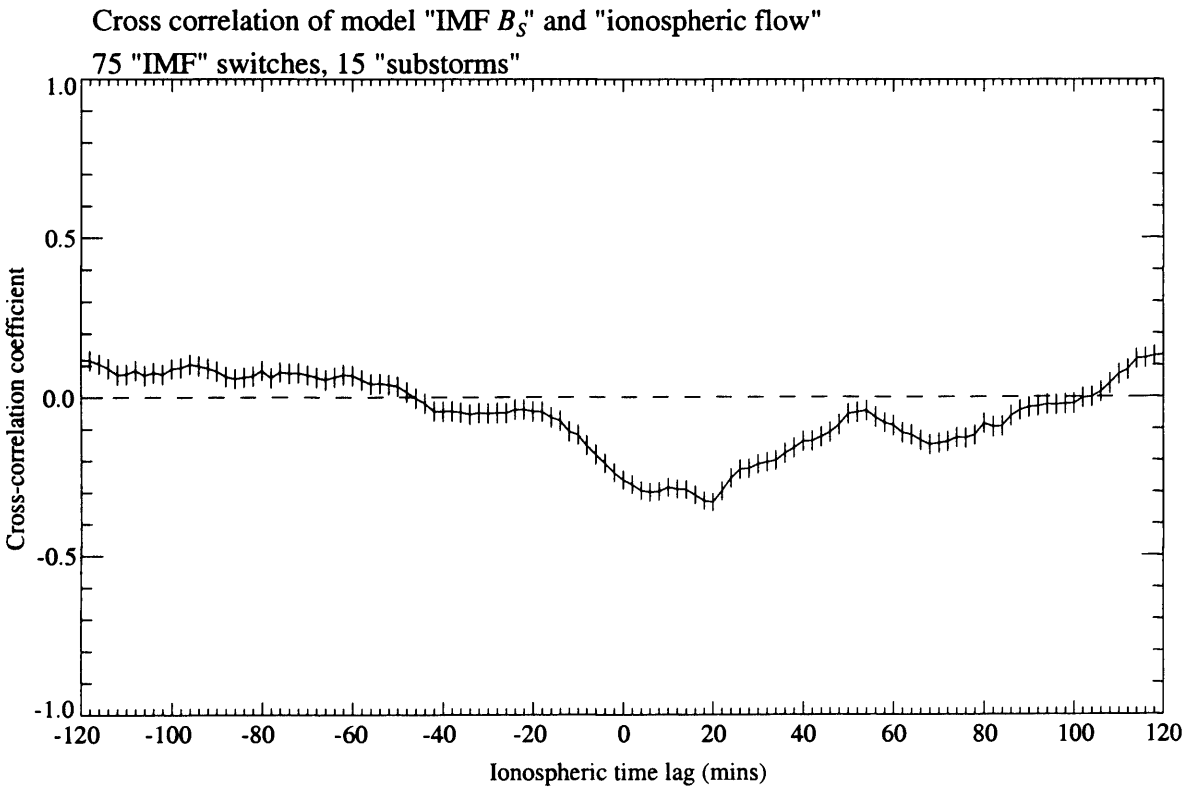

FIGURE 4.4 Cross-correlograms corresponding to the two synthetic "IMF"-"ionospheric velocity" data sets shown in Figure 4.3. The upper panel corresponds to the "velocity" data shown in the middle panel of Figure 4.3, while the lower panel corresponds to the "velocity" data shown in the lower panel of the figure.

changing IMF B_z, relative to the B_z positive "background", then the lag of the peak correlation need not correspond to the flow excitation and decay delay of primary interest here, but may occur at longer delays characteristic of the flow reversal (pattern expansion) time scale. Furthermore one can anticipate that, on the basis of Figure 4.1, such an effect is most likely to occur in the pre-midnight Harang region, where flows typically reverse from west to east as IMF B_z switches from positive to negative. This effect needs to be borne in mind when considering the results presented below.

4.4.3 Results from cross-correlation analysis: dayside response delay

With all the velocity and IMF data organised in the fashion described in the previous sections, the cross-correlation analysis can be performed on each overlapping 2 h interval of local time, to determine the response delay for that local time. Figures 4.5 to 4.10 present representative results for various 2 h MLT intervals, where all the flow data available for the interval have been combined together to produce the results shown. In each panel results for v_E are shown on the left, while those for v_N are shown on the right. The upper graphs in each panel show the cross correlation coefficient versus lag. The error bars show the standard error of the coefficient, given by $\varepsilon = (1-r^2)/(n-2)^{1/2}$, where r is the value of the cross-correlation coefficient and n is the number of data values from which it was determined. This formula is valid when n is large (n>100, say), a condition well satisfied here where the number of 2 min data values in a given 2 h MLT interval varies from a minimum of about 200 to a maximum of about 700 (see Figure 4.11). The 99.9% significance level derived from Student's t-test is also shown by the dot-dash lines; cross-correlation coefficients with magnitudes smaller than this are not considered statistically significant. The lower graphs in each panel then show scatter plots of the respective velocity components versus V^2B_z, derived using the lag corresponding to the peak in the cross-correlation curve as indicated at the top of each plot. The interplanetary parameter plotted is not V^2B_z directly, but $(V(\text{km s}^{-1})/500)^2B_z$, in units of nT. That is, the solar wind speed V has been normalised to a nominal value of 500 km s^{-1} so that the variation of the ionospheric flow with typical IMF B_z values can more easily be appreciated. The solid lines in these plots represent the least-squares best fit to the half-wave rectified interplanetary function (i.e. a linear variation for IMF B_z negative, and a constant value for IMF B_z positive).

Figure 4.5 shows results for the 2 h interval centred on noon (1100-1300 MLT), containing 608 flow measurements. The cross-correlogram for v_E shows a highly significant maximum near zero lag, with a peak coefficient of 0.50 at a lag of 2 min. The uncertainty in the determination of the lag at the peak is quantified from the error bar on the peak value by examining how many adjacent cross-correlation values lie within its limits. In this case four values lie within these limits at longer lags, and none at shorter lags. Thus the "error bar" on the lag of the peak is taken to lie between 2 and 10 min. Secondary and even tertiary peaks are also evident in the cross-correlogram, on both sides of the main peak. Analysis indicates, however, that these are due to auto-correlation in the input interplanetary data at the corresponding periods, and are not due to secondary or tertiary response times in the ionospheric flow. The positive value of the cross-correlation coefficient at the peak implies the existence of westward ionospheric flow (i.e. negative v_E) when IMF B_z is negative. This is confirmed by the scatter-plot shown beneath the cross-correlogram plotted for a lag of 2 min, which exhibits weak averaged westward flows for IMF B_z positive (with no particular trend evident in the data) and increasing westward flows for IMF B_z negative. Since the scatter-plot shows that the enhanced flows present for IMF B_z negative are essentially consistently westward, becoming generally stronger as IMF B_z becomes increasingly negative, it is appropriate according to the above argument to interpret the lag time of the peak correlation as the flow excitation and decay delay time. This conclusion is also consistent with the small lag value (2 min) obtained. That the east-west flow in the noon sector is consistently westward at EISCAT latitudes agrees with the results of *Weimer* [1995] shown in Figure 4.1, where we see that the dusk cell generally extends across noon to give westward flow at noon at lower latitudes. A similar positive correlation and mainly westward flow is also found here in the MLT interval centred on 1100 MLT (not shown), reversing to a negative correlation associated with the eastward flow of the dawn cell at 0800 and earlier MLT (see below). No statistically significant correlation with v_E is found for the intervals centred on 0900 and 1000 MLT.

The right side of Figure 4.5 shows results for v_N in the noon sector. The correlogram shows a clear negative minimum peaking at zero lag (with an "error bar" between -2 and +2 min), with a peak cross-correlation coefficient of -0.42. The negative value implies increasing northward flows (positive v_N) for negative IMF B_z, as confirmed by the scatter plot underneath. Similar negative v_N correlations with relatively short response delays, which may be interpreted as the flow excitation and decay delay time, are found in the

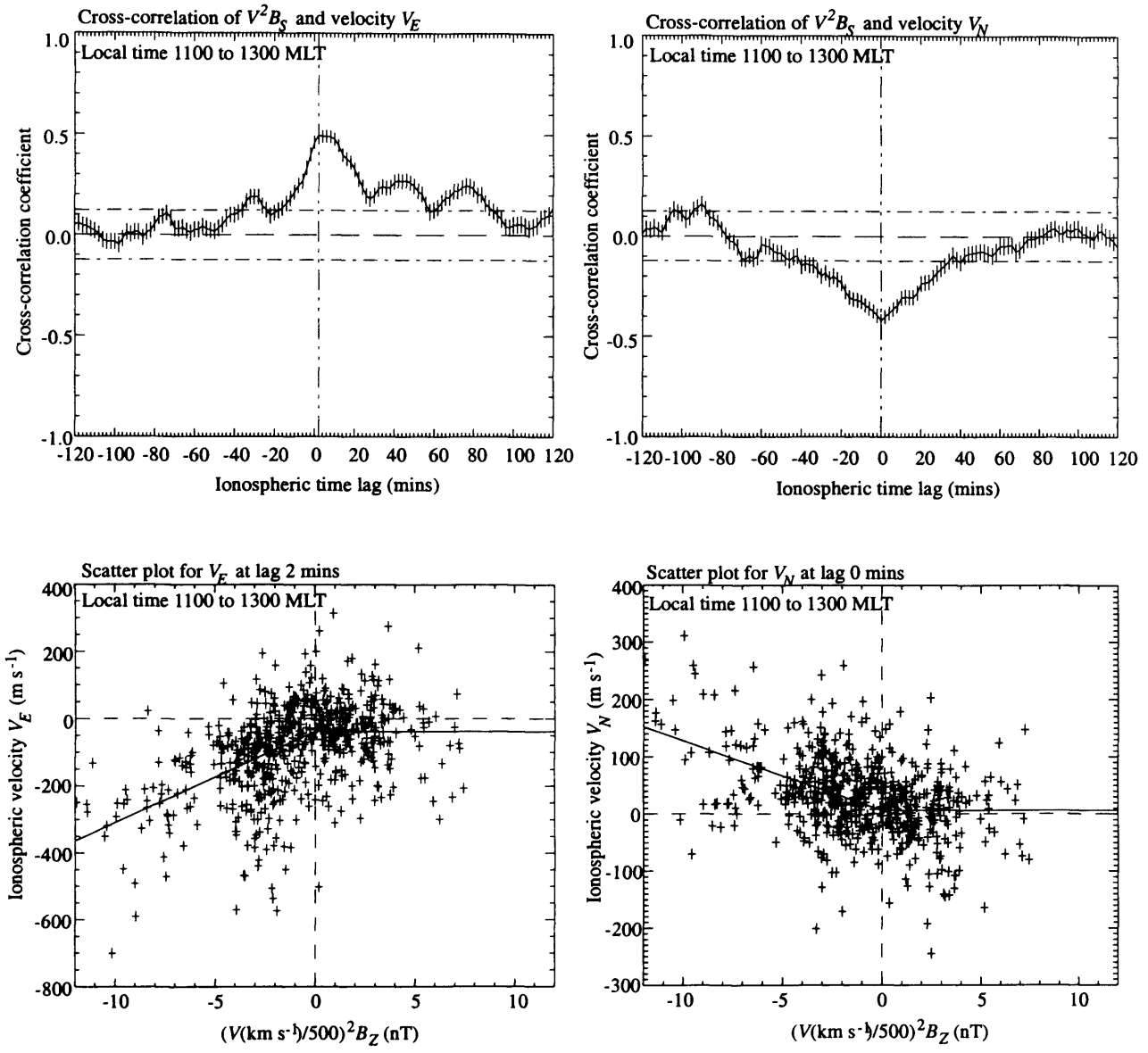

FIGURE 4.5 Results of the cross correlation analysis between V^2B_s and the eastward (left hand) and northward (right hand) flow components for the 2-h interval of local time centred on 1200 MLT. The upper panels show the value of the cross-correlation coefficient versus lag in the interval ±120 min at 2 min resolution, with positive lags representing the physical scenario in which the interplanetary medium leads the ionosphere. The nearly horizontal dot-dashed lines show the 99.9% significance level calculated by the Student's *t*-test. The vertical dot-dashed line marks the peak in the cross-correlogram. The lower panels provide a corresponding scatter plot of the flow component versus $(V(\text{km s}^{-1})/500)^2B_z$ in nT, plotted at the lag of the peak correlation coefficient shown in the plot above. A linear least-squares fit of the ionospheric velocity data to the function V^2B_s is indicated by the solid lines

dayside hours over the interval 0700-1300 MLT, thus spanning the interval ~3 h on either side of the east-west flow reversal at 0900-1000 MLT.

On moving away from noon into the afternoon sector, clear correlations remain with the westward component of the dusk cell flow, while the response of the northward component tends to disappear. Results for the 2 h interval centred on 1500 MLT are shown in Figure 4.6 (containing 708 flow measurements), representative of the interval 1300-1700 MLT. The cross-correlogram for v_E shows a positive maximum (westward flow for negative IMF B_z) at a lag of 4 min (with "error bars" between 0 and 10 min), with a peak value of 0.54. Again, two nearly symmetrical secondary peaks are also present, due to autocorrelation of the interplanetary input. The corresponding scatter plot shows a flow that is now almost exclusively westward, which increases rapidly as IMF B_z becomes more negative. Again, therefore, the lag time of the peak correlation can be interpreted as the excitation and decay delay time of the flow. The correlogram for v_N on the right of Figure 4.6, however, shows no clear peak and no values above the 99.9% significance level. In this case the scatter plot is shown for the 4 min lag determined from v_E, and indicates an essentially zero averaged latitudinal flow in this local time sector, independent of IMF B_z. The averaged flow is thus almost purely westward in this local time sector.

Figure 4.7 shows related results for the dayside dawn cell, for the 2 h interval centred on 0700 MLT (containing 423 flow measurements). These are representative of the results obtained in the interval 0500-0900 MLT, not previously covered in the study by *Etemadi et al.* [1988]. The correlogram for v_E now shows a negative minimum at a lag of 8 min (with an "error bar" between 0 and 8 min), with a peak cross-correlation coefficient of -0.44. The scatter plot confirms that this correlation is related to an increasing eastward flow for IMF B_z negative, with essentially zero averaged flow when IMF B_z is positive. Again, the monotonic dependence of the flow component on IMF B_z indicates that the lag of the peak correlation should be interpreted as the flow excitation and decay delay time. Similar results are obtained for v_N, with a negative peak cross-correlation value of -0.26 occurring at a lag of 8 min (with an "error bar" between 6 and 8 min). This correlation is associated with modestly increasing northward flows for IMF B_z negative, with small averaged flows for B_z positive.

The dayside results surveyed above are indicative of a major control on the flow exerted by the north-south component of the IMF, with response delays at Tromsø of just a few minutes relative to the arrival of first effects at the ionosphere. Delay times are

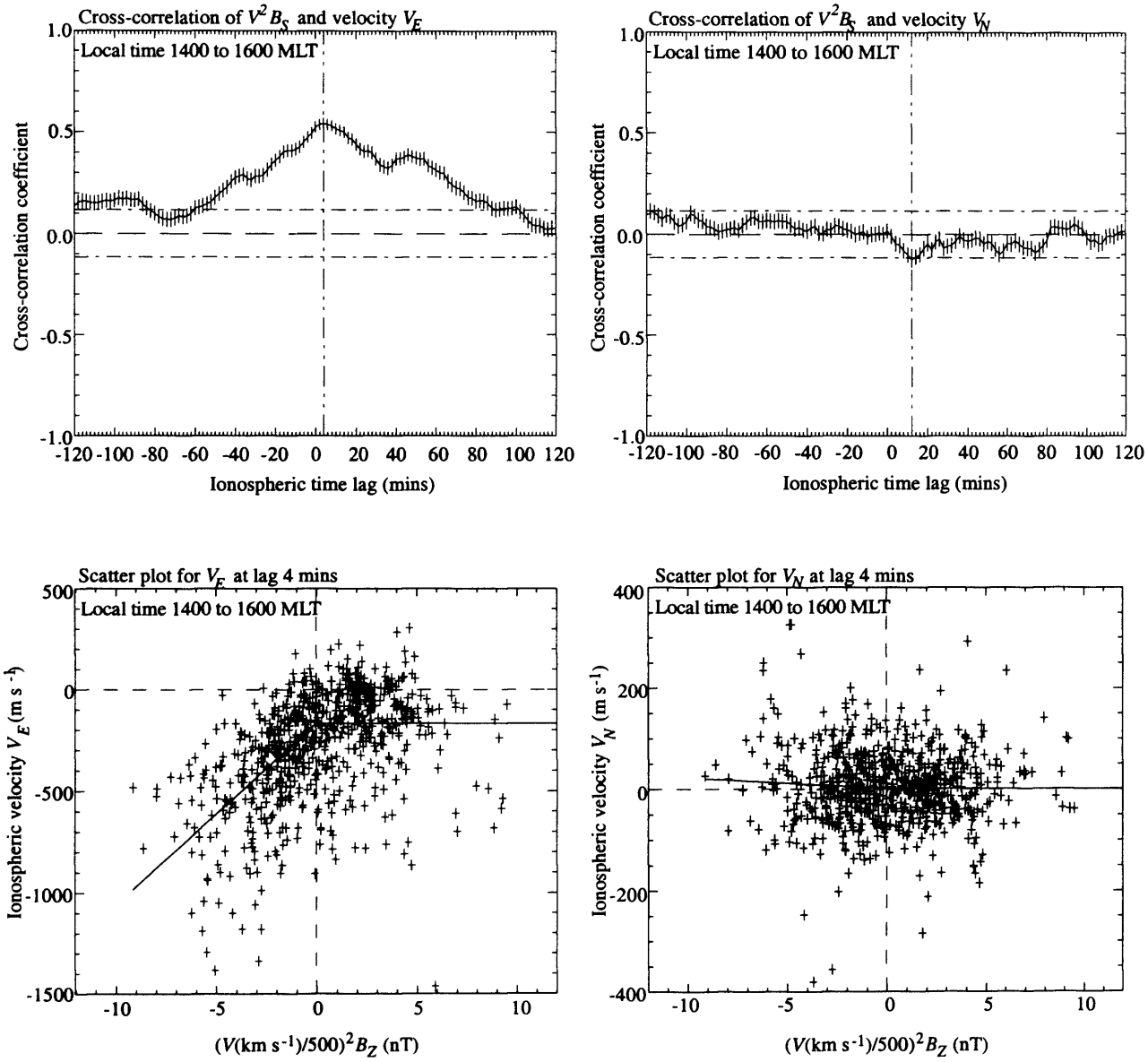

FIGURE 4.6 As for Figure 4.5 except for the 2-h interval centred on 1500 MLT

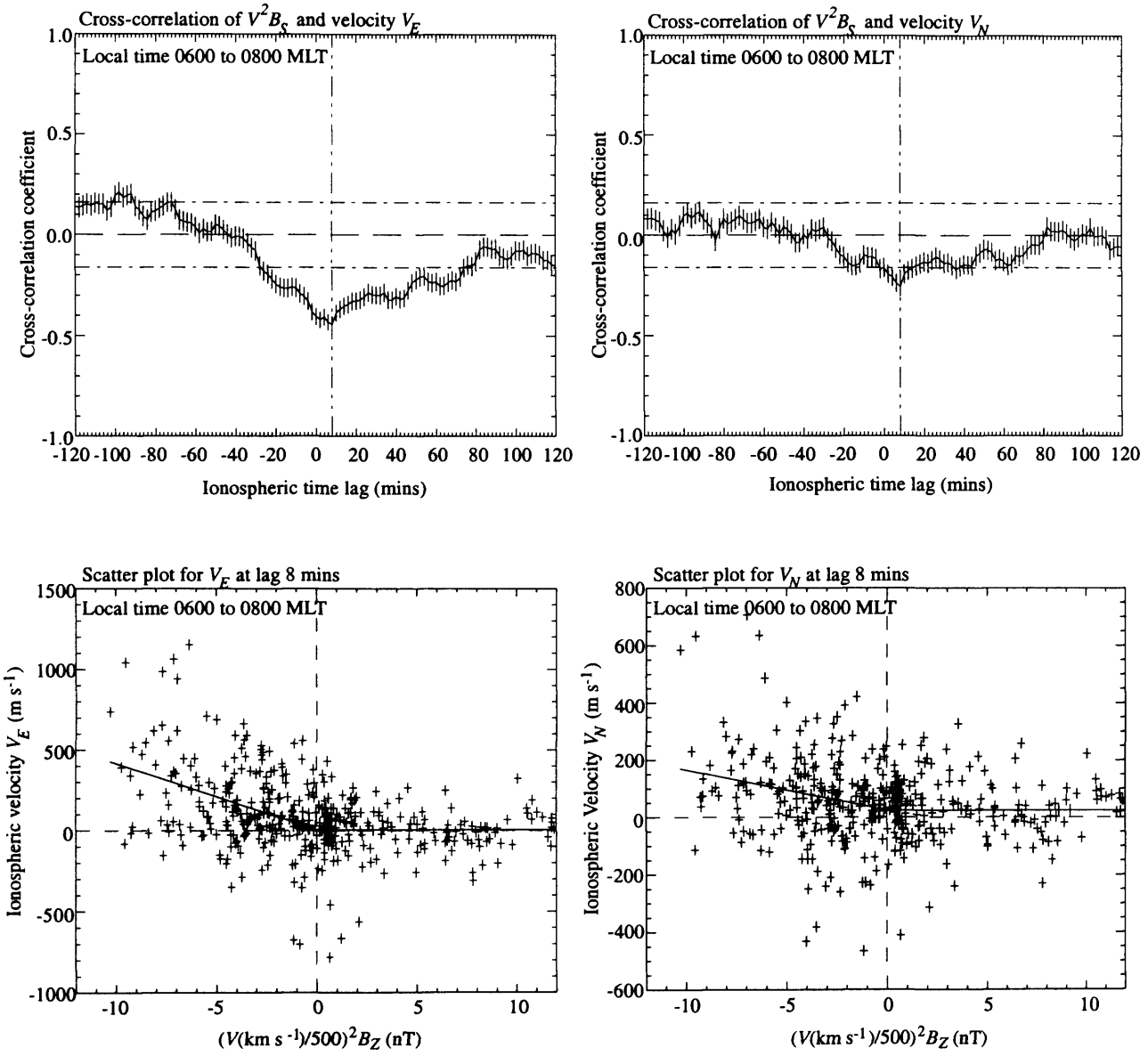

FIGURE 4.7 As for Figure 4.5 except for the 2-h interval centred on 0700 MLT

typically 2-4 min in the noon-afternoon sector of the dusk cell, with an indication of an increase to ~8 min near dawn. In the following section, the cross correlation results obtained from the nightside sector will be discussed.

4.4.4 Results from cross-correlation analysis: nightside response delays

The cross-correlation results for the nightside are not as clear-cut as they are for the dayside. Typically, the cross-correlation coefficients are lower and the extrema less well defined, presumably because of the increasingly important influence on the flow of tail processes compared with magnetopause processes. Nevertheless, the results are indicative of increased response delays of ~5-15 min. Two examples from the post-midnight dawn cell are shown in Figures 4.8 and 4.9. Figure 4.8 shows results for the 2 h interval centred on 0100 MLT (containing 225 flow measurements). Here the cross-correlogram for v_E has a pronounced but broad minimum, with a peak of -0.58 at a lag of 16 min (with an "error bar" between 14 and 34 min). The scatter plot shows that this corresponds to eastward flows which increase strongly with increasingly negative IMF B_z from small average values for IMF B_z positive. No evidence for flow reversal effects are observed in these data, so that the lag time of the peak correlation should be interpreted as the excitation and decay delay time. The cross-correlogram for v_N shows no pronounced peak for positive lags at values above the 99.9% level. The scatter-plot, shown at a lag of 16 min as determined from v_E, indicates weak averaged equatorward flows that barely respond to the IMF. Figure 4.9 similarly shows results for the 2 h interval centred on 0400 MLT (containing 425 flow measurements). Here the correlogram for v_E has a weak minimum of -0.28, but above the 99.9% confidence level, at a lag of 14 min (with a "error bar" between 2 and 16 min). The scatter plot again shows consistently increasing eastward flows with increasing negative IMF B_z, though scattered large values are also present for IMF B_z positive, perhaps due to tail (substorm) effects. As before, the cross-correlogram for v_N shows no pronounced peak above the 99.9% confidence level. The scatter-plot at a lag of 14 min shows weak averaged northward flows, which are independent of the IMF north-south polarity.

The final MLT interval which needs to be discussed is the sector from dusk to pre-midnight, i.e. the MLT hours centred on 1900-2300 MLT corresponding to the nightside region of the dusk cell. Here the results show rather different features, as exemplified by the data for the 2 h interval centred on 2000 MLT displayed in Figure 4.10 (containing 682

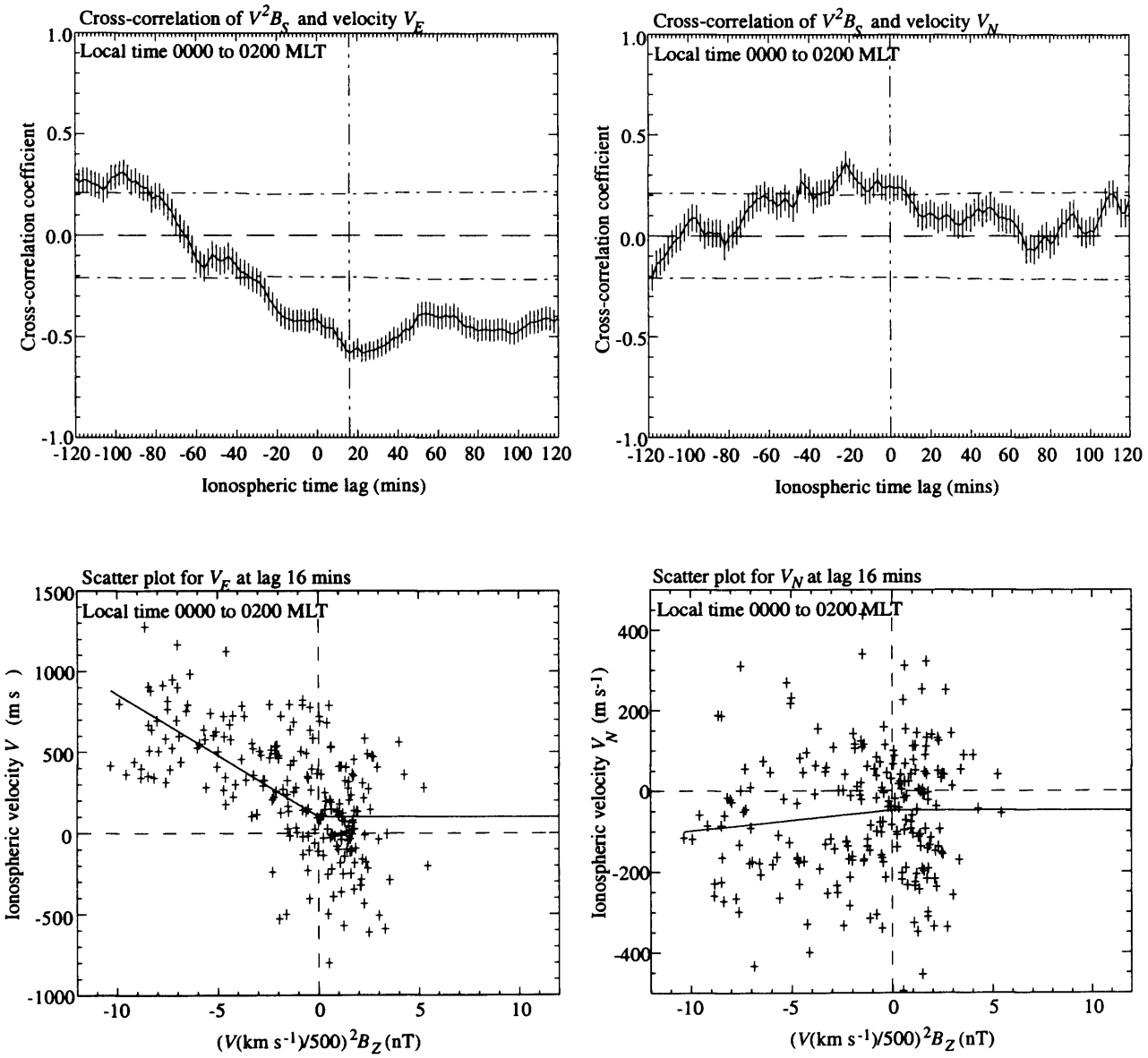

FIGURE 4.8 As for Figure 4.5 except for the 2-h interval centred on 0100 MLT

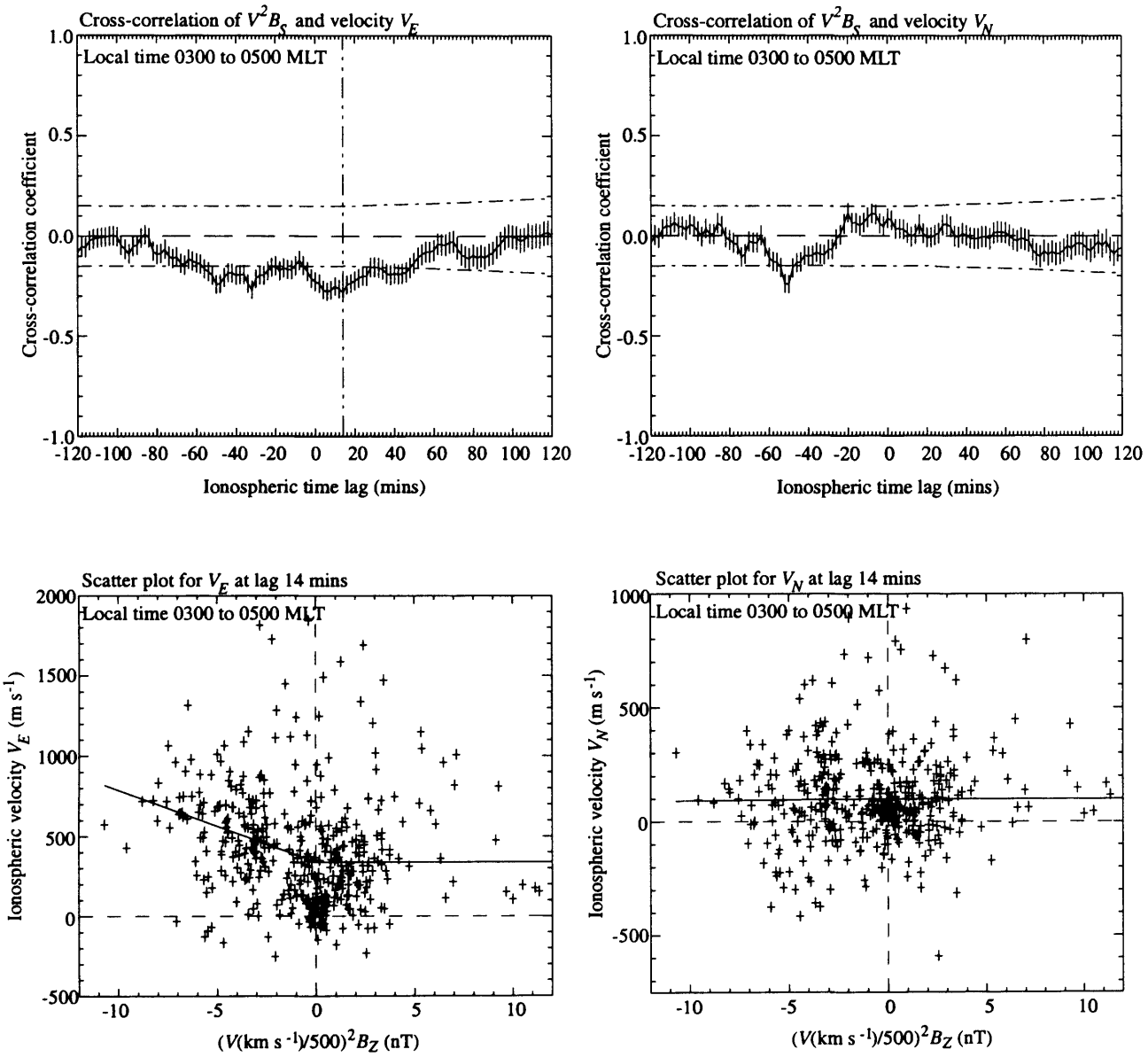

FIGURE 4.9 As for Figure4.5 except for the 2-h interval centred on 0400 MLT

flow measurements). Here the cross-correlogram for v_E shows a broad but well-defined peak at a value of -0.38 with a delay of 34 min (with an "error bar" between 30 and 38 min), a much longer delay than found in other local time sectors discussed. Furthermore, the scatter-plot corresponding to this delay provides clear evidence of non-monotonic behaviour of the east-west flow with IMF B_z, the flow being westward for IMF B_z positive, increasing in strength somewhat for small negative B_z, and then reversing in sense to become eastward for large negative B_z. Very similar behaviour is found in the 2-h interval centred on 1900 MLT, where the lag of the peak correlation again occurs with a delay of 34 min (within an "error bar" between 28 and 44 min). From the previous discussion in §4.4.2, one may infer that this behaviour relates to the passage of the Harang east-west flow reversal across the observing site as the flow system expands with increasing negative IMF B_z. Furthermore it is inferred that the lag of the peak correlation corresponds to the time scale required for the sense of the flow to change relative to the IMF B_z positive "baseline", and not to the excitation and decay delay time as in other local time sectors.

The cross-correlation results for v_E in the MLT intervals centred on 21 and 22 MLT (not shown) are similar to those in Figure 4.10 in that they show that a generally weak but westward flow which is present for IMF B_z positive gives way to an increasing eastward flow when IMF B_z is negative. However, the behaviour is now observed to be nearly monotonic relative to the positive IMF B_z "baseline", with eastward flows appearing for relatively small negative values of IMF B_z, and with little evidence of significant initial enhancements of westward flow. Correspondingly, the lag of the peak correlation decreases towards values which are similar to those obtained at other local times, i.e. 14 min at 2100 MLT (within an "error bar" between 10 and 38 min), and 10 min at 2200 MLT (within an "error bar" between 6 and 24 min). It seems reasonable to infer that these values correspond to a measure of the excitation and decay delay time of the eastward flow in the pre-midnight sector.

Turning to the results for v_N in the pre-midnight Harang region, where, since the considerations which apply to the reversing v_E component no longer hold, we may again suppose a priori that the lag time of the peak correlation will correspond to the excitation and decay delay time. Correspondingly, the correlogram for v_N for the interval centred on 2000 MLT shown in Figure 4.10 does not show a peak at the same lag as for v_E, but rather exhibits a very broad region of positive correlation with a peak of 0.43 at an (unphysical)

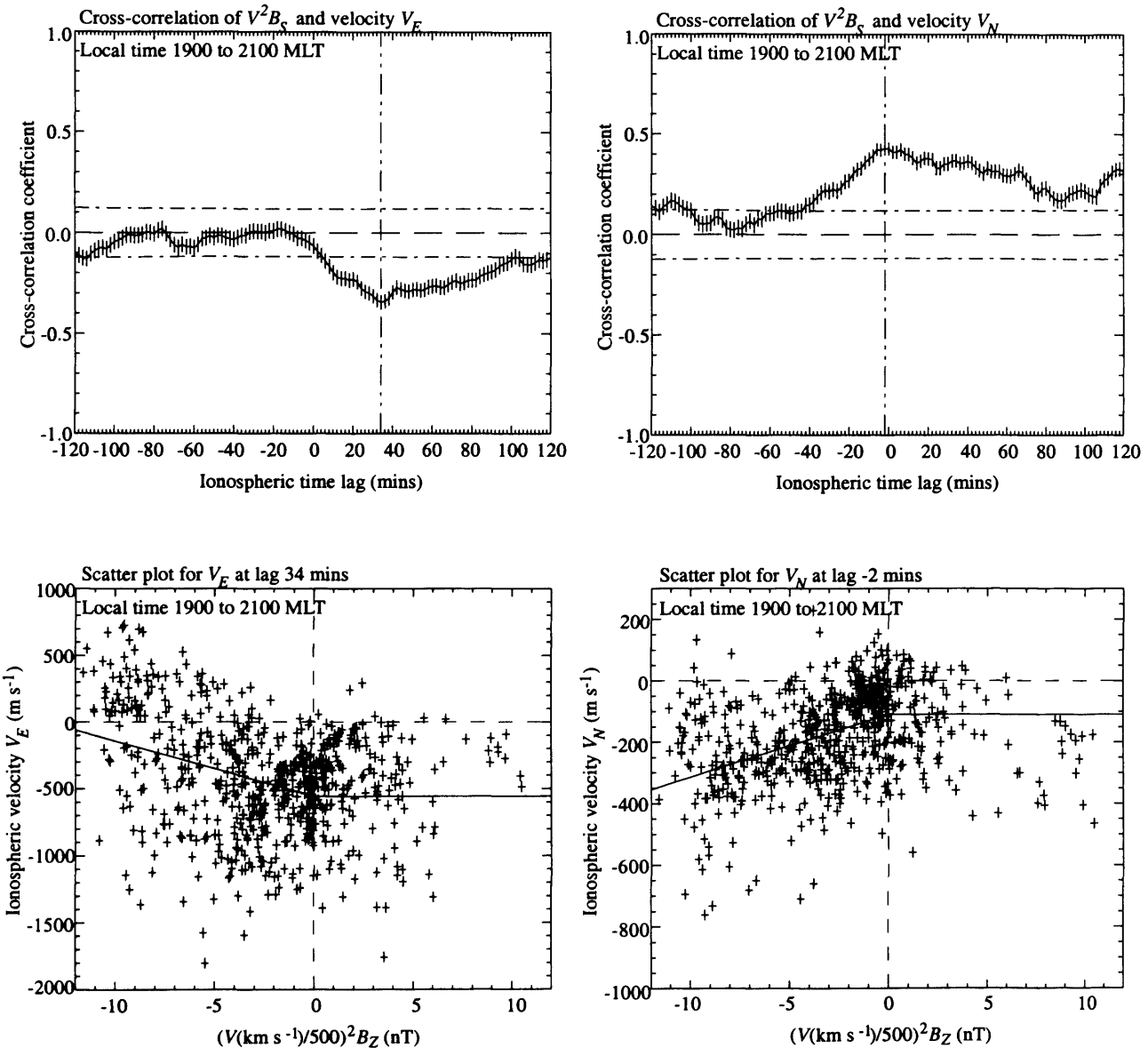

FIGURE 4.10 As for Figure 4.5 except for the 2-h interval centred on 2000 MLT

lag of –2 min (within an "error bar" between -4 and +10 min). The v_N scatter-plot shows a well-defined and monotonic increase in equatorward flow with increasing negative IMF B_z. Similar v_N behaviour is found in the interval centred on 1900 MLT, but this effect dies away with increasing local time, and no significant correlations are found for the interval centred on 2100 MLT and at later local times.

4.5 Overall cross-correlation results

Having presented several cross-correlation results for each flow component in the previous section, summaries illustrating the outcome of the cross-correlation analysis are now presented in Figures 4.11 and 4.12 showing the results for the eastward and northward component of ionospheric flow, respectively. Beginning with Figure 4.11, the top panel firstly shows the number of flow measurements in each 2 h interval of MLT, varying between a minimum of about 200 in the post-midnight sector, to a maximum of about 700 in the afternoon and evening sector, as previously indicated. Beneath this the response delay of the eastward flow component versus MLT is shown, corresponding to the lag of the peak cross-correlation coefficient, with error bars determined as described above (§4.4.3). No value is shown if there was no peak present above the 99.9% confidence level in the cross-correlogram. The third panel displays the peak value of the cross-correlation coefficient itself. The lower two panels then show the slope and intercept of the least-squares lines fitted to the scatter plots at the lag of the peak correlation (as shown in the lower graphs in Figure 4.5 to 4.10). The "intercept" velocity provides a measure of the average flow which is present for northward IMF, while the "gradient" indicates how this baseline value changes in response to various levels of negative IMF B_z.

In line with the above discussion and cross correlograms presented in §4.4.2 and §4.4.3, the results for v_E can be divided into three main regimes. The first is the dayside dusk cell westward flow regime indicated by the square symbols, observed between 1100 and 1700 MLT. Here the flow response delay is typically 2-4 min, and shows no discernible MLT variation within the resolution of this study. The cross-correlation coefficients are typically quite high, between ~0.4 and ~0.7, and tend to increase with local time. The "gradient" values also increase with MLT, corresponding to radar locations which are increasingly centrally located within the dusk flow cell, as do the "intercept" velocities, though the latter remain quite small, less than ~200 m s^{-1}. The second regime corresponds to the dawn cell eastward flow region indicated by the circular symbols,

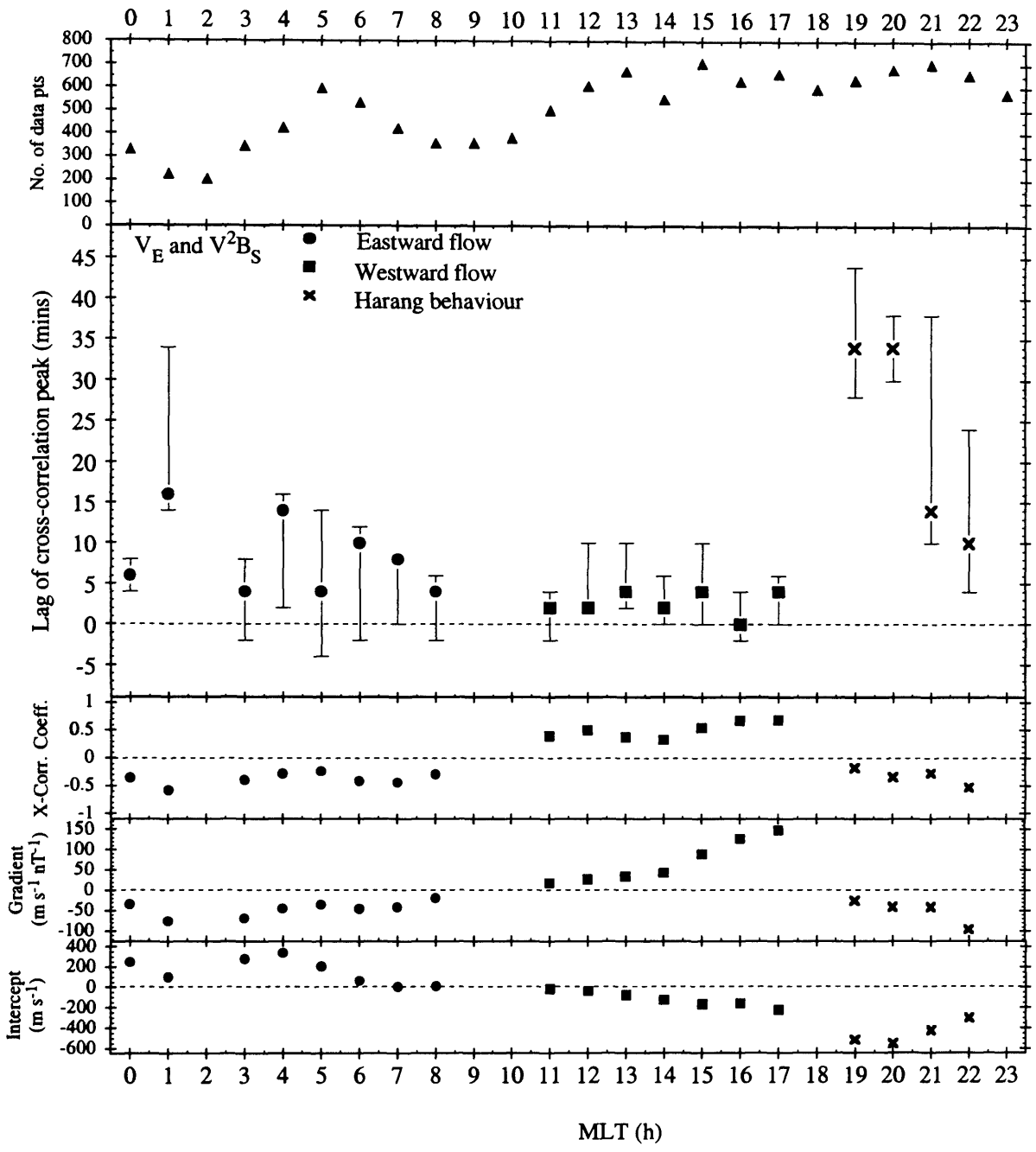

FIGURE 4.11 Summary of cross-correlation results for the v_E component of ionospheric flow. The top panel shows the number of flow measurements in each 2 h interval of MLT used in the study, specifically at zero lag (the number of points may vary slightly with lag due to gaps in the interplanetary data record). Beneath this we show the lag of the peak value of the cross-correlation coefficient (min). In the next panel we show the value of the cross-correlation coefficient at the peak. The lower two panels show the "gradient" and "intercept" values of the lines least squares-fitted to the scatter plots of v_E versus $(V/500)^2B_s$, as shown in the lower panels of Figures 4.5-4.10. The squares indicate results corresponding to the dayside dusk flow cell where the correlation coefficient and "gradient" are positive, while the "intercept" is negative (increasing westward flows for southward IMF). The circles indicate results corresponding to the dawn flow cell where the correlation coefficient and "gradient" are negative, while the "intercept" is positive (increasing eastward flows for southward IMF). The crosses indicate the Harang region of the nightside dusk flow cell where the correlation coefficient, "gradient", and "intercept" are all negative (flow reverses from west to east as the IMF reverses from north to south)

observed between 0000 and 0800 MLT. Here the flow response delay times are short, ~5 min, and similar to the dusk cell values on the dayside (certainly within the error bars), but tend to increase and become more scattered, ~5-15 min, on the nightside. The peak cross-correlation coefficients are lower than for the dusk cell, typically ~0.3-0.4, while in common with the dusk cell, the "gradient" and "intercept" values tend to increase on moving from the dayside to the nightside, before declining somewhat near midnight. The third regime corresponds to the nightside (Harang) region of the dusk cell, observed between 1900 and 2200 MLT, marked by crosses. As noted above, this regime is characterised by the presence of westward flow for northward IMF, reversing to eastward flow for a sufficiently southward IMF, such that the "gradient" and "intercept" are of the same sign, unlike the opposite signs of the other two regions. Here the response delays are very long (~30-40 min) at 1900 and 2000 MLT, but decline to ~10-15 min at 2100 and 2200 MLT as outlined above. As previously indicated, the lag times of the peak correlation in the interval 1900-2000 MLT probably more reflect the time scale for flow reversal from west to east due to expansion and evolution of the flow cells under the influence of southward IMF, rather than to the IMF-modulated flow excitation and decay time scale of main interest here. These two values will consequently be excluded from further analysis of the latter delay time.

Results for v_N shown in Figure 4.12 are more restricted, due to the fact that within the central parts of the flow cells the north-south flow tends to be weak and unresponsive to the IMF. Two regimes are evident, corresponding to the region of negative correlations indicated by the square symbols (northward flow for southward IMF), which span the dayside east-west flow reversal centred on 0900-1000 MLT, and a region of positive correlations indicated by the circles (equatorward flow for southward IMF), which are observed in the dusk and early evening sector. The noon-sector v_N data indicate similar short response delays as found for v_E, and bridge the 'gap' in the latter results in the interval where the east-west flow reverses. Typical cross-correlation coefficients are fairly low, ~-0.3. Values of the "gradient" tend to be higher in the morning than near noon, and the "intercept" remains small throughout. Short response delays are also indicated in the region of positive correlation (equatorward flow) in the dusk and post-dusk sector, though the correlation distributions tend to be very broad (Figure 4.10) and the uncertainties large. Cross-correlation values peak at ~0.6 at 1900 MLT, and "gradient" and "intercept" values tend to increase with increasing local time from dusk towards midnight.

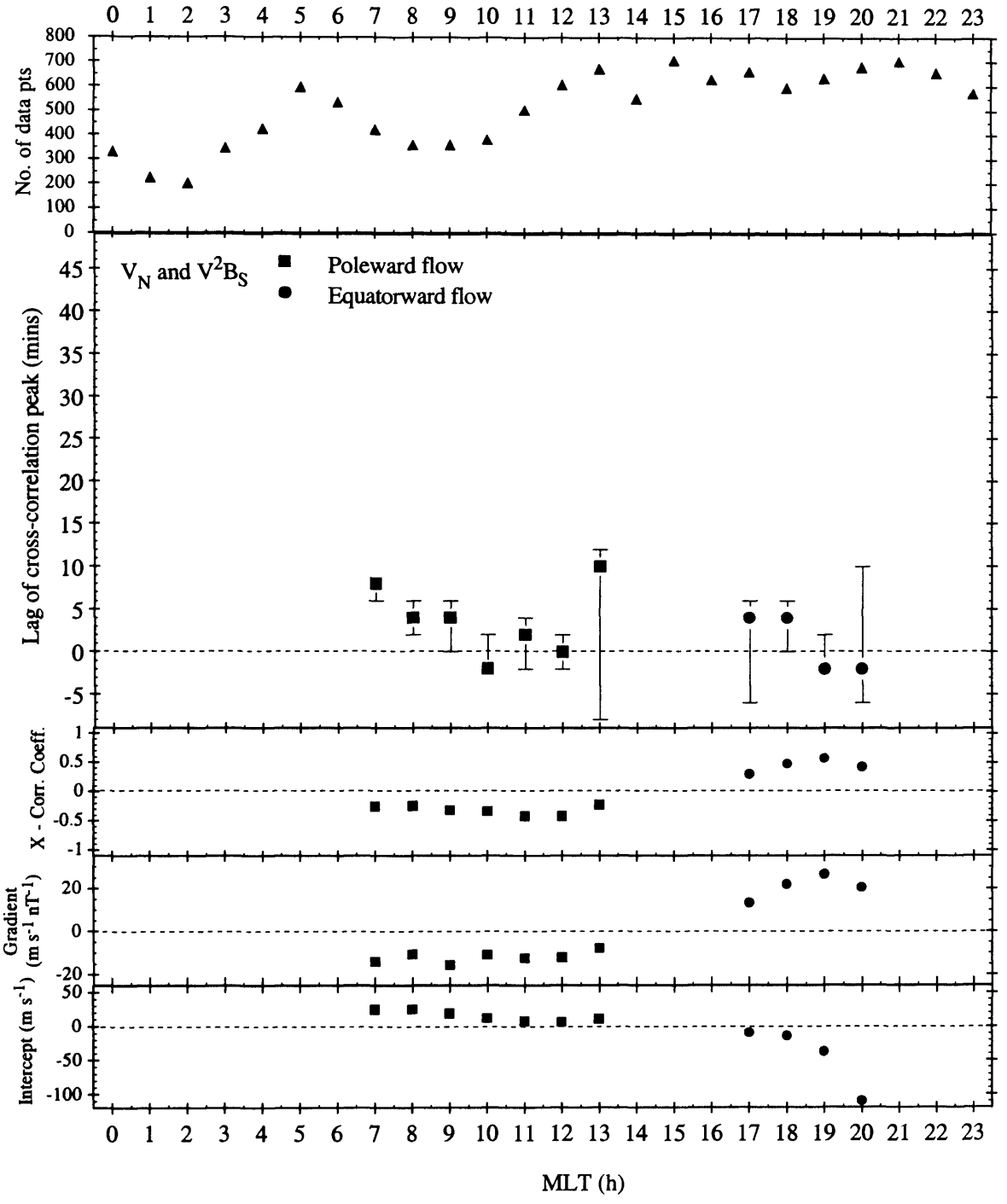

FIGURE 4.12 As for Figure 4.11, except for the v_N component of ionospheric flow. The squares indicate the region of negative cross-correlation values (northward flow for southward IMF), while the circles indicate the region of positive values (equatorward flow for southward IMF)

4.6 Discussion

Considering all of the v_E flow response results shown in Figure 4.11, it can be seen that the data are consistent with short, few-minute response delays on the dayside, and with increased delays on the nightside, though the scatter in the latter values is large. If all of the dayside values from 0700 to 1700 MLT are taken and weighted according to the inverse of the error bar to take account of their varying degrees of certainty, the average delay time is found to be 3.1±0.8 min (the unweighted average is 3.3±0.8 min). These averages are collected together and displayed in Table 4.1. For the nightside values from 2100 to 0500 MLT (excluding the two values at 1900 and 2000 MLT for reasons discussed above) a significantly higher weighted average value of 8.0±2.4 min is calculated (the unweighted average is 9.7±1.9 min). Here the errors are quoted as the standard error of the weighted mean (i.e. the standard deviation divided by the root of the number of samples in the case of equal weights). For the north-south component of the flow, the dayside data shown in Figure 4.12 confirm the short response delays which are present in the noon sector. The weighted average response delay of the v_N values in the interval 0700-1300 MLT is found to be 3.7±1.8 min, entirely consistent with the dayside results for v_E. The v_N results in the dusk sector also indicate short, few-minute delays. These data are comparable to the values obtained from v_E in the pre-dusk sector, but are much shorter than the ~30-40 min values obtained from v_E in the post-dusk sector, for reasons already discussed.

Although the discussion so far has concentrated on the cross-correlation results for the two flow components taken separately, it is also of interest to combine the results together. This significantly improves the MLT coverage, since, as has been shown, the flow responds principally in the east-west component in some sectors, and principally in the north-south component in others. At local times where both components provide an estimate of the flow response delay, the smaller of the two values has been taken on the basis that the true response delay for the flow in a particular MLT sector corresponds to the minimum value obtained, irrespective of the component in which it was observed. The results are shown in Figure 4.13, where square symbols indicate values derived from the east-west flow component, while circles indicate values derived from the north-south flow component; where both components give the same value the point with the smallest error bar is shown. Again the results suggest longer delays on the nightside compared with the dayside, with the weighted average of the dayside values being 2.2±0.9 min (2.7±0.8 min

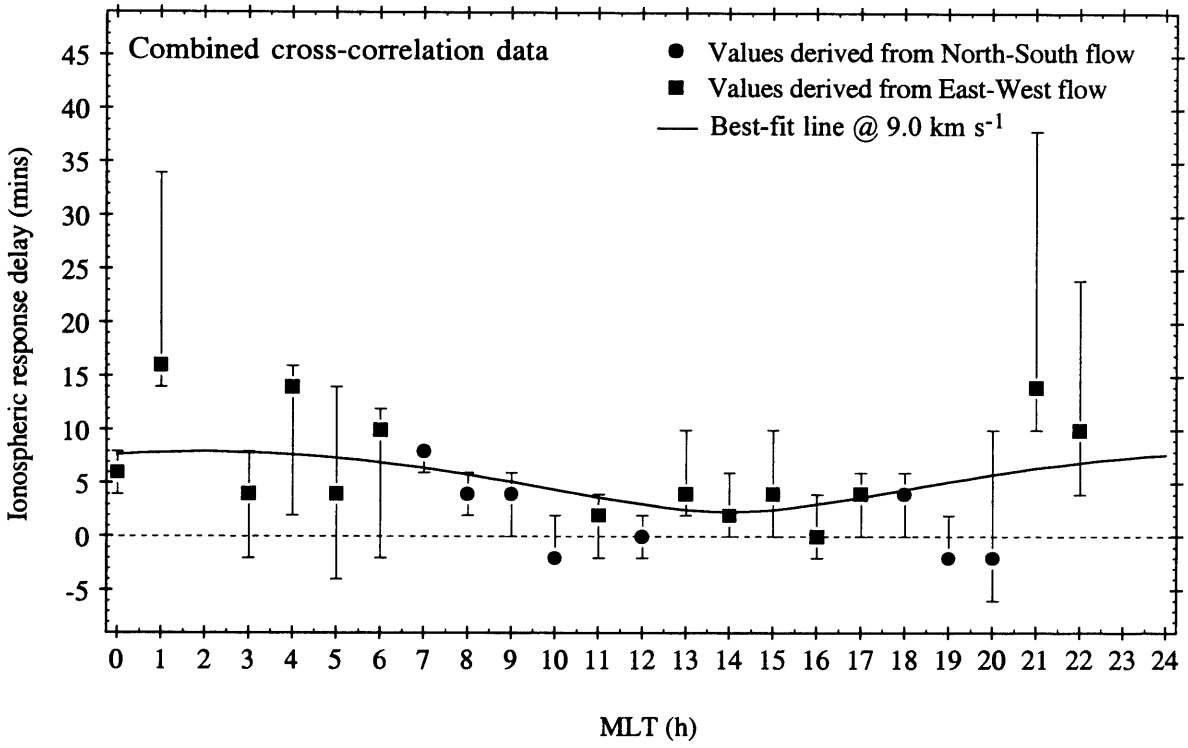

FIGURE 4.13 Response delay values for the combined north-south and east-west cross-correlation data set, where the squares indicate values derived from the east-west flow, and circles values derived from the north-south flow. Where both components provide a value, the lower of the two has been used, and where both give the same value, the data point with the smaller error bars is shown. The solid line shows a simple theoretical curve which has been least-squares fit to these values, in which information propagates radially from the open-closed field line boundary at 77° magnetic latitude. The best-fit line corresponds to a propagation epicentre located at 1400 MLT, and a phase speed of 9.0 km s^{-1}

unweighted), while that for the nightside being 5.5±2.5 min (7.1±2.3 min unweighted). However, the results taken together suggest that the minimum response delay actually occurs in the post-noon sector, near 1400 MLT, rather than at noon itself. Although the scatter in this data set is rather large, the reality of the offset from noon is suggested by the fact that a very similar effect was previously observed in the cross-correlation and event analyses performed by *Etemadi et al.* [1988] and *Todd et al.* [1988], respectively, using EISCAT flow data measured at higher latitudes (71°-73°). If the data in Figure 4.13 is then averaged over the 12-h sectors centred on 1400 MLT and 0200 MLT, the weighted averages are found to be 1.3±0.8 min and 8.8±1.7 min, respectively (see Table 4.1). (The unweighted values are 1.8±0.7 min and 9.6±1.5 min, respectively.) The difference between 'dayside' and 'nightside' response delays is thus estimated as 7.5±1.9 min.

The results shown in Figure 4.13 suggest that at the latitude of EISCAT, at least, IMF-modulated changes in the flow are observed first in the immediate post-noon sector, and then propagate into the nightside, such that the response is delayed in the latter region relative to the former. In order to give an indication of the effective phase speed of that propagation, a simple model has been employed in which, starting at zero delay time, the information propagates radially outwards from the dayside open-closed field line boundary, taken to lie typically at ~77° magnetic latitude (according to observations of the location of the equatorward border of the cusp reported by *Newell et al.* [1989]). The propagation speed and the local time of the epicentre of information propagation have then been stepped (through half-hour intervals of local time) until the least squares best fit to the cross-correlation data in Figure 4.13 has been found. This procedure yields an epicentre located at 1400 MLT (thus validating the division of the data chosen above), and a phase speed of 9.0 km s^{-1}. The best-fit line is superposed on the data in Figure 4.13. It is seen to follow the trends in the data tolerably well, though we would hesitate to call it a 'good fit' due to the large error bars and the consequent scatter in the data.

4.7 Summary

In this chapter, ~300 simultaneous hours of high-latitude ionospheric flow observations obtained by the EISCAT UHF radar have been cross-correlated with measurements of the IMF made by the IMP-8 spacecraft upstream from the Earth's magnetosphere, in order to determine the time scale on which the ionospheric flow responds to changes in the north-south component of the IMF. The field-perpendicular ionospheric flow vectors were determined from the EISCAT CP-1-K experiment, in which

Data set	**Dayside response delay** [*range of MLT*]	**Nightside response delay** [*range of MLT*]	**Nightside-dayside delay difference**
v_E cross-correlation data	3.1±0.8 min [*07-17 MLT*]	8.0±2.4 min [*21-05 MLT*]	4.9±2.6 min
v_N cross-correlation data	3.7±1.8 min [*07-13 MLT*]	–	–
Combined cross-correlation data	2.2±0.9 min [*07-17 MLT*]	5.5±2.5 min [*19-05 MLT*]	3.3±2.9 min
Combined cross-correlation data	1.3±0.8 min [*09-19 MLT*]	8.8±1.7 min [*21-07 MLT*]	7.5±1.9 min

TABLE 4.1 Averaged flow response delays in different local time sectors derived from the various data sets employed in the cross-correlation study. In each case the contributing data points have been weighted according to the inverse of their uncertainty estimate.

the plasma velocity is continuously monitored with 2 min resolution at an altitude of 278 km along the field line at Tromsø (66.3° magnetic latitude). The data cover all magnetic local times, though with a preference for the hemisphere centred on dusk compared with the hemisphere centred on dawn. The flow data were divided into overlapping 2 h intervals of MLT, and cross-correlated with the half-wave rectifier function V^2B_s, where the latter data were suitably shifted in time to take account of the propagation of the IMF from the spacecraft to the subsolar magnetopause, and its effects from thence to the cusp ionosphere. A similar cross-correlation analysis was previously performed by *Etemadi et al.* [1988] using data from the EISCAT 'Polar' experiment (at latitudes ~71°-73°), but the analysis only spanned the dayside hours between ~1030 and ~1700 MLT, corresponding mainly to the westward flows of the 'dusk' flow cell. Here these results have been extended to include the dayside dawn flow cell and the nightside hours.

The cross-correlation results show that for the east-west flow component statistically significant peaks in the cross-correlation coefficient are obtained at nearly all local times, except principally for the pre-noon hours (~0900-1000 MLT) where the east-west flow reverses in sense between the flow cells. However, the nightside cross-correlation coefficients are typically smaller than on the dayside and the results correspondingly more scattered. The majority of the scatter-plots for this flow component corresponding to the peak cross-correlation coefficient show relatively weak averaged flows for northward IMF which change monotonically as V^2B_s becomes increasingly negative. The lag of the peak correlation is this case is interpreted as the IMF-modulated flow excitation and decay delay time, typically lying in the range 0-15 min. However, in the pre-midnight Harang region the response times become significantly longer (~30-40 min), while the corresponding scatter plots for the east-west flow show the presence of non-monotonic behaviour. These longer delays and non-monotonic behaviour of the flow in response to strengthening negative B_z conditions have been explained in terms of expansion of the convection flow cells, as opposed to the excitation and decay of convection. Such data were excluded from the subsequent analysis.

The average east-west flow response delay time for the dayside cross-correlation data, weighted according to the inverse of the uncertainty estimates of the values, is found to be 3.1±0.8 min. This value is closely comparable to the corresponding results of *Etemadi et al.* [1988] when the ~2 min propagation from the magnetopause to the

ionosphere is (as here) subtracted. On the nightside, the weighted average value increases to 8.0±2.4 min, where the results from the 1900-2000 MLT Harang region have been omitted. Statistically significant responses of the north-south flow are more restricted in MLT, and are confined to the dayside interval 0700-1300 MLT for poleward flows excited by southward IMF, and to the dusk sector 1700-2000 MLT for equatorward flows excited by southward IMF. The weighted average response delay of the former values is 3.7±1.8 min, entirely compatible with the dayside results for the east-west flow. The dusk-sector values are also consistent with a relatively small delay in the range 0-5 min, though the cross-correlation distributions are typically very broad and the error bars correspondingly large.

When these data are suitably combined together they indicate that the minimum response delay occurs at ~1400 MLT. The overall weighted average delay for the 12-h sector centred on 1400 MLT is 1.3±0.8 min, while that for the 12-h sector centred on 0200 MLT is 8.8±1.7 min. The implication is that information about IMF-related modulations of the flow propagates through the ionosphere away from the postnoon sector. In order to quantify the phase speed of that propagation a simple model has been fitted to the combined data in which information propagates radially outwards from an epicentre located on the dayside open-closed field line boundary (taken to lie at 77° magnetic latitude) at a constant phase speed. In this case the best fit is obtained for an epicentre centred at 1400 MLT and a phase speed of 9.0 km s^{-1}.

CHAPTER 5

Event study to determine the ionospheric flow response to sharp polarity changes in the IMF B_z component

5.1 Introduction

In the previous chapter, ionospheric flow response delays for all local times were calculated by means of a cross-correlation analysis conducted on ~300 h of simultaneous EISCAT velocity data and IMF data from the IMP-8 spacecraft. The results indicate the diurnal variation in the flow excitation with short delays over the dayside and increasing delays towards the nightside. However, the nature of the statistical analysis is such that all of the data is taken as one unit and a characteristic response delay is determined over the entire 2 h interval in question. An alternative method of analysis is to conduct an 'event-study' on the same simultaneous data set offering several advantages over the statistical analysis of the previous chapter. Firstly, through the 'event-analysis' the direct-driven flow response to the IMF polarity changes can be determined at all local times, and in particular at local times where the flow is known to vary in spatial extent as well as in response to IMF changes. The longer response delays associated with the expansion of the flow cells on the nightside (Harang) region are evident in the cross-correlation results in that local time sector, however in the 'event-analysis' such effects can be accounted for through visual inspection of the data. Secondly, the response of the flow to northward and southward turns of the IMF can be investigated separately and any systematic differences can be between these can be highlighted. Thirdly, the time scale on which the flow strengthens or weakens after the first response to the IMF changes can also be determined through the 'event-analysis'. The main disadvantage of the 'event-analysis' is the subjectivity of the analysis procedure, although a rigorous method is followed to try to keep the subjectivity to a minimum.

In order to complement the results of the cross-correlation analysis reported in the previous chapter and also for the reasons stated above, an 'event analysis' study was thus undertaken in the manner of *Todd et al.* [1988] using the same data set as the statistical study. The entire ~300 h of IMF data were searched for the occurrence of sharp polarity changes in the IMF B_z component, and then concurrent measurements of the ionospheric

flow were examined to find the time at which the first response was observed, relative to the arrival time of first possible IMF effects. The latter time was determined from the IMP-8 interplanetary data in essentially the same way as for the cross-correlation analysis (see §4.2), except that the orientation of the "phase front" of the IMF was determined and employed for each 'event' individually, with the delay time calculated from solar wind plasma data averaged over the same 10-15 min intervals on either side of the 'event' (the IMF discontinuity) as were used to average the field for the "phase front" (discontinuity normal) analysis. The time of the ionospheric flow response was then determined as the centre-time of the 2-min radar data averaging interval that showed the first enduring change that could be ascribed to the effect of the IMF, outside of the range of previous fluctuations of the flow data. Overall, the responses to a total of 69 such interplanetary 'events' were analysed in this study. Prior to showing the overall results, several individual examples in various local time sectors will be presented in the following section to show the typical response delays determined.

5.2 Event analysis

5.2.1 Results from the event analysis for data on the dayside

An example of the data is presented in Figure 5.1, where the 2 h interval spanning 0900-1100 UT on 14 February 1996 is shown, corresponding to 1130-1330 MLT in the noon sector. The top panel of the figure shows IMF B_z, while the centre and lower panels show the field-perpendicular ionospheric flow velocity components, v_N positive towards magnetic north and v_E positive towards magnetic east. The results of *Weimer* [1995] reproduced in Figure 4.1 indicate that the flow should be small for IMF B_z positive, while westward and northward ('dusk cell') flows should appear for IMF B_z negative. Correspondingly, at the start of the interval when IMF B_z was positive, the observed flow scatters about zero. However, two sharp southward turns of the IMF occurred, observed at IMP-8 at 0925 and 1019 UT, which are marked by the vertical dashed lines in the upper panel. The first effects in the ionosphere, determined from the individual orientations of the field discontinuities concerned as indicated above, are then expected at 0938 and 1032 UT (the delay being 13 min in both cases), as indicated by the vertical dashed lines in the lower two panels. It can be seen that both southward turns resulted in the excitation of ~200-300 m s^{-1} westward flows and less distinct poleward flows, as expected, with first

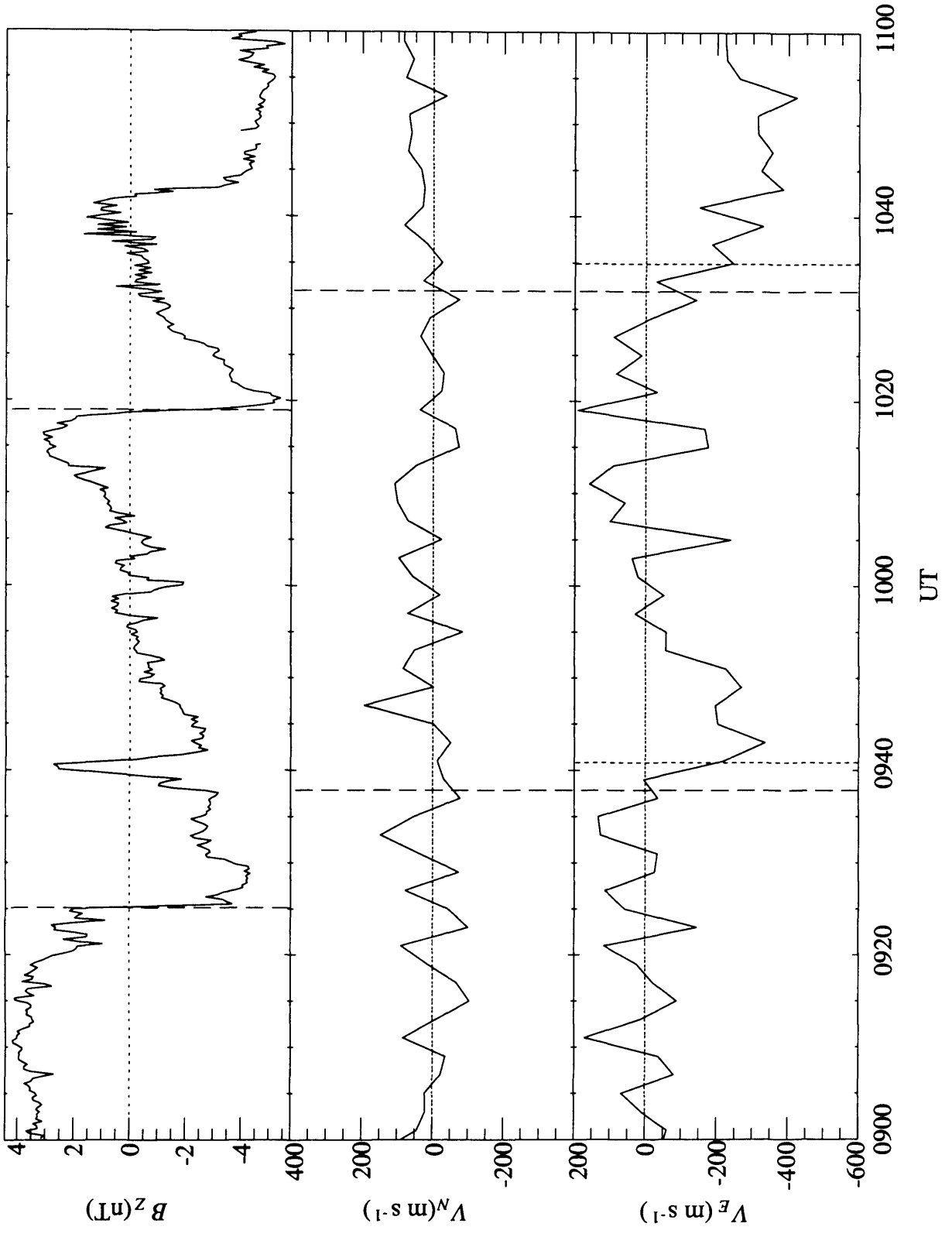

FIGURE 5.1 Simultaneous IMP-8 magnetic field data and EISCAT CP-1-K velocity data for the interval 0900-1100 UT (1130-1330 MLT) on 14 February 1996. The top panel shows 15 s values of the IMF B_z field component, while the lower two panels show 2 min values of the magnetic north and magnetic east components of the field-perpendicular velocity measured by the radar. Two southward turnings of the IMF are marked by the dashed vertical lines in the upper panel, whose effects are expected to arrive in the ionosphere at the times indicated by the dashed vertical lines in the lower panels. The times at which the first clear effects were observed in the flow components are shown by the dotted vertical lines in the lower panels

changes occurring at about 0941 and 1035 UT respectively, as marked by the vertical dashed lines in the lower panel. The response delays are thus about 3 min in each case, within an uncertainty band that is ~2 min. The flow response is thus very prompt near noon, in conformity with the previous results e.g. of *Etemadi et al.* [1988] and *Todd et al.* [1988]. These authors reported a ~5 min response delay in this local time sector, but they did not subtract the ~2 min magnetopause-to-ionosphere propagation delay in the IMF signal which we have included here. Also the response delays are consistent with the corresponding results from the cross-correlation analysis in this local time sector (Figure 4.5).

Moving into the mid-afternoon local time sector (1430-1630 MLT) of the dusk flow cell, Figure 5.2 shows data obtained for the interval 1200-1400 UT on 16 March 1994, (see also the correlation results in Figure 4.6). The format is the same as for Figure 5.1. Two periods of predominantly southward fields can be seen in the IMF, observed by IMP-8 in the intervals 1213-1229 UT and 1304-1329 UT, respectively, as indicated by the vertical dashed lines in the upper panel. (Short-term variations of the field on times scales less than ~5 min are neglected, since no ionospheric response can be discerned.) The effect of the first southward turn at 1213 UT is estimated to have arrived at the ionosphere at 1225 UT (a delay of 12 min relative to IMP-8, indicated by the first vertical dashed line in the lower panels), and is clearly associated with the onset of a flow which is directed westward and (weakly) equatorward. The response delay is somewhat obscured in this case by a one-point data gap centred at 1223 UT, but when data is resumed 1225 UT the weak equatorward flow is clearly already in progress, while the westward flow is not clearly increasing consistently and at larger values than those occurring previously until 1229 UT. The response delay of v_N is therefore taken to be essentially zero, while that of v_E is about 4 min. The effect of the subsequent northward turn of the IMF, observed by IMP-8 at 1229 UT (second dashed line in the upper panel), is estimated to have arrived at the ionosphere at 1240 UT (second dashed line in the lower panels). The cessation of the perturbation in v_N is rather gradual, from which no timing information is deduced, while the first time at which the westward flow is observed to decline (outside the range of general fluctuations in the data) occurs at 1245 UT, with a delay of 5 min. The westward flow then died away gradually from ~500 to ~100 m s^{-1} over an interval of ~20 min, as previously observed in this MLT sector by *Todd et al.* [1988]. The IMF then turned south again at 1304 UT, with effects reaching the ionosphere at 1314 UT (third dashed lines).

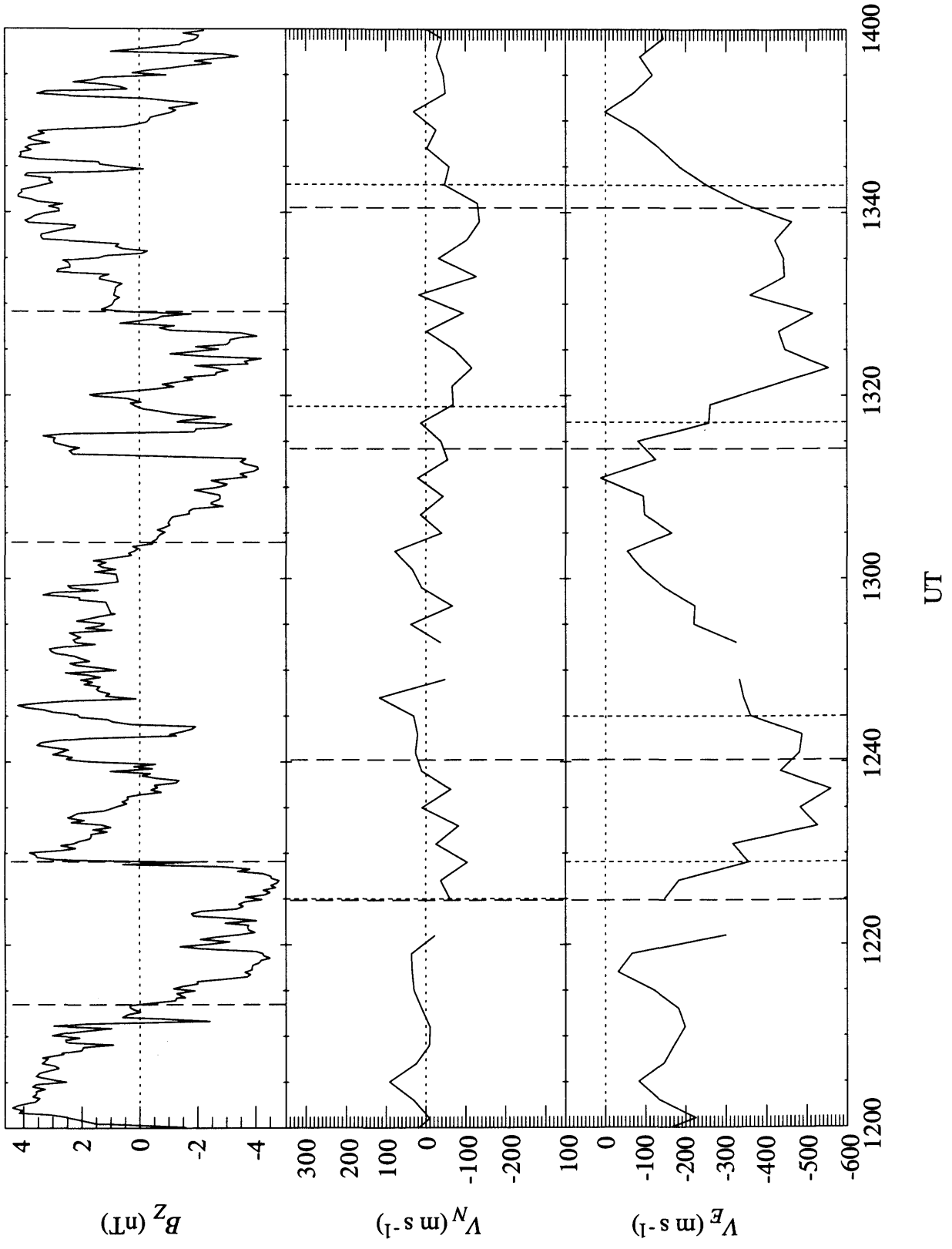

FIGURE 5.2 As for Figure 5.1, except for the interval 1200-1400 UT (1430-1630 MLT) on 16 March 1994

The first measurements exhibiting a clear enhancement in the flow are centred at 1319 UT in v_N, with a delay of 5 min, and at 1317 UT in v_E, with a delay of 3 min. Finally, an enduring northward turn took place at 1329 UT, reaching the ionosphere at 1341 UT (fourth dashed lines). Both flow components show a first clear response at 1343 UT, with a delay of 2 min, declining to small values over a ~10 min interval. Overall, therefore, small response delays in both flow components of typically ~5 min or less are inferred. These individual observations are therefore entirely compatible with the results of the cross-correlation analysis in this MLT sector discussed in the previous chapter (Figure 4.6), which show peak correlations with a delay of 4 min for the east-west flow component, though there are no significant responses in the north-south flow in the data set as a whole.

In Figure 5.3 corresponding data for the dayside dawn flow cell is shown, for the interval 0420-0620 UT (0650-0850 MLT) on 19 June 1996. Here sharp southward turns of the IMF were observed by IMP-8 at 0454, 0517, and 0542 UT (the second, third, and fifth dashed lines in the upper panel), which lead to excitation of relatively weak eastward and poleward flows (essentially simultaneously) at 0509, 0539, and 0601 UT (related dotted lines in the lower panels), with delays relative to first possible effects (related dashed lines in the lower panels) of 5, 12, and 8 min, respectively. Sharp northward turns were also observed at 0436 and 0531 UT (the first and fourth set of vertical lines), leading to decay of those flows starting at 0457 and 0551 UT, with delays relative to first effects of 10 and 9 min, respectively. Response delays are thus typically ~10 min in this interval, compatible with the cross-correlation results for the post-dawn flow shown previously in Figures 4.7 and 4.11.

Results from the event analysis on the dayside, in general, correspond very well with those results from the cross-correlation analysis in the previous chapter. Short delays (~2-4 min) are determined for those events located in the vicinity of noon with an indication of perhaps a slightly longer delay (~10 min) toward dawn. Delays determined from events in the afternoon sector seem to follow the trend of the short time delays around noon. In the following section, data taken from the evening and nightside sectors are presented, to try to establish the response of the directly-driven component of the flow to changes in the IMF B_z.

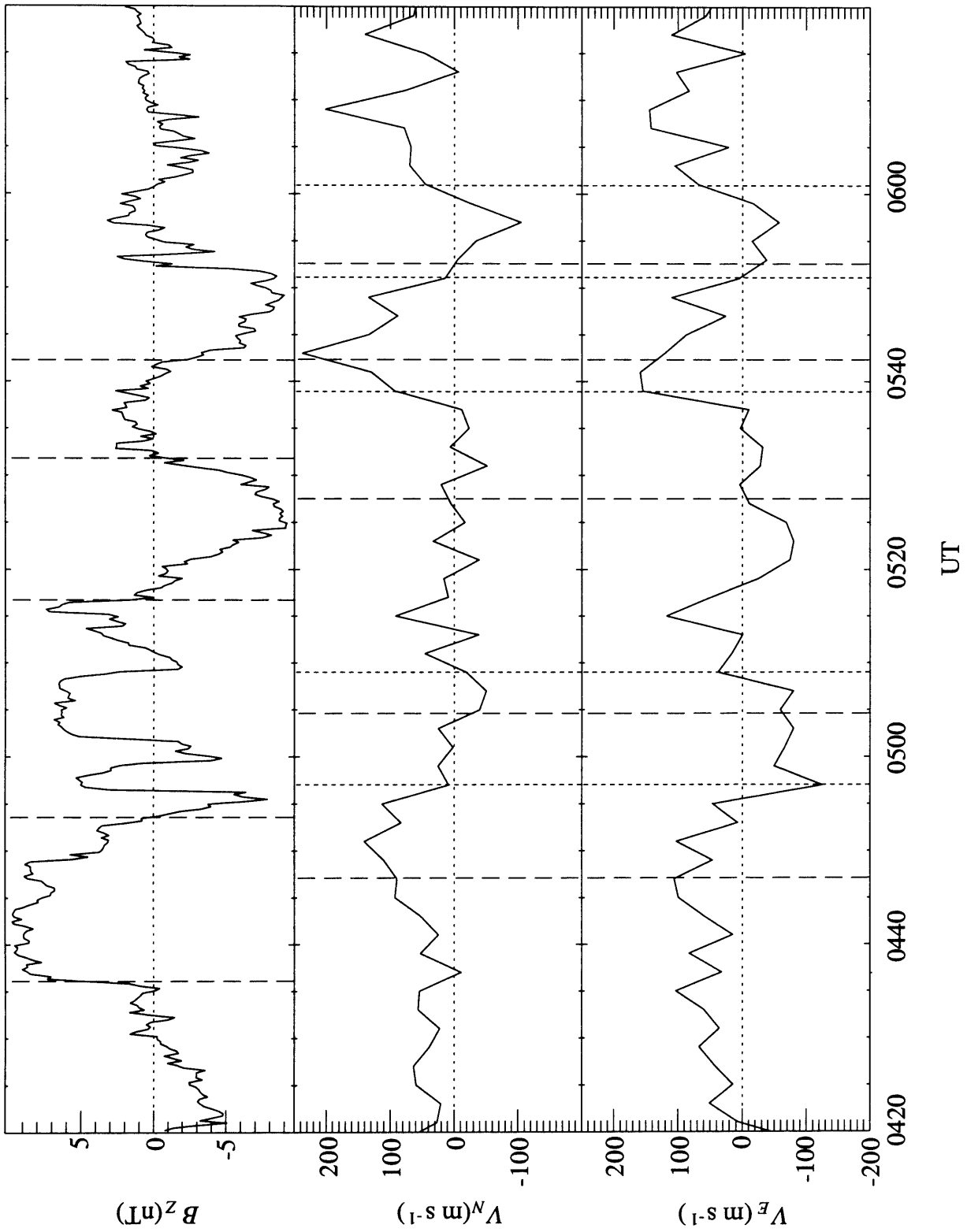

FIGURE 5.3 As for Figure 5.1, except for the interval 0420-0620 UT (0650-0850 MLT) on 19 June 1996

5.2.2 Results from the event analysis for data on the nightside

Figure 5.4 shows results for an interval spanning midnight, 2045-2245 UT (2315-0115 MLT) on 15 March 1994. Several potentially corresponding IMF and flow features appear during this interval, including the flow pulse centred on ~2135 UT which may be related to a brief interval of southward field beginning at ~2120 UT. However, attention is restricted here to the ~15 min surge in eastward flow centred near 2200 UT which appears to relate to an interval of southward IMF of similar duration centred near 2145 UT. Here the response delay after the southward turning is timed at 8 min, while that after the northward turning is 6 min. These values certainly lie within the range of those determined from the cross-correlation analysis in this MLT sector, as shown previously in Figure 4.11. It is worthwhile to comment that when considering the nightside flow data, magnetic records from the IMAGE and SAMNET magnetometer chains in the Scandinavian sector were examined in order to ensure that flow variations associated with substorms were not misidentified as IMF-related flow changes. Substorm process can be fairly readily identified from the magnetic data by observing Pi2 pulsations and associated enhancements in the ground magnetic signals (see §2.2.5). During the above interval, for example, a Pi2 signal was observed by stations of the SAMNET chain starting at ~2110 UT (indicated by the arrow in Figure 5.4), well before the flow enhancement discussed above, but no clear substorm-associated onset was related to the flow enhancement itself.

The last local time sector which is of particular interest is the nightside dusk region where results of a somewhat different character were observed as illustrated in Figure 5.5. These data were obtained for the 2 h interval spanning 1630-1830 UT (1900-2100 MLT) on 18 June 1996. In this interval a north to south switch in IMF B_z took place at 1701 UT (dashed line in the upper panel), following which (apart from brief intervals) a southward field of ~-1 to -3 nT then endured for more than 1.5 h. Thus not only the initial response of the flow can be discerned, but also its long-term behaviour under essentially continuous negative IMF B_z. The first effects of the southward turn are estimated to have arrived at the ionosphere at 1712 UT (dashed line in the lower panel), following which a weak equatorward flow and enhanced westward flow developed. The weak (~50-100 m s^{-1}) equatorward flows are present at and after 1717 UT (dotted line in the middle panel), with a delay of 5 min, while the westward flow developed more gradually over a ~40 min interval, with a less well-defined onset. The time beyond which this flow development is unquestionably in progress has been set at 1723 UT as marked by the dotted line in the

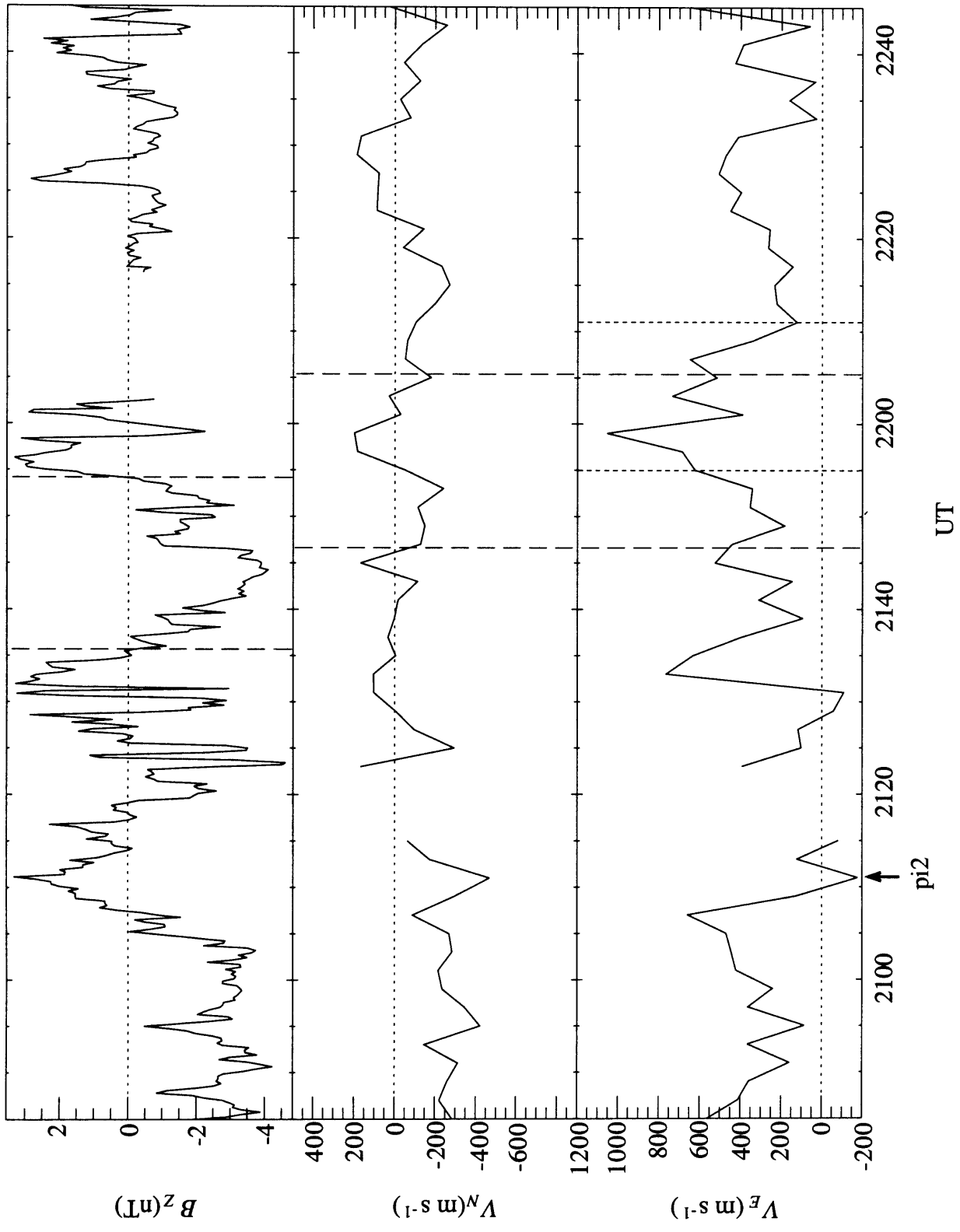

FIGURE 5.4 As for Figure 5.1, except for the interval 2045-2245 UT (2315-0115 MLT) on 15 March 1994

lower panel, with a delay of 11 min, though it could be argued as having started earlier, at the time of excitation of the equatorward flow. Significant further development of the westward flow, from ~100 to ~500 m s^{-1}, occurred gradually after this time, presumably related to the expansion of the region of open flux and flow cells during this interval. It may be remembered that the cross-correlation results for this MLT sector, shown in Figure 4.10 in the previous chapter, indicate peak correlations of the east-west flow with a lag of 34 min, with westward flows occurring for positive and small negative IMF B_z reversing to become eastward for large negative IMF B_z. The event shown here in Figure 5.5 indicates that the response of the east-west flow in this sector to the onset of relatively weak negative IMF B_z is a westward flow with a prompt onset (a delay of only ~5-10 min) which then develops in magnitude over a few tens of minutes, thus supporting the suggestion in the previous chapter that the long cross-correlation delays found for v_E in this MLT sector are related to the time scale for the expansion of the flow cells rather than to the initial excitation of flow. In the present example, however, the flow did not subsequently reverse to eastward as in the cross-correlation results, presumably because IMF B_z was not sufficiently negative for a sufficient interval. The flow speed of the solar wind was rather low during this interval, $V \approx 390$ km s^{-1}, such that with IMF B_z typically ~-2 nT we have $(V/500)^2 B_z \approx -1$ nT. It is then noted from Figure 4.10 that eastward flows are typically present in this MLT sector only for $(V/500)^2 B_z$ less than ~-4 nT. On the other hand, the rapid (5 min) response of the north-south component of the flow seen in Figure 5.5 is compatible with the results of the cross-correlation analysis for this flow component (Figure 4.10), which shows a broad peak near zero lag with an "error bar" spanning the range from -4 to +10 min.

5.3 Overall event analysis results and discussion

With the examples presented in the previous section illustrating the method employed to determine the response delays in this study, which naturally is not without its ambiguities on occasion, the remainder of the 300 h of simultaneous data was analysed in a similar fashion. The overall event analysis results are shown in Figures 5.6 and 5.7, where the flow response delay is plotted versus MLT. Results for the east-west flow component are shown in Figure 5.6 totalling ~69 individual events, where red symbols indicate response delays determined from flow enhancements following southward turns of the IMF (approximately two-thirds of events), while large blue symbols indicate delays

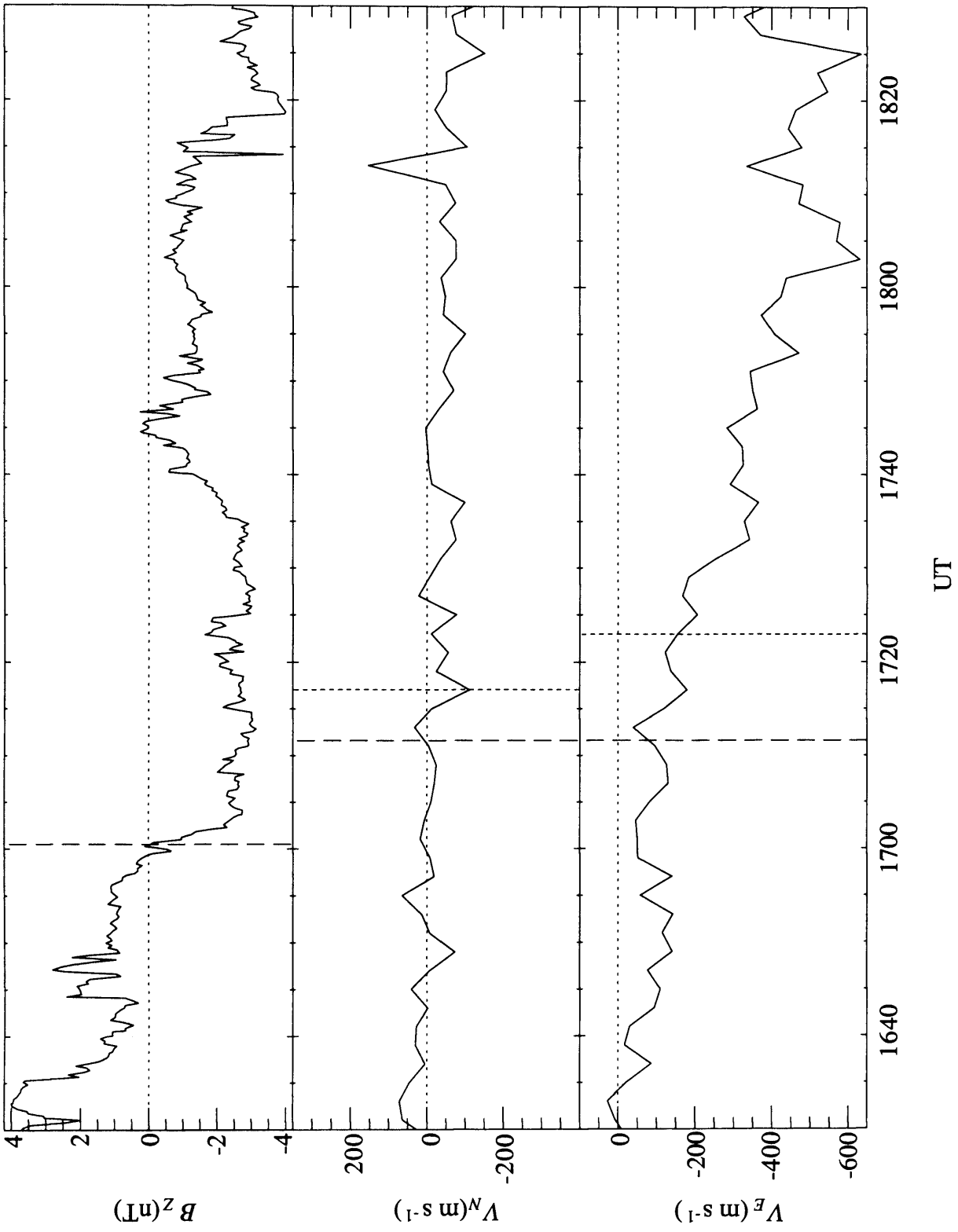

FIGURE 5.5 As for Figure 5.1, except for the interval 1630-1830 UT (1900-2100 MLT) on 18 June 1996

determined from flow decreases following northward turns. The observations are densely populated in the afternoon and early evening sectors since this is where the majority of the simultaneous data is located, but there are observations where the cross-correlation analysis (see Chapter 4) left gaps, e.g. the prenoon sector 0900-1000 MLT. For purposes of easy comparison, the results from the cross-correlation study (previously shown in Figure 4.11) are superposed over this figure, shown by the smaller black symbols with error bars joined by the dashed line. As in Figure 4.11, all circular symbols indicate the excitation of eastward flow for negative IMF B_z, usually corresponding to the dawn cell, while square symbols indicate that the excitation of westward flow for negative IMF B_z, usually corresponding to the dusk cell. Several points are worth noting. First, no distinction is apparent between the response delays determined from southward as opposed to northward turns of the field. Thus the propagation of information through the ionosphere concerning the onset of flow following a southward turn of the IMF appears to occur on essentially the same time scale as the propagation of the start of the decay following a northward turn. Second, the event analysis results are in overall agreement with the cross-correlation results, such that the values determined in a given MLT sector generally fall within the "error bars" of the cross-correlation values in that sector. The main exception occurs in the immediate post-dusk region, where, as stated in the previous section, the 'event' delays are typically short (~5-15 min) and comparable to results in the adjacent sectors, while the cross-correlation delays are much longer (~35 min). The origins of this effect have already been discussed in terms of the expansion of the flow pattern over the observation site (see §4.4.4). The nature of the event study allows the calculation of the response delay of the direct-driven ionospheric flow after changes in the IMF conditions are incident in the ionosphere. It is also noticeable, however, that the 'event' delays are typically a few minutes longer than the cross-correlation delays in the pre-noon east-west flow reversal region spanning 0800-1100 MLT. The origins of this difference are not obvious. Third, the results again show a minimum delay occurring in the immediate post-noon hours at ~1400 MLT, with a trend towards larger delays at night compared with the dayside. The average delay time for the dayside is 5.4±0.5 min shown in Table 5.1, compared with 3.1±0.8 min from the corresponding cross-correlation analysis also shown in this table. For the nightside, the average delay time is 11.6±1.4 min (Table 5.1), compared with 8.0±2.4 min from the cross-correlation analysis. The event

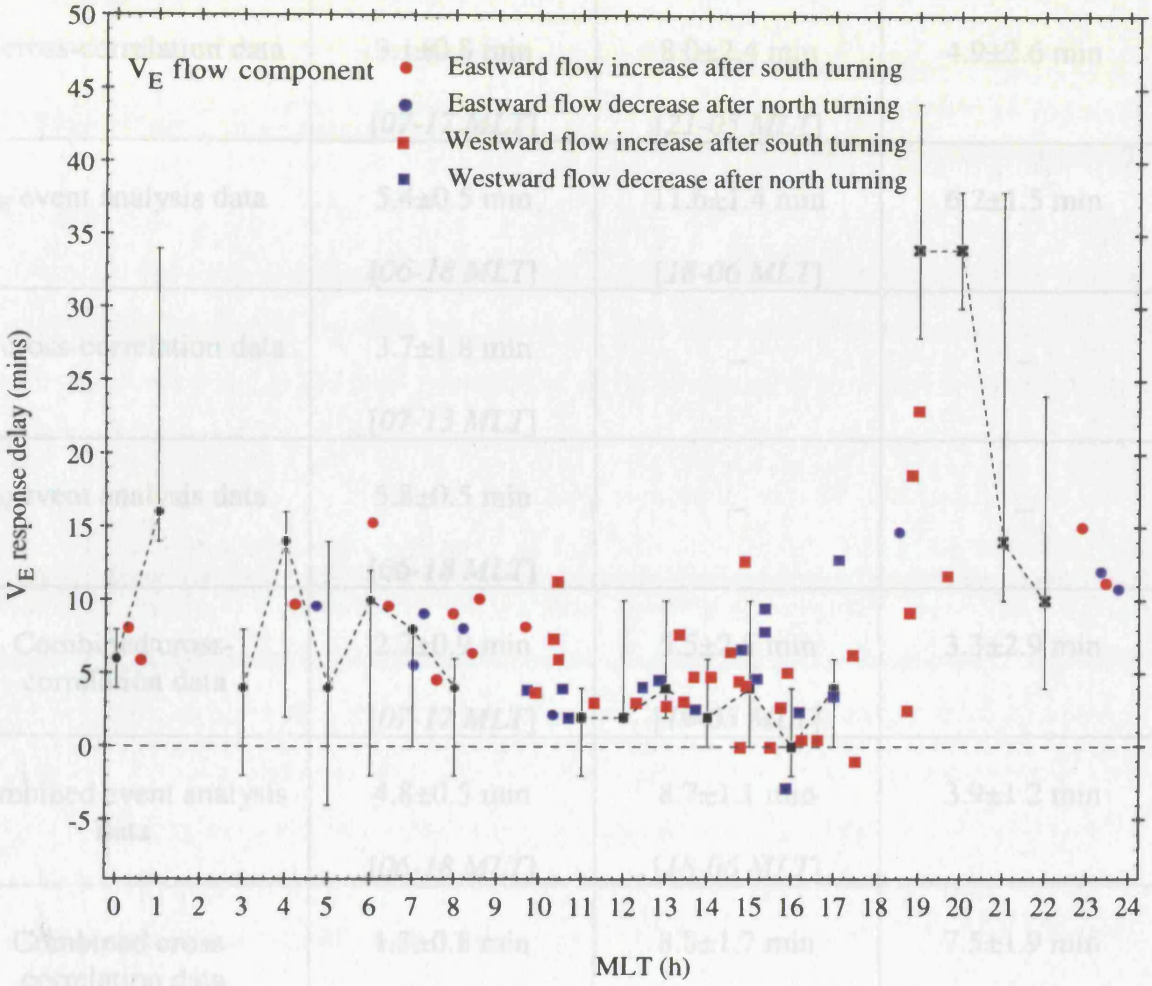

FIGURE 5.6 Ionospheric flow response delays versus MLT determined from the event analysis keyed to sudden changes in the sense of the north-south component of the IMF, for the east-west component of flow. Red symbols indicate delay times determined from the onset of increases in flow associated with southward turns of the IMF, while blue symbols indicate response delays determined from the onset of flow decay associated with northward turns of the IMF. Circular symbols indicate that the flow excited is eastward, generally corresponding to the dawn flow cell, while squares indicate the flow is westward, generally corresponding to the dusk flow cell. These data are plotted over the delay times determined from the v_E cross-correlation analysis as in Figure 4.11 (smaller black symbols with error bars joined by dashed lines)

Data set	Dayside response delay [*range of MLT*]	Nightside response delay [*range of MLT*]	Nightside-dayside delay difference
v_E cross-correlation data	3.1±0.8 min [*07-17 MLT*]	8.0±2.4 min [*21-05 MLT*]	4.9±2.6 min
v_E event analysis data	5.4±0.5 min [*06-18 MLT*]	11.6±1.4 min [*18-06 MLT*]	6.2±1.5 min
v_N cross-correlation data	3.7±1.8 min [*07-13 MLT*]	–	–
v_N event analysis data	5.8±0.5 min [*06-18 MLT*]	–	–
Combined cross-correlation data	2.2±0.9 min [*07-17 MLT*]	5.5±2.5 min [*19-05 MLT*]	3.3±2.9 min
Combined event analysis data	4.8±0.5 min [*06-18 MLT*]	8.7±1.1 min [*18-06 MLT*]	3.9±1.2 min
Combined cross-correlation data	1.3±0.8 min [*09-19 MLT*]	8.8±1.7 min [*21-07 MLT*]	7.5±1.9 min
Combined event analysis data	4.8±0.5 min [*08-20 MLT*]	9.2±0.8 min [*20-08 MLT*]	4.4±0.9 min

TABLE 5.1 Averaged flow response delays in different local time sectors derived from the various data sets employed in the event study, together with the results from the cross-correlation study.

analysis delay times for v_E are thus in reasonable accord with the cross-correlation delay times, though typically longer by ~2-3 min (corresponding to one or two flow data points).

Results for the north-south component are shown in Figure 5.7 in a similar format to Figure 5.6, except that circular symbols indicate equatorward flow for negative IMF B_z, while square symbols indicate poleward flow (as in Figure 4.12). The average response delay determined from the dayside data is 5.8±0.5 min, again comparable with the corresponding dayside cross-correlation result of 3.7±1.8 min. The number of nightside determinations and their distribution in MLT is insufficient to allow a meaningful average to be taken.

As with the cross-correlation results, both the east-west and north-south flow 'event' data have been combined together, by taking the true response delay to correspond to the first response observed in the flow irrespective of the component in which it was observed. Therefore, in Figure 5.8 this minimum delay time versus MLT is shown for all 69 events analysed in this study. The red symbols represent results obtained from flow enhancements following southward turns of the IMF (46 events), while the blue symbols represent results from the onset of flow decays following northward turns of the IMF (23 events). As before, no systematic differences are observed between these cases. Similarly, square symbols indicate that the first response was seen in the east-west flow component (38 events), circular symbols that the first response was seen in the north-south flow component (18 events), and triangles indicate simultaneous responses in both components (13 events). No clear MLT trends are observed in these types of response. However, evidence is again obtained of increasing delays from dayside to nightside, with minimum delays in the post-noon sector. The average delay for the dayside data is 4.8±0.5 min, while the average for the nightside data is 8.7±1.1 min (Table 5.1). Noting the post-noon minimum, however, if instead the average is taken over the 12-h sector centred on 1400 MLT a value of 4.8±0.5 min as before is found, while if the average over the 12-h sector centred on 0200 MLT is calculated, a value of 9.2±0.8 min is obtained (Table 5.1). To illustrate this difference directly, Figure 5.9 shows normalised histograms of the distribution of delay times for the 12-h sector centred on 1400 MLT (Figure 5.9a), and for the 12-h sector centred on 0200 MLT (Figure 5.9b). The data are shown in 2-min bins, normalised to the total number of events in the two regions. The average values given above are indicated by the arrow and dot-dashed line. The two distributions are clearly different, with the nightside values being shifted to longer delay times compared with the

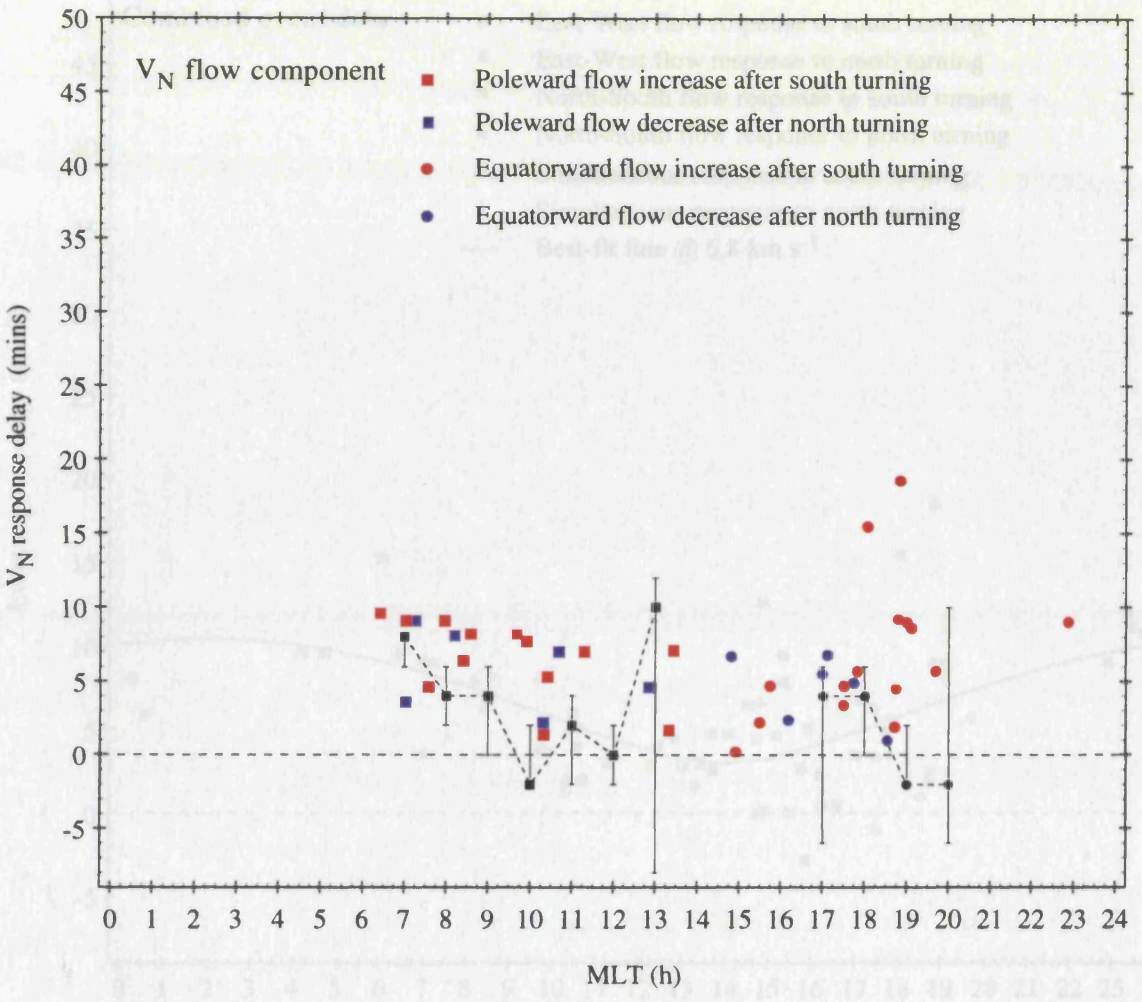

FIGURE 5.7 As for Figure 5.6, except for the north-south flow component. The square symbols indicate poleward flow, while the circular symbols indicate equatorward flow. These data are plotted over the delay times determined from the v_N cross-correlation analysis as in Figure 4.12 (smaller black symbols with error bars joined by dashed lines)

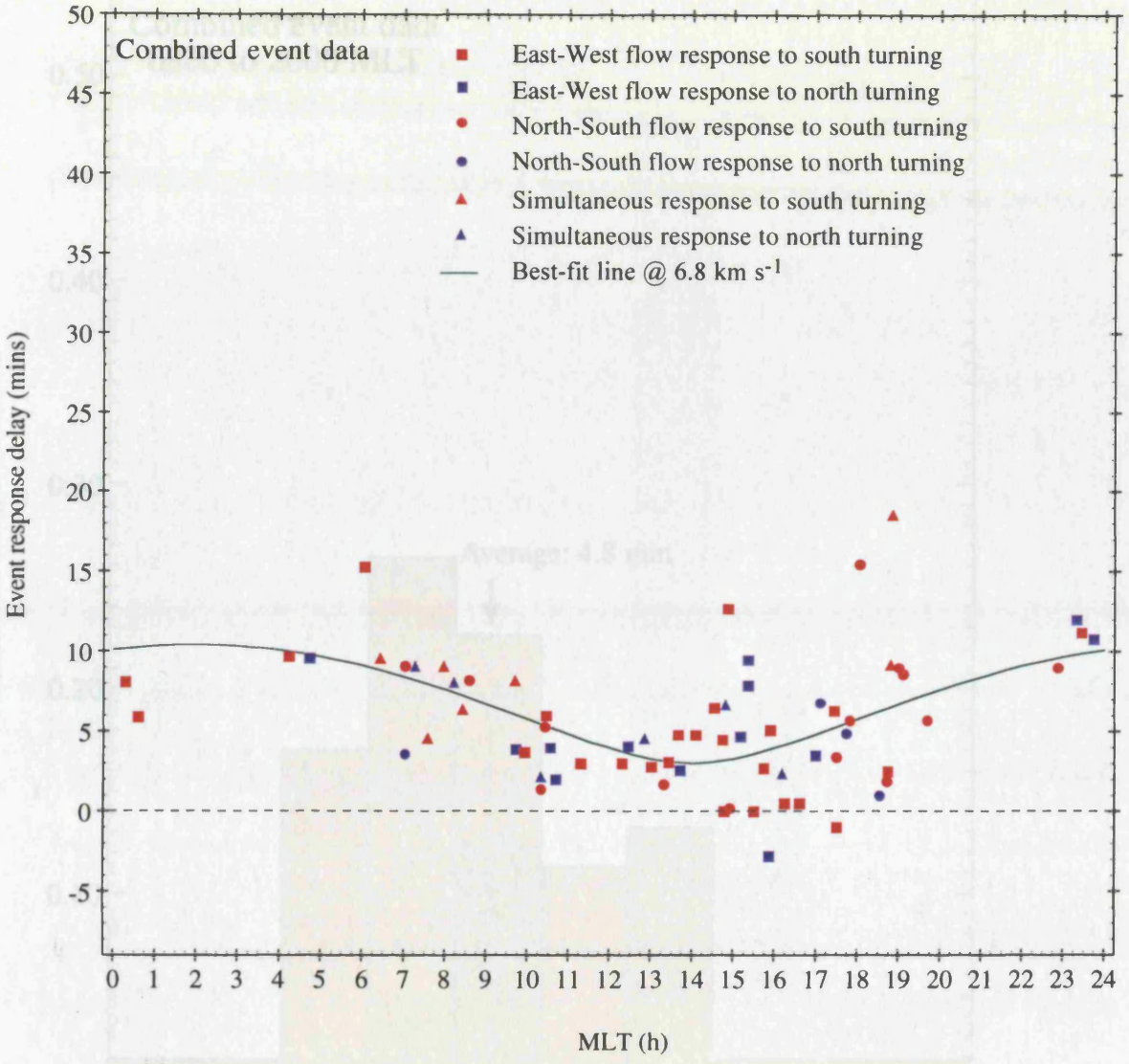

FIGURE 5.8 As for Figure 5.6, except that the minimum delay is shown for each event, irrespective of which flow component is involved. Red symbols indicate responses to southward turns of the IMF, while blue symbols indicate responses to northward turns of the IMF. Responses observed first in the east-west flow component are shown by squares, while those observed first in the north-south component are shown by circles. If both components responded simultaneously the symbol is plotted as a triangle. These data have been least-squares fit to the same simple theoretical model as in Figure 4.13, shown by the solid green line. In this case the best-fit epicentre of information propagation was also found to lie at 1400 MLT, while the expansion phase speed was found to be 6.8 km s^{-1}

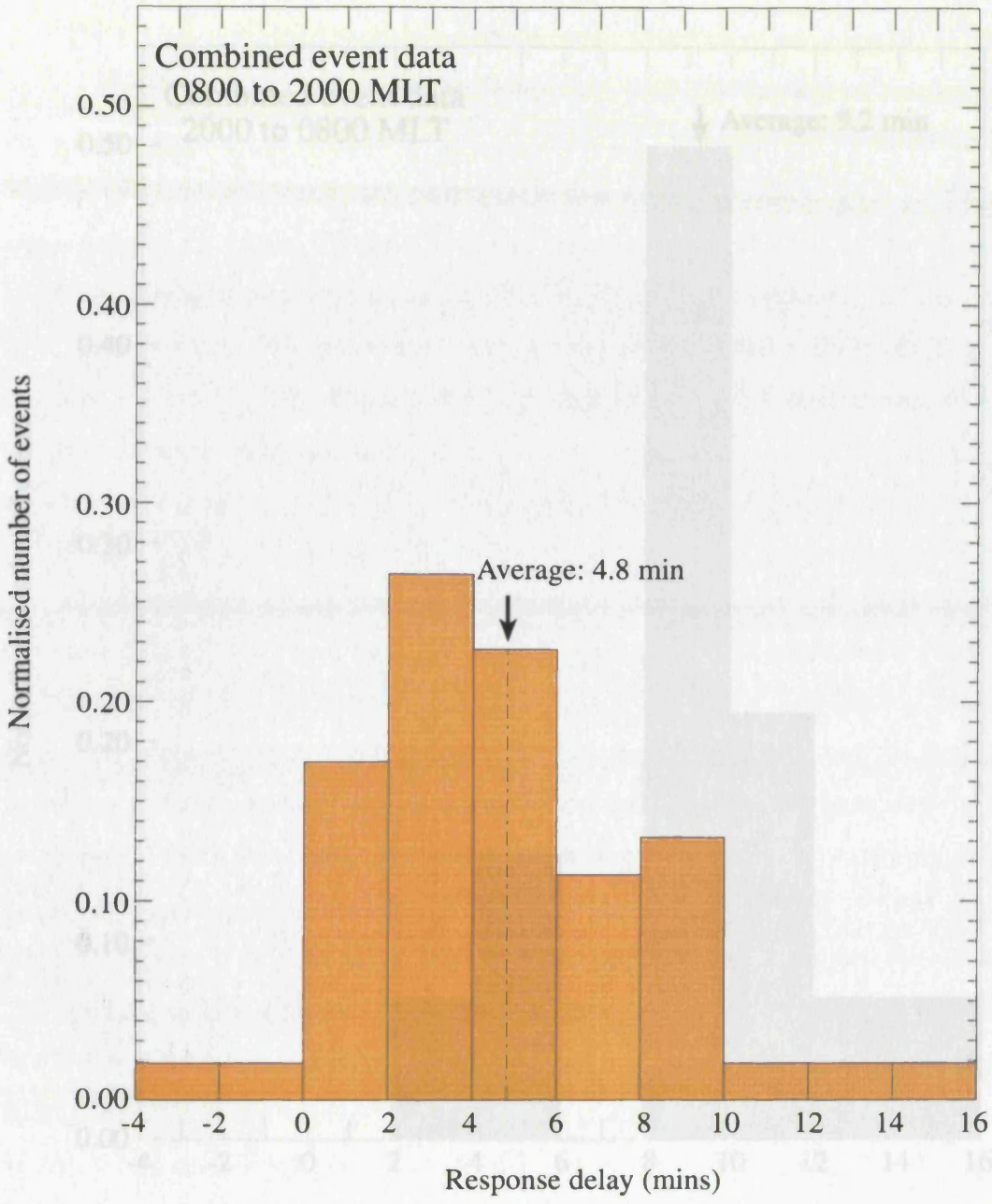

FIGURE 5.9a Histogram showing the normalised distribution of the number of events contributing to each 2-min bin of ionospheric flow delay time, for the 12-h local time sector centred on 1400 MLT. The average delay of all the dayside events is marked by the arrow and dot-dashed line

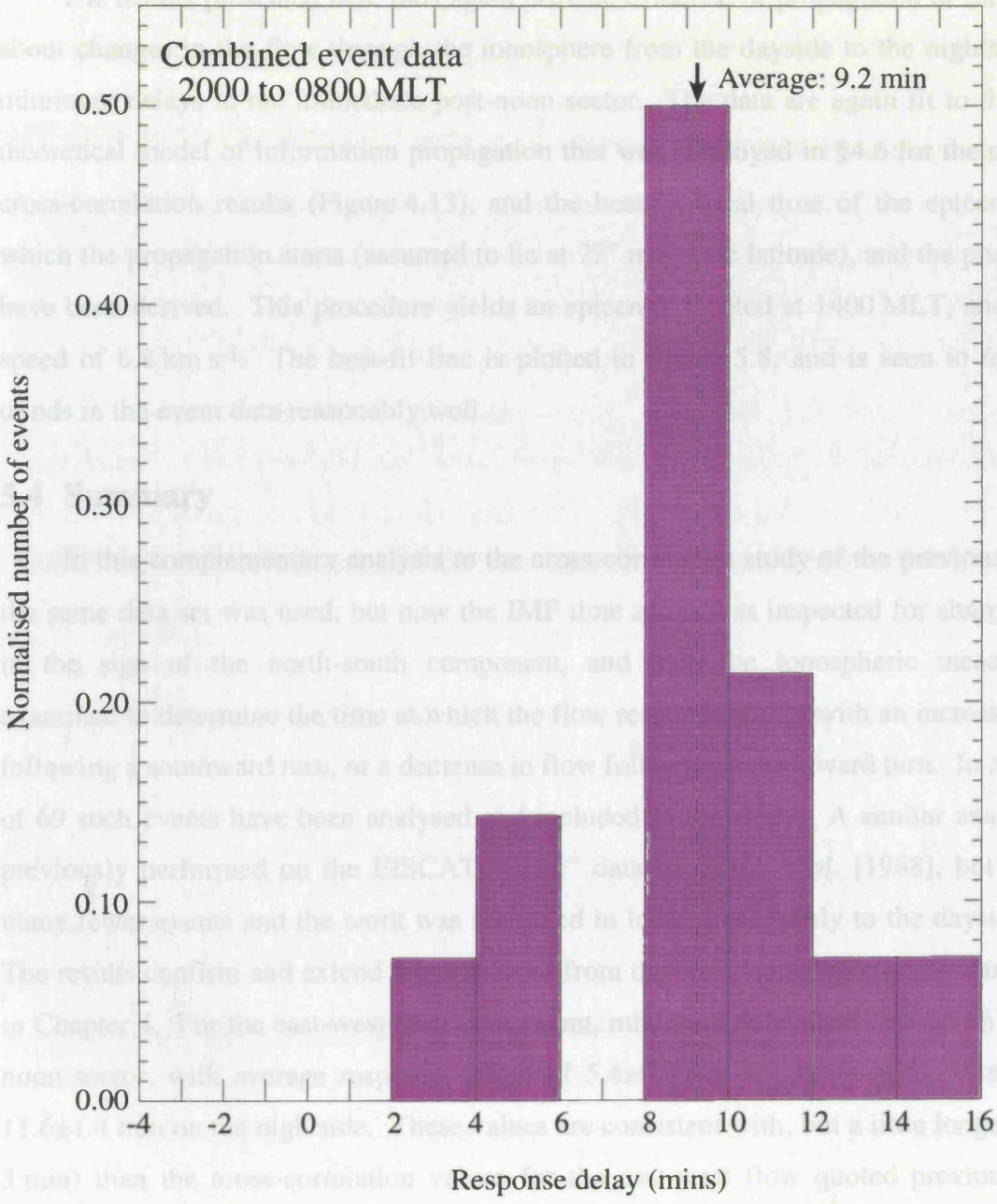

FIGURE 5.9b. As for Figure 5.9a except for the 12-h local time sector centred on 0200 MLT

dayside values. Even so, it should again be emphasised that the delay times are found to be relatively short at all local times, with the difference between the 1400 MLT sector and 0200 MLT sector average values being only 4.4±0.9 min.

The results presented here thus again provide evidence of propagation of information about changes in the flow through the ionosphere from the dayside to the nightside, with minimum delays in the immediate post-noon sector. The data are again fit to the simple theoretical model of information propagation that was employed in §4.6 for the combined cross-correlation results (Figure 4.13), and the best fit local time of the epicentre from which the propagation starts (assumed to lie at 77° magnetic latitude), and the phase speed have been derived. This procedure yields an epicentre located at 1400 MLT, and a phase speed of 6.8 km s^{-1}. The best-fit line is plotted in Figure 5.8, and is seen to follow the trends in the event data reasonably well.

5.4 Summary

In this complementary analysis to the cross-correlation study of the previous chapter, the same data set was used, but now the IMF time series was inspected for sharp changes in the sign of the north-south component, and then the ionospheric measurements examined to determine the time at which the flow responds, either with an increase in flow following a southward turn, or a decrease in flow following a northward turn. In all, a total of 69 such events have been analysed and included in the study. A similar analysis was previously performed on the EISCAT "Polar" data by *Todd et al.* [1988], but included many fewer events and the work was restricted in local time mainly to the dayside hours. The results confirm and extend those derived from the cross-correlation study summarised in Chapter 4. For the east-west flow component, minimum delays are centred on the post-noon sector, with average response delays of 5.4±0.5 min on the dayside, increasing to 11.6±1.4 min on the nightside. These values are consistent with, but a little longer (by ~2-3 min) than the cross-correlation values for the east-west flow quoted previously. No distinction was apparent between the response times determined from the onset of flow excitation following southward turns, and the onset of flow decay following northward turns. For the north-south flow component, the dayside average was found to be 5.8±0.5 min, with insufficient event determinations being available on the nightside to take a meaningful average.

The event data for both flow components were also combined together, and the flow response delay taken to correspond to the first flow change observed in each event,

irrespective of which component is involved. These data again show a minimum delay in the post-noon sector, with increased response delays on the nightside. When the simple theoretical model outlined above is fitted to this data, it is found that the best fit is again obtained for an epicentre of information propagation centred on 1400 MLT, with a phase speed of 6.8 km s^{-1}. The average of the delays for the 12-h sector centred on 1400 MLT was found to be 4.8±0.5 min, increasing to 9.2±0.8 min for the 12-h interval centred on 0200 MLT.

It may be noted that the post-noon minimum in the response delay found here (and in the cross-correlation analysis) was also observed in the earlier studies by *Etemadi et al.* [1988] and *Todd et al.* [1988]. This asymmetry may possibly reflect the Parker spiral structure of the IMF, which should generally produce a 'first contact' of a similarly oriented interplanetary tangential discontinuity with the post-noon magnetopause. Examination of our interplanetary data shows that the plane of the discontinuities were indeed preferentially oriented in this direction. The phase speed of propagation is also consistent with the values deduced from the earlier, more limited, studies by *Etemadi et al.* [1988], *Todd et al.* [1988], *Lockwood et al.* [1993b], and *Saunders et al.* [1992], whose data are consistent with values in the range 5-10 km s^{-1}. The short (several minute) response delays found here are also consistent with the overall delays of 8±8min found in the study presented by *Ridley et al.* [1998]. However, the latter authors also interpreted their data as indicating an essentially simultaneous response (within ~1 min) at all local times over the high-latitude region. This conclusion is not in accord with the finding of longer response times on the nightside than on the dayside, as indicated by results from the event study and the statistical study, though the difference between the day-night responses is only ~6 min (Table 5.1). Finally we note that the response times determined from the two studies are much shorter than the values of ~20-30 min determined by *Hairston and Heelis* [1995] using DMSP spacecraft data. We thus concur with these authors that the response times which they deduced are more characteristic of the development of the flow pattern as a whole following changes in the IMF, rather than the IMF-modulated flow excitation and decay delay which has been the primary concern here.

CHAPTER 6

Effect of the IMF B_y component on the flow on closed auroral zone field lines

6.1 Introduction

The large-scale flow in the high-latitude ionosphere is strongly modulated by the strength and orientation of the IMF, with the most significant flow enhancements associated with the IMF B_z component, principally during southward ($-B_z$) conditions [e.g. *Reiff and Burch*, 1985; *Weimer*, 1995]. The flow effects in response to the polarity changes of the IMF B_z component have previously been discussed in depth in Chapter 4 and 5. However, the flow is also known to respond to the IMF B_y, on both open and closed field lines, as has been described in §2.2.4. The overall effect of IMF B_y on open field lines can be described to a first approximation as the addition of a zonal westward circulation to the antisunward flow for positive B_y in the northern hemisphere, and an eastward zonal circulation for negative B_y, and vice versa for the southern hemisphere. These flow perturbations correctly describe the flows in the cusp region immediately poleward of the open-closed field line boundary associated with the Svalgaard-Mansurov effect in ground-based cusp magnetic data [e.g. *Jørgensen et al.*, 1972; *Friis-Christensen and Wilhjelm*, 1975; *Iijima et al.*, 1978] and the asymmetric flows over the polar cap [e.g. *Heppner*, 1972; *Heppner and Maynard*, 1987].

On closed field lines the IMF B_y influence, as described in §2.2.4, is observed to produce an apparent lack of conjugacy between the flows in the northern and southern hemispheres [*Newell et al.*, 1989; *Holzworth and Meng*, 1984], implying that the magnetic field must be distorted in the presence of IMF B_y such that actual conjugacy is maintained. *Cowley* [1981] and *Cowley et al.* [1991] showed theoretically that through the addition of a simple magnetospheric perturbation field in the direction of IMF B_y the required asymmetries observed on closed field lines could be produced, as is illustrated in Figure 2.8. Subsequently, such a perturbation field has been observed in geosynchronous orbit data, corresponding to a dipole magnetic latitude of 67° in the ionosphere [*Cowley and Hughes*, 1983; *Wing et al.*, 1995].

In this chapter, therefore, a detailed study of the auroral zone ionospheric flow under the influence of IMF B_y will be presented using tristatic velocity measurements obtained from the EISCAT UHF radar overhead at Tromsø (66.3° magnetic latitude) and IMF B_y data from the IMP-8 spacecraft. The data set totalled ~300 h and a cross-correlation analysis was conducted to determine the effect of IMF B_y on the flow in the closed field line region. Also, in a similar manner to the work of *Cowley* [1981] and *Cowley et al.* [1991], the field line distortions which are produced by the addition of a perturbation field in the direction of IMF B_y were modelled, and the flow perturbations determined and compared with those obtained from the statistical analysis.

6.2 Data sets and cross-correlation procedure

The data sets used in this study were the same as that for the previous cross-correlation study with IMF B_z described in Chapter 4. Approximately 300 h of tristatic velocity vectors measured overhead at Tromsø, located in the auroral zone at a magnetic latitude of 66.3°, using the EISCAT UHF radar running the CP-1-K programme, were combined with IMF B_y data from the IMP-8 spacecraft. Since the velocity data are integrated over 2 min intervals, the IMF data were similarly averaged after subtraction of the propagation delay from the spacecraft to the cusp ionosphere (see §4.2). The velocity components, v_E and v_N, were then separated into overlapping 2 h intervals of local time, as before, and cross-correlated with IMF B_y over time lags of ±120 min having further separated the IMF B_y data according to the sign of the simultaneous IMF B_z prior to cross-correlation. By dividing the IMF B_y data in this fashion any differences observed between the two sets of cross-correlation results can be attributed to the appropriate IMF B_z polarity. Since the ionospheric flow is strongest in the presence of southward IMF conditions, as shown previously, one would initially assume that the perturbation effect of IMF B_y would also be more apparent under these conditions. Figures 6.1 and 6.2 show two examples of the cross-correlation results obtained in the 2 h intervals 1500-1700 MLT and 2000-2200 MLT respectively. In the first interval, the cross-correlation results for each velocity component and IMF B_y during northward IMF conditions are shown, whereas the second interval shows results obtained during southward IMF conditions. The data is presented in the same format as Figures 4.5-4.10, described in §4.4.3. The top graphs present the cross-correlation results for v_E (left panel) and v_N (right panel), whereas the bottom graphs show the corresponding scatter plots for the respective flow components versus B_y derived for a particular lag from the correlation curve. The solid line in the

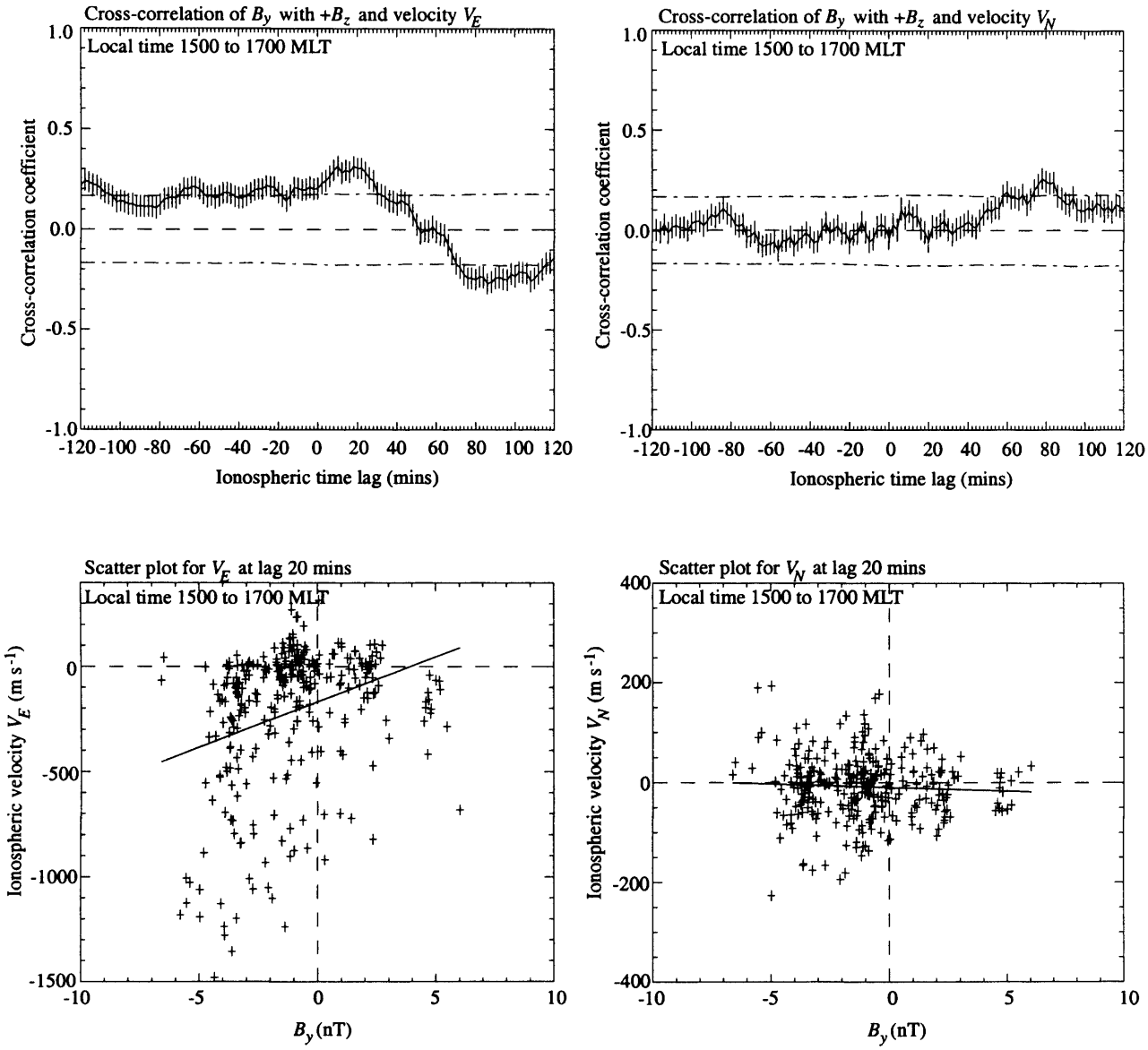

FIGURE 6.1 Cross correlation results of IMF B_y with v_E and v_N during positive IMF B_z conditions in the 2 h interval 1500-1700 MLT. These plots are in the same format as those previously described in Chapter 4 (Figures 4.5-4.10). The v_E correlation results are shown on the left, while those for v_N are shown on the right. The dot-dashed lines indicate the 99.9% significane level as determined from the Student's t-test. The scatter plots for each component are shown below, calculated at a lag of 20 min. The solid line in the scatter plots is the linear least-squares fit line from which the gradient and intercept are determined.

scatter plots represents the least-squares best fit to the data, giving an indication of how the flow varies as a function of IMF B_y. The dot-dashed lines on the cross-correlation plots represent the 99.9% significance level as derived from the Student's t-test.

In both these examples, the most noticeable feature is the broad nature of the cross-correlograms, with positive correlations present over several tens of minutes. In the left panel of Figure 6.1 (v_E correlation) many of the cross-correlation coefficients lie above the 99.9% significance level, indicating that many of the correlation coefficients are statistically significant, despite the low cross-correlation value. A peak in the cross-correlation coefficient occurs at a lag of ~10 min, though the correlation coefficients are similar over a range ~10-22 min. Many of the cross-correlograms obtained for the dayside hours showed a distinct lack of peaks in the data set, suggesting that although a response to IMF B_y was apparent in the data, the actual response delay was not clearly determined. The most likely explanation for this can be thought of in terms of IMF B_y having long periods of consistent sense over the range of individual data sets which contribute to a particular 2 h MLT interval. By combining different 2 h bins of data in which IMF B_y has been consistently positive or negative over the range, the resulting cross-correlogram would show the effect of IMF B_y on the velocity but would not produce a peak highlighting the delay at which the response occurred. To investigate the persistence of the IMF B_y data set, auto-correlation functions were determined for several 2 h intervals and compared with the corresponding auto-correlation of IMF B_z for which clear peaks in the cross correlograms were generally observed. In general, the IMF B_y results produced a broad auto-correlation peak in comparison to that obtained for IMF B_z, indicating that there is more persistence in the IMF B_y data set than in the IMF B_z, as would be expected. Thus, in order to examine the effect of IMF B_y on the ionospheric flow in detail, physically reasonable standard delays of 10, 20, 30 min were taken for all MLT. As indicated in the previous chapter, the excitation and decay time scale is ~10 min, while full reconfiguration takes ~30 min. The bottom panels in Figure 6.1 show the scatter plots corresponding to the particular cross-correlation results at a delay of 20 min, with the bottom left panel showing results for the east-west velocity. The scatter plot for this flow component illustrates the reason for the strong correlation with an obvious trend in the data brought about by the westward decreasing flow as IMF B_y increases to more positive values. The most important result from the scatter plot is the gradient of the regression line as this provides information about the variation in the ionospheric flow in response to IMF B_y, per nT of the IMF field. Thus it gives a measure of the perturbation flow generated in the presence of

IMF B_y, in units of m s^{-1} per nT of IMF B_y. The slope of the regression line for this flow component is calculated as ~40 m s^{-1} nT^{-1}.

In contrast to these large correlation values, the north-south velocity does not show any response to IMF *By*. The cross-correlogram shows a minimal response in this flow component with the cross-correlation coefficients averaging around zero over most of the delay range. Similarly the scatter plot, again generated at a lag of 20 min, shows that the flow does not appear to alter in the presence of IMF B_y, although there is a very small negative tilt to the regression line, indicating an equatorward flow as IMF B_y turns positive. However, since the cross-correlation coefficients are so small, it is probable that this effect is due to the random variations in the flow data, as opposed to anything distinctly linked to IMF B_y.

Moving onto Figure 6.2, cross-correlation results for the 2 h interval 2000-2200 MLT are presented using IMF B_y data with southward IMF B_z conditions. Again there is an extended range of strong positive correlation coefficients with v_E (top left panel) for several tens of minutes centred on ~30 mins. The broad and flat nature of the cross-correlogram is also consistent with the persistence in IMF B_y, as was described previously. Nevertheless there is a strong response in this flow component to IMF B_y and this is illustrated in the scatter plot plotted below for a lag of 20 min. The flow clearly turns eastward for positive B_y with the regression line indicating a strong positive gradient of ~40 m s^{-1} nT^{-1}. Similar scatter plots were obtained for the other two standard delays used and will be presented in the form of summary plots in the following section.

The left-hand panels show the correlation results for the northward velocity component, with many of the cross-correlation coefficients near zero. There is a slight excursion to higher positive correlation values between ~10-40 min, suggestive of poleward flow for positive IMF B_y. This is confirmed by the scatter plot displayed below for a lag of 20 min, with decreasing equatorward flow as IMF B_y increases to more positive values. However the perturbation effect associated with this flow component is only ~8 m s^{-1} nT^{-1}, which is very small in comparison with the other flow component.

Having now presented two examples illustrating the form of the cross-correlation obtained in this study, it is instructive to view the results as a function of local time to try to identify any trends in the response to IMF B_y.

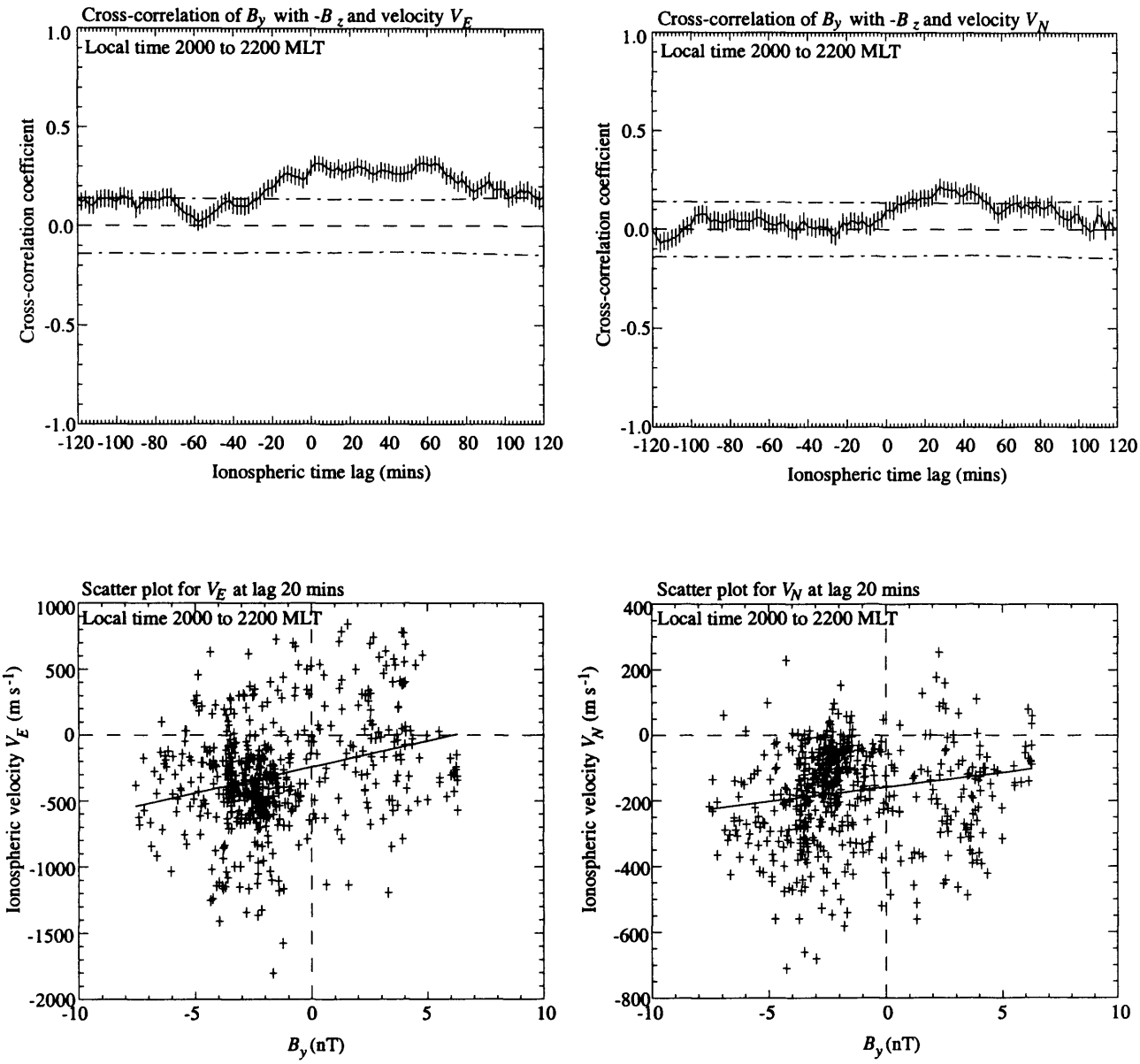

FIGURE 6.2 Cross correlation results of IMF B_y with v_E and v_N during negative IMF B_z conditions in the 2 h interval 2000-2200 MLT. See text for details.

6.3 The B_y-associated perturbation flow: Observations

Figures 6.3 and 6.4 present stacked plots of the overall results from the cross-correlation study for negative and positive IMF B_z conditions respectively, with the panel on the left showing the results for the v_E component, while that on the right shows the results for the v_N component. From the top down, these panels show the cross-correlation coefficient, followed by the probability that this value occurred by chance, the slope of the regression line in m s^{-1} nT^{-1}, and finally the intercept of the regression line given in m s^{-1}, representing the flow component value for B_y=0. The three coloured lines (blue, green and red) represent the three delay times (10, 20, 30 min respectively) used to calculate the parameters. In the top panels the error bar shows the standard error of the cross-correlation coefficient given by the equation quoted in §4.4.3, and is only plotted here on the line representing the 20 min delay time. This is simply to give an indication as to the relative importance of those correlation coefficients obtained on the dayside and nightside.

Looking at all three coloured lines, there does not appear to be much difference between the results from the different delay times, indicating that the cross-correlograms are fairly consistent over the times shown. The cross-correlation coefficients for the v_E data (left panel) are small over the dayside with corresponding high probability values, and increasing correlation coefficients over the nightside where the probability values are much smaller. The high probabilities suggest that these values could be within the noise of the data, whereas where the probability is lower the results are more reliable, such as those on the nightside. There is, nevertheless, a consistency in the data particularly on the nightside, with large positive correlations over many hours of local time. Correspondingly, the 'gradient' of the regression line is also large and positive in these regions, implying that an eastward perturbation flow is present for positive IMF B_y, and a westward flow for negative IMF B_y. The result is apparent in both left-hand panels (v_E results) of Figures 6.3 and 6.4, although the cross-correlation results are slightly more scattered in Figure 6.4. However, the trend in the data is still present, with the 'gradient' indicating the size of the perturbation flow.

On the right of these figures, the results from v_N are shown in a similar format. Here, again, although the cross-correlation coefficients are weak there appears to be a noticeable effect. In Figure 6.3, the v_N correlation results show the presence of small equatorward perturbation flows between ~0400-1300 MLT (negative correlation values), and small poleward perturbation flows over the afternoon and nightside sectors for positive IMF B_y.

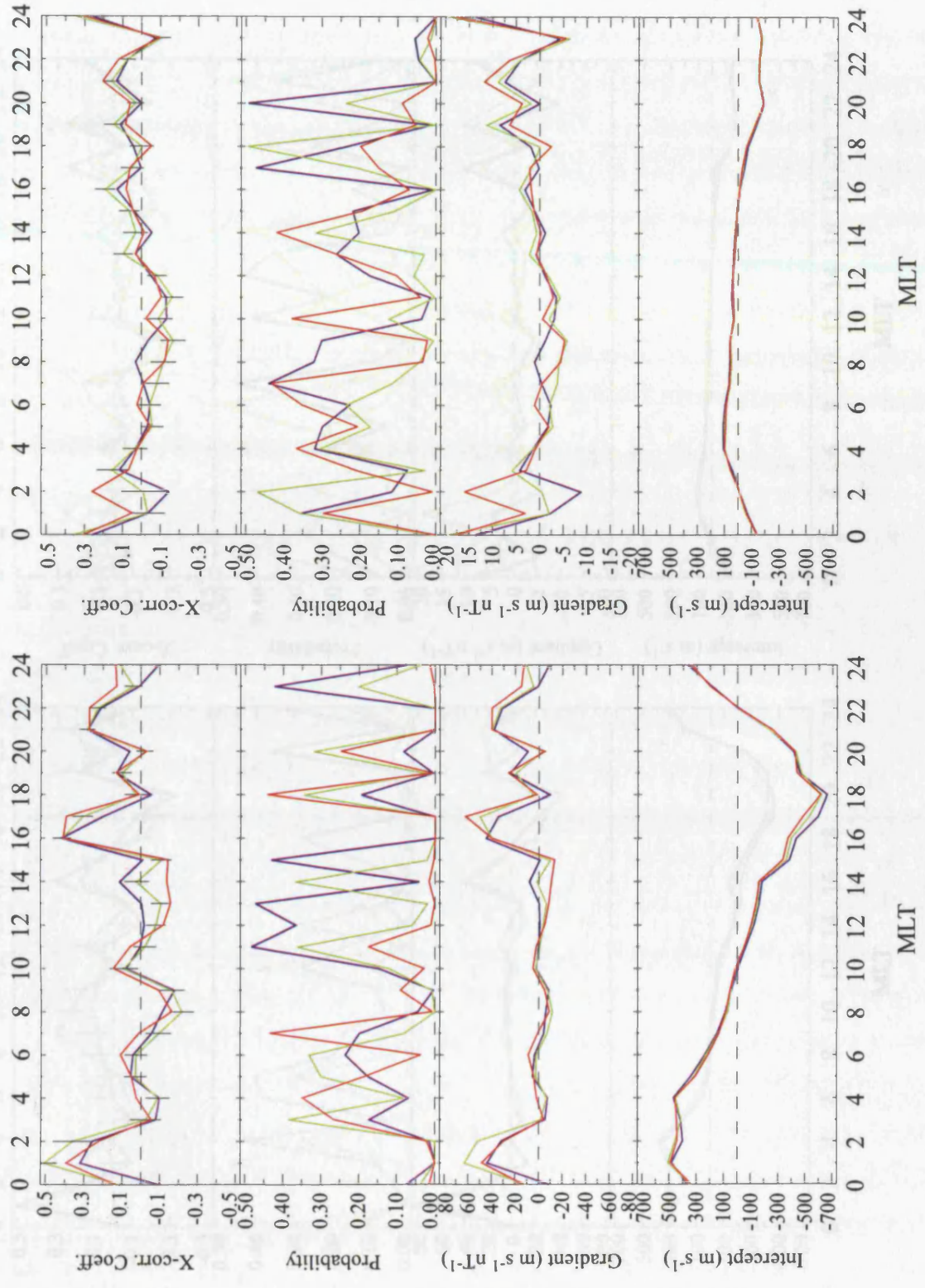

FIGURE 6.3 Stacked plots presenting the overall IMF B_y cross-correlation results during southward IMF conditions versus local time. Left panel shows the results from the v_E component, and the right panel presents the results from v_N. Four parameter are shown: the cross correlation coefficient, the probability that this value occurred by chance, the gradient of the regression line and the intercept value. The three coloured lines indicate the three delay times, 10, 20 and 30 mins, used to determine the gradient and the intercept values from the scatter plots.

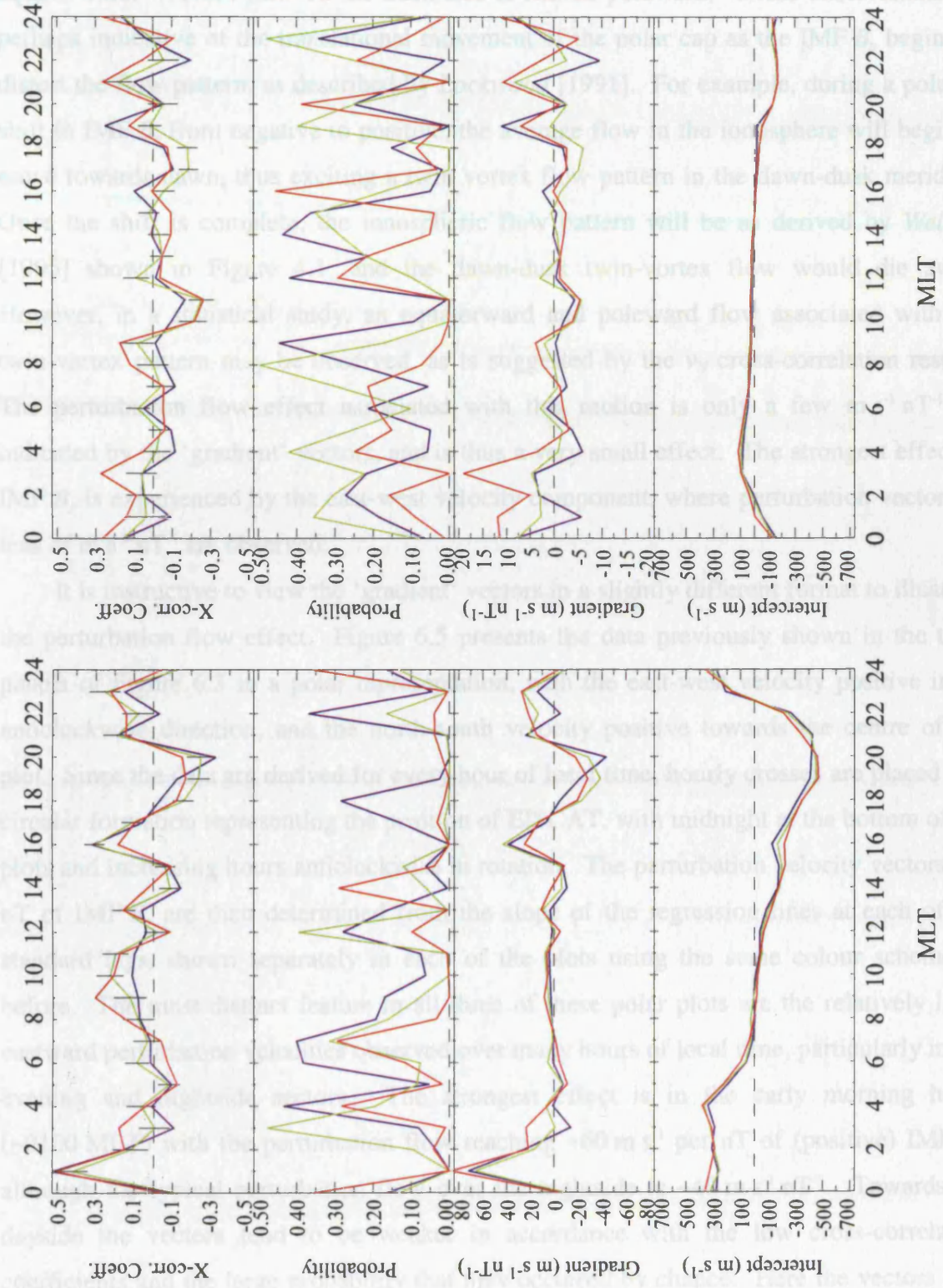

FIGURE 6.4 Same format as Figure 6.3 except now showing the IMF B_y cross-correlation results during northward IMF conditions.

This implies that for positive IMF B_y, flow on the dawn side is preferentially shifted equatorward, whereas flow on the dusk side is shifted poleward. These observations are perhaps indicative of the translational movement of the polar cap as the IMF B_y begins to distort the flow pattern, as described by *Lockwood* [1991]. For example, during a polarity shift in IMF B_y from negative to positive, the average flow in the ionosphere will begin to move towards dawn, thus exciting a twin vortex flow pattern in the dawn-dusk meridian. Once the shift is complete, the ionospheric flow pattern will be as derived by *Weimer* [1995] shown in Figure 4.1, and the dawn-dusk twin-vortex flow would die away. However, in a statistical study, an equatorward and poleward flow associated with the twin-vortex pattern may be observed, as is suggested by the v_N cross-correlation results. The perturbation flow effect associated with this motion is only a few m s^{-1} nT^{-1}, as indicated by the 'gradient' vectors, and is thus a very small effect. The strongest effect of IMF B_y is experienced by the east-west velocity component, where perturbation vectors of tens of m s^{-1} nT^{-1} are observed.

It is instructive to view the 'gradient' vectors in a slightly different format to illustrate the perturbation flow effect. Figure 6.5 presents the data previously shown in the third panels of Figure 6.3 in a polar representation, with the east-west velocity positive in an anticlockwise direction, and the north-south velocity positive towards the centre of the plot. Since the data are derived for every hour of local time, hourly crosses are placed in a circular formation representing the position of EISCAT, with midnight at the bottom of the plots and increasing hours anticlockwise in rotation. The perturbation velocity vectors per nT of IMF B_y are then determined from the slope of the regression lines at each of the standard lags, shown separately in each of the plots using the same colour scheme as before. The most distinct feature in all three of these polar plots are the relatively large eastward perturbation velocities observed over many hours of local time, particularly in the evening and nightside sectors. The strongest effect is in the early morning hours (~0100 MLT) with the perturbation flow reaching ~60 m s^{-1} per nT of (positive) IMF B_y, although the typical perturbation flow over the nightside is ~40 m s^{-1} nT^{-1}. Towards the dayside the vectors tend to be weaker in accordance with the low cross-correlation coefficients and the large probability that they occurred by chance. Here the vectors tend to point in a westward direction for many hours of local time, although the velocities are very small, and may not be significant. Where the vectors are particularly small, for example at 1200 and 1300 MLT in the 10 min delay plot, the vectors do not provide significant information to the overall pattern. In general, however, the perturbation flow

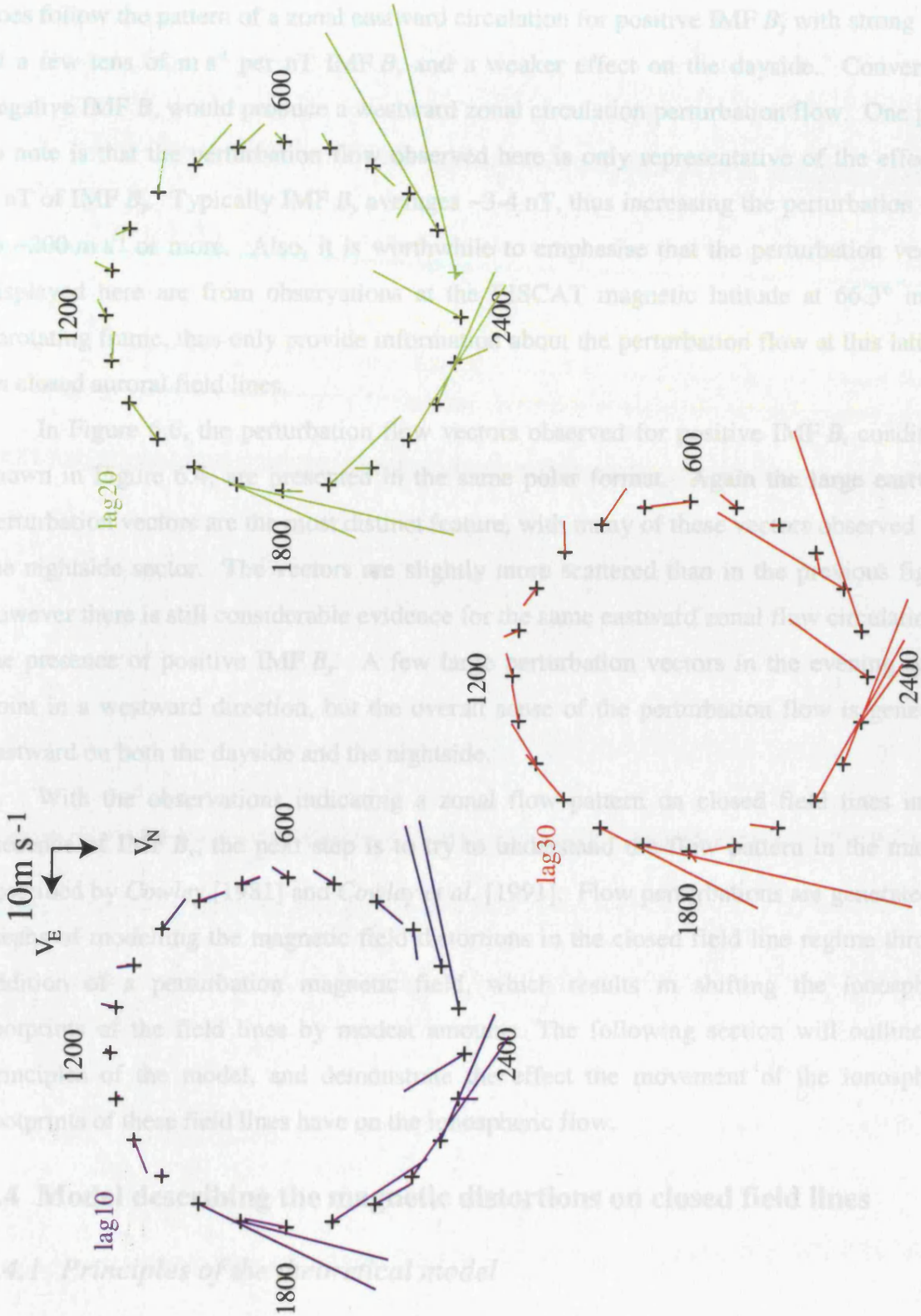

FIGURE 6.5 Polar plots illustrating the 'gradient' information taken from Figure 6.3 combining both perturbation velocity components. Perturbation vectors per nT of IMF B_y calculated during southward IMF conditions. The three lag times are shown as separate plots. The scale represents the size of the vectors with the direction as indicated.

does follow the pattern of a zonal eastward circulation for positive IMF B_y with strong flow of a few tens of m s^{-1} per nT IMF B_y and a weaker effect on the dayside. Conversely, negative IMF B_y would produce a westward zonal circulation perturbation flow. One point to note is that the perturbation flow observed here is only representative of the effect of 1 nT of IMF B_y. Typically IMF B_y averages ~3-4 nT, thus increasing the perturbation flow to ~200 m s^{-1} or more. Also, it is worthwhile to emphasise that the perturbation vectors displayed here are from observations at the EISCAT magnetic latitude at 66.3° in the corotating frame, thus only provide information about the perturbation flow at this latitude on closed auroral field lines.

In Figure 6.6, the perturbation flow vectors observed for positive IMF B_z conditions shown in Figure 6.4, are presented in the same polar format. Again the large eastward perturbation vectors are the most distinct feature, with many of these vectors observed over the nightside sector. The vectors are slightly more scattered than in the previous figure, however there is still considerable evidence for the same eastward zonal flow circulation in the presence of positive IMF B_y. A few large perturbation vectors in the evening sector point in a westward direction, but the overall sense of the perturbation flow is generally eastward on both the dayside and the nightside.

With the observations indicating a zonal flow pattern on closed field lines in the presence of IMF B_y, the next step is to try to understand the flow pattern in the manner described by *Cowley* [1981] and *Cowley et al.* [1991]. Flow perturbations are generated by means of modelling the magnetic field distortions in the closed field line regime through addition of a perturbation magnetic field, which results in shifting the ionospheric footprints of the field lines by modest amounts. The following section will outline the principles of the model, and demonstrate the effect the movement of the ionospheric footprints of these field lines have on the ionospheric flow.

6.4 Model describing the magnetic distortions on closed field lines

6.4.1 Principles of the theoretical model

The basic concept of distorting the magnetic field structure by the addition of a perturbation field has previously been discussed in §2.2.4 and §6.1. The field distortions cause the ionospheric footprints of these field lines to move by small amounts due to the field mapping, creating a perturbation flow associated with the distortion of the field lines and thus the field mapping. If one assumes a fixed pattern of flow in the magnetospheric

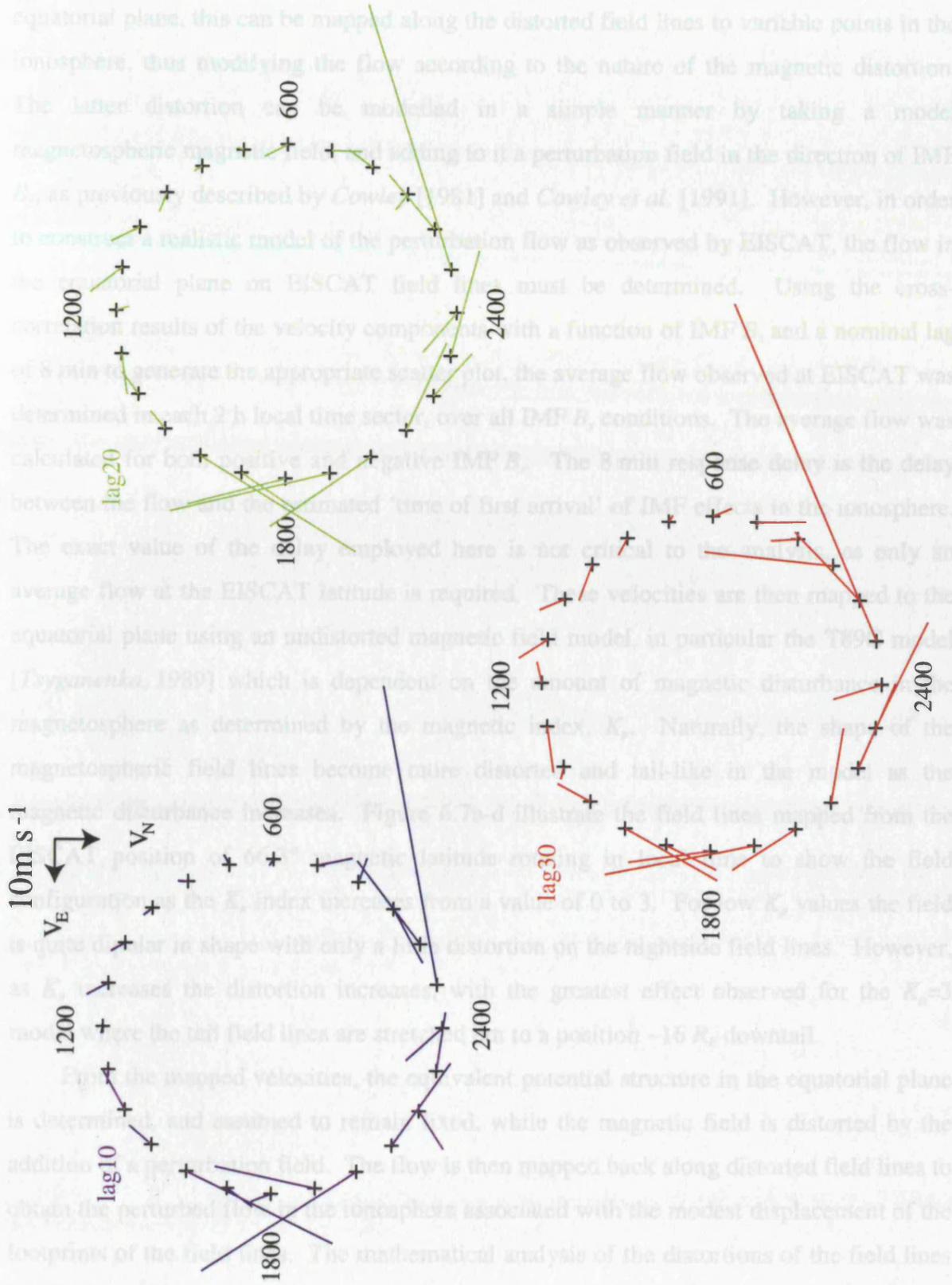

FIGURE 6.6 Same format as Figure 6.5 except using the 'gradient' information taken from Figure 6.4 during northward IMF conditions.

equatorial plane, this can be mapped along the distorted field lines to variable points in the ionosphere, thus modifying the flow according to the nature of the magnetic distortion. The latter distortion can be modelled in a simple manner by taking a model magnetospheric magnetic field, and adding to it a perturbation field in the direction of IMF B_y, as previously described by *Cowley* [1981] and *Cowley et al.* [1991]. However, in order to construct a realistic model of the perturbation flow as observed by EISCAT, the flow in the equatorial plane on EISCAT field lines must be determined. Using the cross-correlation results of the velocity components with a function of IMF B_z and a nominal lag of 8 min to generate the appropriate scatter plot, the average flow observed at EISCAT was determined in each 2 h local time sector, over all IMF B_y conditions. The average flow was calculated for both positive and negative IMF B_z. The 8 min response delay is the delay between the flow and the estimated 'time of first arrival' of IMF effects in the ionosphere. The exact value of the delay employed here is not critical to the analysis, as only an average flow at the EISCAT latitude is required. These velocities are then mapped to the equatorial plane using an undistorted magnetic field model, in particular the T89C model [*Tsyganenko*, 1989] which is dependent on the amount of magnetic disturbance in the magnetosphere as determined by the magnetic index, K_p. Naturally, the shape of the magnetospheric field lines become more distorted and tail-like in the model as the magnetic disturbance increases. Figure 6.7a-d illustrate the field lines mapped from the EISCAT position of 66.3° magnetic latitude rotating in local time to show the field configuration as the K_p index increases from a value of 0 to 3. For low K_p values the field is quite dipolar in shape with only a little distortion on the nightside field lines. However, as K_p increases the distortion increases, with the greatest effect observed for the K_p=3 model where the tail field lines are stretched out to a position ~16 R_E downtail.

From the mapped velocities, the equivalent potential structure in the equatorial plane is determined, and assumed to remain fixed, while the magnetic field is distorted by the addition of a perturbation field. The flow is then mapped back along distorted field lines to obtain the perturbed flow in the ionosphere associated with the modest displacement of the footprints of the field lines. The mathematical analysis of the distortions of the field lines and the perturbation flow is discussed in the following section.

One final point to make is that the average flow in the ionosphere calculated as discussed above represents the flow in the corotating frame of the Earth. In order to determine the total flow in the equatorial plane, the effects of corotation must be included in the analysis, which for the latitude of EISCAT, will increase the east-west flow by

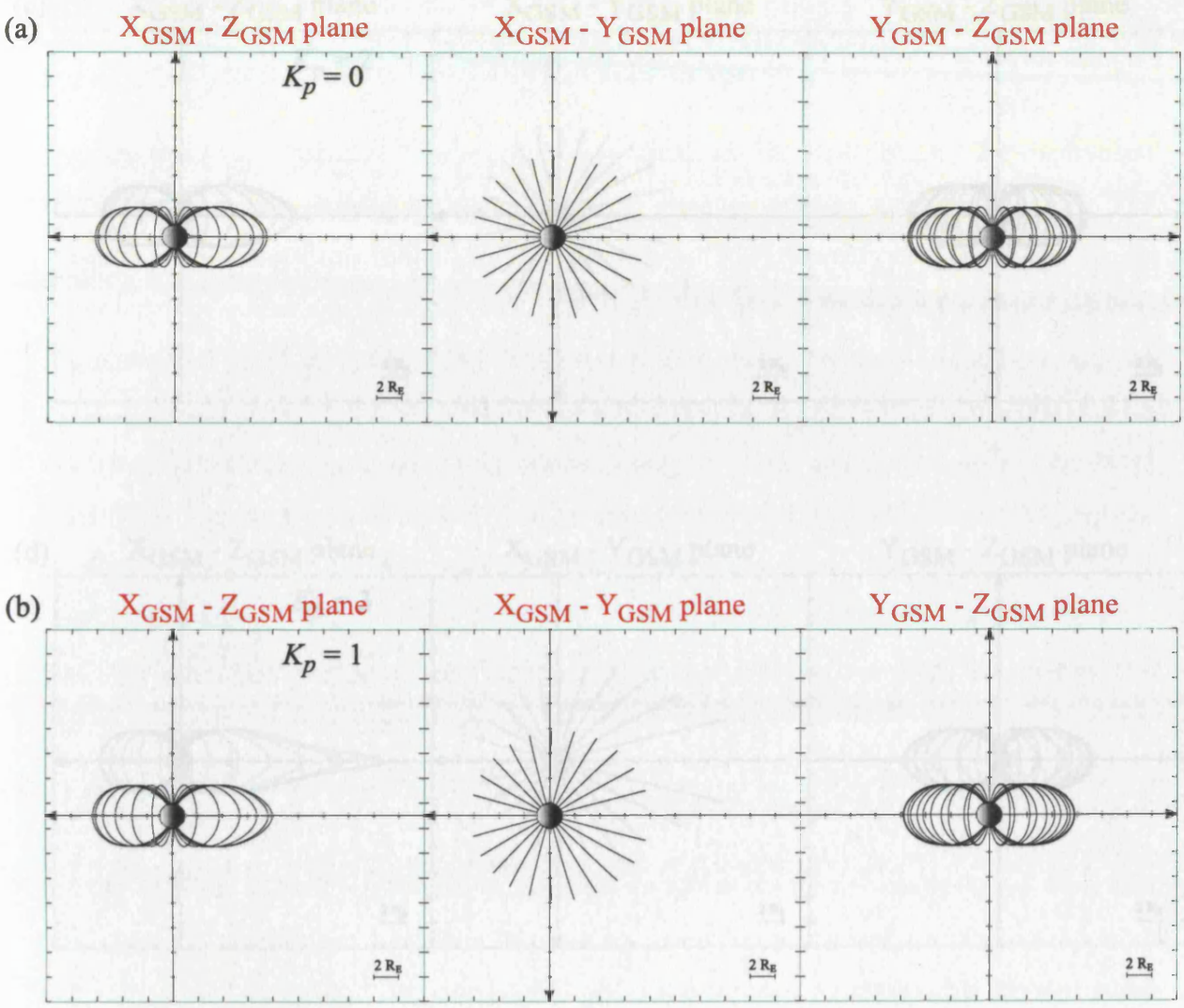

FIGURE 6.7 Tsyganenko magnetospheric field models for **a.** K_p=0 and **b.** K_p=1. The field lines are mapped from the position of EISCAT at 66.3° magnetic latitude, and for every hour of local time. The dipole tilt angle has been set to zero so that the field is symmetric in the both the equatorial plane and the noon-midnight meridian. All three planar projections are shown to illustrate the effect of increasing the magnetic index.

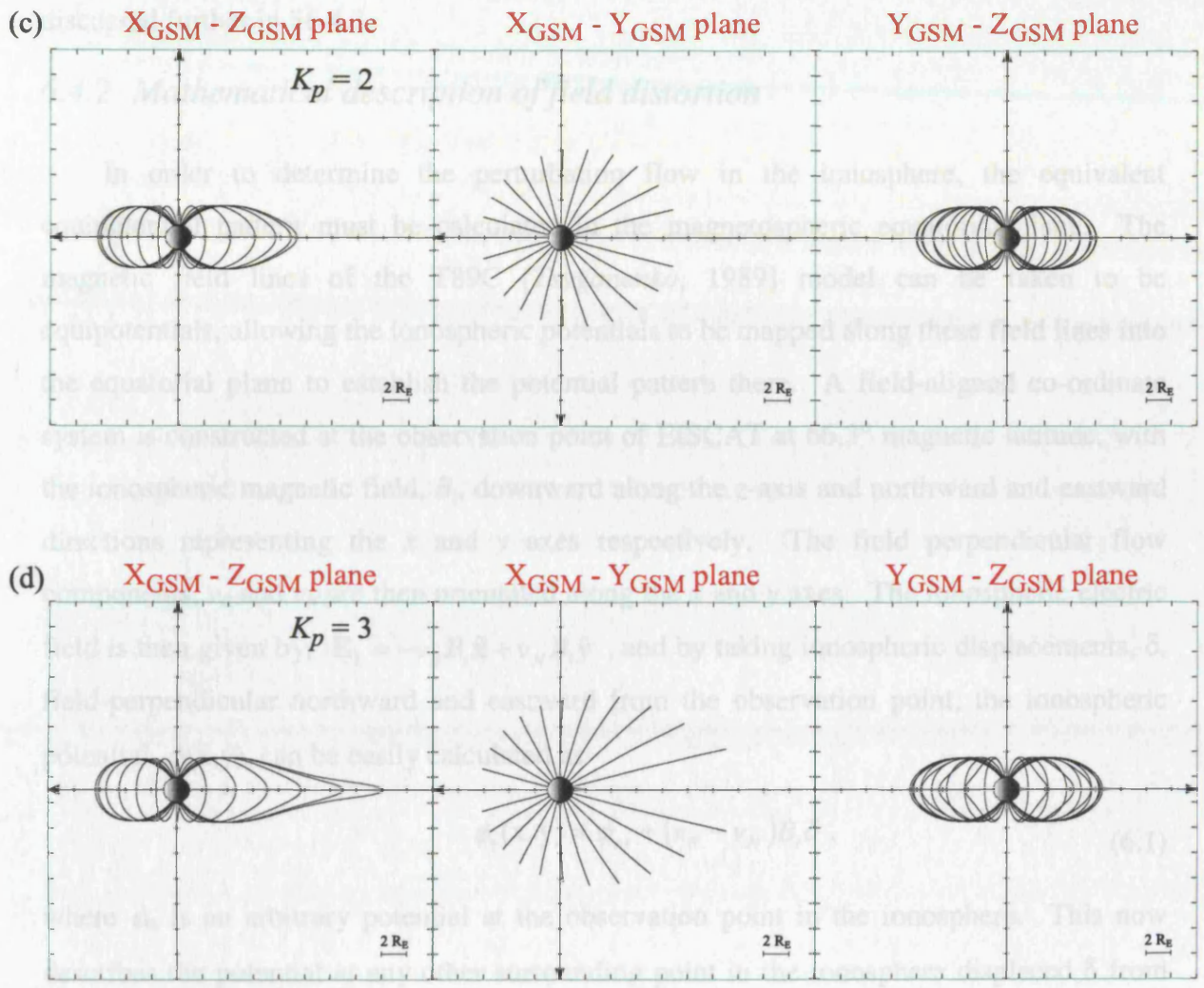

FIGURE 6.7 Tsyganenko magnetospheric field models for **c.** K_p=2 and **d.** K_p=3. Notice how the tail field lines become significantly distorted when K_p increases to 3.

~185 m s^{-1}. However, as will be shown in a later section, the ionospheric perturbation flow derived from the field mapping associated with this increase in east-west flow is minimal, and does not significantly affect the overall perturbation flow observed due to the distortion of the magnetospheric field in the presence of IMF B_y. This point will be discussed further in §6.4.3.

6.4.2 Mathematical description of field distortion

In order to determine the perturbation flow in the ionosphere, the equivalent equipotential pattern must be calculated in the magnetospheric equatorial plane. The magnetic field lines of the T89C [*Tsyganenko*, 1989] model can be taken to be equipotentials, allowing the ionospheric potentials to be mapped along these field lines into the equatorial plane to establish the potential pattern there. A field-aligned co-ordinate system is constructed at the observation point of EISCAT at 66.3° magnetic latitude, with the ionospheric magnetic field, B_i, downward along the z-axis and northward and eastward directions representing the x and y axes respectively. The field perpendicular flow components, v_E and v_N are then orientated along the x and y axes. The ionospheric electric field is then given by, $\mathbf{E_i} = -v_E B_i \hat{\mathbf{x}} + v_N B_i \hat{\mathbf{y}}$, and by taking ionospheric displacements, δ, field-perpendicular northward and eastward from the observation point, the ionospheric potential, $\phi_i(x,y)$, can be easily calculated as

$$\phi_i(x,y) = \phi_{oi} + (v_E - v_N) B_i \delta \,, \tag{6.1}$$

where ϕ_{0i} is an arbitrary potential at the observation point in the ionosphere. This now describes the potential at any other surrounding point in the ionosphere displaced δ from the observation position. The ionospheric observation point, together with the northward and eastward displacements are then mapped into the equatorial plane using the undistorted T89C [*Tsyganenko* 1989] field model. For simplicity, we assume only the case of zero dipole tilt.

Since the field lines are equipotentials to a first approximation, the potentials determined at each of the three points in the ionosphere are exactly those at the mapped position in the magnetospheric equatorial plane. Thus from the displacements of these points in the magnetosphere, the potential structure corresponding to the known potentials at those points can be determined in the following manner. The general equation for the potential in the equatorial plane is given by

$$\Phi_M(dX, dY) = \phi_{0_i} + \frac{\partial \Phi_M}{\partial X} dX + \frac{\partial \Phi_M}{\partial Y} dY \quad , \tag{6.2}$$

where dX and dY are the X and Y magnetospheric displacements in the equatorial plane from the mapped observation point (X_0, Y_0). The potential at the mapped northward displacement is known to be $\phi_{0_i} + v_E B_i \delta$ from Eq. 6.1, and at the mapped eastward displacement, $\phi_{0_i} - v_N B_i \delta$. From Eq. 6.2, the potential in the equatorial plane can then be expressed in terms of these quantities, as follows

$$\frac{\partial \Phi_M}{\partial X} dX_1 + \frac{\partial \Phi_M}{\partial Y} dY_1 = v_E B_i \delta$$

$$\frac{\partial \Phi_M}{\partial X} dX_2 + \frac{\partial \Phi_M}{\partial Y} dY_2 = -v_N B_i \delta \quad , \tag{6.3 a,b}$$

where dX_1 and dY_1 are the magnetospheric displacements of the northward mapped point, and dX_2 and dY_2 are the displacements of the eastward mapped point from the mapped observation point (X_0, Y_0). By solving Eqs. 6.3a and b for the partial derivatives, the potential pattern in the equatorial plane can be expressed completely in terms of the displacements of the mapped field lines and the observed ionospheric velocities.

$$\frac{\partial \Phi_M}{\partial X} = B_i \delta \left(\frac{v_E dY_2 + v_N dY_1}{dX_1 dY_2 - dX_2 dY_1} \right)$$

$$\frac{\partial \Phi_M}{\partial Y} = -B_i \delta \left(\frac{v_E dX_2 + v_N dX_1}{dX_1 dY_2 - dX_2 dY_1} \right) \tag{6.4 a,b}$$

Now the perturbation field is added to the T89C [*Tsyganenko*, 1989] field model, and the ionospheric points are again traced along the field lines to different positions in the equatorial plane. The EISCAT observation point is now mapped along the perturbed field lines to a position ($X_0+\Delta X_0$, $Y_0+\Delta Y_0$), the northward point to a position ($X_0+\Delta X_0+dX_1'$, $Y_0+\Delta Y_0+dY_1'$) and the eastward point to ($X_0+\Delta X_0+dX_2'$, $Y_0+\Delta Y_0+dY_2'$). These positions are easily obtained from the field mapping procedure. The displacement between the observation point mapped using the unperturbed and perturbed field models give the (ΔX_0, ΔY_0) coordinates. Whilst (dX_1', dY_1') and (dX_2', dY_2') are the magnetospheric displacements from the observation point mapped using the perturbed field model and the northward and eastward ionospheric points respectively also mapped using the perturbed field model. From the known potential structure in the equatorial plane, the

magnetospheric potentials at these new locations can be easily determined from Eqs. 6.2 and 6.4. Thus the perturbed ionospheric electric fields and the new perturbed ionospheric velocities associated with these potentials can be calculated as follows

$$v_N' = \frac{E_{y_i}'}{B_i} = -\frac{1}{B_i}\frac{\partial \phi_i'}{\partial y_i} = -\frac{1}{B_i \delta}\left(\frac{\partial \Phi_M}{\partial X} dX_2' + \frac{\partial \Phi_M}{\partial Y} dY_2'\right)$$

$$v_E' = -\frac{E_{x_i}'}{B_i} = \frac{1}{B_i}\frac{\partial \phi_i'}{\partial x_i} = \frac{1}{B_i \delta}\left(\frac{\partial \Phi_M}{\partial X} dX_1' + \frac{\partial \Phi_M}{\partial Y} dY_1'\right) \quad . \quad (6.5\ a,b)$$

The dashed symbols represent those quantities associated with the perturbed field model. The partial derivatives of the magnetospheric potentials are simply those previously derived in Eqs. 6.4. Substituting in these values gives the perturbed eastward and northward velocities in the ionosphere as

$$v_E' = \frac{v_E\left(dX_1' dY_2 - dX_2 dY_1'\right) + v_N\left(dX_1' dY_1 - dX_1 dY_1'\right)}{\left(dX_1 dY_2 - dX_2 dY_1\right)}$$

$$v_N' = \frac{v_N\left(dX_1 dY_2' - dX_2' dY_1\right) + v_E\left(dX_2 dY_2' - dX_2' dY_2\right)}{\left(dX_1 dY_2 - dX_2 dY_1\right)} \quad . \quad (6.6\ a,b)$$

All of the parameters present in Eqs. 6.6 can either be obtained directly from observations (the v_E and v_N values) or from the field mapping procedure (the dX and dY values), using the unperturbed and then the perturbed field models. To implement the field mapping, ionospheric displacements of ~10 km were used and a step length of ~30 m for the integration of the field lines. By altering the size of the ionospheric displacement by a factor of two, it was established that the 10 km displacement was sufficiently small that the electric field in the ionosphere was constant over the range of the displacement, giving an accurate representation of the potential associated with the ionospheric velocities measured. The perturbation field can take any form, although for the purpose of this study, an IMF B_y-related field is employed, as will now be discussed.

6.4.3 Model results using simple prescribed flow patterns

Prior to presenting the results using the real EISCAT velocities, it is imperative to understand the influence the addition an IMF B_y field has on each of the flow components separately. To this end, the perturbation flow resulting from a constant northward and constant eastward flow are determined individually. Also since the magnetospheric model

is K_p-dependent, it is important to understand the effect the field changes have on the perturbation velocities produced. Figure 6.8 shows the flow perturbations associated with a constant northward ionospheric flow of 100 m s^{-1} at each MLT. This has been mapped into the equatorial plane using four different K_p values in the T89C [*Tsyganenko*, 1989] model, perturbed by adding to it a 1 nT B_y field. The top panel shows the eastward perturbation flow component, whilst the lower panel shows the northward perturbation flow component. The four coloured lines represent the different magnetospheric models used in the field mapping procedure. The largest perturbation flow effect is observed in the eastward flow component, with weak eastward flow over the dayside and stronger westward flow on the nightside. Notice that as K_p increases the perturbation flow also increases on the nightside as the field lines become more distorted and tail-like. For K_p=0, 1 and 2, the field structure is principally dipolar in shape, as illustrated in Figures 6.7, producing a v_E perturbation flow for these three cases of a few tens of m s^{-1}. However, once K_p increases to a value of 3, the field structure changes considerably (Figure 6.7d), causing the v_E perturbation flow to increase by a factor of ten to several hundreds of m s^{-1}. Thus the field structure has an important effect on the size of the perturbation flow observed in the ionosphere, and should be kept in mind when interpreting the results from the modelled flow velocities in the following section.

Nevertheless, the main flow features observed here are perturbation flows which are directed eastward on the dayside, and westward on the nightside with a typical value of ~20 m s^{-1} at midnight, not including the large flow derived using the K_p=3 model, (compared with the undisturbed 100 m s^{-1} northward flow initially assumed). The origin of this effect is easy to understand with reference to Figure 2.8 (§2.2.4) where a dipole field is distorted under the influence of a perturbation B_y field. On the noon-midnight meridian a northward ionospheric velocity implies a sunward-directed streamline in the equatorial plane. The distorted field lines then map to points which are increasingly displaced into the postnoon sector with increasing latitude. Since the locus of these points in the ionosphere is also a streamline, an increasing eastward perturbation flow with increasing latitude is implied from an original purely northward ionospheric flow. The same effect produces westward flow in the midnight meridian for an initial northward flow as assumed here. The latitudinal displacements of the field lines in the dawn-dusk meridian produce little effect on a purely northward flow. The effect is greater on the nightside than on the dayside because the undisturbed T89C [*Tsyganenko*, 1989] model field is more compressed on the dayside than on the nightside, such that the effect of the added

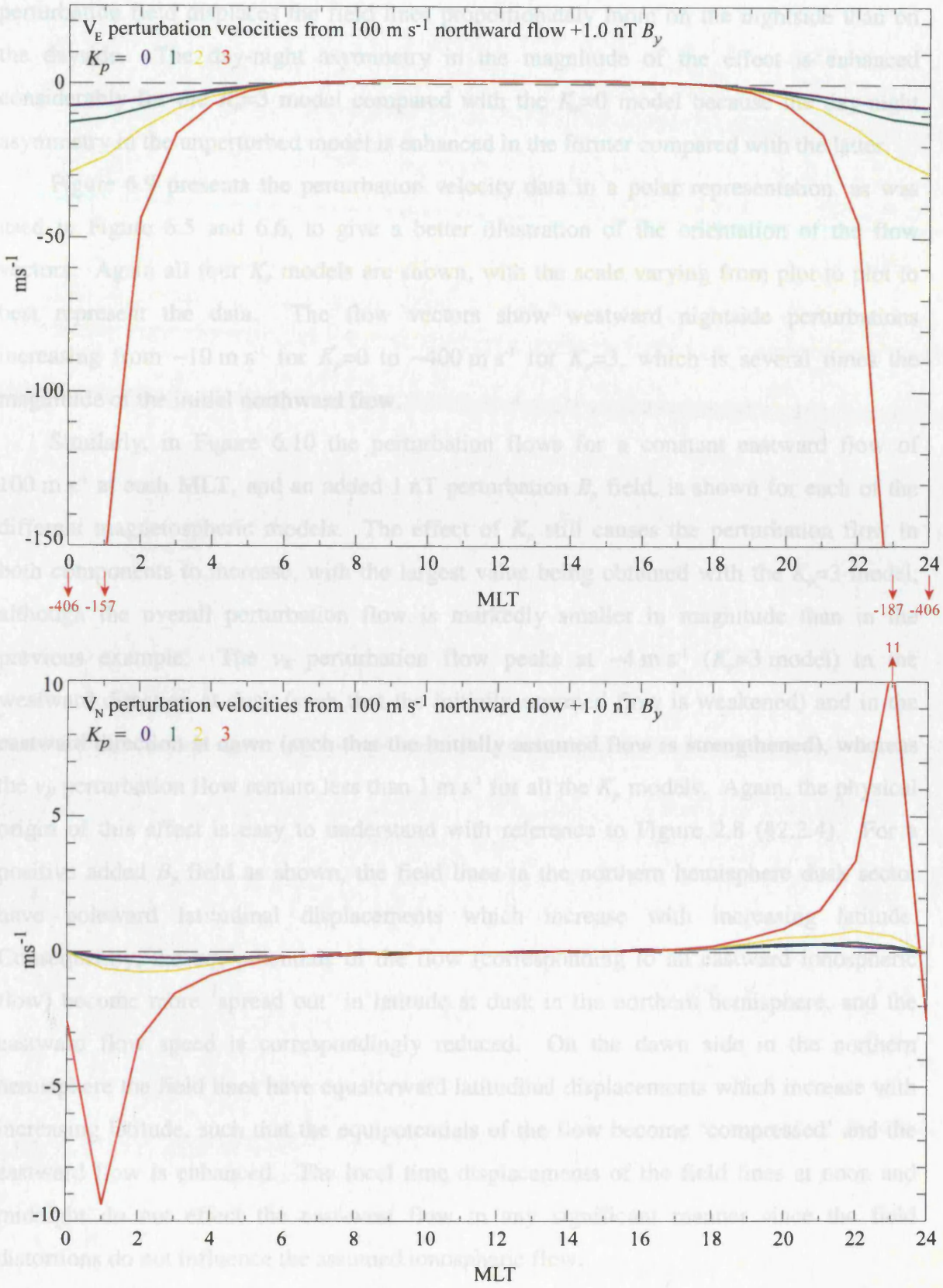

FIGURE 6.8 Ionospheric flow perturbations versus local time produced using an initial 100 m s^{-1} northward flow and a 1 nT perturbation B_y field. The coloured lines indicate the different K_p values used in the Tsyganenko magnetospheric model. The top panel shows the eastward component of the flow perturbation, and the bottom panel shows the northward component. Notice the strong perturbation flow produced when a K_p=3 magnetospheric model is used.

perturbation field displaces the field lines proportionately more on the nightside than on the dayside. The day-night asymmetry in the magnitude of the effect is enhanced considerably for the K_p=3 model compared with the K_p=0 model because the day-night asymmetry in the unperturbed model is enhanced in the former compared with the latter.

Figure 6.9 presents the perturbation velocity data in a polar representation, as was used in Figure 6.5 and 6.6, to give a better illustration of the orientation of the flow vectors. Again all four K_p models are shown, with the scale varying from plot to plot to best represent the data. The flow vectors show westward nightside perturbations increasing from ~10 m s^{-1} for K_p=0 to ~400 m s^{-1} for K_p=3, which is several times the magnitude of the initial northward flow.

Similarly, in Figure 6.10 the perturbation flows for a constant eastward flow of 100 m s^{-1} at each MLT, and an added 1 nT perturbation B_y field, is shown for each of the different magnetospheric models. The effect of K_p still causes the perturbation flow in both components to increase, with the largest value being obtained with the K_p=3 model, although the overall perturbation flow is markedly smaller in magnitude than in the previous example. The v_E perturbation flow peaks at ~4 m s^{-1} (K_p=3 model) in the westward direction at dusk (such that the initially assumed flow is weakened) and in the eastward direction at dawn (such that the initially assumed flow is strengthened), whereas the v_N perturbation flow remain less than 1 m s^{-1} for all the K_p models. Again, the physical origin of this effect is easy to understand with reference to Figure 2.8 (§2.2.4). For a positive added B_y field as shown, the field lines in the northern hemisphere dusk sector have poleward latitudinal displacements which increase with increasing latitude. Consequently, the equipotentials of the flow (corresponding to an eastward ionospheric flow) become more 'spread out' in latitude at dusk in the northern hemisphere, and the eastward flow speed is correspondingly reduced. On the dawn side in the northern hemisphere the field lines have equatorward latitudinal displacements which increase with increasing latitude, such that the equipotentials of the flow become 'compressed' and the eastward flow is enhanced. The local time displacements of the field lines at noon and midnight do not effect the east-west flow in any significant manner since the field distortions do not influence the assumed ionospheric flow.

Figure 6.11 again illustrates the flow perturbation in a polar plot. It is important to point out that the perturbation effect due to an initial eastward flow (as shown here) is considerably smaller than that due to an initial northward flow shown previously. Here the perturbation vectors are only a few m s^{-1}, compared to the tens and hundreds of m s^{-1}

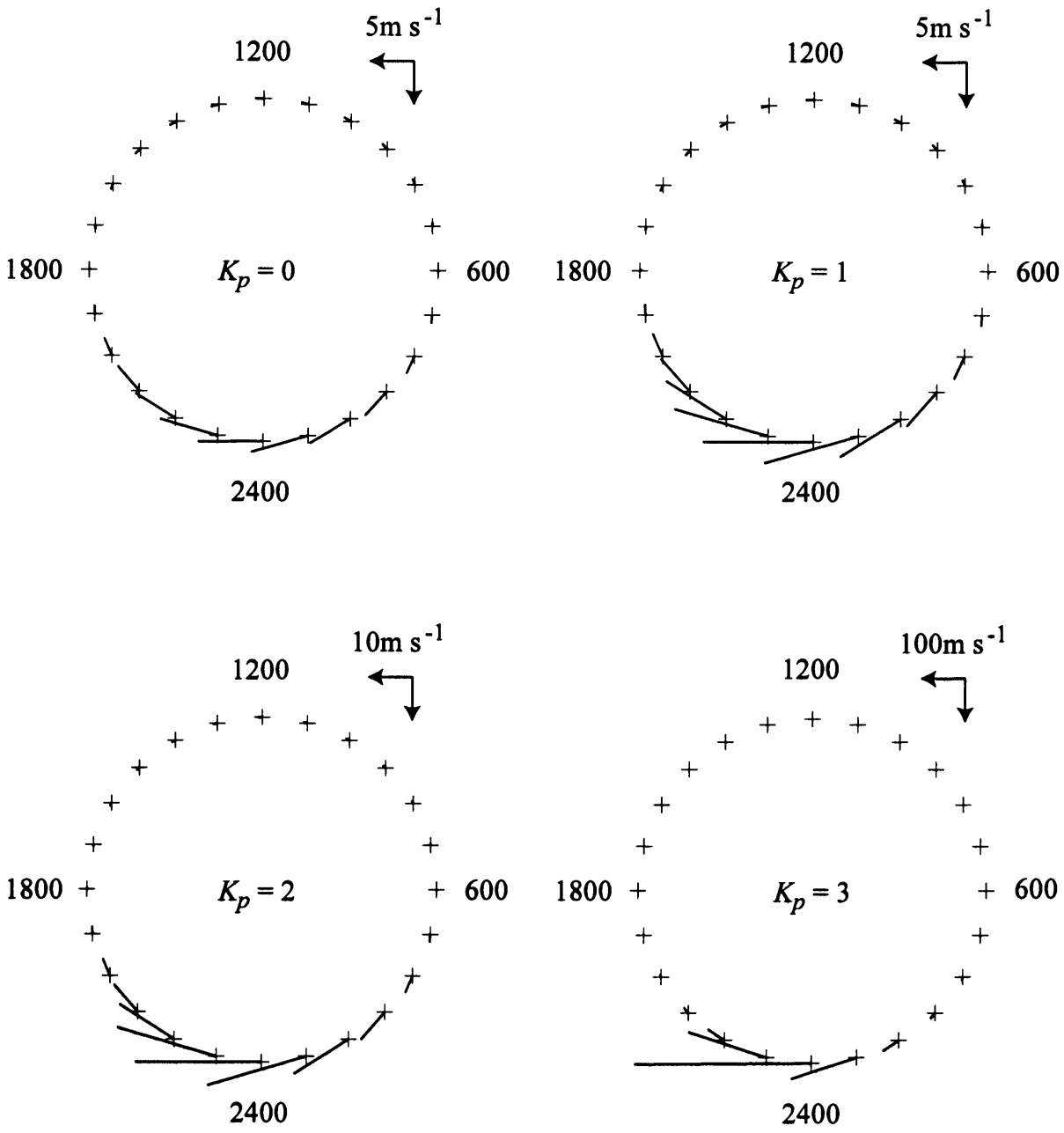

FIGURE 6.9 Polar representation of the perturbation flow vectors (shown separately in Figure 6.8) derived from an initial 100m s^{-1} northward flow and a 1 nT B_y perturbation field. The four plots illustrate the different K_p dependent magnetospheric models used in the analysis. The key to the right of each of the plots indicates the relative size of the perturbation flow calculated with positive northward velocity towards the centre of the plot and positive eastward in an anticlockwise direction.

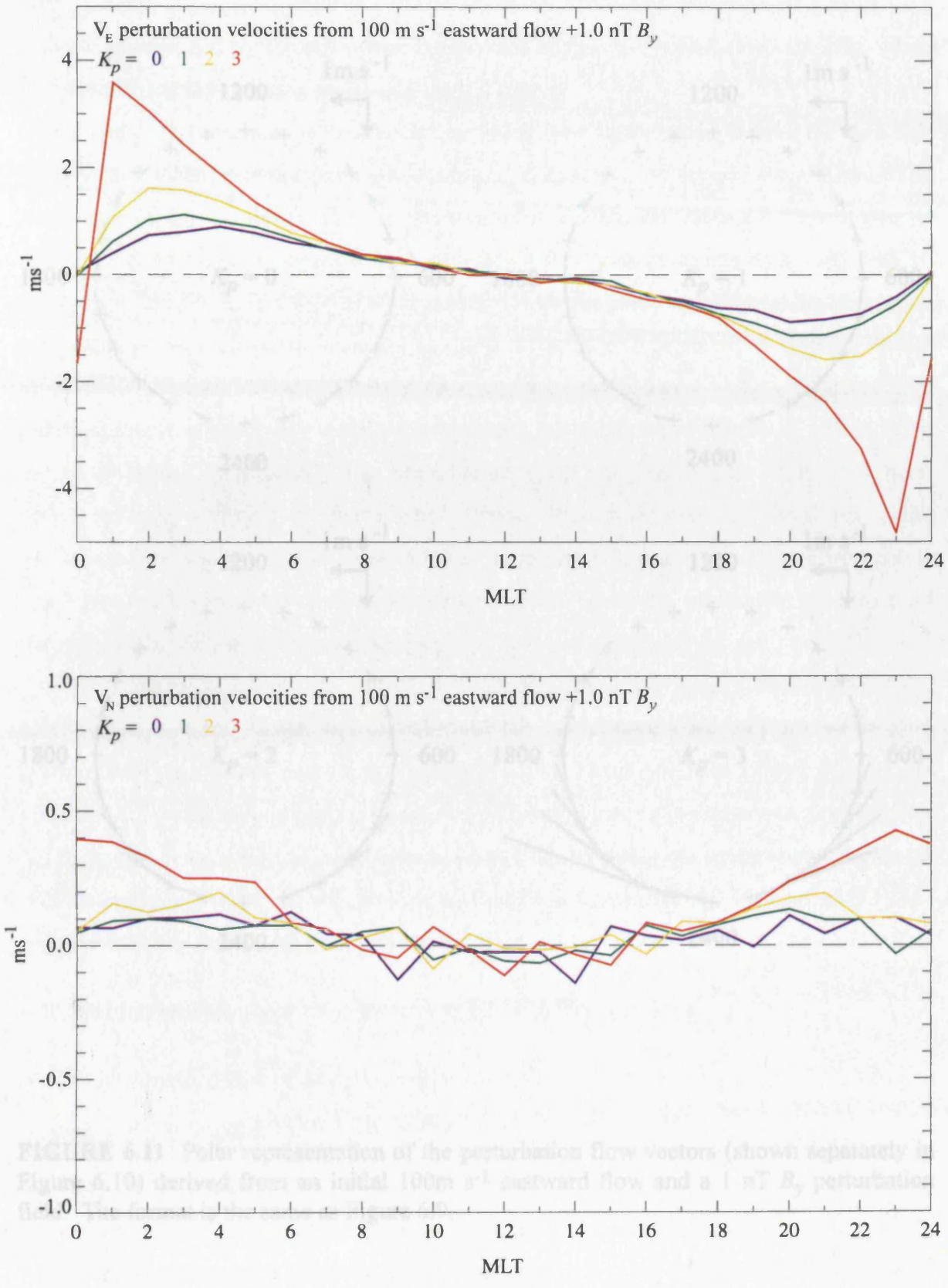

FIGURE 6.10 Ionospheric flow perturbations versus local time produced using an initial 100 m s^{-1} eastward flow and a 1 nT perturbation B_y field. The format is the same as that in Figure 6.8.

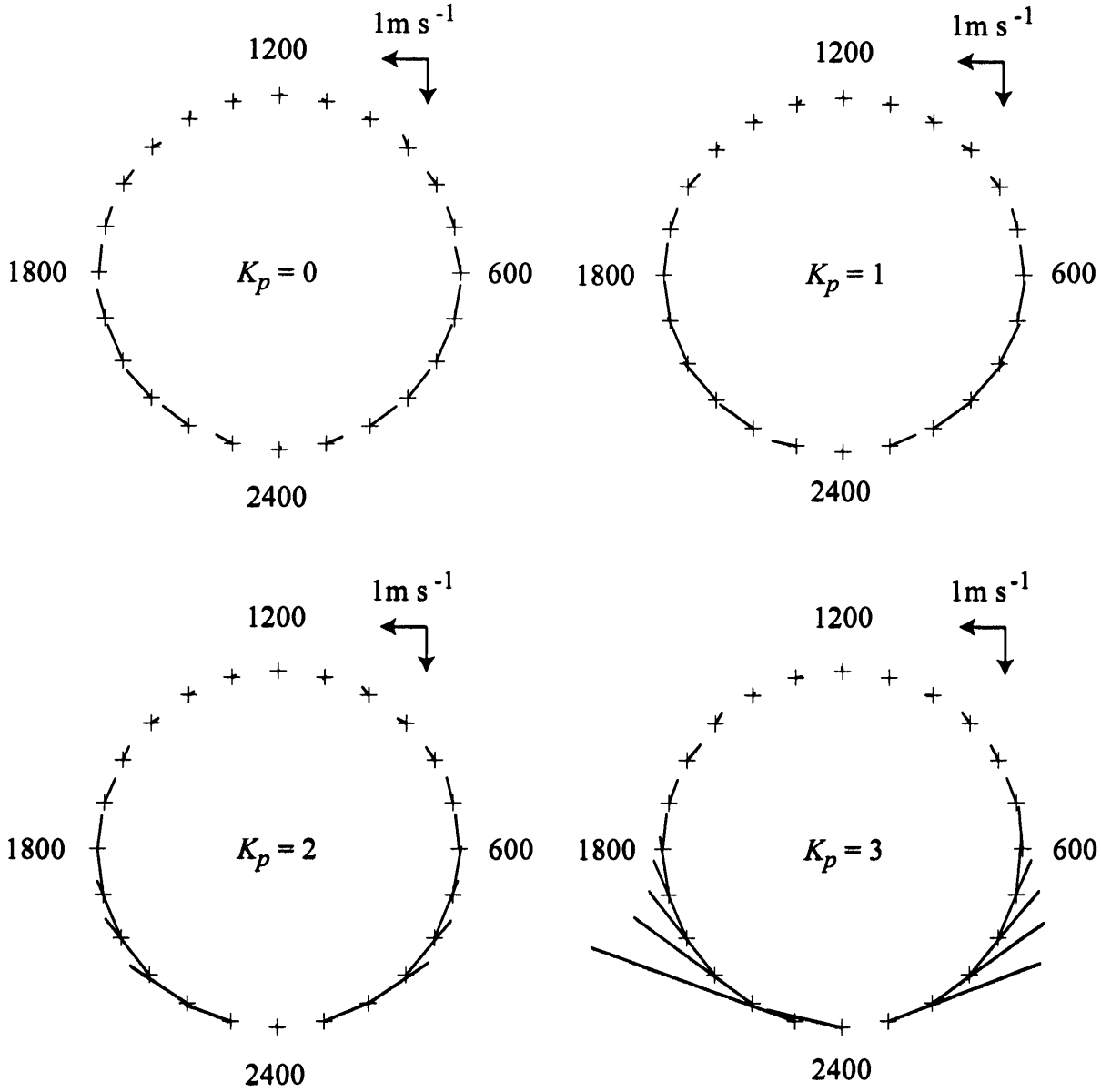

FIGURE 6.11 Polar representation of the perturbation flow vectors (shown separately in Figure 6.10) derived from an initial 100m s^{-1} eastward flow and a 1 nT B_y perturbation field. The format is the same as Figure 6.9.

derived using the same magnitude northward flow. Thus the predominant perturbation effect is determined by the northward component of the undistorted flow velocity, while the perturbation flow itself is in the east-west direction.

Finally, a natural source of constant east-west flow in the ionosphere is the flow due to corotation when viewed from a non-corotating frame, such as the equatorial plane. The magnitude of the corotation flow is approximately double the eastward flow shown in Figure 6.10, where it is clear that the perturbation flow generated due to a +1nT IMF B_y penetration field is only a few m s^{-1} at most. Under the same conditions, the maximum effect the east-west corotation velocity can have on the overall perturbation flows is double this, where the perturbation flows are proportional to the added perturbation magnetic field provided that it remains very small compared with the background field at all points along the field lines. Realistically the perturbation field will be smaller than used here, correspondingly reducing the perturbation flows. Thus it is clear that the effect of the corotation flow when trying to determine the perturbation effect of the field distortions is small in comparison to the other flow component, and hence the subsequent analysis does not include the corotation flow correction.

In geophysical cases, the overall perturbation flows are simply added vectorially according to the magnitude and direction of the initial northward and eastward flows present, with the greatest contribution arising from the initial northward flow. Also, if the addition of a perturbation magnetic field in a different direction is considered (e.g. with an X component as well as a Y component), the pattern of perturbation flows is correspondingly rotated around the Z axis, though not perfectly so, because of the day-night asymmetry in the background magnetic field.

6.5 Perturbation flow results using EISCAT velocities

6.5.1 Determination of the perturbation field

In order to be able to compare the flow perturbation results obtained from the model directly with the slopes of the regression lines shown in Figures 6.5 and 6.6, which indicate the perturbation flows per nT of IMF B_y, a perturbation field corresponding to a 1 nT B_y field in the interplanetary magnetic field has to be added to the T89C [*Tsyganenko*, 1989] model. A study by *Nagai* [1987] using the GOES 3 satellite measuring magnetic perturbations at geosynchronous orbit revealed that the influence of IMF B_y was to create a perturbation field near midnight which is a fraction ~0.3-0.6 of the IMF B_y, increasing with

increasing latitude. Similarly, observations by *Cowley and Hughes* [1983] showed that the average perturbation field in the evening sector observed at geosynchronous orbit was a fraction 0.3 of the B_y field in the interplanetary medium. More recently, *Wing et al.* [1995] have used ~5-6 years of geosynchronous satellite data from GOES 6 and GOES 7, and correlated the *y*-component of the magnetic field measured at the satellites with the *y*-component of the IMF. The results clearly show the partial penetration of the IMF B_y field at the orbit of the satellites corresponding to a fraction ~0.3 at noon and ~0.8 at midnight of IMF B_y. Since the latitude of EISCAT roughly projects to geosynchronous orbit (at least for relatively undistorted cases), a perturbation field sinusoidally varying between 0.3 at noon and 0.8 at midnight has been employed to represent the penetration of a 1 nT IMF B_y field. That is, the perturbation field is given by

$$B_y = (0.55\text{-}0.25\cos\psi)\ \text{nT}\ , \tag{6.7}$$

where ψ is the azimuthal angle measured from noon.

6.5.2 *Perturbation flow results during southward IMF*

The perturbation field model described previously is now used to determine the flow perturbations obtained from the averaged EISCAT flow velocities separated into IMF B_z negative and positive, respectively. Figure 6.12a illustrates the average flow pattern under southward IMF conditions determined from the method outlined in §6.4.1 using a nominal lag of 8 min, presented in the same polar format as the previous figures. It exhibits the expected twin-vortex nature of the flow, with poleward and equatorward (antisunward) components near noon and midnight respectively, and westward and eastward (sunward) components near dusk and dawn, though with the axis rotated westward by ~2 h of MLT away from noon-midnight. Similar observations of this rotated property of the flow pattern were previously reported by *Burrage* [1988] using observations from the SABRE radar. The average flow velocities measured are consistent with what one would typically expect, with the strongest flows of ~500 m s^{-1} in a westward direction in the dusk sector.

These velocities were mapped into the equatorial plane using the T89C [*Tsyganenko* 1989] magnetic field model with K_p=0 and 3, where the corresponding magnetospheric velocities were calculated from the potential pattern described by Eqs. 6.2 and 6.4. The resulting flow vectors are presented in Figures 6.12b, with the K_p=0 model shown on the left and the K_p=3 model shown on the right. The velocities are plotted in the

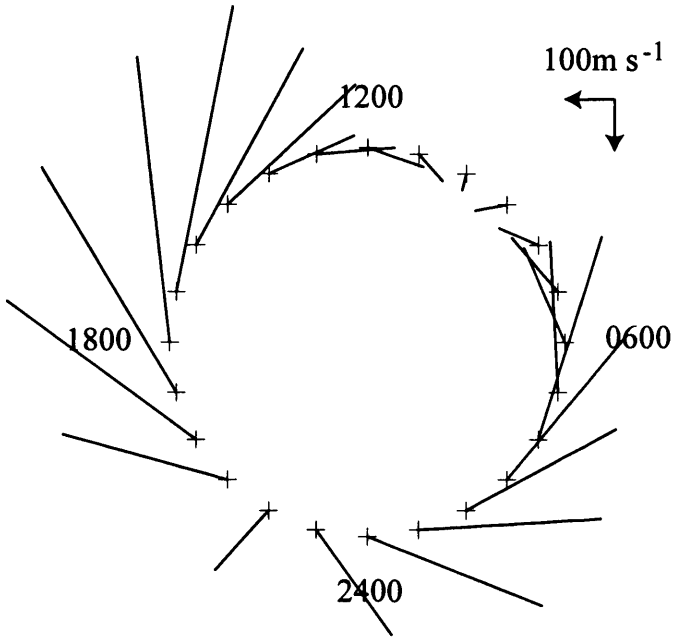

FIGURE 6.12a. Averaged ionospheric flows at the locations of EISCAT during southward IMF. Velocity vectors are positive northward towards the centre of the plot and positive eastward anticlockwise. The flows were derived from scatter plots from the cross correlograms using a nominal lag of 8 min.

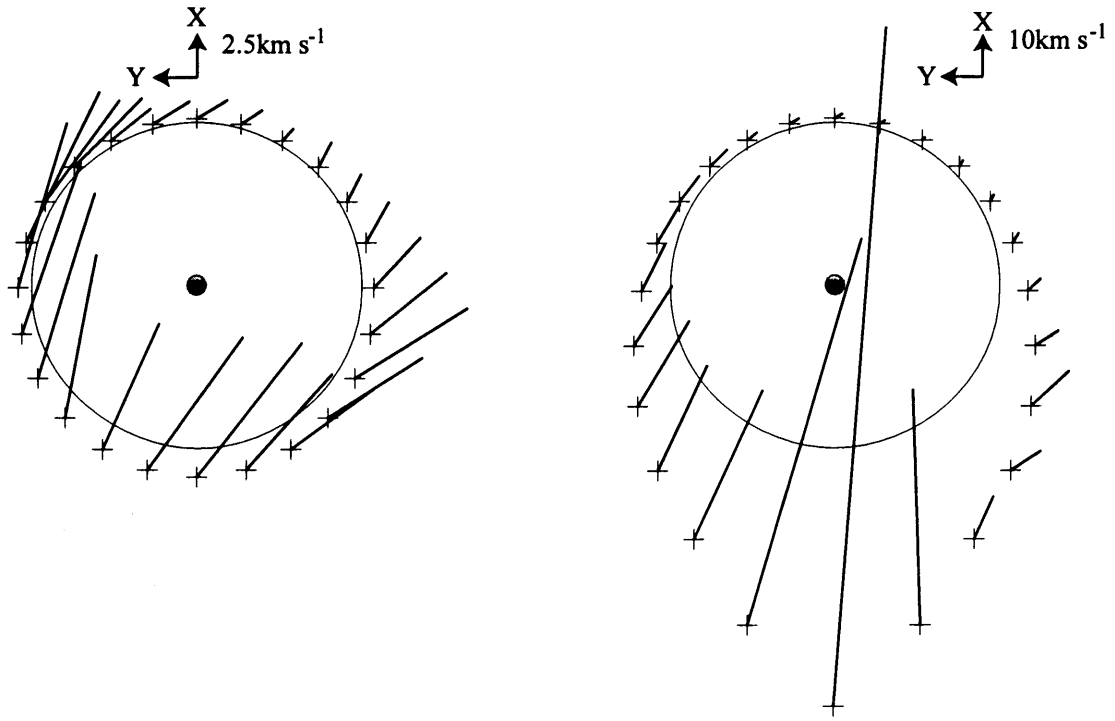

FIGURE 6.12b. Mapped EISCAT flows into the magnetospheric equatorial plane using different K_p values to alter the magnetospheric model, as viewed from looking down onto the northern polar cap. Positive X direction is towards the top of the page and the positive Y direction pointing towards the left. The left diagram shows the mapped velocities using K_p=0, whereas the right diagram shows the results from the K_p=3 model. The solid circle indicates the mapped location of EISCAT along dipolar field lines, at an L-shell of 6.2 R_E. The crosses represent the actual position of the mapped EISCAT field lines into the equatorial plane from where the equatorial velocities originate.

magnetospheric equatorial plane with the Sun at the top of the page (positive X direction) and dusk on the left (positive Y duskward). The solid circle represents the mapped position of EISCAT for an undistorted dipole field, corresponding to an *L*-shell value of 6.2 R_E, whereas the crosses indicate the position of the mapped field lines in the equatorial plane. For K_p=0, the position of the mapped field lines are very close to the *L*-shell position of EISCAT, since this magnetically-quiet field model is not that dissimilar to a dipole model, however the points all lie outside the circle. This is probably due to a symmetric ring current at ~5-7 R_E distorting the magnetospheric field to produce a slightly distorted field on the dayside causing the mapped positions to be slightly further out than typically expected. Equatorial velocities increase from ~1 km s^{-1} on the dayside to ~10 km s^{-1} over the nightside, with the flow predominantly oriented in a sunward direction though slightly rotated in a westward sense. Increasing the magnetic index results in the distortion of the nightside field in particular, with the field lines stretching out into a long tail (see Figure 6.7d), producing large equatorial flows of ~several hundreds of km s^{-1} in this region. The position of the mapped field lines now line much further away from the undistorted dipolar position of EISCAT on the nightside, indicating the level of distortion due to the increase in the magnetic index. The dayside field lines are not much affected by the increase in K_p and consequently the equatorial velocities here do not change a great deal.

The perturbation flow vectors derived from the averaged EISCAT velocities during southward IMF conditions, mapped into the equatorial plane using the different K_p-dependent T89C (*Tsyganenko*, 1989] magnetospheric models and the addition of the perturbation field as determined from the results of *Wing et al.* [1995] (see §6.5.1) are presented in Figure 6.13. The format of this figure is the same as that used in Figures 6.8 and 6.10, with the top panel showing the eastward perturbation component, and the lower panel showing the northward perturbation flow component. The four coloured lines show the results for the different magnetic models dependent on the K_p indices. The perturbation flow is by far the strongest in the east-west component, creating a zonal eastward flow at all local times for positive B_y, with the strongest effect in the midnight sector. The v_N perturbation flow is very weak at all local times, although there is a slight indication of an equatorward perturbation flow in the dusk sector for positive B_y. Again the distortion of the magnetospheric field increases as K_p=3, producing an unreasonably large east-west perturbation flow of several hundreds of m s^{-1} (compared with observations), whereas the lower K_p values produce an effect of several tens of m s^{-1} for this flow component,

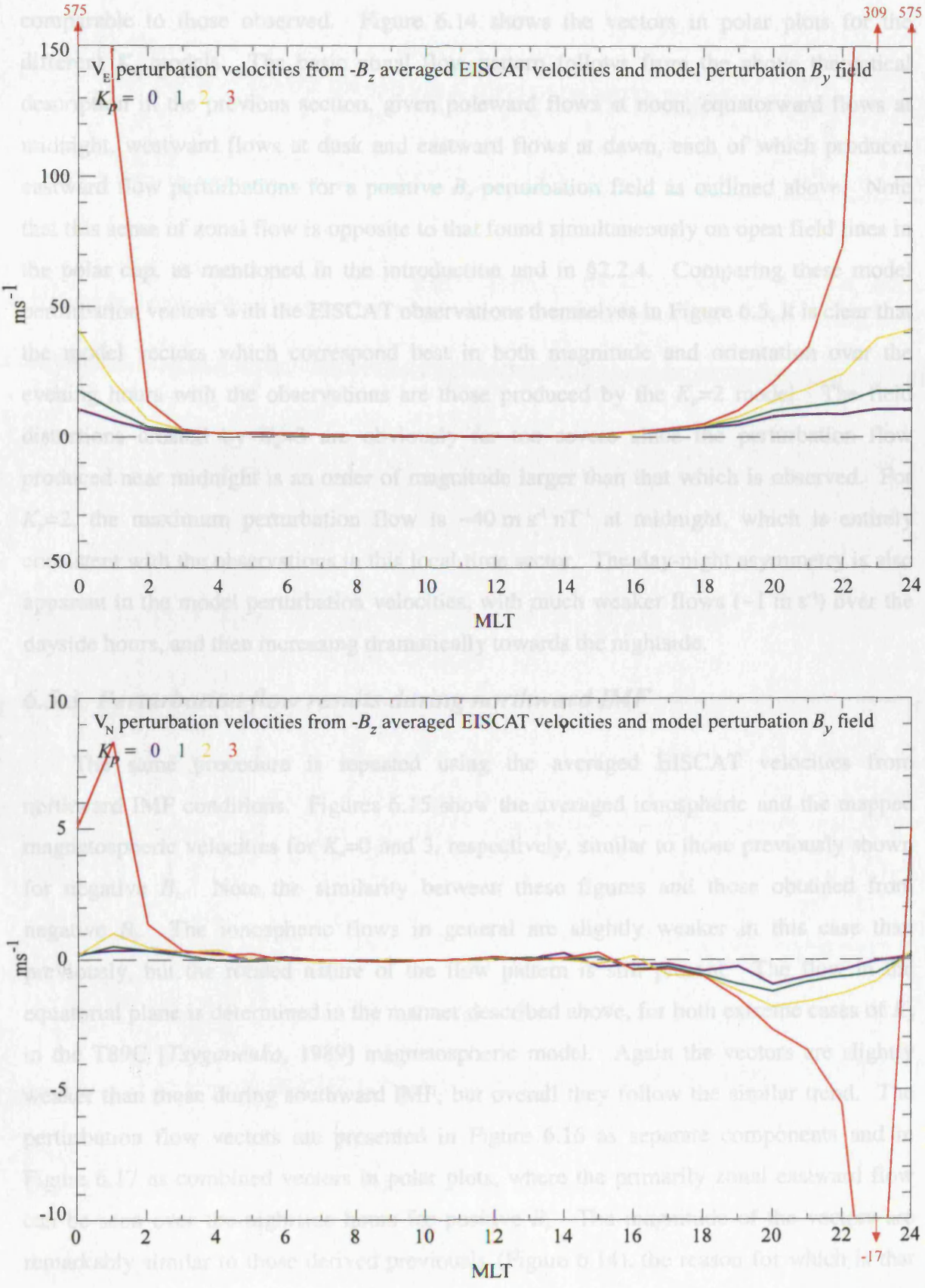

FIGURE 6.13 Ionospheric flow perturbations versus local time produced using the averaged EISCAT velocities during southward IMF conditions and a B_y perturbation field corresponding to 1 nT of IMF B_y. The plot is in the same format as Figures 6.8 and 6.10, with the coloured lines representing the different K_p magnetospheric models and the separate panels displaying the separate perturbation velocity components.

comparable to those observed. Figure 6.14 shows the vectors in polar plots for the different K_p models. The basic zonal flow pattern follows from the above theoretical description in the previous section, given poleward flows at noon, equatorward flows at midnight, westward flows at dusk and eastward flows at dawn, each of which produces eastward flow perturbations for a positive B_y perturbation field as outlined above. Note that this sense of zonal flow is opposite to that found simultaneously on open field lines in the polar cap, as mentioned in the introduction and in §2.2.4. Comparing these model perturbation vectors with the EISCAT observations themselves in Figure 6.5, it is clear that the model vectors which correspond best in both magnitude and orientation over the evening hours with the observations are those produced by the K_p=2 model. The field distortions created by K_p=3 are obviously far too severe since the perturbation flow produced near midnight is an order of magnitude larger than that which is observed. For K_p=2, the maximum perturbation flow is ~40 m s^{-1} nT^{-1} at midnight, which is entirely consistent with the observations in this local time sector. The day-night asymmetry is also apparent in the model perturbation velocities, with much weaker flows (~1 m s^{-1}) over the dayside hours, and then increasing dramatically towards the nightside.

6.5.3 Perturbation flow results during northward IMF

The same procedure is repeated using the averaged EISCAT velocities from northward IMF conditions. Figures 6.15 show the averaged ionospheric and the mapped magnetospheric velocities for K_p=0 and 3, respectively, similar to those previously shown for negative B_z. Note the similarity between these figures and those obtained from negative B_z. The ionospheric flows in general are slightly weaker in this case than previously, but the rotated nature of the flow pattern is still present. The flow in the equatorial plane is determined in the manner described above, for both extreme cases of K_p in the T89C [*Tsyganenko*, 1989] magnetospheric model. Again the vectors are slightly weaker than those during southward IMF, but overall they follow the similar trend. The perturbation flow vectors are presented in Figure 6.16 as separate components and in Figure 6.17 as combined vectors in polar plots, where the primarily zonal eastward flow can be seen over the nightside hours for positive B_y. The magnitude of the vectors are remarkably similar to those derived previously (Figure 6.14), the reason for which is that the initial averaged EISCAT velocities were also similar. One may perhaps assume that the magnetosphere may be in a quieter state due to the positive IMF B_z conditions and so a lower value of K_p ought to be used. However, there does not appear to be an appreciable

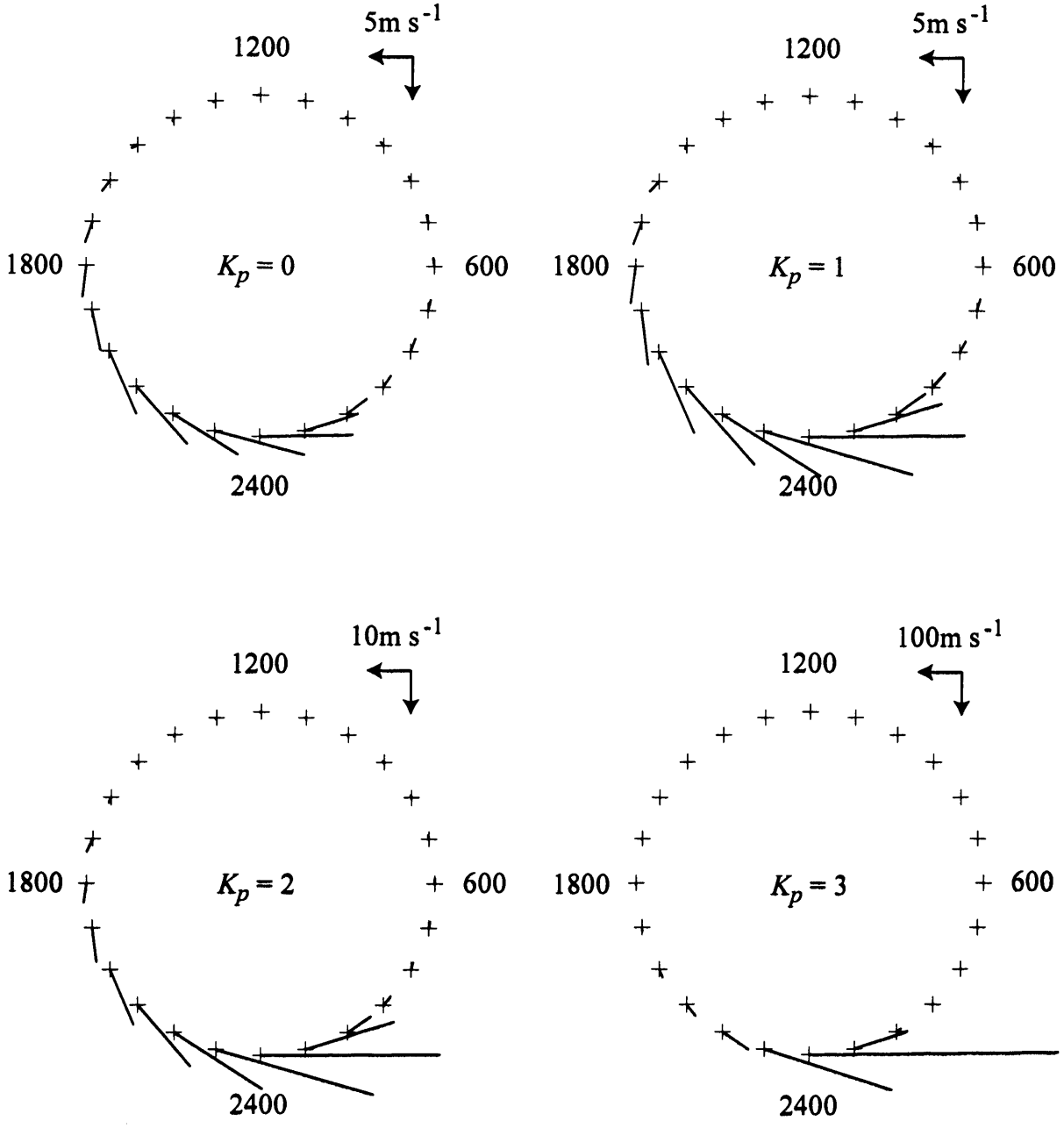

FIGURE 6.14 Same format as Figures 6.9 and 6.11, except now the averaged EISCAT velocities during southward IMF conditions (as shown in Figure 6.12a) have been used together with a perturbation B_y field corresponding to an IMF B_y field of 1 nT, as described in the text. The perturbation vectors derived indicate the flow effect per nT of IMF B_y and can be directly compared to the observations shown in Figure 6.5.

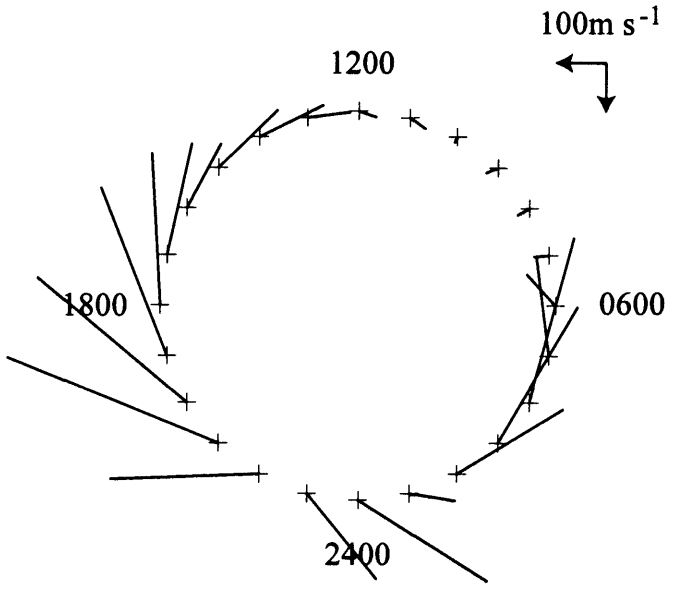

FIGURE 6.15a. Same format as Figure 6.12a, except for the averaged ionospheric flows at the locations of EISCAT during northward IMF.

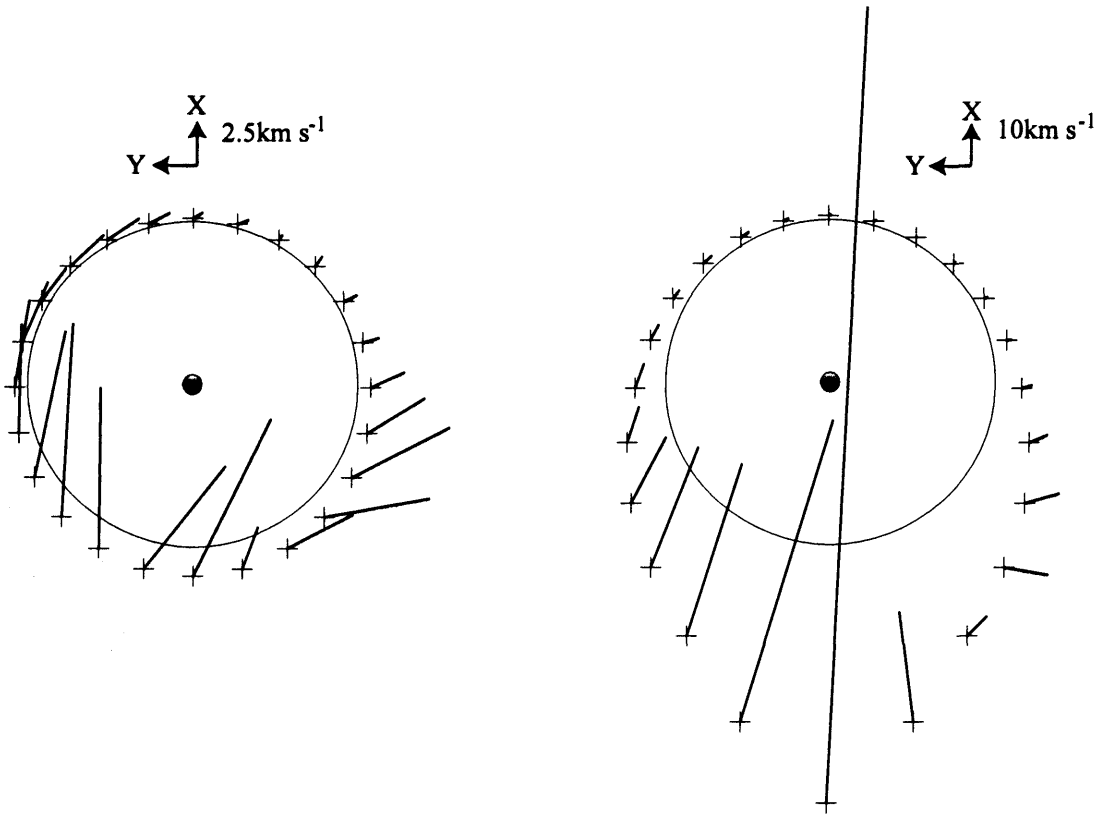

FIGURE 6.15b. Same format as Figure 6.12b, using the positive IMF B_z averaged flows at EISCAT mapped into the magnetospheric equatorial plane using K_p=0 (left diagram) and K_p=3 (right diagram) in the Tsyganenko magnetosphere model. The solid circle indicates the mapped location of EISCAT along dipolar field lines, at an L-shell of 6.2 R_E. The crosses represent the actual position of the mapped EISCAT field lines into the equatorial plane from where the equatorial velocities originate.

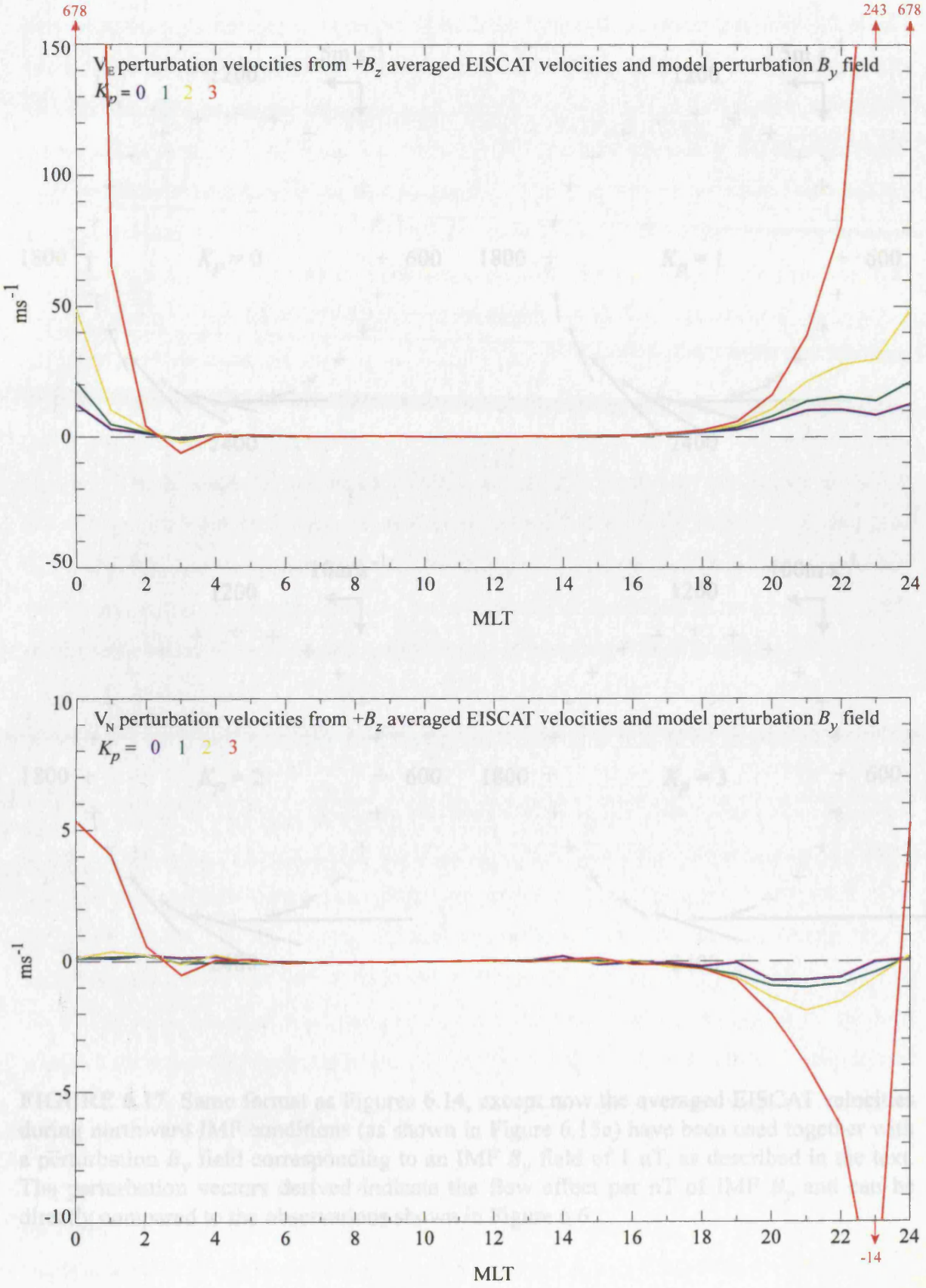

FIGURE 6.16 Same format as Figure 6.13 except using the positive IMF B_z averaged EISCAT velocities, as shown in Figure 6.15a.

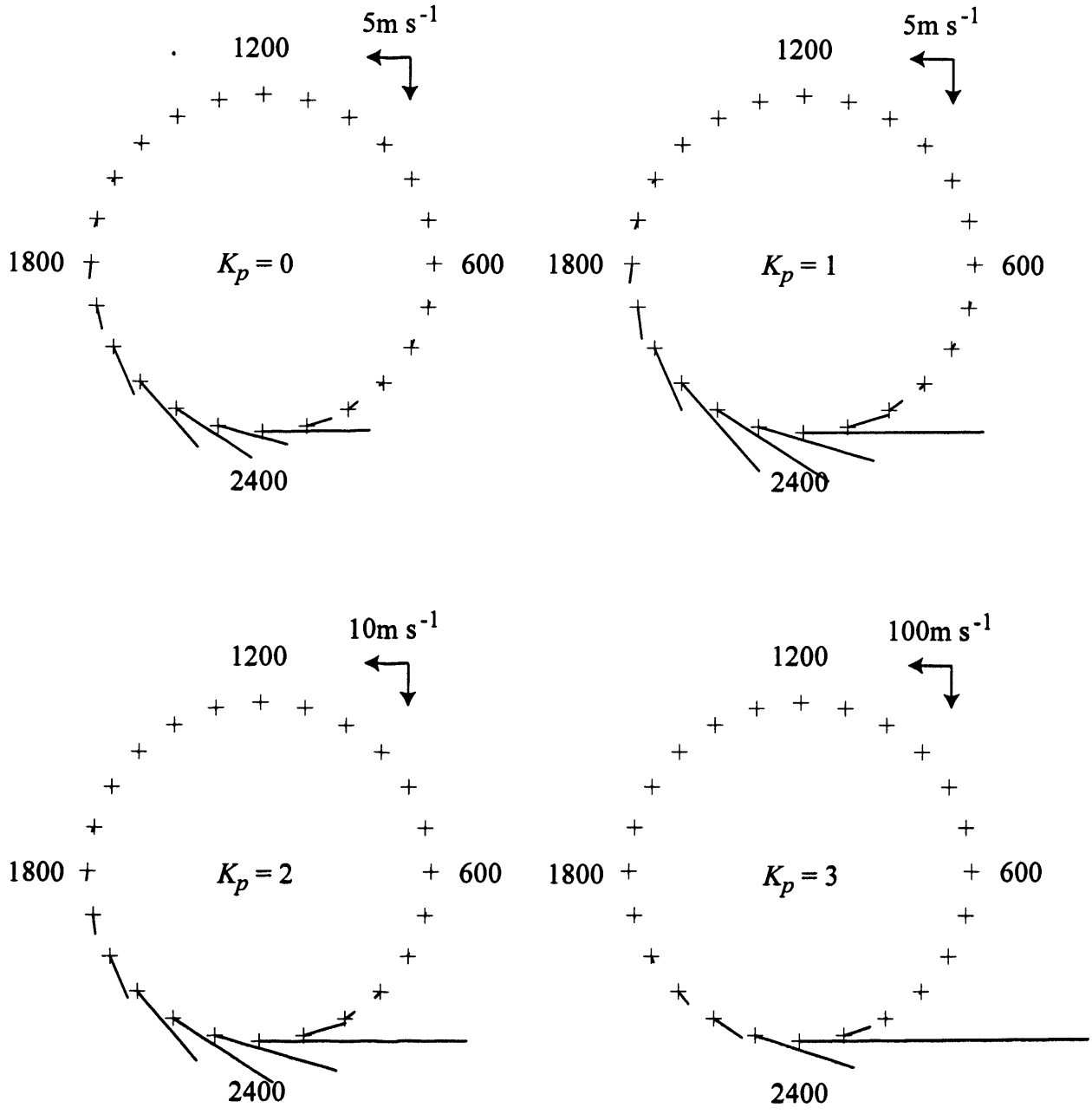

FIGURE 6.17 Same format as Figures 6.14, except now the averaged EISCAT velocities during northward IMF conditions (as shown in Figure 6.15a) have been used together with a perturbation B_y field corresponding to an IMF B_y field of 1 nT, as described in the text. The perturbation vectors derived indicate the flow effect per nT of IMF B_y and can be directly compared to the observations shown in Figure 6.6.

difference between the perturbation flow produced by the K_p=0, 1 and 2 models. It is only when K_p increases to a value of 3 that the perturbation flow changes considerably. The sense of the flow generated using the perturbation field models is in accordance with the observations presented in Figure 6.6, with the K_p=2 model providing the most accurate representation in both magnitude and orientation. The observed perturbation flows reach a maximum value of ~80 m s^{-1} at 0100 MLT, although the average eastward perturbation flow is lower at ~30 m s^{-1}. These compare very well with the flow derived for the K_p=2 model, reaching a maximum of ~50 m s^{-1} at midnight.

For the two data sets used in this study (positive and negative IMF B_z), the most popular values of K_p were calculated from the geomagnetic data available. It was found that a value of K_p=3 best describes the magnetic activity of the two data sets, with the positive IMF B_z data set favouring slightly lower K_p values and the negative IMF B_z favouring slightly higher values. Nevertheless, the typical value for both the data sets used in the analysis presented here is K_p=3. The Tsyganenko magnetospheric model obviously overestimates the amount of distortion that occurs under these conditions producing much larger perturbation flows than expected when a perturbation B_y field is added.

6.6 Summary

A detailed analysis of ~300 h of EISCAT observations of the overhead flow at Tromsø, corresponding to a magnetic latitude of 66.3° in the closed field line region has been undertaken to try to determine the effect the IMF B_y field has on the ionospheric flow. To this end, a cross-correlation study was conducted between the ionospheric flow components and IMF B_y, having further separated the IMF B_y data according to the simultaneous sign of the IMF B_z. Cross correlograms were produced for 2 h intervals of local time with 1 h resolution, and although a response to IMF B_y was clear in the data, many of the cross-correlograms lacked any obvious peak, particularly those on the dayside hours. Moving into the afternoon and evening sectors, the cross-correlation coefficients tended to be higher and provided an indication of possible peaks in the data with lags of a few 10s of min, as Figures 6.1 and 6.2 illustrate. By taking suitable standard delays to represent the time scale over which the flow changes occurred, the perturbation flows associated with IMF B_y are well determined (Figure 6.5 and 6.6), with the most marked effect observed in the nightside hours. For southward IMF conditions (Figure 6.5), the perturbation flows, calculated from the 'gradient' of the regression line associated with the cross-correlation of the flow components with IMF B_y, are observed to be directed

eastward at most local times for positive IMF B_y, peaking at ~60 m s^{-1} nT^{-1} at 0100 MLT, though typically at a slightly lower value of ~40 m s^{-1} nT^{-1} over the nightside region. The perturbation flow is strongest over the evening and nightside hours, with an indication of similar though considerably weaker eastward flows over the dayside. The three delay times chosen (10, 20, 30 min) do not display any significant difference, suggesting that the response of the flow to IMF B_y changes can not be determined from this study. This is also apparent from the lack of peaks in the cross-correlogram, and due to the persistence in the IMF B_y data sets. However, the *flow effect* of IMF B_y is clear, and produces a strong zonal eastward flow which is of the order of a few 10s of m $s^{-1}nT^{-1}$. During northward IMF conditions (Figure 6.6), the perturbation flow results are more scattered, but still exhibit the zonal eastward flow in the presence of positive IMF B_y. Again the strongest effect occurs in the nightside with a perturbation flow of ~80 m $s^{-1}nT^{-1}$ at 0100 MLT (typically ~30 m s^{-1} nT^{-1} over the nightside), although there are also strong westward flows in the evening sector.

To try to understand these flow perturbations, the hypothesis that they could be created by the magnetic field distortions due to the partial penetration of the IMF B_y component into the closed field line region was tested. This idea has previously been discussed by *Cowley* [1981] and *Cowley et al.* [1991], and results in the movement of the ionospheric footprints of these field lines, and hence produces a steady perturbation flow in the ionosphere, even when the flow in the magnetospheric equatorial plane remains unchanged. The T89C [*Tsyganenko*, 1989] magnetospheric field model was used with a range of K_p values (0, 1, 2, 3) to show the extent of the distortion of the magnetospheric field under different magnetic conditions. Using the results of *Wing et al.* [1995] to determine the strength of the perturbation field associated with an external IMF B_y field of 1 nT, the perturbation flow vectors were determined. The results demonstrate that the structure of the magnetospheric field plays a key role in determining the size of the perturbation flow effect. As the magnetospheric field becomes more distorted under the influence of strong magnetic activity, the effect of adding a perturbation field becomes more pronounced, since the size of the added field becomes comparable to the actual field strength on the nightside. This causes a large perturbation flow due to the large displacement between the mapped field lines. Under magnetically quiet conditions, the field is much more dipolar in shape and hence stronger, so the addition of a perturbation field has a smaller effect, producing weak perturbation flows.

Nevertheless, all of the magnetospheric models produce a zonal eastward perturbation flow, although the magnitude of the effect is dominated by the choice of model. A magnetic index of K_p=2 gives the best overall agreement with the observed perturbation vectors determined from both northward and southward IMF conditions. Large flow vectors of ~30-40 m s^{-1} nT^{-1} are derived using this model on the nightside, which is in agreement with those observed. On the dayside, the model shows very weak perturbation vectors, if any at all, which then increase towards the nightside, providing the day-night asymmetry observed in the data.

CHAPTER 7

Summary and conclusions

7.1 Introduction

In this thesis, the effects of solar-terrestrial coupling have been explored in depth, with particular reference to the excitation and decay of plasma flows in the ionospheric region due to changes in the interplanetary magnetic field. The shape and magnitude of the ionospheric flow is known to be modulated in a definite manner in response to changes in the IMF. Many studies have been conducted to try to determine the time scale upon which this response occurs. This thesis provides both statistical and case-study analyses of a large amount of data where the results show the local time variation of the response delay as observed at the EISCAT latitude of 66.3°. Previous studies have not been able to provide the 24 h local time coverage that has been presented here, and therefore have been unable to offer an overall picture of how the flow evolves from the dayside to the nightside. The results in this thesis offer strong support for the excitation and decay flow model proposed by *Cowley and Lockwood* [1992, 1997], with the initial response of the flow occurring on the dayside and the information propagating into the nightside at a phase speed of ~5-10 km s^{-1}.

Also the perturbation flow effects on closed field lines associated with the *y*-component of the IMF were investigated by means of a statistical analysis. The results were explained by means of a model describing the distortion of the field lines in the manner discussed by *Cowley* [1981] and *Cowley et al.* [1991], in which a constant flow in the equatorial plane is mapped along variable field lines into the polar ionosphere. A summary detailing the main results in this thesis is presented in the following section.

7.2 Summary of principal results

7.2.1 Ionospheric flow response delays to IMF B_z changes

A database of ~300 simultaneous hours of high-latitude ionospheric flow observations obtained by the EISCAT UHF radar at a magnetic latitude of 66.3°and measurements of the IMF made by the IMP-8 spacecraft upstream from the Earth's magnetosphere was established over the years 1993-1997. In the first instance, a statistical cross-correlation

analysis was performed on this data set to determine the time scale upon which the ionospheric flow responds to changes in the interplanetary conditions. The results indicate that there are two distinct time scales involved in establishing the flow in the ionosphere after IMF changes take place. The majority of the cross-correlation results involving the east-west flow component showed statistically significant peaks at almost all local times, except in the pre-noon hours where the flow reversal occurred for this flow component. Many of the scatter plots associated with the peak lag from the cross-correlation displayed relatively weak flow for northward IMF which increased monotonically as V^2B_s became more negative, and the lag time was interpreted as the IMF-modulated flow excitation and decay delay time, lying in the range 0-15 min. However, the cross-correlation results obtained in the pre-midnight Harang region demonstrate a distinctly different form to those at other local times. Here the peak of the cross correlograms indicated a significantly longer (~30-40 min) response time although the short time scale response was also evident in the data. The scatter plots associated with the longer response delay showed the presence of non-monotonic behaviour, which subsequently led to the response time being explained in terms of the expansion of the convection flow cells, as opposed to the excitation and decay of convection. Such responses were discarded from the subsequent analysis, since a different feature of the flow was being observed.

Nevertheless, the diurnal variation of the flow response delay between the dayside and the nightside was determined. The average east-west flow response delay time for the dayside cross-correlation data, weighted according to the inverse of the uncertainty estimates of the values, was found to be 3.1±0.8 min, increasing on the nightside to 8.0±2.4 min. Statistically significant responses of the north-south flow were more restricted in MLT, mainly confined to the dayside interval 0700-1300 MLT for poleward flows excited by southward IMF, and the dusk sector 1700-2000 MLT for equatorward flows excited by southward IMF. The weighted average response delay of the former values was 3.7±1.8 min, entirely compatible with the dayside results for the east-west flow. When the data from both velocity components were suitably combined together they indicated that the minimum response delay occurred at ~1400 MLT, implying that information about IMF-related modulations propagates through the ionosphere away from the postnoon sector. The overall weighted average delay for the 12-h sector centred on 1400 MLT was 1.3±0.8 min, while that for the 12-h sector centred on 0200 MLT was 8.8±1.7 min. The phase speed of the information propagating at a constant rate radially

outwards from an epicentre centred at 1400 MLT located on the dayside open-closed field line boundary (taken to lie at 77° magnetic latitude) was calculated to be 9.0 km s^{-1}.

Continuing the study of the response delay determination, an 'event study' was conducted on the same data set. In this study the IMF time series was inspected for sharp polarity changes of the IMF B_z, and the ionospheric measurements examined to determine the time at which the flow responds, either with an increase in flow following a southward turn, or a decrease in flow following a northward turn. A total of 69 such events were analysed, two-thirds of which were flow excitations in response to southward turns of the IMF. For the east-west flow component, minimum delays were centred on the post-noon sector, with average response delays of 5.4±0.5 min on the dayside, increasing to 11.6±1.4 min on the nightside. These values are consistent with, but a little longer (by ~2-3 min) than the cross-correlation values for the east-west flow quoted previously. For the north-south flow component, the dayside average was found to be 5.8±0.5 min, with insufficient event determinations being available on the nightside to take a meaningful average.

The event data for both flow components were also combined together in the same manner as for the cross-correlation study. These data again showed a minimum delay in the post-noon sector, with increased response delays on the nightside. When the simple theoretical model outlined above was fitted to this data, the best fit curve was again obtained for an epicentre of information propagation centred on 1400 MLT, but now with a phase speed of 6.8 km s^{-1}. The average of the delays for the 12-h sector centred on 1400 MLT was found to be 4.8±0.5 min, increasing to 9.2±0.8 min for the 12-h interval centred on 0200 MLT.

Thus both the cross-correlation analysis and the 'event study' provide supporting evidence of an initial short (few minute) response delay on the dayside, increasing to longer response delays (~ten minutes) on the nightside. These results are in accordance with the previous studies of *Etemadi et al.* [1988] and *Todd et al.* [1988], where they also observed the diurnal variation of the flow response, although the local time coverage in these studies was significantly less than has been presented in this thesis. The short response delays found here are also consistent with the overall delays of 8±8min found in the study presented by *Ridley et al.* [1998]. However, the latter authors also interpreted their data as indicating an essentially simultaneous response (within ~1 min) at all local times over the high-latitude region. This conclusion is not in accord with the finding of longer response times on the nightside than on the dayside, as indicated by results from the

event study and the statistical study, though the difference between the day-night responses is only ~6 min (Table 5.1).

7.2.2 *IMF B_y effect on flow on closed auroral zone field lines*

Having demonstrated in Chapters 4 and 5 the effect of IMF B_z on the ionospheric flow together with the time scale over which the changes take place, attention was then turned to investigate the influence of IMF B_y on the ionospheric flow. Since EISCAT is located in the region of closed auroral zone field lines, any effect observed due to IMF B_y would correspond to flow on closed field lines. To this end the ~300 hours of plasma flow data were analysed in a statistical cross-correlation analysis with IMF B_y, having further separated the IMF B_y data according to the polarity of IMF B_z. The results indicate that although there is a flow response to IMF B_y the actual response delay could not be determined with any precision due to the very broad peaks in the cross-correlograms. Further investigation showed that the broad peaks in the cross-correlograms was at least partly due to persistence in the IMF B_y data sets, as would be expected. The largest cross-correlation coefficients were found in the afternoon and evening hours, although no distinct peak was observed in the cross correlogram. By taking suitable standard delays to represent the time scale over which the flow changes occurred, the perturbation flows associated with the IMF B_y were clearly visible (Figure 6.5 and 6.6), with the most marked effect being observed in the nightside hours. The perturbation flow was calculated from the 'gradient' of the regression line in the scatter plot associated with the cross-correlation of the flow components with IMF B_y, and showed an eastward-directed flow perturbation at most local times for positive B_y peaking at ~60 m s^{-1} nT^{-1} at 0100 MLT. The average perturbation flow was estimated at a slightly lower value of ~40 m s^{-1} nT^{-1} over the nightside region. Both southward and northward IMF conditions gave similar results with a strong zonal eastward flow in the presence of a positive IMF B_y perturbation field.

The effect of the partial penetration of IMF B_y into the magnetospheric field was mathematically modelled to determine if the field distortions and movements of the ionospheric footprints of auroral zone field lines due to IMF B_y were sufficient to create the perturbation flows observed. The K_p-dependent Tsyganenko magnetospheric model was used, together with the perturbation B_y field determined by *Wing et al.* [1995] corresponding to 1 nT of IMF B_y field, to determine the strength of the perturbation flow. The mathematical analysis showed that the perturbation effect associated with the field distortion did indeed create a zonal eastward flow at all local times, however the

magnitude of this effect was critically dependent on the choice of magnetospheric model used. By choosing a magnetically quiet magnetosphere (K_p=0), the perturbation flow was predicted to be only a few tens m $s^{-1}nT^{-1}$, whereas as K_p increased to a value of 3, the perturbation flow effect increased to several hundreds of m $s^{-1}nT^{-1}$. The reason for the increase in the perturbation flow was simply the increase in the distortion of the magnetospheric field lines in the model as the magnetic activity increased. As the field lines, particularly on the nightside where the perturbation flow effect is largest, become more tail-like under more strongly disturbed conditions, the addition of a perturbation field comparable in strength to the unperturbed field causes a large displacement of the field lines. This correspondingly results in a large perturbation flow in the ionosphere.

Nevertheless, all of the magnetospheric models produced a zonal eastward perturbation flow, although the magnitude of the effect was dominated by the choice of model. A magnetic index of 2 gave the best overall agreement with the observed perturbation vectors determined from both northward and southward IMF conditions. Large flow vectors of ~30-40 m s^{-1} nT^{-1} were derived using this model on the nightside, which are in agreement with those observed. On the dayside, the model showed very weak perturbation vectors, if any at all, which then increased towards the nightside, providing the day-night asymmetry observed in the data.

7.3 Suggestions for future work

An important point to note in the work presented in this thesis is the localised nature of all of the plasma flow observations. The ionospheric flow vectors are only measured at the position of EISCAT at a magnetic latitude of 66.3° and a height of 278 km in the F-region. This restriction should be overcome in future work by using other radar system. In particular the SuperDARN network of coherent radars [*Greenwald et al.*, 1995] provides global coverage of the ionosphere and can be used in a similar manner to EISCAT to obtain data containing information about the ionospheric plasma configurations as IMF changes occur. The nature of a coherent radar system is to measure line-of-sight velocities at a number of range gates along the length of the radar beams. The beam then progresses in longitude to provide a wide area coverage in which the plasma velocities are measured. Typically a 16-beam scan mode for the SuperDARN radar takes ~2min although the scan resolution can be decreased by a factor of four, thus allowing the plasma configuration in a large area to be monitored on a very short time scale. The SuperDARN network presently covers ~12h of local time and a vast amount of high time resolution data exists from these

radar to conduct case study-type analyses. By collating all the SuperDARN line-of-sight velocity observations during particular polarity changes in IMF B_z, convection maps can be created to demonstrate the flow configuration at the resolution of the scan mode. *Ruohoniemi and Baker* [1998] have recently developed the 'map_potential' model whereby the global ionospheric convection pattern is calculated by a mathematical fitting technique using all available l-o-s velocities measured by the SuperDARN radar, together with data from a statistical model dependent on the IMF conditions at the time of interest. The SuperDARN radar network covers ~12 h of local time in the northern hemisphere and so would provide a vast amount of data to input into the 'map_potential' model. This would give an accurate description of the flow configuration at high-time resolution, from which the evolving nature of the convection pattern can be determined. With perfect data coverage, the overall development of the ionospheric convection pattern in response to changing IMF conditions can be followed in detail.

Also many of the SuperDARN radar point over the polar region providing a large amount of high-latitude coverage, thus offering an insight into the response of the flow at such latitudes inside the open field line region. A progression of the results presented here would be that the flow response should be shorter as the observation point approaches the open-closed field line boundary, since this would be the location of 'first contact' as reconnection occurs at the magnetopause boundary. As one progresses away from this region the response delay increases as the information propagates over the observation point. Thus if a large amount of ionospheric flow data near the open-closed field line boundary were analysed to calculate the response delays as done here, then theoretically even shorter response delays ought to be observed. By using the SuperDARN network these theories can be tested and the day-night asymmetry in the flow can also be investigated further.

Further study involving the influence of IMF B_y on the ionospheric flow in both the open and closed field line regions can also be undertaken. The results presented here have solely involved the closed auroral zone flows, showing that a zonal eastward perturbation flow occurs for a positive B_y perturbation field. Several studies can be conducted to extend the results presented here. Firstly, it is clear that the shape and distortion of the actual magnetospheric field model used is of great importance when trying to model the perturbation effects. Thus it would be sensible to try to determine as accurately as possible the configuration of the magnetosphere as an initial state before any perturbation field is added. New Tsyganenko models have been derived which include information about the

solar wind/IMF conditions as well as the magnetic activity within the magnetosphere. This may prove to be a better model since many more parameters are used to determine the shape and size of the magnetosphere. Also the amount of penetration of IMF B_y into the magnetosphere needs to be studied in greater detail. The perturbation field used to derive the results presented in this thesis was calculated from a statistical analysis of a large amount of geosynchronous satellite data [*Wing et al.*, 1995]. The penetration effect of IMF B_y was determined as a fraction of the external IMF B_y present. However, the results from other studies using similar data sets [*Nagai*, 1987; *Cowley and Hughes*, 1983] calculate a perturbation field differing by almost a factor of two on the nightside where the distortion is greatest. There seems to be a certain amount of disagreement about how much the IMF B_y field actually penetrates into the magnetosphere and this is one of the crucial elements of establishing the size of the perturbation flow created due to the distortion of the field lines. By decreasing the perturbation field by a factor of two, the perturbation flow would also decrease by roughly the same factor.

References

Akasofu, S.-I., The development of the auroral substorm, *Planet. Space Sci.*, **12**, 273, 1964.

Axford, W.I. and C.O. Hines, A unifying theory of high-latitude geophysical phenomena and geomagnetic storms, *Can. J. Phys.*, **39**, 1961.

Baker, D.N., E.W. Hones Jr., J.B. Paynes and W.C. Feldman, A high time resolution study of interplanetary parameter correlations with *AE*, *Geophys. Res. Lett.*, **8**, 170, 1981.

Baker, D.N., R.D. Zwiki, S.J. Bame, E.W. Hones Jr., B.T. Tsurutani, E.J. Smith and S. -I. Akasofu, An *ISEE 3* high time resolution study of interplanetary parameter correlations with magnetospheric activity, *J. Geophys. Res.*, **88**, 6230, 1983.

Bargatze, L.F., D.N. Baker, R.L. McPherron, and E.W. Hones Jr., Magnetospheric impulse response for many levels of geomagnetic activity, *J. Geophys. Res.*, **90**, 6387, 1985.

Baumjohann, W., Ionospheric and field-aligned current systems in the auroral zone: A concise review, *Adv. Space Res.*, **2**, 55 1983.

Beynon, W.J.G. and P.J. Williams, Incoherent scatter of radio waves from the ionosphere, *Rep. Prog. Phys.*, **41**, 909, 1978.

Bowles, K.L., Observations of vertical incidence scatter from the ionosphere at 41 Mc/sec., *Phys. Rev. Lett.*, **1**, 454, 1958.

Burch, J.L, P.H. Reiff, J.D. Menietti, R.A. Hellis, W.B. Hanson, S.D. Shawham, E.G. Shielley, M. Sugiura, D.R. Weimer and J.D. Winningham, IMF By dependent plasma flow and Birkeland currents in the dayside magnetosphere 1., Dynamics Explorer Observations, *J. Geophys. Res.*, **90**, 1577, 1985.

Burrage, M, Radar studies of high-latitude convection flows, Ph.D. Thesis, University of Leicester, UK, 1988.

Burton, R.K., R.L. McPherron, and C.T. Russell, An empirical relationship between interplanetary conditions and D_{st}, *J. Geophys. Res.*, **90**, 4204, 1975.

Chapman, S. and V.C.A. Ferraro, A new theory of magnetic storms, *Nature*, **126**, 129, 1931.

Chapman, S. and V.C.A. Ferraro, A new theory of magnetic storms, *Terr. Magn. Atmosph. Elec.*, **36**, 171-186, 1932.

Clauer, C.R., and R.L. McPherron, Mapping the local time-universal time developments of magnetospheric substorms using mid-latitude magnetic observations, *J. Geophys. Res.* **79**, 2811, 1974.

Clauer, C.R. and Y. Kamide, DP-1 and DP-2 current system for the March 22, 1979 substorms, *J. Geophys. Res.*, **90**, 1343, 1985.

Clauer, C.R. and E. Friis-Christensen, high-latitude dayside electric fields and currents during strong northward interplanetary magnetic field: Observation and model simulation, *J. Geophys. Res.*, **93**, 2749, 1988.

Clauer, C.R., R.L. McPherron, C. Searls and M. Kivelson, Solar wind control of auroral zone geomagnetic activity, *Geophys. Res. Lett.*, **8**, 915, 1981.

Cowley, S.W.H., A qualitative study of the reconnection between the Earth's magnetic field and an interplanetary magnetic field of arbitrary orientation, *Radio Sci.*, **8**, 903, 1973.

Cowley, S.W.H., Magnetospheric asymmetries associated with the Y-component of the IMF, *Planet. Space Sci.*, **29**, 79, 1981.

Cowley, S.W.H., Solar wind control of magnetospheric convection, *Proc. Conf. Achievements of the IMS*, ESA SP-217, p.483, 1984.

Cowley, S.W.H., The auroral ionosphere and its coupling to the magnetosphere and solar wind, in *Modern Ionospheric Science*, p.32, 1996.

Cowley, S.W.H. and W. Hughes, Observations of an IMF sector effect in the Y magnetic field component at geostationary orbit, *Planet. Space Sci.*, **31**, 73, 1983.

Cowley, S.W.H. and M. Lockwood, Excitation and decay of solar wind-driven flows in the magnetosphere-ionosphere system, *Ann. Geophysicae*, **10**, 103, 1992.

Cowley, S.W.H. and M. Lockwood, Incoherent scatter radar observations related to magnetospheric dynamics, *Adv. Space Res.*, **20**, (4/5)873, 1997.

Cowley, S.W.H., J.P. Morelli and M. Lockwood, Dependence of convective flows and particle precipitation in the high-latitude ionosphere on the *X* and *Y* components of the interplanetary magnetic field, *J. Geophys. Res.*, **96**, 5557, 1991.

Cowley, S.W.H., A.P. van Eyken, E.C. Thomas, P.J. Williams and D.M. Willis, Studies of the cusp and auroral zone with incoherent scatter radar: the scientific and technical case for a polar-cap radar, *J. Atmos. Terr. Phys.*, **52**, 645, 1990.

Davies, K., Ionospheric radio propagation, *Dover*, 1966.

de la Beaujardière, O., D.S. Evans, Y. Kamide and R.P. Lepping, response of the auroral oval precipitation and magnetospheric convection to changes in the interplanetary magnetic field, *Ann. Geophys.*, **5**, 519, 1987.

Dougherty, J.P. and D.T. Farley, A theory of incoherent scatter of radio waves by a plasma: 3. Scattering in a partly ionised gas, *J. Geophys. Res.*, **66**, 5473, 1963.

du Castel, F. and G. Vasseur, Evaluationdes performances d'un sondeur ionosphérique à diffusion incohérent, *Ann. Telecommun.*, **27**, 239, 1972.

Dungey, J.W., Interplanetary field and the auroral zone, *Phys. Res. Lett.*, **6**, 47-48, 1961.

Dungey, J.W., The structure of the exosphere or adventures in velocity space, in *Geophysics, the Earth's Environment*, eds. C. DeWitt, J. Hieblot, and A. Lebeau, Gordon and Breach, New York, p503, 1963.

Elphic, R.C., M. Lockwood, S.W.H. Cowley, and P.E. Sandholt, Flux transfer events at the magnetopause and in ionosphere, *Geophys. Res. Lett.*, **17**, 2241, 1990

Etemadi, A., S.W.H. Cowley, M. Lockwood, B.J.I. Bromage, D.M. Willis, and H. Lühr, The dependence of high-latitude dayside ionospheric flows on N-S component of IMF: a high time resolution correlation analysis using EISCAT 'Polar' and AMPTE-UKS and IRM data, *Planet. Space Sci.*, **36**, 471, 1988.

Evans, J.V., Theory and practice of ionosphere study by Thomson scatter radar, *Proc. IEEE*, **57**, 496, 1969.

Fabry, C., *C. r. hedb. Seance Acad. Sci.*, Paris, **187**, 777, 1928.

Fairfield, D., Average and unusual locations of the Earth's magnetopause and bow shock, *J. Geophys. Res.*, **76**, 6700, 1971.

Farley, D.T., Incoherent scatter correlation function measurements, *Radio Sci.*, **4**, 935, 1969.

Farley, D.T., Multiple-pulse incoherent scatter correlation function measurements, *Radio Sci.*, **7**, 661, 1972

Fejers, J., Scattering of radio waves by an ionised gas in thermal equilibrium, *J. Geophys. Res.*, **65**, 2635, 1960.

Folkestad, K., T. Hagfors and S. Westerlund, EISCAT: An updated description of technical charcteristics and operational capabilities, *Radio Sci.*, **18**, 867, 1983.

Freeman, M.P. and D.J. Southwood, The effect of magnetospheric erosion on mid- and high latitude ionospheric flows, *Plant. Space Sci.*, **36**, 509, 1988.

Freeman, M.P., C.J. Farrugia, L.F. Burlaga, M.R. Hairston, M.E. Greenspan, J.M. Ruohoniemi, and R.P. Lepping, The interaction of a magnetic cloud with the earth:

ionospheric convection in the northern and southern hemispheres for a wide range of quasi-steady interplanetary magnetic field conditions, *J. Geophys. Res.*, **98**, 7633, 1993.

Friis-Christensen, E. and J. Wilhjelm, Polar cap currents for different directions of the interplanetary magnetic field in the y-z plane, *J. Geophys. Res.*, **80**, 1248, 1975.

Friis-Christensen, E., M.A. Hendry, C.R. Clauer and S. Vennerstrøm, Ionospheric travelling convection vortices observed near the polar cleft: A triggered response to sudden changes in the solar wind, *Geophys. Res. Lett.*, **15**, 253, 1988.

Gordon, W.E., Incoherent scatter of radio waves by free electrons with application to space exploration by radar, *Proc. IRE*, **46**, 1824, 1958.

Gosling, J.T., M.F. Thomsen, S.J. Bame, R.C. Elphic, and C.T. Russell, Plasma flow reversals in the dayside magnetopause and the origin of the asymmetric polar cap convection, *J. Geophys. Res.*, **95**, 8741, 1990.

Gosling, J.T., J.S. Asbrigde, S.J. Bame and W.C. Feldman, Solar wind speed variations 1962-1974, *J. Geophys. Res.*, **81**, 5061, 1976.

Greenwald, R.A., K.B. Baker, J.M. Ruohoniemi, J.R. Dudeney, M. Pinnock, N. Martin, J.M. Leonard, and R.P. Lepping, Simultaneous conjugate observations of dynamic variations in high-latitude dayside convection due to changes in IMF B_y, *J. Geophys. Rev.*, **95**, 8057, 1990.

Greenwald, R.A. , K.B. Baker, J.R. Dudeney, M. Pinnock, T.B. Jones, E.C. Thomas, J.-P. Villain, J.-C. Cerisier, C. Senior, C. Hanuise, R.D. Hunsucker, G. Sofko, J. Koehler, E. Nielsen, R. Pellinen, A.D.M. Walker, N. Sato and H. Yamagishi, DARN/SuperDARN: A global view of the dynamics of high-latitude convection, *Space. Sci. Rev.*, **71**, 761, 1995.

Hagfors, T., Density fluctuations in a plasma in a magnetic field with applications to the ionosphere, *J. Geophys. Res.*, **66**, 1699, 1961.

Hagfors, T., P.S. Kildal, H.J. Kärcher, B. Liesenkötter and G. Schroer, VHF parabolic cylinder antenna for incoherent scatter radar research, *Radio Sci.*, **17**, 1607, 1982.

Hairston, M.R., and R.A. Heelis, Response time of the polar convection pattern to changes in the north-south direction of the IMF, *Geophys. Res. Lett.*, **22**, 631, 1995.

Hargreaves, J.K., The solar-terrestrial environment, *Cambridge Atmospheres and Space Science Series*, Cambridge University Press, 1992.

Heppner, J.P., Polar cap electric field distributions related to the interplanetary magnetic field direction, *J. Geophys. Res.*, **27**, 4877, 1972.

Heppner, J.P. and N.C. Maynard, Empirical high-latitude electric field models, *J. Geophys. Res.*, **92**, 4467, 1987.

Holzer, T.E., in *Solar System Plasma Physics Vol. 1*, North Holland, p103, 1979.

Holzer, R.E., and J.A. Slavin, An evaluation of three predictors of geomagnetic activity, *J. Geophys. Res.*, **87**, 2558, 1982.

Holzworth, R.H. and C.-I Meng, Auroral boundary variations and the interplanetary magnetic field, *Planet. Space Sci.*, **32**, 25, 1984.

Hones, E.W., in *Magnetic Reconnection*, ed. Hones, A.G.U. Monograph 30, 1984.

Hundhausen, A.J., An interplanetary view of coronal holes, in *Coronal Holes and High Speed Wind Streams*, ed. J.B. Zirker, Boulder Colorado Associated University Press, p.225, 1977.

Hundhausen, A.J., The solar wind, in *Introduction to Space Physics*, eds. M.G. Kivelson and C.T. Russell, Cambridge University Press, p.91, 1995.

Iijima, T, R. Fujii, T.A Poterma and N.A. Saflekos, Field-aligned currents in ths outh polar cusp and their relationship to the interplanetary magnetic field, *J. Geophys. Res.*, **83**, 5595, 1978.

Jørgensen, T.S., E. Friis-Christensen, and J. Wilhjelm, Interplanetary magnetic field and high-latitude ionospheric currents, *J. Geophys. Res.*, **77**, 1976, 1972.

Kennel, Ch.F., Convection and substorms, paradigms of the magnetospheric phenomenology, in *International Series on Astronomy and Astrophysics*, Oxford University Press, p.1, 1995.

Kivelson, M.G. and C.T. Russell, *Introduction to Space Physics*, Cambridge University Press, 1995.

Lehtinen, M. S. and I. Häggström, A new modulation principal for incoherent scatter measurements, *Radio Sci.*, **22**, 625, 1987.

Lester, M., O. de la Beaujardière, J.C. Foster, M.P. Freeman, H., Lühr, J.M., Ruohoniemi and W. Swider, The response of the large scale ionospheric convection pattern to changes in the IMF and substorms: Results from the SUNDIAL 1987 campaign, *Ann. Geophysicae*, **11**, 556, 1993.

Lockwood, M., A.P. van Eyken, B.J.I. Bromage, D.M. Willis and S.W.H. Cowley, Eastward propagation of a plasma convection enhancement following a southward turning of the interplanetary magnetic field, *Geophys. Res. Lett.*, **13**, 72, 1986.

Lockwood, M and M.P. Freeman, Recent observations relating to solar wind-magnetosphere coupling, *Philos. Trans. R. Soc. London Ser. A*, **328**, 98, 1989.

Lockwood, M, S.W.H. Cowley and M.P. Freeman, The excitation of plasma convection in the high-latitude ionosphere, *J. Geophys. Res.*, **95**, 7961, 1990.

Lockwood, M., The excitation of ionospheric convection, *J. Atmos. Terr. Phys.*, **53**, 177, 1991.

Lockwood, M., Solar wind-Magnetosphere coupling, *Proc. of the EISCAT Internat. School in Corsica*, edited by D. Alcaydé, September 1995.

Lockwood, M., I.W. McCrea, G.H. Millward, R.J. Moffet and H. Rishbeth, EISCAT observations of ion composition and temperature anisotropy in the high-latitude F-region, *J. Atmos. Terr. Phys.*, **55**, 895, 1993a.

Lockwood, M., J. Moen, S.W.H. Cowley, A.D. Farmer, U.P. Løvhaug, H. Lühr, and V.N. Davda, Variability of dayside convection and motions of the cusp/cleft aurora, *Geophys. Res. Lett.*, **20**, 1011, 1993b.

Lockwood, M. and S.W.H. Cowley, Comment on "A statistical study of the ionospheric convection response to changing interplanetary magnetic field conditions using the assimilative mapping of ionospheric electrodynamics technique" by A. J. Ridley et al., *J. Geophys. Res.*, **104**, 4387, 1999.

Lui, A.T.Y., A synthesis of magnetospheric substorm models, *J. Geophys. Res.*, **96**, 1849, 1991.

Lyons, L.R., A simple model for polar cap convection patterns and generation of θ auroras, *J. Geophys. Res.*, **90**, 1561, 1985.

Mansurov, S.M., New evidence of the relationship between magnetic fields in space and on Earth, *Geomagn. Aeron.*, Engl. Transl., **9**, 662, 1969.

McPherron, R.C., Growth phase of a magnetospheric substorm, *J. Geophys. Res.*, **75**, 5529, 1970.

McPherron, R.L. and R.H. Manka, Dynamics of the 1054 U.T. March 2, 1979 substorm event: CDAW 6, *J. Geophys. Res.*, **90**, 1175, 1985.

Moorcroft, R.J. and K. Schlegel, Evidence for non-Maxwellian ion velocity distributions in the F-region, *J. Atmos. Terr. Phys.*, **50**, 455, 1988.

Mozer, F.S., W.D. Gonzales, F. Bogott, M.C. Kelley and S. Schutz, High-latitude electric field and the three-dimensional interaction between the interplanetary and terrestrial magnetic fields, *J. Geophys. Res.*, **79**, 56, 1974.

Nagai, T, Interplanetary magnetic field B_y effects on the magnetic field at synchronous orbit, *J. Geophys. Res.*, **92**, 11215, 1987.

Newell, P.T., C.-I. Meng, D.G. Sibeck, and R.P. Lepping, Some low-altitude cusp dependencies on the interplanetary magnetic field, *J. Geophys. Res.*, **94**, 8921, 1989.

Nishida, A., Coherence of geomagnetic *DP-2* fluctuations with interplanetary magnetic variation, *J. Geophys. Res.*, **73**, 1795, 1968.

Nishida, A. and Y. Kamide, Magnetospheric processes preceding the onset of an isolated substorm: a case study of the March 31, 1978 substorm, *J. Geophys. Res.*, **88**, 7005, 1983.

Opgenoorth, H.J. and R.J. Pellinen, The reaction of the global convection electrojets to the onset and expansion of the substorm current wedge, in *Substorms-4*, eds. S. Kokubun and Y. Kamide, Astrophysics and Space Science Library, p.663, March 1999.

Parker, E.N., Dynamics of interplanetary gas and magnetic fields, *Astrophys. J.*, **128**, 664-76, 1958.

Perreault, P. and S.-I. Akasofu, A study of geomagnetic storms, *Geophys. J. R. Astr. Soc.*, **54**, 547, 1978.

Pellinen, R.J., W. Baumjohann, W.J. Heikkila, V.A. Sergeev, A.G. Yahnin, G. Marklund, and A.O. Melnikov, Event study of pre-substorm phases and their relation to the energy coupling between the solar wind and magnetosphere, *Planet. Space Sci.*, **30**, 371, 1982.

Peredo, M., J.A. Slavin, E. Mazur and S.A. Curtis, Three dimensional position and shape of the bow shock and their variation with the Alfvénic, sonic and magnetosonic Mach numbers and interplanetary magnetic field orientation, *J. Geophys. Res.*, **100**, 7907, 1995.

Petrinec, S.P. and C.T. Russell, External and internal influences on the size and shape of the magnetopause, *Geophys. Res. Lett.*, **20**, 339, 1993.

Poulter, E.M., W. Allan, J.G. Keys, and E. Nielsen, Plasmatrough ion mass densities determined from ULF pulsation eigenperiods, *Planet. Space Sci.*, **32**, 1069, 1984.

Priest, E.R., Introduction to solar activity, in *Solar system magnetic fields*, ed. E. R. Priest, Dordrecht: Reidel Publishing Cot., (p.1-24), 1985.

Priest, E.R., The Sun and its magnetohydrodynamics, in *Introduction to Space Plasma Physics*, ed. M. G. Kivelson and C. T. Russell, (p.58-89), 1995.

Reiff, P.H., and J.L. Burch, IMF By-dependent plasma flow and Birkeland currents in the dayside magnetosphere. 2. A global model for northward and southward IMF, *J. Geophys. Res.*, **90**, 1595, 1985.

Reiff, P.H., R.W. Spiro, and T.W. Hill, Dependence of polar cap potential drop on interplanetary parameters, *J. Geophys. Res.*, **86**, 7639, 1981.

Reiff, P.H., R.W. Spiro, R. A. Wolf, Y. Kamide and J. H. King, Comparison of polar cap potential drops estimated from solar wind and ground magnetometer data: CDAW 6, *J. Geophys. Res.*, **90**, 1318, 1985.

Ridley, A.J., L. Gang, C.R. Clauer and V.O. Papitashvili, A statistical study of the ionospheric convection response to changing interplanetary magnetic field conditions using the assimilative mapping of ionospheric electrodynamics technique, *J. Geophys. Res.*, **103**, 4023, 1998.

Ridley, A.J., G. Lu, C.R. Clauer and V.O. Papitashvili, Reply, *J. Geophys. Res.*, **104**, 4393, 1999.

Rishbeth, H, *European Space Agency Rep*, **ESA SP-135**, 85, 1978.

Rishbeth, H., P.R. Smith, S.W.H. Cowley, D.M. Willis, A.P. van Eyken, B.J.I. Bromage and S.R. Crothers, Ionospheric response to changes in the interplanetary magnetic field observed by EISCAT and AMPTE-UKS, *Nature*, **318**, 451, 1985.

Rishbeth, H. and P.J. Williams, The EISCAT ionospheric radar: The systema dn its early results, *Q. J. R. Astr. Soc.*, **26**, 478, 1985.

Roelof, E.C. and D.G. Sibeck, Magnetopause shape as a bivariate function of interplanetary magnetic field B_Z and solar wind dynamic pressure, *J. Geophys. Res.*, **98**, 21421, 1993.

Rostoker, G.,S.-I Akasofu, J. Foster, R.A. Greenwald, Y. Kamide, K. Kawaski, A.T.Y. Lui, R.L. McPherron and C.T. Russell, Magnetospheric substorm-definition and signatures, *J. Geophys. Res.*, **85**, 1663, 1980.

Ruohoniemi, J.M., R.A. Greenwald, O. de la Beaujardière, and M. Lester, The response of the high-latitude dayside ionosphere to an abrupt northward transition in the IMF, *Ann. Geophysicae*, **11**, 544, 1993.

Ruohoniemi, J.M., and R.A. Greenwald, The response of high-latitude convection to a sudden southward IMF turning, *Geophys. Res. Lett.*, **25**, 2913, 1998.

Ruohoniemi, J.M., and K.B. Baker, Large scale imaging of high-latitude convection with the Super Dual Auroral Radar Network HF radar observation, *J. Geophys. Res.*, **103**, 20797, 1998.

Russell, C.T. and R.C. Elphic, ISEE observations of Flux Transfer Events at the dayside magnetopause, *Geophys. Res. Lett.*, **6**, 33, 1979.

Saunders, M., M.P. Freeman, D.J. Southwood, S.W.H. Cowley, M. Lockwood, J.C. Samson, C.J. Farrugia, and T.J. Hughes, Dayside ionospheric convection changes in response to long-period interplanetary magnetic field oscillations: determination of the ionospheric phase velocity, *J. Geophys. Res.*, **97**, 19373, 1992.

Siscoe, G.L. and T.S. Huang, Polar cap inflation and deflation, *J. Geophys. Rev.*, **90**, 543, 1985.

Stern, D.P, A study of the electric field in the open magnetospheric model, *J. Geophys. Res.*, **78**, 729, 1973.

Svalgaard, L., Sector structures of the interplanetary magnetic field and daily convection of geomagnetic fields at high latitudes, *Geophys. Pap.*, **R-6**, Dan. Meteorl. Inst., Copenhagen, Denmark, 1968.

Taylor, J.R.T, M. Lester and T.K. Yeoman, A superposed epoch analysis of geomagnetic storms, *Ann. Geophysicae*, **12**, 1174, 1994.

Thomson, J.J., *Conduction of electricity through gases*, Cambridge University Press, 1906.

Todd H., S.W.H. Cowley, M. Lockwood, D.M.Willis, and H. Lühr, Response time of the high-latitude dayside ionosphere to sudden changes in the N-S component of IMF, *Planet. Space Sci.*, **36**, 1415, 1988.

Turunen, T., GEN-SYSTEM – A new experimantal philosophy for EISCAT radars, *J. Atmos. Terr. Phys.*, **48**, 777, 1986.

Tyganenko, N.A., A magnetospheric magnetic field model with a warped tail current sheet, *Planet. Space Sci.*, **37**, 5, 1989.

Vasyliunas, V. M., Plasma distribution and flow, in *Physics of the Jovian Magnetosphere*, ed. A. J. Dessler (p.395-453), Cambridge University Press, 1983.

Villante, U., Some remarks on the structure of the distant neutral sheet, *Plant. Space Sci.*, **23**, 723, 1975.

Wannberg, G., I. Wolf, L. –G. Vanhainen, K. Koskenniemi, J. Röttger, M. Postila, J. Markkanen, R. Jacobsen, A. Stenberg, R. Larsen, S. Eliassen, S. Heck and A. Huuskonen, The EISCAT Svalbard radar: A case study in modern incoherent scatter radar system design, *Radio Sci.*, **32**, 2283, 1997.

Weimer, D.R., Models of the high-latitude electric potentials derived with a least error fit of spherical harmonic coefficients, *J. Geophys. Res.*, **100**, 19595, 1995.

Willis, D.M, M. Lockwood, S.W.H. Cowley, A.P. van Eyken, B.J.I. Bromage, H. Rishbeth, P.R. Smith, and S.R. Crothers, A survey of simultaneous observations of

the high-latitude ionosphere and interplanetary magnetic field with EISCAT and AMPTE-UKS, *J. Atmos. Terr. Phys.*, **48**, 987, 1986.

Wing, S., P.T Newell, D.G. Sibeck and K.B. Baker, A large statistical study of the entry of interplanetary magnetic field *y*-component into the magnetosphere, *Geophys. Res. Lett.*, **22**, 2083, 1995.

Yeoman, T. K., M. D. Burrage, M. Lester, T. R. Robinson and T. B. Jones, Long term variations of radar auroral backscatter and the interplanetary sector structure, *J. Geophys. Res.*, **95**, 14885, 1990.